EURASIAN JOURNAL OF CHEMISTRY

2025. Vol. 30 No. 1(117)

EURASIAN JOURNAL OF CHEMISTRY

2025

Volume 30, No. 1 (117)

Founded in 1996

Published 4 times a year

Karaganda
2025

CONTENTS

ORGANIC CHEMISTRY

PHYSICAL AND ANALYTICAL CHEMISTRY

CHEMICAL TECHNOLOGY

ORGANIC CHEMISTRY

Kirti N. Sarwade[1] ⓘⅅ, Kuldeep B. Sakhare[1] ⓘⅅ,
Mahadeo A. Sakhare[1] ⓘⅅ, Shailendrasingh V. Thakur[2]* ⓘⅅ

[1]Department of Chemistry, Balbhim Arts, Science and Commerce College, Beed, Maharashtra, India;
[2]Department of Chemistry, Milliya, Arts, Science and Management Science College, Beed, Maharashtra, India
(*Corresponding author′s e-mail: svthakur1972@gmail.com)

Neuroprotective, Anticancer and Antimicrobial Activities
of Azo-Schiff Base Ligand and Its Metal Complexes

The synthesis of metal complexes of Mn(II), Co(II), Ni(II), Cu(II) Zn(II) and VO(II) from azo-Schiff base ligand was carried out by the condensation reaction of (*E*)-5-chloro-2-hydroxy-3-((3-nitrophenyl)diazenyl) benzaldehyde and 2-amino-4-nitrophenol. The structure of the synthesized azo-Schiff base ligand was confirmed by 1H-NMR spectra, mass spectra, FT-IR spectra. After confirmation of the azo-Schiff base ligand, metal complexes of Mn(II), Co(II), Ni(II), Cu(II), Zn(II) and VO(II) were synthesized using metal salts. These synthesized metal complexes were characterized by FT-IR spectra, elemental analysis, electronic spectra, thermal analysis, X-ray powder diffraction, molar conductivity etc. In biological studies, the neuroprotective and anticancer activities of azo-Schiff base ligand and metal complexes were investigated by methylthiazole tetrazolium (MTT) assay on SHSY-5Y Neuroblastoma Cell line and MCF-7 human breast cancer cell line using Tacrine (TAC) and 5-Flourouracil (5-FU) as reference standard drugs, respectively. Also, antimicrobial potential was screened against two gram-positive (*Staphylococcus aureus* and *Bacillus subtilis*), two gram-negative (*Klebsiella pneumonia* and *Pseudomonas aeruginosa*) bacteria and three fungi (*Penicillium chrysogenum*, *Tricoderma viride*, and *Aspergillus niger*). Based on all the data obtained, it was concluded that metal complexes exhibit higher biological activity than ligands based on the azo-Schiff base.

Keywords: azo-Schiff base ligand, coordination compounds, metal complexes, azomethine, biological activity, neuroprotective, anticancer, antimicrobial.

Introduction

Breast cancer is the most common type of cancer and the second leading cause of death for women globally. We lose almost 50000 women worldwide each year due to the breast cancer. Designing effective drugs to manage drug resistance and its side effects is a challenge [1, 2]. The progressive neurodegenerative brain disorder known as Alzheimer's disease that cause neuronal death in the brain and it causes dementia, memory loss, cognitive impairment, severe behavioural abnormalities and finally death. Alzheimer's disease affects around 40 million peoples now and is predicted to reach 150 million by 2050. Many scientists from the world are busy to find effective solution on the breast cancer as well as Alzheimer's disease [3–5]. The Schiff base ligands are extensively used in the metal-ligand chemistry, medicinal chemistry, organic synthesis as catalyst [6]. Schiff bases exhibit different biological activities such as anticancer, antimycobacterial, antibacterial, antidepressant, antianalgesic, antidiabetic, antiviral, anti-infective [7–12]. The Schiff base is condensation product of primary amine with aldehyde. This reaction was firstly studied by noble prize winner, German scientist chemist Hugo Schiff in 1864 [13]. Metal complexes of Schiff base ligands have attracted to researcher because of biological activity in addition to their applications and spectroscopic charac-

teristics and also the presence of donor atoms including nitrogen, oxygen and sulphur [14]. They are used as medications to treat cardiovascular disease, diabetes, cancer and inflammation [15]. According to the literature review, derivatives of salicylaldehyde with one or more halogen atoms in the aromatic ring exhibited a variety of biological activities including antifungal, antibacterial and antimicrobial properties [16].

In the present study, we have focused on the synthesis of novel azo halogenated salicylaldehyde and their Schiff base ligand with 2-amino-4-nitrophenol and its metal complexes.

Experimental

Materials and Methods

Spectrochem supplied all compounds used at analytical grade. The solvents which included petroleum ether, ethanol, ethyl acetate and n-hexane were obtained from a nearby supplier and purified via distillation. The progress of reactions was tracked using thin-layer chromatography utilizing pre-coated aluminium sheets. Mass spectra were captured using a MALDI-TOF mass spectrometer. ^{1}H-NMR spectra were recorded on BRUKER 400MHz ^{1}H-NMR-spectrometer in DMSO, TMS was utilized as the internal standard. Infrared spectra were recorded with FTIR-spectrophotometer (SHIMADZU) and KBr pellets encompassing the spectral range from 4000 to 400 cm^{-1}. Electronic spectra were scanned using SHIMADZU Model 1800 UV-spectrophotometer in DMSO encompassing at room temperature the wavelength range of 200 to 600 nm. A digital conductivity meter model 304 was used to measure molar conductivity in a DMSO solvent. Using TGA instruments the complexes were subjected to a nitrogen environment for thermal analysis.

Biological Activity

Neuroprotective Activity and Anticancer Activity by MTT Assay

The Neuroprotective and Anticancer activity of azo-Schiff base ligand and its metal complexes was carried out using 3-(4, 5-dimethyl thiazol-2-yl)-2, 5-diphenyl tetrazolium bromide (MTT) assay on the SHSY-5Y Neuroblastoma Cell line and MCF-7 human breast cancer cell line respectively. 1×10^4 cells/ml in culture medium was incubated for 24 hours at 37 °C with 5 % CO$_2$. The cell line was seeded at 1×10^4 cells/well in 100 μl of culture medium at a concentration of 70 μl. 100 μl of the sample was placed into each micro plate. In control wells DMSO (0.2 % in PBS) and cell lines were grown. Every sample was incubated for three rounds. In order to determine the percentage of living cells following cultivation and the survival rate of control cells by controls were maintained. In a CO$_2$ incubator with 5 % CO$_2$ cell cultures were maintained at 37 °C for 24 hours. After the incubation period 20 μl of MTT reagent was applied and the media was completely removed. Cells were cultivated for four hours at 37 °C in a CO$_2$ incubator following MTT injection used a microscope to look for formazan crystal development in the wells. Only living cells were able to transform the yellowish MTT into a dark-coloured formazan. After removing the medium, 200 μl DMSO was added and the mixture was left at 37 °C. Using an Elisa microplate reader set to 570 nm in wavelength 3 samples absorbance were measured in order to conduct analysis. The percent of inhibition and cell viability is calculated by formula given below:

$$\text{Inhibition percentage} = \frac{\text{Control OD} - \text{Sample OD}}{\text{Control OD}} \times 100 \, ;$$

$$\text{Viability percentage} = \frac{\text{Absorbance of treated cells}}{\text{Absorbance of control cells}} \times 100 \, .$$

Antimicrobial activity

The National Committee for Clinical Laboratory Standards (NCCLS) 2002 standards were followed for conducting the antibacterial activity utilizing the agar disk diffusion method. To begin, Petri dishes were prepared using MHA (Mueller-Hinton) for bacterial cultures and PDA (Potato Dextrose) for yeast cultures. Preparation of McFarland 0.5 turbidity standards by using the solution of 0.5 ml BaCl$_2$·2H$_2$O (Barium Chloride Dihydrate) + 99.5 ml of H$_2$SO$_4$ with constant stirring to maintain the suspension and stored in a dark room at 22 to 25 °C. Following the incubation, the application of azo-Schiff base ligand and the metal complexes was made to agar plates that had been previously inoculated. Each plate underwent a visual examination. The resulting zones of inhibition displayed a uniform circular pattern within the growth lawn. The diameters of these inhibition zones along with the diameter of the well in millimetres were measured using sliding callipers and recorded.

Synthesis of Azo-Halogenated Salicylaldehyde

The Azo halogenated salicylaldehyde named (*E*)-5-chloro-2-hydroxy-3-((3-nitrophenyl)diazenyl) benzaldehyde has been synthesized by the diazotization coupling reaction [17].

Diazonium Salt Formation

Solution (a): In 100 ml beaker 5.138 g (0.0372 mol) of 3-nitroaniline, added 25 ml concentrated hydrochloric acid and 20 ml cold distilled water. The solution was cooled to 0 °C using an ice-salt bath.

Solution (b): In a 100 ml beaker 3.105 g (0.045 mol) of sodium nitrite dissolved in 15 ml distilled water and the solution cooled to 0 °C using an ice-salt bath. Solution (b) was added dropwise to a solution (a) while stirring continuously once both solutions (a) and (b) had attained 0 °C. During the addition, the reaction temperature was maintained below 10 °C. A pinch of urea was added to decompose the excess nitrous acid and filtered the diazonium salt solution.

Azo-coupling reaction: 5.824 g (0.0372 mol) of 5-Chlorosalicylaldehyde dissolved in 10 % of NaOH solution and stirred to make the clear solution, cooled the solution to 0 °C in ice-salt bath. Then the above solution of diazonium salt was added to this solution of salicylaldehyde with constant stirring. The reaction mixture was stirred in ice-salt bath for ten minutes after the addition was finished. After obtaining the product with a golden yellow colour, it was filtered, cleaned with cold distilled water, recrystallized and kept in an airtight container (Scheme 1).
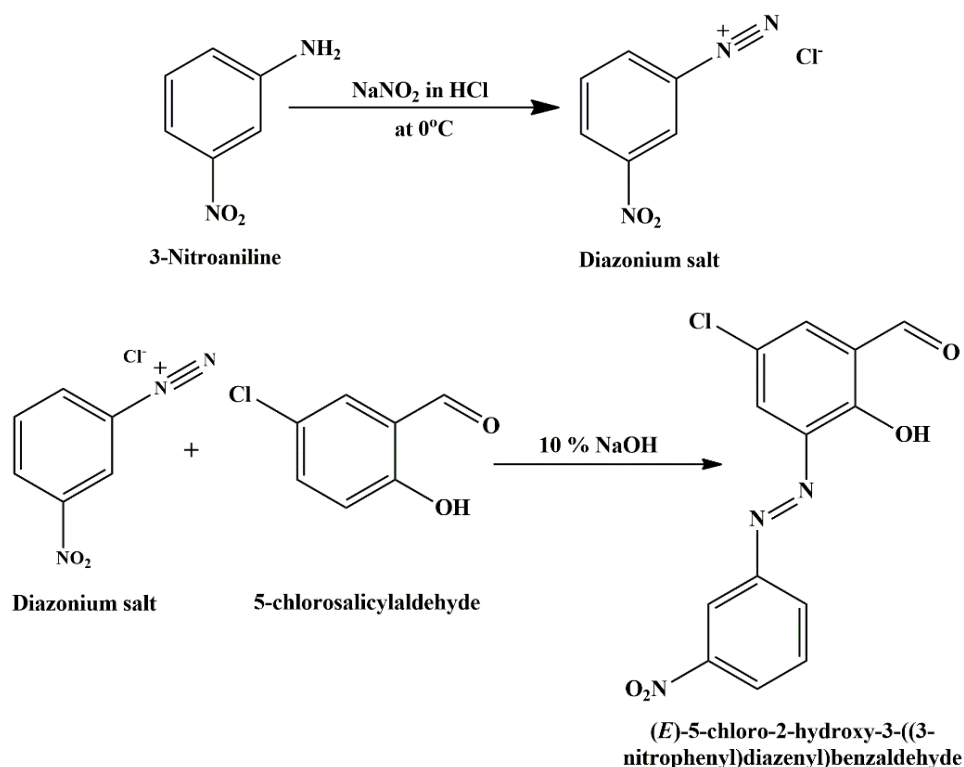
Scheme 1. Synthesis of Azo-halogenated salicylaldehyde

General Procedure of Synthesis of Azo-Schiff Base Ligand (L)

The azo-Schiff base ligand was synthesized by using 3.050 g (0.01 mol) of (*E*)-5-chloro-2-hydroxy-3-((3-nitrophenyl) diazenyl) benzaldehyde dissolved in 25 ml of hot ethanol and 1.541 g (0.01 mol) of 2-amino-4-nitrophenol dissolved in 15 ml of hot ethanol. These two ethanolic solutions were mixed and then refluxed with a temperature range of 70–80 °C for duration of 60 minutes. The reaction's progress was continuously monitored by thin-layer chromatography (TLC). The reaction mixture yielded a solid product with an orange precipitation at room temperature. This solid product was isolated by filtration and recrystallized using ethanol. The product was dried in vacuum over anhydrous $CaCl_2$ overnight to give analytically pure product in good yields [17, 18].
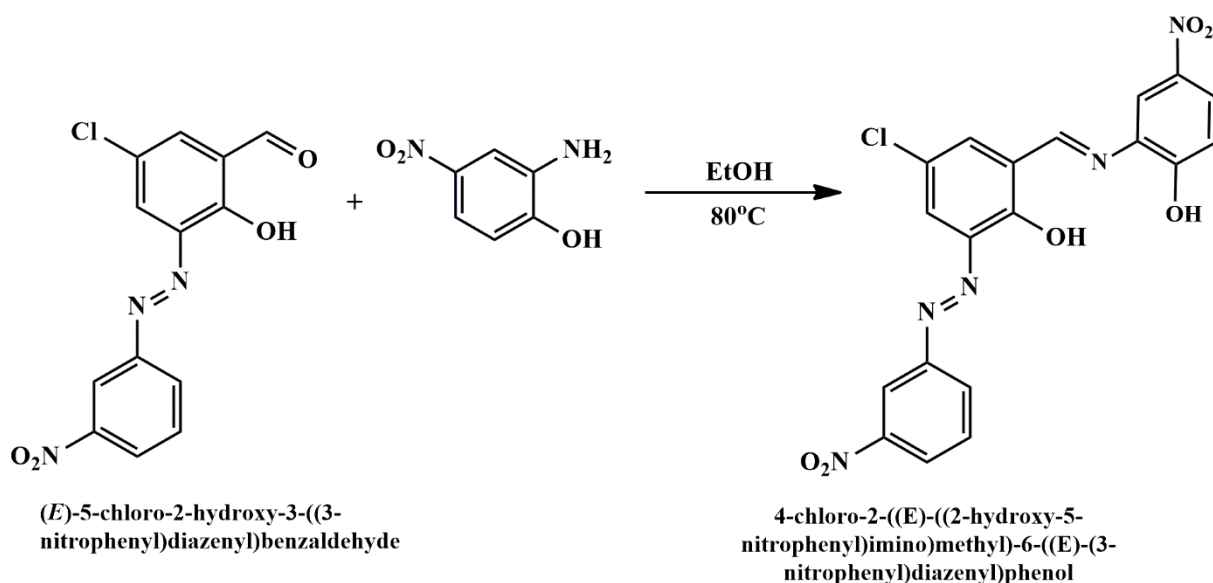
Scheme 2. Synthesis of Azo-Schiff base ligand

General Procedure of Synthesis of Metal Complexes (M)

0.441 g (0.001mol) of azo-Schiff base ligand (L) was dissolved in 15 ml of ethanol. Simultaneously, 0.001 mole of metal acetate salts, including Mn(II), Co(II), Ni(II), Cu(II), Zn(II) metals and the sulphate of VO(II) were dissolved in 15 ml of ethanol. These two ethanolic solutions were mixed and refluxed for a period of 4 hours within the temperature range of 60–80 °C. The reaction resulted in the formation of various coloured metal complexes in the reaction mixture. These complexes were subsequently isolated by filtration, washed with cold ethanol and then dried under vacuum [19].
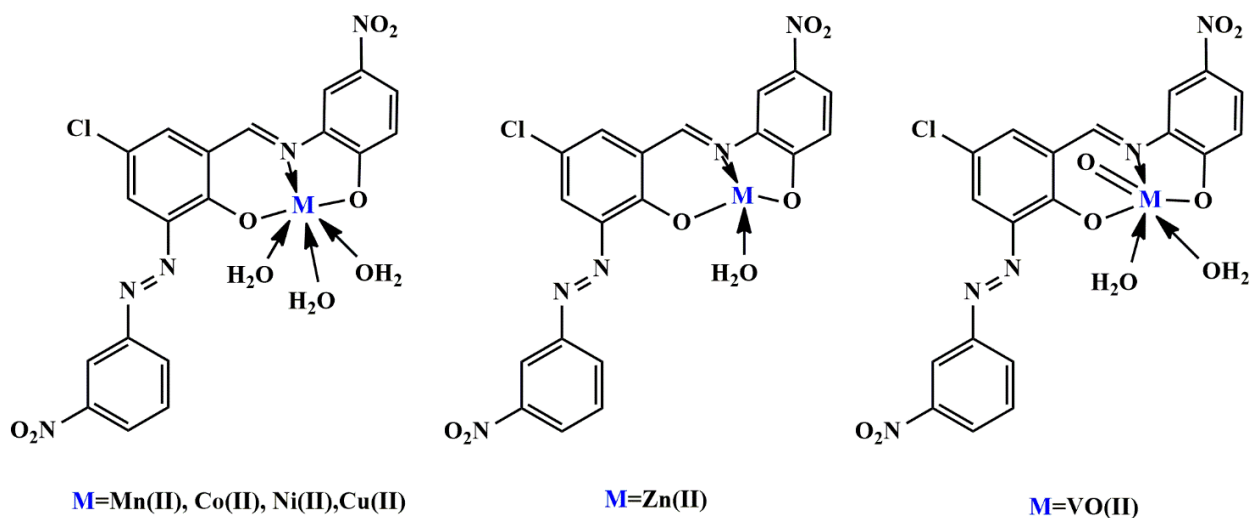
Scheme 3. Proposed structure of metal complexes

Results and Discussion

The synthesized azo-Schiff base ligand (L) and its metal complexes (M) display distinct colours. The metal complexes are insoluble in water but soluble in organic solvents such as chloroform, DMSO and DMF. They are stable in an air. Physicochemical data of azo-Schiff base ligand and metal complexes is shown in Table 1.

Physiochemical data of azo-Schiff base ligand and metal complexes

No	Compounds	Physical Appearance	Melting Point, °C	Yield, %	Elemental Analysis Found, % (Calculated in %)		
					C	H	N
1	Azo-salicylaldehyde	Golden yellow	127–132	78	50.99 (51.08)	2.50 (2.64)	12.30 (13.75)
2	Ligand (L)	Orange	160–167	72	51.20 (51.66)	3.04 (2.74)	15.25 (15.85)
3	Mn (II) Complex	Brown	>300	54	46.30 (46.13)	1.52 (2.04)	15.05 (14.16)
4	Co (II) Complex	Dark Brown	>300	65	41.52 (41.29)	3.58 (2.92)	13.08 (12.67)
5	Ni (II) Complex	Brown	>300	51	41.21 (41.30)	3.13 (2.92)	13.11 (12.68)
6	Cu (II) Complex	Green	>300	73	40.16 (40.94)	2.78 (2.89)	12.02 (12.57)
7	Zn (II) Complex	Yellow	>300	68	43.96 (43.62)	2.00 (2.31)	12.92 (13.39)
8	VO (II) Complex	Green	>300	55	43.22 (43.49)	2.01 (2.31)	13.96 (13.35)

Spectroscopic Analysis

Mass Spectra of Azo Halogenated Salicylaldehyde and Azo-Schiff Base Ligand (L)

The mass spectra in Figures S1, S2 show a peak at m/z 306.1(M+1) and m/z 442.21(M+1), indicating the formation of azo halogenated salicylaldehyde and azo Schiff base ligand (L), respectively.

^{1}H-NMR Spectra of Azo Halogenated Salicylaldehyde and Azo-Schiff Base Ligand (L)

*Azo halogenated salicylaldehyde (*Fig. S3)*:* ^{1}H NMR (400 MHz, DMSO) δ 10.97 (s, 1H), 10.22 (s, 1H), 8.64–8.22 (m, 1H), 8.20–7.80 (m, 1H), 7.77–7.59 (m, 2H), 7.12 (dd, J = 8.6 Hz, 2H) [20].

Azo-Schiff base ligand (L) (Fig. S4)*:* ^{1}H NMR (400 MHz, DMSO) δ 13.12 (s, 1H), 10.25 (s, 1H), 9.11 (s, 1H), 8.30 (d, J = 2.7 Hz, 1H), 8.12 (dd, J = 9.0, 2.8 Hz, 1H), 7.85 (d, J = 2.7 Hz, 1H), 7.57 (dd, J = 8.8, 2.8 Hz, 1H), 7.52–7.43 (m, 2H), 7.41 (dd, J = 8.7, 2.8 Hz, 1H), 7.15 (d, J = 9.0 Hz, 1H), 7.04 (d, J = 3.8 Hz, 1H) [21].

IR Spectra of L and Metal Complexes

The IR spectra of the azo-Schiff base ligands and metal complexes are shown in Figures S5–S11 and listed in Table 2. In the IR spectra of azo-Schiff base ligand band appeared at 1595 cm^{-1} which shifted to lower frequencies in the range of 1571–1577 cm^{-1} in all the metal complexes. This change implies that the metal ion and the nitrogen of the Schiff base enter into coordination, resulting in the formation of metal complexes [22]. The phenolic -OH group was identified by a large band in ligand located at 3195 cm^{-1} and 3108 cm^{-1}. Interestingly, this band vanished in every metal complex indicating that the phenolic oxygen had coordinated by deprotonation. This observation is further supported by the IR spectra of ligand where a >C–O band at 1232 cm^{-1} shifted to higher frequencies range of 1255–1273 cm^{-1} in all the metal complexes [23, 24]. The azo group's band was originally observed at 1384 cm^{-1}. New bands in the range of 441–447 cm^{-1} and 518–528 cm^{-1} respectively appeared in the metal complexes and were attributed to M–N and M–O vibrations [20]. These findings suggest the formation of coordination bonds among the metal ions and ligand leading to changes in IR spectra which provide insights into the chelation process. The band of >C–Cl exhibited at 642–650 cm^{-1} in ligand and metal complexes. A band of –OH rocking at 821–837 cm^{-1} suggests the presence of coordinated water in all metal complexes [25]. The azo-Schiff base coupled to the metal ion in a tridentate manner according to the overall infrared data.

FTIR stretching frequency of azo-Schiff base ligand and metal complexes in cm^{-1}

Sr. No	Compounds	OH– (Phenolic)	>C=N– (Azomethine)	–N=N–	>C–O	>C–Cl	M–N	M–O
1	Ligand (L)	3108, 3195	1595	1384	1232	642	–	–
2	Mn (II)	–	1573	1373	1271	648	447	525
3	Co (II)	–	1571	1373	1255	648	447	522
4	Ni (II)	–	1577	1373	1257	650	441	526
5	Cu (II)	–	1575	1373	1257	646	443	518
6	Zn (II)	–	1573	1377	1273	648	439	526
7	VO (II)	–	1575	1375	1271	648	447	528

Electronic Spectra and Magnetic Susceptibility of L and Metal Complexes (M)

The electronic spectra of azo-Schiff base ligand and metal complexes were recorded in DMSO (Dimethylsulfoxide) at ambient temperature between 200–600 nm. The electronic spectra were used to characterize the ligand field surrounding the central metal ion. The electronic spectrum of L contains bands at 290 as well as at 250 nm, due to the $n\to\pi^*$ and $\pi\to\pi^*$ transitions. Mn(II) complexes exhibit bands in their electronic spectra at 350 nm which could indicate an octahedral geometry suggested metal to ligand charge transfer transition. The electronic spectra of Co(II) complexes show broad peaks at 420, 370, and 340 nm, which can be tentatively assigned to $^4T_{1g}\to{}^4T_{2g}$, $^4T_{1g}\to{}^4T_{1g(P)}$ and $^4T_{1g}\to{}^4A_{2g}$, respectively. The magnetic moment (μ) value of 3.92 µB suggests that the Co(II) ion is arranged in an octahedral form. The electronic spectra of Ni(II) complexes show bands at 420, 370 and 340 nm which may be tentatively assigned to $^3A_{2g}\to{}^3T_{2g}$, $^3A_{2g}\to{}^3T_{1g(f)}$ and $^3A_{2g}\to{}^3T_{1g(P)}$ correspondingly. The value of the µat 2.98 µB suggests an octahedral geometry around the Ni(II) ion. Cu(II) complexes electronic spectra showed bands at 420 and 350 nm which may be assigned to $^2E_g\to{}^2T_{2g}$ and ligand to metal charge transitions correspondingly. The value of the magnetic moment at 1.82 µB suggests an distorted octahedral geometry around Cu(II) ion. Electronic spectra of Zn(II) complexes at 360 nm,, which can mediate charge transfer from the metal to the ligand, show a diamagnetic moment suggesting tetrahedral geometry. The VO(II) complex shows bands at 440, 390 and 325 nm, which may be attributed to the $^2B_2\to{}^2E$, $^2B_2\to{}^2B_1$ and $^2B_2\to{}^2A_1$ transfers. The value of the magnetic moment is 1.79 µB, which is characteristic of the geometry of a square pyramidal structure [26–28]. The absorption band is shown in Figure S12.

Measurement of Molar Conductance of L and Metal Complexes (M)

The measured molar conductance values for L and the metal complexes in a 10^{-3} M dimethylsulfoxide (DMSO) solution at room temperature ranged between 8.5 to 13 S·mol^{-1}·cm^2. The relatively low conductance values listed in Table 3 clearly indicate that both L and the metal complexes are non-electrolytic in nature [29].

T a b l e   3

Magnetic moment and molar conductance of azo-Schiff base ligand and metal complexes

Sr. No.	Compounds	Molar conductance in S·mol^{-1}cm^2	Magnetic Moment in µB	Proposed Structure
1	Ligand (L)	–	–	–
2	Mn (II) Complex	9.2	5.12	Octahedral
3	Co (II) Complex	8.5	3.92	Octahedral
4	Ni (II) Complex	10	2.98	Octahedral
5	Cu (II) Complex	13	1.82	Octahedral
6	Zn (II) Complex	8.5	Dia.	Tetrahedral
7	VO (II) Complex	12	1.79	Square Pyramidal

Thermal Analysis of Metal Complexes (M)

The thermal stability of the metal complexes synthesized from azo-Schiff base ligand was evaluated under a nitrogen atmosphere covering a temperature range from ambient temperature to 800 °C. The decomposition of the metal complexes took place in two distinct steps. In the first step, the loss of coordinated water molecule takes place up to 250 °C in all metal complexes. Finally, the ligand loss occurred in the temperature range of 300–500 °C and at last metal oxides were formed above 500 °C [25]. The graph observed from the data is given in Figure S13.

Powder X-Ray Diffraction of Metal Complexes (M)

The P-XRD of metal complexes derived from ligand were scanned in the range from 2θ = 20–80° at wavelength of 1.540 Å. This is given in Table 4 and Figure S14. The Mn(II) and Co(II) complex shows orthorhombic crystal system. The metal complexes Ni(II), VO(II) show monoclinic and Cu(II), Zn(II) show the triclinic crystal system [24].

T a b l e 4

P-XRD metalcomplexes

Sr. No.	Compounds	No. of reflections	Maxima (2θ)	d-Value	Lattice Constant(Å)	Unit cell volume	Axis and Axis angle	Z-Value	Crystal System
1.	Mn(II) Complex	17	9.34	9.462	$a = 7.3928$ $b = 10.4467$ $c = 18.9250$	1461.585	$a \neq b \neq c$ and $\alpha = \beta = \gamma = 90°$	8	Orthorhombic
2.	Co(II) Complex	14	10.39	8.509	$a = 4.7487$ $b = 5.9711$ $c = 17.0170$	482.516	$a \neq b \neq c$ and $\alpha = \beta = \gamma = 90°$	4	Orthorhombic
3.	Ni(II) Complex	13	11.32	7.807	$a = 7.8473$ $b = 7.7271$ $c = 9.2429$	557.614	$a \neq b \neq c$ and $\alpha = \gamma = 90° \neq \beta$	4	Monoclinic
4.	Cu(II) Complex	11	6.81	12.976	$a = 9.4450$ $b = 10.3974$ $c = 13.3661$	1173.400	$a \neq b \neq c$ and $\alpha \neq \beta \neq \gamma \neq 90°$	2	Triclinic
5.	Zn(II) Complex	14	5.31	16.627	$a = 4.3633$ $b = 9.2982$ $c = 16.7339$	662.568	$a \neq b \neq c$ and $\alpha \neq \beta \neq \gamma \neq 90°$	2	Triclinic
6.	VO(II) Complex	23	26.36	12.041	$a = 25.5512$ $b = 7.5077$ $c = 17.0818$	3088.439	$a \neq b \neq c$ and $\alpha = \gamma = 90° \neq \beta$	8	Monoclinic

Biological Activity of L and Metal Complexes

Neuroprotective Activity

The Neuroprotective activity of L and metal complexes was conducted using the MTT assay on the SHSY-5Y Neuroblastoma cell line at different concentration. The results are shown in Table 5.

T a b l e 5

Anti-Alzheimer activity of azo-Schiff base ligand and metal complexes

Sr. No	Compounds	Concentration of Sample (μg/ml)	Cell Viability in %	IC50
1	Standard TAC	25	70.20	49.01
		50	77.41	
		100	78.68	
2	L	25	46.92	78.51
		50	47.92	
		100	47.89	
3	Co(II) Complex	25	39.82	93.28
		50	39.68	
		100	40.55	
4	Cu(II) Complex	25	70.01	50.59
		50	73.59	
		100	75.39	
5	Zn(II) Complex	25	70.59	52.28
		50	70.17	
		100	72.78	

Based on the data presented in Table 5, it can be concluded that Cu(II) and Zn(II) complexes exhibit higher neuroprotection than the ligand and the Co(II) complex compared to the standard reference drug tacrine. The IC50 of Cu(II) and Zn(II) complexes is 50.59 and 52.28 μg/ml. These metal complexes are non-toxic to SHSY-5Y Neuroblastoma cell line. In neurodegenerative disorders, the Schiff base ligand Cu(II) and Zn(II) complexes are frequently dysregulated. Greater cell viability is preferable in the neuroprotective dis-

orders as it shields to the SHSY-5Y Neuroblastoma Cell line from harm which is ideal for neuroprotection [30–33].

Anticancer Activity

The anticancer activity for both L and the metal complexes was examined using the MTT assay on the MCF-7 human breast cancer cell line at different concentration. The results are shown in Table 6.

T a b l e 6

Anticancer activity of azo-Schiff base ligand and metal complexes

Sr. No	Compounds	Concentration of Sample (µg/ml)	Cell Inhibition in %	IC50
1	Standard 5-FU	10	79.14	44.99
		40	83.29	
		100	88.79	
2	L	10	24.38	102.56
		40	37.06	
		100	39.78	
3	Co(II) Complex	10	69.20	51.22
		40	71.40	
		100	77.72	
4	Cu(II) Complex	10	38.79	84.44
		40	43.62	
		100	47.95	
5	Zn(II) Complex	10	46.47	76.75
		40	50.60	
		100	51.53	

As can be seen in Table 6, the Co(II) complex should have anticancer components that are more active in inhibiting the growth of MCF-7 breast cancer cell line compared to other metal complexes. The Co(II) complex demonstrated good anticancer activity compared to L against standard drug 5-FU [34, 35].

Antimicrobial Activity

In our investigation, we evaluated the antibacterial activities of L and its metal complexes against gram-positive bacteria i.e. *Staphylococcus aureus* and *Bacillus subtilis* as well as gram-negative bacteria i.e. *Klebsiella pneumonia* and *Pseudomonas aeruginosa*. We also examined their antifungal activity against *Penicillium chrysogenum*, *Tricoderma viride,* and *Aspergillus niger*. The results are shown in Table 7.

T a b l e 7

Antimicrobial activity of azo-Schiff base ligand and metal complexes (Zone of inhibition in mm)

Sr. No.	Compounds	Antibacterial activity				Antifungal activity		
		S. aureus	*B. subtilis*	*K. pneumoniae*	*P. aeruginosa*	*P. Chrysogenum*	*T. Viride*	*A. Niger*
1	Ligand (L)	11	14	10	8	8	8	12
2	Mn (II)	16.5	23.5	19.5	8	15.5	30.5	24
3	Co (II)	18	21	16	18.5	19.5	27	21.5
4	Ni (II)	17.5	13	19.5	14	20.5	29.5	8
5	Cu (II)	18	19	15	16.5	24.5	24.5	8
6	Zn (II)	16.5	20	14	12.5	8	20.5	19
7	VO(II)	10	15	13	16	12	15	12
8	Tetracycline	19	25	20	19	–	–	–
9	Fluconazole	–	–	–	–	25	35	26

The results of antibacterial screening in Table 7 showed that Mn(II), Co(II), Ni(II), Cu(II) and Zn(II) metal complexes exhibit greater activity than ligand but less than that of standard reference drug tetracycline. In the antifungal screening the Mn(II), Co(II), Ni(II) and Zn(II) complexes exhibited a higher activity and

Cu(II) and VO(II) complexes demonstrated moderate level of activity than ligand in comparison to the standard reference drug fluconazole [36, 37].

Conclusions

In this paper, we presented the synthesis and characterization of novel azo-Schiff base ligand and its transition metal complexes. From the findings of various spectrochemical techniques, we confirmed that ligand show tridentate behaviour, forming bonds with metal through the azomethine nitrogen and phenolic oxygen atoms. The P-XRD analysis of the complexes revealed a variety of crystal systems including orthorhombic, monoclinic and triclinic structures. The Cu(II) and Zn(II) complexes exhibited greater neuroprotective activity and Co(II) complex shows better anticancer activity than azo-Schiff base ligand. The metal complexes exhibit higher antimicrobial activity than azo-Schiff base ligand. The azo-Schiff base ligand is active, but if metal complexes are made by coordinating various metal salts the activities increase.

Supporting Information

The Supporting Information is available free at https://ejc.buketov.edu.kz/index.php/ejc/article/view/222/182

Author Information*

The authors' names are presented in the following order: First Name, Middle Name and Last Name

Kirti Navnath Sarwade — PhD Student, Department of Chemistry, Balbhim Arts, Science and Commerce College, Balbhim Chowk, Killa maidan, Beed-431122, Maharashtra, India; e-mail: sarwadekirti@gmail.com; https://orcid.org/0009-0001-1401-6535

Kuldeep Bhaskar Sakhare — PhD Student, Department of Chemistry, Balbhim Arts, Science and Commerce College, Balbhim Chowk, Killa maidan, Beed-431122, Maharashtra, India; e-mail: kuldeep.org.chem@gmail.com; https://orcid.org/0009-0001-2236-3182

Mahadeo Abarao Sakhare — Professor, Department of Chemistry, Balbhim Arts, Science and Commerce College, Balbhim Chowk, Killa maidan, Beed-431122, Maharashtra, India; e-mail: sakharema.chem@gmail.com; https://orcid.org/0000-0003-3653-797X

Shailendrasingh Virendrasingh Thakur (*corresponding author*) — Professor and Head, Department of Chemistry, Milliya Arts, Science & Management Science College, Balbhim Chowk, Killa Maidan, Beed-431122, Maharashtra, India; e-mail: svthakur1972@gmail.com; https://orcid.org/0009-0004-5021-1401

Author Contributions

The manuscript was written through contributions of all authors. All authors have given approval to the final version of the manuscript. CRediT: **Kirti Navnath Sarwade** investigation, methodology; *Shailendrasingh Virendrasingh Thakur* conceptualization, visualization; **Kuldeep Bhaskar Sakhare** writing-original draft, formal analysis; **Mahadeo Abarao Sakhare** validation, writing-review & editing.

Acknowledgments

Conflicts of Interest

The authors declare no conflict of interest, financial or otherwise.

References

1 Noor, U., Faisal, R., Saqib, A., Syed, A.T., Iqbal, A., Sumera, Z., Muhammad, Z., Paula, L.D., Muhammad, N.T., Jamshed, I., & Ali, H. (2020). Synthesis, characterization, and anticancer activity of Schiff bases. *Journal of Biomolecular Structure and Dynamics, 38*(11), 3246–3259. https://doi.org/10.1080/07391102.2019.1654924

2   Somayeh, F., Behnam, K., Kong, M.L., Najihah, M.H., Kit, M.C., & Fatemeh, A. (2015). Synthesis, structural characterization, and anticancer activity of a monobenzyltincompound against MCF-7 breast cancer cells. *Drug Des Devel Ther., 9,* 6191–6201. https://doi.org/10.2147/DDDT.S87064

3   Alzheimer's Association (2015). Alzheimer's disease facts and figures. *Alzheimers Dement., 11*, 332. https://doi.org/10.1016/j.jalz.2015.02.003

4   Burmaoglu S., Yilmaz A.O., Polat M.F., Kaya R., & Gulcin I.O. (2019). Synthesis and biological evaluation of novel trischalcones as potent carbonic anhydrase, acetylcholinesterase, butyrylcholinesterase and α-glycosidase inhibitors. *Bioorg. Chem., 85,* 191. https://doi.org/10.1016/j.bioorg.2018.12.035

5   Cakmak R., Ay B., Cinar E., Basaran E., Akkoc S., Boga, M., & Tas, E. (2023). Synthesis, spectroscopic, thermal analysis and *in vitro* cytotoxicity, anticholinesterase and antioxidant activities of new Co(II), Ni(II), Cu(II), Zn(II), and Ru(III) complexes of pyrazolone-based Schiff base ligand. *J. Mol. Struct., 1292,* 136225. https://doi.org/10.1016/j.molstruc.2023.136225

6   Aprajita, Mukesh C. (2023). New Ni(II) and Cu(II) Schiff base coordination complexes derived from 5-Bromosalicylaldehyde and 3-picoyl amine/ethylenediamine: Synthesis, structure, Hirshfeld surface and molecular docking study with SARS-CoV-2 7EFP-main protease. *Polyhedron, 232,* 116296. https://doi.org/10.1016/j.poly.2023.116296

7   Maria, S., Jehangir, K., Robina, Naz., Muhammad, Z., Syed, W.A. Shah., Riaz, U., Sumaira, N., Ahmed, Bari., Hafiz, M.M., Syed, S.A., Siddique, A.A., & Muhammad, S. (2021). Schiff base ligand L synthesis and its evaluation as anticancer and antidepressant agent. *Journal of King Saud University — Science, 33(2),* 101331. https://doi.org/10.1016/j.jksus.2020.101331

8   Rauf, A., Afzal, S., Khurram, S.M., Abdul Aziz, K., Rashda, A., Muhammad, A.Y., Asad, M.K., Abdur Rahman, K., Irfan, Z.Q., Heinz-Bernhard, K., & Zia-ur-R. (2017). Synthesis, spectroscopic characterization, DFT optimization and biological activities of Schiff bases and their metal(II) complexes, *J. Mol. Struct., 1145*, 132–140. https://doi.org/10.1016/j.molstruc.2017.05.098

9   Nagesh, G.Y., & Mruthyunjayaswamy, B.H.M. (2015) Synthesis, characterization and biological relevance of some metal(II) complexes with oxygen, nitrogen and oxygen (ONO) donor Schiff base ligand derived from thiazole and 2-hydroxy-1-naphthaldehyde. *J. Mol. Struct. 1085*, 198–206. https://doi.org/10.1016/j.molstruc.2014.12.058

10   Kenan, B., Nevin, T., Ahmet, S., & Naki, C. (2019). Synthesis, structural characterization andbiological activities of metal(II) complexes with Schiff bases derived from 5-bromosalicylaldehyde : Ru(II) complexes transfer hydrogenation. *Journal of Saudi Chemical Society, 23*, 205–214. https://doi.org/10.1016/j.jscs.2018.06.002

11   Maram, T.B., Reem, M.A., Mohamed, R.S., & Laila, H.A. (2019). Synthesis, structural characterization, DFT calculations, biological investigation, molecular docking and DNA binding of Co(II), Ni(II) and Cu(II) nanosized Schiff base complexes bearing pyrimidine moiety. *Journal of Molecular Structure, 1183*, 298–312. https://doi.org/10.1016/j.molstruc.2019.02.001

12   Manjari, J., Sabura Begum, P.M., & Prathapachandra Kurup, M.R. (2020). Structural, spectral and biological investigations on Cu(II) and Zn(II) complexes derived from NNO donor tridentate Schiff base: Crystalstructure of a 1D Cu(II) coordination polymer. *Journal of Molecular Structure, 1206*, 127682. https://doi.org/10.1016/j.molstruc.2020.127682

13   Rana, H.A.M., Hanaa, A.H., & Mohd, A.A. (2022). Preparation and Characterization of Novel Schiff Base Derived From 4-NitroBenzaldehyde and Its Cytotoxic Activities. *Int J Mol Cell Med., 11*(4), 285–296. http://doi.org/10.22088/IJMCM.BUMS.11.4.285

14   Priyanka, D., Kiran, S., & Bhagavati, K. (2023). Synthesis, spectroscopic, quantum, thermal and kinetics, antibacterial and antifungal studies: Novel Schiff base 5-methyl-3-((5-bromosalicylidene) amino)-pyrazole and its transition metal complexes. *Results in Chemistry, 5,* 100813. https://doi.org/10.1016/j.rechem.2023.100813

15   Kumarasamy, S., & Subramaniam, V. (2021). Synthesis, spectral elucidation, antibacterial, antioxidant and DNA studies of ONNO tetradentate Schiff base metal(II) complexes derived from Benzene-1,4-dicarboxaldehyde. *Indian Journal of Chemistry, 60A,* 682–691. https://doi.org/10.56042/ijca.v60i5.30505

16   Deepak, T., Madhuri, C., Prateek, T., Swati, A., Pravita, K., Deepansh, S., Aruna, C., & Sulekh, C. (2021). Synthesis, Characterization, Antimicrobial, MTT assay, DFT study of Co(II), Ni(II), Cu(II) and Zn(II) Complexes with some New Schiff Base Ligands. *Egyptian Journal of Chemistry, 64*(9), 4995–5008. 10.21608/ejchem.2021.47433.2964

17   Shinde, A. H., & Patil, C.J. (2020). Synthesis and Characterization of Azo Schiff Bases and their Lactam Derivatives. *Asian Journal of Chemistry, 32*, 1520–1524. https://doi.org/10.14233/ajchem.2020.22657

18   Raziyeh, A., Masoumeh, O., & Saeid, A. (2023). Three and four inputs combinational logic circuits based on a azo-azomethine chemosensor for the detection of Ni^{2+} and CN$^-$/OAC$^-$ ions: Experimental and DFT studies. *Journal of Photochemistry & Photobiology, A: Chemistry, 434*, 114231. https://doi.org/10.1016/j.jphotochem.2022.114231

19   Anitha, C., S. Sumathi, S., Tharmaraj, P., & Sheela, C.D. (2011). Synthesis, Characterization, and Biological Activity of Some Transition Metal Complexes Derived from Novel Hydrazone Azo Schiff Base Ligand. *International Journal of Inorganic Chemistry, 2011,* 1–8. http://doi.org/10.1155/2011/493942

20   Sahoo, J., Parween, G., Sahoo, S., Mekap, S.K., Sahoo, S., & Paidesetty, S.K. (2016). Synthesis, spectral characterization, in silico and in vitro antimicrobial investigations of some Schiff base metal complexes derived from azo salicylaldehyde analogus. *Indian Journal of Chemistry, 55*, 1267–1276.

21   Athmar, A.K., Ibtihal, K.K., & Abid, A.M.A. (2022). Synthesis and Spectral Identification of New Azo-Schiff Base Ligand Derivative from Aminobenzylamine and its Novel Metal Complexes with Cu(II), Zn(II) and Hg(II). *International Journal of Drug Delivery Technology, 12*(1), 150–156. http://doi.org/10.25258/ijddt.12.1.27

22 Singh, K., Kumar, Y., Puri, P., Sharma, C., & Aneja K.R. (2017). Antimicrobial, spectral and thermal studies of divalent cobalt, nickel, copper and zinc complexes with triazole Schiff bases. *Arabian Journal of Chemistry,* 10**,** 978–987. http://dx.doi.org/10.1016/j.arabjc.2012.12.038

23 Bharate, Y.N., Sakhare, K.B., Survase, S.A., & Sakhare, M.A. (2023). Synthesis, Characterization And Antibacterial Studies Of Ni(II), Co(II) Acetate And VO(II) Complexes Of Schiff Base Ligand. *Heterocyclic Letters, 13,* 45–52. https://www.heteroletters.org/issue131/Paper-5.pdf

24 Devi, J., Yadav, M., Kumar, D., Naik, L.S., & Jindal, D.K. (2018). Some divalent metal (II) complexes of salicylaldehyde-derived Schiff bases: Synthesis, spectroscopic characterization, antimicrobial and in vitro anticancer studies. *Applied Organometallic Chemistry. 33*, e4693. http://dx.doi.org/10.1002/aoc.4693

25 Sakhare, K.B., Sarwade, K.N., Bharate, Y.N., & Sakhare, M.A. (2024). Anticancer activity of Schiff base ligand (*E*)-4-((5-chloro-2-hydroxybenzylidene)amino)-1,5-dimethyl-2-phenyl-1H-pyrazol-3(2H)-one and its Co(II), Cu(II) and Zn(II) metal complexes. *J. Serb. Chem. Soc.*, 89(2), 165–175. https://doi.org/10.2298/JSC230803092S

26 Salih Al-Hamdani, A. A., Balkhi, A.M., Falah, A., & Shaker, S.A. (2015). New Azo-Schiff Base Derived With Ni(II), Co(II), Cu(II), Pd(II) And Pt(II) Complexes: Preparation, Spectroscopic Investigation, Structural Studies And Biological Activity. *Journal of Chilean Chemical Society, 60(1),* 2774. http://dx.doi.org/10.4067/S0717-97072015000100003.

27 Zoubi, W.A., Al-Hamdani, A.A.S., & Kaseem, M. (2016). Synthesis and antioxidant activities of Schiff bases and their complexes: a review. *Appl. Organomet. Chem., 30*(10), 810–817. https://doi.org/10.1002/aoc.3506

28 Anupama, B., Padmaja, M., & Gyana Kumari, C. (2012). Synthesis, Characterization, Biological Activity and DNA Binding Studies of Metal Complexes with 4-Aminoantipyrine Schiff Base Ligand. *E-Journal of Chemistry*, 9(1), 389–400, https://doi.org/10.1155/2012/291850

29 Sawant, R., Wadekar, J., Ukirde, R., & Barkade, G. (2021).Synthesis, Molecular Docking and Anticancer Activity of Novel 1,3-Thiazolidin-4-Ones. *Pharmaceutical Sciences, 27*(3), 345–352, http://dx.doi.org/10.34172/PS.2020.95

30 Silva, S., Marto, J., Gonclves, L., Almeida, A.J., & Vale, N. (2020). Formulation, Characterization and Evaluation against SH-SY5Y Cells of New Tacrine and Tacrine-MAP Loaded with Lipid Nanoparticles. *Nanomaterials (Basel), 10*(10), 1–14, https://doi.org/10.3390/nano10102089

31 Okkay, U., & Okkay, I.F. (2022). In vitro neuroprotective effects of allicin on Alzheimer's disease model of neuroblastma cell line. *J. Surg. Med*., *6*, 209–212.https://doi.org/10.28982/josam.1068336

32 Jayalkshmi R, Jayakkumar V, Dhivya P, & Rajavel R. (2017). Synthesis and Characterization of 4-Amino Antipyrine Based Schiff Base Complexes: Antimicrobial, Cytotoxicity and DNA Cleavage Studies. *International Journal of Engineering Research & Technology, 6,* 1–9. https://doi.org/10.17577/ijertv6is080005

33 Ahmad-Fauzi, A.B., Hadariah, B., & Karimah K. (2012). Synthesis, Characterization and Neurotoxicity Screening of Schiff Base Ligands and Their Complexes. *Advanced Materials Research, 554–556*, 938–943. https://doi.org/10.4028/www.scientific.net/AMR.554-556.938

34 Abdel-Rahman, L.H., Abu-Dief, A.M., El-Khatib, R.M., & Abdel-Fatah, S.M. (2016). Synthesis and Characterization of Azo Schiff Bases and their β-Lactam Derivatives. *Bioorg. Chem., 69,* 140–152. https://doi.org/10.1016/j.bioorg.2016.10.009

35 Abdel-Rahman, L.H., Abu-Dief, A.M., El-Khatib R. M., & Abdel-Fatah S.M. (2016). Sonochemical synthesis, DNA binding, antimicrobial evaluation and *in vitro* anticancer activity of three new nano sized Cu(II), Co(II) and Ni(II) chelates based on tridentate NOO imine ligands precursors for metal oxides. *J. photochemistry and photobiology,* 00, 1-31. http://doi.org/10.1016/j.jphotobiol.2016.06.052

36 Maram T.B., Reem M.A., Mohamed R.S., & Laila H. Abdel-Rahman (2019). Synthesis, structural characterization, DFT calculations, biological investigation, molecular docking and DNA binding of Co(II), Ni(II) and Cu(II) nanosized Schiff base complexes bearing pyrimidine moiety. *Journal of Molecular Structure, 1183,* 298–312. https://doi.org/10.1016/j.molstruc.2019.02.001

37 Kalluru S., Dammu L.K., Nara S.K., & Jyotinimmagadda V.V. (2023). Synthesis and characterization of Schiff base, 3-Hydroxy-4-(3-Hydroxy Benzylidene Amino) Benzoic acid and their Ni(II) and Zn(II) metal complexes. *J. Adv. Sci. Res., 14,* 35–39. https://doi.org/10.55218/JASR.202314105

Article

UDC 547.7; 544.18

https://doi.org/10.31489/2959-0663/1-25-3

Ammar A. Awad[1*] , Mohammed N. Maged[1] , Dhulfiqar A. Abed[2] , Osamah N. Wennas[3] , Noor Z. Kbah[4] , Ayad A. Disher[5]

[1]Department of Chemistry, College of Education for Pure Sciences, University of Kerbala, Holly Kerbala, Iraq;
[2]Department of Pharmaceutical Chemistry, College of Pharmacy, Al Mustaqbal University, Babylon, Iraq;
[3]Department of Pharmaceutical Chemistry, College of Pharmacy, Al-Zahraa University for Women, Karbala, Iraq;
[4]Department of Pharmaceutics, College of Pharmacy, Al-Zahraa University for Women, Karbala, Iraq;
[5]Department of Chemistry, College of Science, University of Babylon, Babylon, Iraq
(*Corresponding author's e-mail: almosawy2014@gmail.com)

Synthesis, Docking Study and Biological Evaluation of Naproxen-Based Heterocyclic Derivatives

A series of Naproxen-based heterocyclic derivatives (NA1-NA4) were designed, synthesized, and evaluated for their antibacterial and anticancer activities. These heterocyclic derivatives were developed by integrating Naproxen with various heterocycles, including indole, benzothiophene, benzothiazole, and pyrazole, in order to enhance efficacy while reducing gastrointestinal side effects. The synthesized compounds were characterized using FT-IR, 1H NMR, and 13C NMR spectroscopy. The antibacterial activity was evaluated against *S. aureus* (Gram-positive) and two Gram-negative bacteria (*P. aeruginosa* and *K. pneumonia*) by measuring the diameter of the zone of inhibition. Compounds NA2 and NA3 showed promising inhibitory activity against the tested bacteria compared to amoxicillin. The anticancer activity of NA1-NA4 compounds against the MDA-MB-231 human breast cancer cell line was assessed by determining the IC50 values (the concentration required to inhibit 50 % of cell viability). NA1 and NA3 exhibited notable antiproliferative effects with IC50 values of 11.81 and 11.08 μg/mL, respectively. Molecular docking studies of compounds NA1-NA4 were performed against COX-2 enzyme (PDB Code: 3NT1) using MOE software. The compounds showed strong binding affinities, indicating potential anti-inflammatory properties. Collectively, the antibacterial, anticancer, and molecular docking data suggest that these Naproxen derivatives possess promising multifunctional therapeutic potential.

Keywords: Naproxen derivatives, heterocyclic compounds, COX-2 inhibition, MTT assay, antibacterial, anticancer, breast cancer, anti-inflammatory properties

Introduction

Cancer is characterized by the rapid growth of abnormal cells that can spread to other parts of the body, eventually leading to death [1]. Globally, cancer has become the leading cause of mortality, with the number of deaths projected to reach 16.4 million by 2040 [2]. It is estimated that 30–50 % of cancer-related deaths could be prevented through early detection, effective treatment, and long-term care. Breast, lung, and colorectal cancers currently represent the most prevalent cancer types based on incidence rates. In terms of treatment, cancer has remained at the forefront of advancements in surgery, radiotherapy, chemotherapy, and hormonal therapies. However, most currently available anticancer agents are associated with dose-limiting toxicity, drug resistance, and limited selectivity [3]. Therefore, the development of new chemotherapeutic agents capable of overcoming these challenges is of critical importance.

Naproxen is both a COX inhibitor and a strong anti-inflammatory agent. However, one of the most common problems associated with oral Naproxen administration is gastrointestinal disorders [4, 5]. This adverse effect is primarily attributed to the presence of a free carboxylic acid group. Therefore, masking this acidic group has been proposed as an effective strategy to reduce or eliminate gastrointestinal side effects [6]. It has been reported that the therapeutic index for NSAIDs can be improved by synthesizing ester prodrugs of Naproxen, which serve as promoieties [7]. Compounds containing naproxen amide have also shown consistent anti-inflammatory properties [8]. Additionally, it has been observed that amide derivatives of Naproxen, such as Naproxen glycolamide, exhibit anti-inflammatory activity with significantly less gastric damage compared to the parent drug [9]. Compared to conventional Naproxen, amide prodrugs of Naproxen derivatives have demonstrated strong anti-inflammatory activity [10].

The anticancer properties of Naproxen and its derivatives have also been extensively studied, with several derivatives reported to inhibit the proliferation of various cancer cell lines [11, 12]. For instance, Naproxen derivatives such as propanamide and urea analogues have shown promising activity in suppressing colon cancer growth [13]. Moreover, 1,3,4-oxaadiazole derivatives exhibit significant activity against epidermal growth factor receptor (EGFR) [14], while hydrazide and hydrazone derivatives display potent inhibition of vascular endothelial growth factor receptor-2 (VEGFR-2) [15]. Triazole derivatives have also been found to effectively target histone deacetylases (HDACs) [16]. Naproxen's propanamide derivatives have demonstrated notable antimicrobial activity against both Gram-positive and Gram-negative bacteria, including *Escherichia coli* and *Pseudomonas aeruginosa* [10, 17]. These antibacterial effects are comparable to those of standard antibiotics such as ciprofloxacin (for Gram-negative bacteria) and ampicillin (for Gram-positive bacteria) [18]. Furthermore, Naproxen administration has been shown to reduce tumor progression in tumor-bearing rats [11, 12]. Strong suppression of histone deacetylase has been demonstrated by a naproxen hydroxamic acid derivative [5]. Overall, Naproxen represents a promising scaffold for the development of novel therapeutic agents with antiviral, anticancer activities [17, 19, 20], including potential applications in bladder cancer prevention [21].

Heterocycles are considered a vital component in medicinal chemistry. Benzofused and five-membered heterocycles motifs, in particular, represent a significant class of compounds with well-documented anticancer and antibacterial activities [22–25]. Derivatives of benzothiazole, benzothiophene, and indole, for example, have demonstrated notable antimicrobial and antitumor properties [26].

Based on the importance of these heterocycles, we designed a new series of Naproxen-based heterocyclic derivatives. The heterocycles were conjugated to the Naproxen core via its carboxylic acid moiety, aiming to mask this functional group and thereby reduce its associated gastrointestinal side effects. The synthesized analogs were evaluated for their anticancer and antibacterial activities (Fig. 1). Furthermore, molecular docking study was conducted to assess the potential of these compounds as analgesic and anti-inflammatory agents.
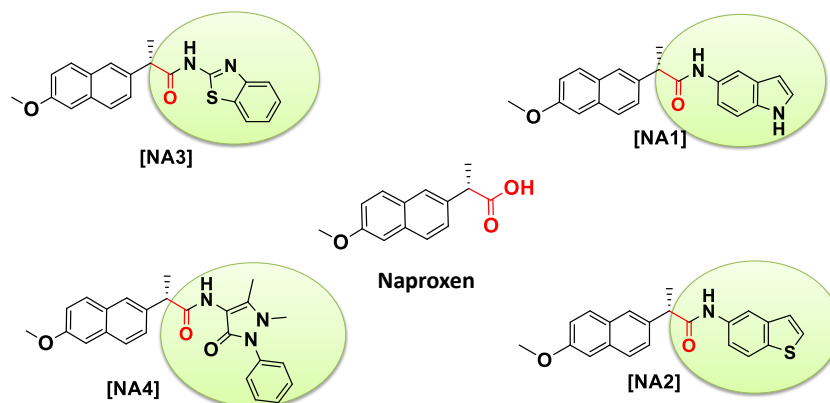
Figure 1. Chemical structures of the newly designed Naproxen-based heterocyclic analogues (NA1–NA4)

Experimental

Material and Methods

All chemical reagents used in this study were of analytical grade and were supplied by Sigma-Aldrich, Fluka, CDH, and Thomas Baker. Naproxen was purchased from Leyan Company (China). Melting points were determined using a Gallenkamp MFB-600 melting point apparatus (Stuart). FT-IR spectra were recorded on a Shimadzu IRAffinity-1S spectrometer. ^{1}H NMR (400 MHz) and ^{13}C NMR (100 MHz) spectra were recorded on a Bruker Multinuclear Spectrometer.

Synthesis of Naproxen acid chloride [27]

To a stirred solution of Naproxen (1.0 g, 4.34 mmol, 1 equiv.) in dichloromethane (DCM, 20 mL), phosphorous trichloride (128 µL, 1.450 mmol, 0.33 equiv.) was added. The resulting mixture was stirred at 0 °C for one hour, then allowed to warm to room temperature (RT) and stirred overnight. The solution was then transferred to a 50 mL round-bottom flask to remove the precipitated phosphorous acid. Thin-layer

chromatography (TLC) was performed to confirm the complete consumption of Naproxen. The resulting mixture was used directly in the subsequent steps without further workup.

Synthesis of (N-(1H-indol-5-yl)-2-(6-methoxynaphthalen-2-yl) propenamide [NA1]

To a solution of acid chloride, [27], in DCM, (0.57 g, 4.34 mmo of 1l)H-indol-5-amine and triethyla-mine (0.73 ml, 5 mmol) were added with stirring at RT for 18 hours. Upon completion of the reaction, the organic layer was removed. The crude product was dissolved in 50 mL of ethyl acetate, then washed sequentially with 50 mL of 5 % NaOH solution and 50 mL of 2 N HCl. The organic phase was dried over anhy-drous magnesium sulfate, and the solvent was removed under reduced pressure using a rotary evaporator. The desired product was obtained as a pink solid (0.96 g, 64 % yield).

FT-IR v_{max}, cm^{-1}: 3211 (N–H, and NH, Amide), 3066 and 3024 (C–H, aromatic), 2929 (C–H, aliphatic), 1653 (CO, Amide), 1595–1435 (aromatic rings); ^{1}H NMR (500 MHz, DMSO), ppm: 10.65 (s, 1H, CO–NH–), 9.68 (s, 1H, Ar–NH–), 7.88–7.26 (11 H, Ar–H), 3.97 (s, 3H, O–CH$_3$), 3.91 (m, 1H, CO–CH–), 1.57 (d, $J = 1$ Hz, 3H, –CH$_3$). ^{13}C NMR (125 MHz), ppm: 172.48 (1C, CO), 152.79 (1C, MeO–C), 132.63–101.06 (17C, Ar–C), 51.21 (1C, –OCH$_3$), 33.30 (1C, Ar (Me)–CH–CO), 14.14 (1C, –CH$_3$) (Figures S1-S3).

Synthesis of N-(benzo[b]thiophen-5-yl)-2-(6-methoxynaphthalen-2-yl) propenamide [NA2]

To a pre-cooled solution of NAC in DCM, benzo[b]thiophen-5-amine (0.647 g, 4.34 mmol) and tri-ethylamine (0.73 mL, 5.00 mmol) were added and left to stir at RT for 18 hours.

After completion of the reaction, the solvent was evaporated, and the crude product was dissolved in 50 mL of ethyl acetate. The solution was washed sequentially with 50 mL of 5 % NaOH solution, 50 mL of 2 N HCl, and a saturated NaCl solution. The organic layer was dried over anhydrous magnesium sulfate, and the solvent was removed under reduced pressure using a rotary evaporator, affording the product as brown crystals (1.2 g, 76 % yield). FT-IR v_{max}, cm^{-1}: 3255 (–NH, Amide), 3064 (C–H, aromatic), 1662 (CO, Am-ide), 1556–1435 (aromatic carbons). ^{1}H NMR (500 MHz, DMSO), ppm: 10.25 (s, 1H, CO–NH–), 7.81–7.14 (m, 11 H, Ar–H), 3.86 (s, 3H, methoxy), 3.81 (d, 1H, $J = 1$ Hz, CO–CH–), 1.45 (d, $J = 2$ Hz, 3H, –methyl). ^{13}C NMR (125 MHz), ppm: 173.22 (1C, CO), 157.09 (1C, Methoxy-C), 145–105.69 (17C, Aro-matic-C), 55.12 (1C, Methoxy), 44.64 (1C, Aromatic (Me)-CH-CO), 18.44 (1C — Methyl) (Figures S4-S6).

Synthesis of N-(benzo[d]thiazol-2-yl)-2-(6-methoxynaphthalen-2-yl)propanamide [NA3]

To a pre-cooled [27] solution in DCM, (0.65 g, 4.34 mmol) of benzo[d]thiazol-2-amine and (0.73 ml, 5 mmol) of triethylamine was added and left to stir at RT for 18 hours. After completion of the reaction, the solvent was evaporated, and the crude product was recrystallized from 70 % ethyl acetate/hexane mixture (50 mL of ethyl acetate) to afford off-white crystals (0.80 g, 50 % yield). FT-IR v_{max}, cm^{-1}: 3343 (–NH, Am-ide), 2953, 2908, and 2868 (C–H, aliphatic), 1666 (CO, Amide), 1606-1427 (aromatic rings); ^{1}H NMR (500 MHz, DMSO), ppm: 12.52 (s, 1H, amide NH), 7.98–7.12 (m, 11 H, aromatic-H), 3.95 (s, 1H, –CH–), 3.86 (s, 3H, methoxy), 1.53 (d, $J = 2$ Hz, 3H, methyl). ^{13}C NMR (125 MHz), ppm: 175.48 (thiazole-C–NH–), 172.69 (1C, CO) 157.51 (1C, methoxy–C), 150.38-104.56 (16 C, aromatic–C), 56.16 (1C, –methoxy), 45.02 (1C, Ar(methyl)–CH–CO), 19.11 (1C, methyl) (Figures S7-S9).

Synthesis of N-(1,5-dimethyl-3-oxo-2-phenyl-2,3-dihydro-1H-pyrazol-4-yl)-2-(6-methoxynaphthalen-2-yl) propanamide [NA4]

To a pre-cooled [27] solution in DCM, (0.88 g, 4.34 mmol) of 4-Aminoantipyrine and (0.73 ml, 5 mmol) of triethylamine were added and the reaction mixture was stirred at RT for 18 hours. After comple-tion of the reaction, the solvent was evaporated, and the crude product was dissolved in 50 mL of ethyl ace-tate, washed successively with 5 % NaOH solution (50 mL) and 2 N HCl (50 mL). The organic layer was then washed with saturated NaCl solution, dried over anhydrous magnesium sulfate, and concentrated using a rotary evaporator to afford the desired product as brown crystals (1.50 g, 83 % yield). FT-IR v_{max}, cm^{-1}: 3257 (–NH, Amide), 3043 (C–H, Aromatic) 2972 and 2920 (C–H, aliphatic), 1660 (CO, Amide), 1620–1427 (aromatic rings); ^{1}H NMR (500 MHz, DMSO): 9.01 (s, 1H, amide-NH–), 8.00–7.37 (m, 11 H, aromatic-H), 3.25 (s, 3H, methoxy-CH$_3$), 3.09 (q, $J = 2$ Hz, 1H,), 2.25 (s, 3H, methyl), 2.23 (s, 3H, methyl), 1.18 (d, $J = 2$ Hz, 3H, methyl). ^{13}C NMR (125 MHz), ppm: 172.97 (1C, CO–NH), 168.64 (CO), 158.16 (1C, MeO–C), 134–116.20 (18 C, Ar–C), 58.28 (1C, –OCH$_3$), 46.10 (1C, Ar(Me)–CH–CO), 24.17, 16.20, and 12.96 (3C, 3 CH$_3$) (Figures S10–S12).

Antibacterial Activity

The antibacterial activity of the synthesized compounds (50 mg/mL) was evaluated against three pathogenic bacterial strains, namely *S. aureus* (Gram-positive) and *P. aeruginosa* and *E. coli* (Gram-negative). Dimethyl sulfoxide (DMSO) was used as a negative control, and amoxicillin at a concentration of 50 µg/mL was used as the standard reference drug. All tests were performed in duplicate at 37 °C. After 24 hours of incubation, the diameter of the inhibition zone was measured and recorded.

Culture and Cell Lines

The human breast cancer cell line (MDA-MB-231) was obtained from the Pasteur Institute, Iran. The cells were cultured in RPMI-1640 medium (Gibco) supplemented with 10 % fetal bovine serum (FBS), penicillin (100 U/mL), and streptomycin (0.1 mg/mL). The cancer cells were incubated under standard conditions: humidified atmosphere with 5 % CO_2 at 37 °C.

MTT Test for Cell Viability in MCF7 Cells

To evaluate cell viability, the MTT assay was performed following standard protocols described by Wang, Rui, et al. and Mahdi, Zainab H., et al. [28, 29]. The absorbance was measured at 570 nm using an ELISA microplate reader. The results were expressed as IC_{50} values, determined as the concentration of compound required to cause 50 % inhibition of cell viability.

Molecular Docking Studies

Molecular docking facilitates understanding of ligand-enzyme interactions, predicts the binding conformations of ligands within a protein's active site, and assists in the design of novel, potent inhibitors. In this study, molecular docking analysis was performed using MOE docking software (version 2019) [30] to evaluate the binding behavior of the naproxen-COX-2 complex (oxidoreductase, PDB Code: 3NT1) [31]. The protein structure files were obtained from the Protein Data Bank (PDB). Water molecules (H_2O) were removed prior to docking to avoid potential interference with ligand binding. The docking analysis using MOE revealed key insights into the position, size, and characteristics of the COX-2 binding site within the 3NT1 structure, which are critical parameters for the development of selective COX-2 inhibitors [32]. The COX-2 active site is located within a hydrophobic pocket that plays a crucial role in ligand accommodation. This binding cavity is sufficiently spacious to allow the binding of structurally diverse ligands [30]. Ser530, Val523, and Leu531 were identified as the key amino acid residues involved in ligand-enzyme interactions, contributing significantly to ligand specificity and binding affinity [33]. All compounds were sketched and cleaned using ChemDraw 22.2.0, and geometry optimization was carried out using MOE software prior to docking. The docking scores and binding interactions of the designed and synthesized compounds are summarized in Table 3.

Results and Discussion

Chemistry

The newly synthesized compounds (NA1-NA4) were obtained via direct amidation of various aromatic amines with the acyl derivative of Naproxen, as illustrated in Scheme. In the first step of the synthesis, Naproxen acyl chloride was prepared by treating naproxen with phosphorous trichloride (PCl_3) in dichloromethane (DCM) at RT for 30 hours. Completion of the reaction was confirmed by the formation of a white solid precipitate of phosphorous acid, and by monitoring the complete consumption of Naproxen using thin-layer chromatography (TLC). After formation, the Naproxen acyl chloride solution was cooled, and the solution of the respective amine was added dropwise under continuous stirring. The mixture was stirred for 18 hours, which was also the maximum reaction time required for the synthesis of compound NA4.

The structures of compounds NA1-NA4 were confirmed by spectroscopic analysis. The FT-IR spectra of all synthesized compounds showed the disappearance of the broad bands corresponding to the COOH group and the carbonyl of Naproxen, and the appearance of characteristic amide (NH) bands at 3211, 3343, 3255, and 3257 cm^{-1}, along with amide carbonyl (C=O) stretches at 1653, 1662, 1666, and 1660 cm^{-1}, respectively. The ^1H NMR spectra exhibited characteristic amide proton signals at 10.65, 10.25, 12.52, and 9.01 ppm, respectively, with the disappearance of the broad signal previously attributed to the carboxylic acid proton of Naproxen. Additionally, the ^{13}C NMR spectra showed distinct signals for the amide carbonyl carbons at 172.48, 173.22, 172.29, and 172.97 ppm.
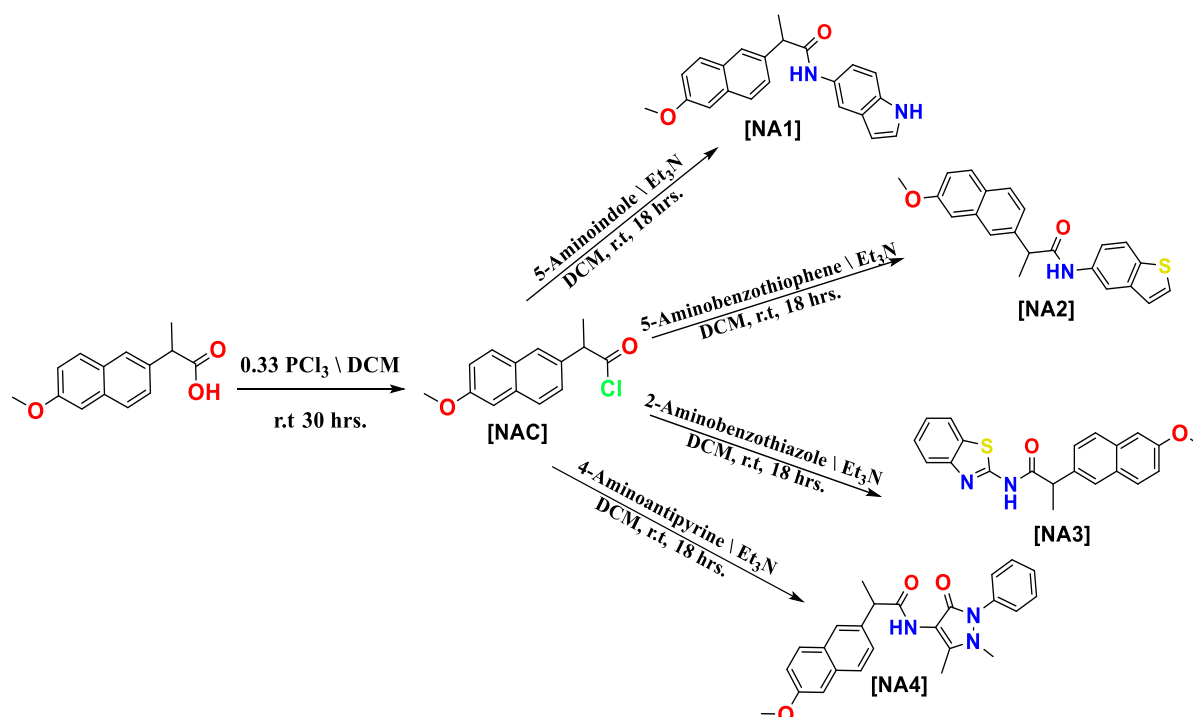
Scheme. Synthesis of compounds NA1-NA4

Antibacterial Activity

A solution of each synthesized compound (NA1-NA4) at a concentration of 5 μg/mL in 1 mL of DMSO was prepared to evaluate the preliminary antibacterial activity. The susceptibility testing technique [34] was employed against *E. Coli, P. aeruginosa, Proteus, K. pneumonia* and *S. aureus*.

Furthermore, dimethyl sulfoxide was used as a negative control, as it has no effect on bacterial growth. The antibacterial activity of each compound is expressed by the diameter of the inhibition zone (in millimeters, mm), as shown in Table 1 and Figure 2.

T a b l e 1

The diameter of inhibition zone of compounds (NA1–NA4)
against *P. aeruginosa, E. Coli, K. pneumonia, Proteus* and *S. aureus*

Sample code	*P. aeruginosa*	*E. Coli*	*K. pneumoniae*	*Proteus*	*S. aureus*
NA1	12	20	13	0	12
NA2	26	20	22	10	30
NA3	32	16	30	18	35
NA4	13	10	0	0	5
Amoxicillin	28	26	20	16	30

Compounds NA2 and NA3 exhibited the highest antibacterial activity among the tested compounds, particularly against *P. aeruginosa*, *K. pneumonia*, and *S. aureus*. The inhibition zone diameters for NA2 were 26 mm, 22 mm, and 30 mm, respectively, while those for NA3 were 32 mm, 30 mm, and 35 mm, demonstrating comparable or even superior activity to the standard drug amoxicillin. This enhanced activity may be attributed to the presence of sulfur-containing heterocyclic moieties, which are known to contribute significantly to antimicrobial efficacy [35].
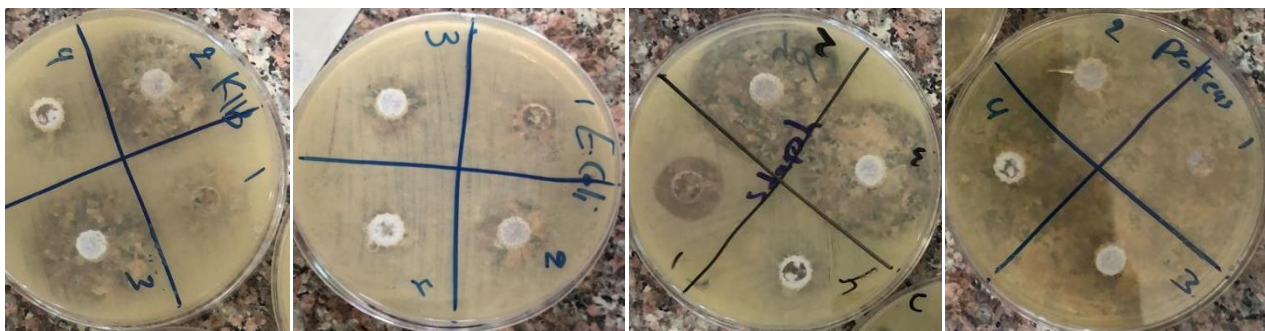
1 — NA1; *2* — NA2; *3* — NA3; *4* — NA4

Figure 2. Antibacterial activity of NA1–NA4

Cell Viability Assay

Based on the results, the synthesized compounds NA1-NA4 exhibited notable cytotoxic activity against the selected cancer cell line when compared to the standard drug, doxorubicin. Compounds NA1 and NA3 demonstrated potent inhibitory effects, with IC_{50} values of 11.81 µg/mL and 11.08 µg/mL, respectively. Compounds NA2 and NA4 also showed considerable inhibitory activity, both with IC_{50} values of 12.05 µg/mL, as presented in Figure 3A–D.

a) NA1

b) NA2

c) NA3

d) NA4 IC_{50}
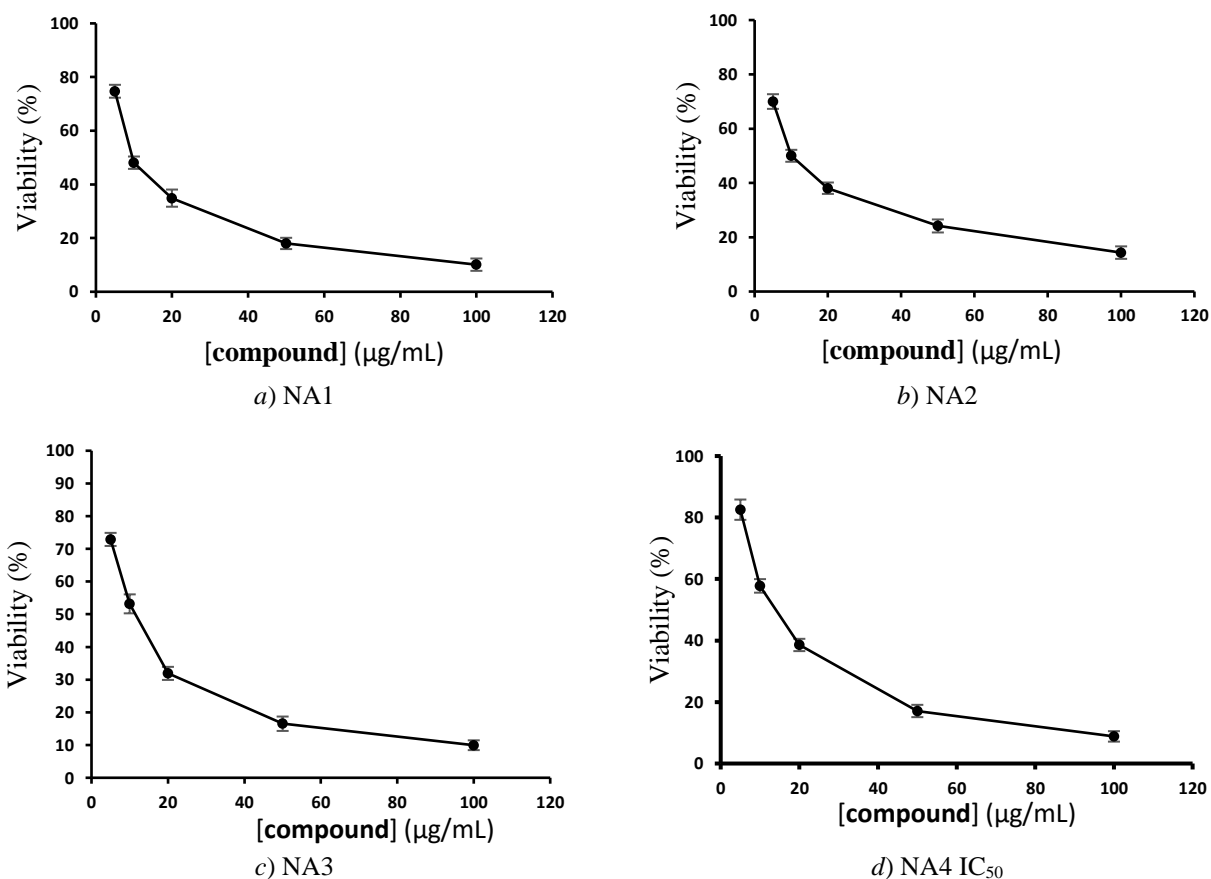
Figure 3. Cell viability diagram for compound NA1 (*a*), NA2 (*b*), NA3 (*c*), and NA4 (*d*)

IC₅₀ values for the tested compounds compared to the standard

Compound	MDA-MB-231
	IC50 (µM)
Standard (Doxorubicin)	9.81
NA1	11.81
NA2	12.05
NA3	11.08
NA4	15.16

Molecular Docking Studies

Molecular docking simulations were performed to evaluate the potential anti-inflammatory activity of the synthesized analogues (NA1–NA4) against COX-2. The study employed Molecular Operating Environment (MOE) software, which enables detailed visualization, characterization, and assessment of protein-ligand interactions. MOE provided detailed information on the ligand positioning and key interactions with receptor-binding residues, along with high-quality graphical representations. Docking analysis revealed that the proposed compounds (NA1-NA4) bind at the same active site as Naproxen within the COX-2 enzyme (oxidoreductase), with additional interactions observed at conserved residues of the Naproxen-binding pocket. The newly synthesized compounds exhibited improved binding affinities, with S-scores ranging from ― 8.7078 to –8.3094 kcal/mol, and low root-mean-square deviation (RMSD) values ranging from 1.0012 to 1.6844, in comparison to Naproxen, which showed a binding energy of –7.1006 kcal/mol and RMSD value of 1.9156. These results suggest that the designed derivatives possess a stronger binding affinity toward the COX-2 active site, potentially enhancing their anti-inflammatory efficacy. Furthermore, the higher structural congruency of these ligands with the target site as visualized in Figures 4–8 supports their improved binding performance, as summarized in Table 3.

Binding properties of the synthesized compounds with Oxidoreductase (PDB code: 3NT1)

Compound	S-score (Kcal/mol)	RMSD	No. of binding sites	Binding amino acids
Naproxen 3NT1	–7.1006	1.9156	3	Arg120, Tyr 355, Ala527
NA 1	–8.4290	1.6844	3	Arg120, Tyr 115, Val 116
NA2	–8.3094	1.4927	2	Arg120, Val 116
NA3	–8.7078	1.0012	2	Two Arg120
NA4	–8.4155	1.4196	4	Arg120, Tyr 355, Val 349, Glu 524

a) 3D model   *b*) 2D model
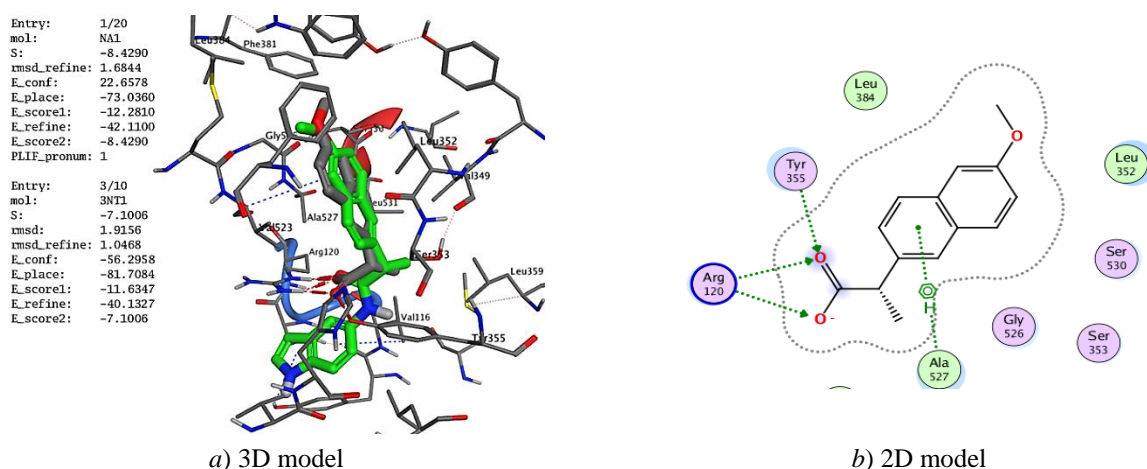
Figure 4. Interactions of native ligand Naproxen and NA1 with COX-2 oxidoreductase (PDB Code: 3NT1)

a) 3D model　　　　　　　　　　　　　　　*b*) 2D model
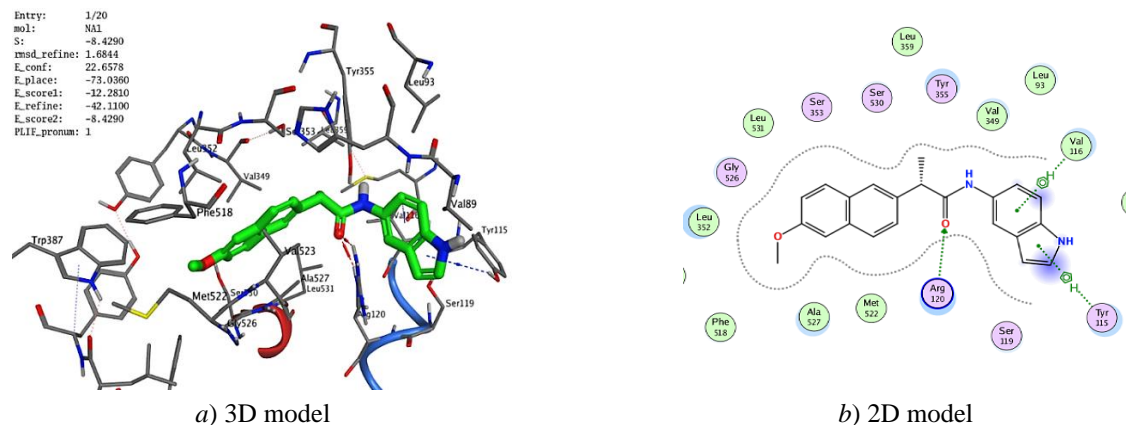
Figure 5. Interactions of NA1 ligand with COX-2 oxidoreductase (PDB Code: 3NT1)

a) 3D model　　　　　　　　　　　　　　　*b*) 2D model
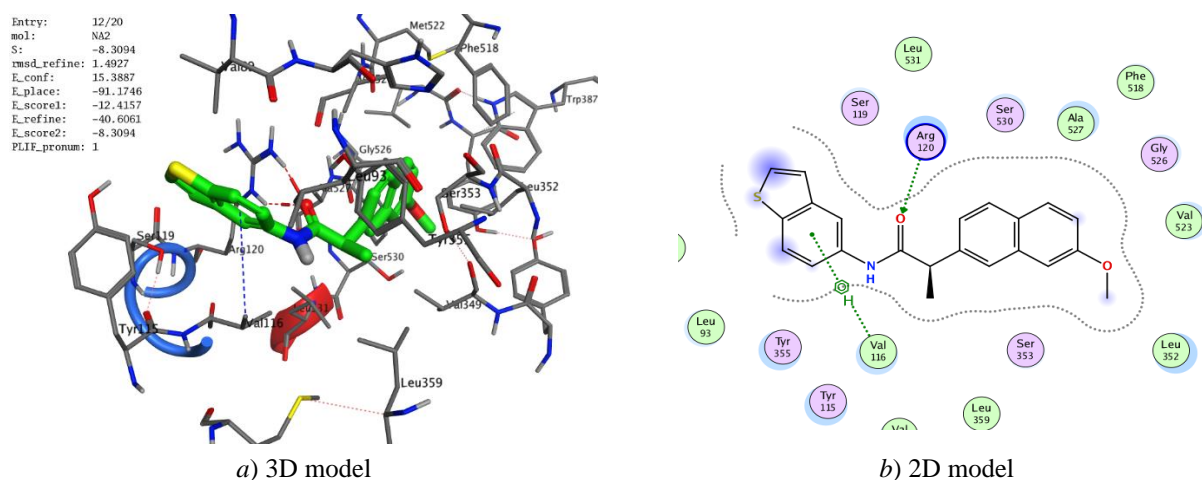
Figure 6. Interactions of NA3 ligand with COX-2 oxidoreductase (PDB Code: 3NT1)

a) 3D model　　　　　　　　　　　　　　　*b*) 2D model
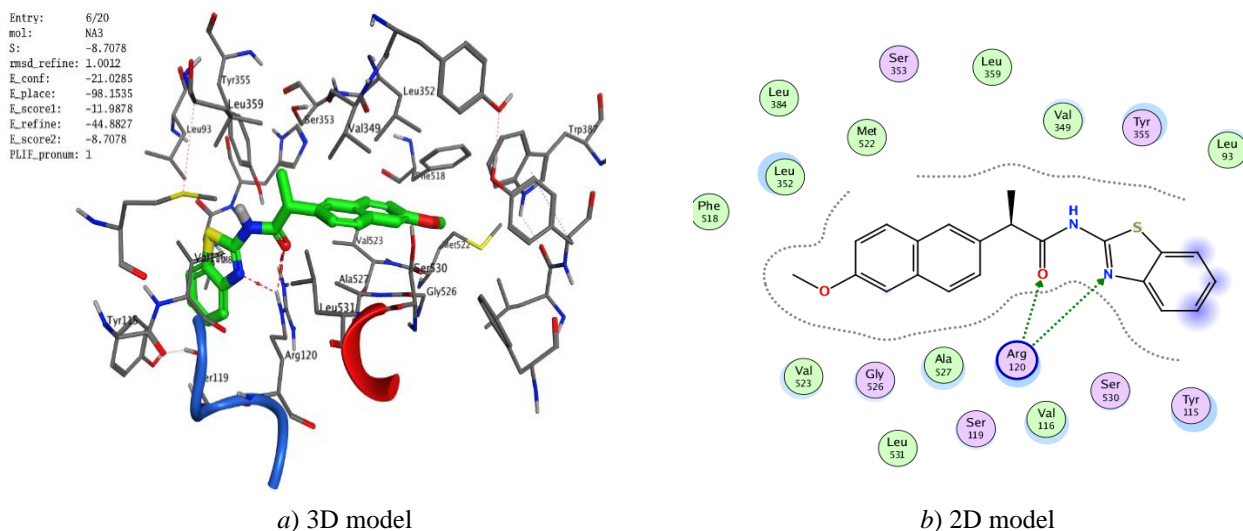
Figure 7. Interactions of NA4 ligand with COX-2 oxidoreductase (PDB Code: 3NT1)

Entry: 12/20
mol: NA2
S: −8.3094
rmsd_refine: 1.4927
E_conf: 15.3887
E_place: −91.1746
E_score1: −12.4157
E_refine: −40.6061
E_score2: −8.3094
PLIF_pronum: 1

a) NA1 — 3NT1

Entry: 1/20
mol: NA1
S: −8.4290
rmsd_refine: 1.6844
E_conf: 22.6578
E_place: −73.0360
E_score1: −12.2810
E_refine: −42.1100
E_score2: −8.4290
PLIF_pronum: 1

b) NA2 — 3NT1

Entry: 6/20
mol: NA3
S: −8.7078
rmsd_refine: 1.0012
E_conf: −21.0285
E_place: −98.1535
E_score1: −11.9878
E_refine: −44.8827
E_score2: −8.7078
PLIF_pronum: 1

c) NA3 — 3NT1

Entry: 17/20
mol: NA4
S: −8.4155
rmsd_refine: 1.4196
E_conf: 92.4786
E_place: −55.9223
E_score1: −11.4557
E_refine: −34.2427
E_score2: −8.4155
PLIF_pronum: 1

d) NA4 — 3NT1

Figure 8. The 3D receptor surface interactions of NA1-NA4 ligand
with COX-2 oxidoreductase (PDB Code: 3NT1)

Conclusion

In conclusion, the newly designed Naproxen-based heterocyclic derivatives (NA1-NA4) have been synthesized and demonstrated strong biological activity as antibacterial and anticancer agents. Antibacterial screening revealed that NA2 and NA3 exhibited significant inhibitory effects, with inhibition zones reaching 32 mm against *P. aeruginosa* and 35 mm against *S. aureus*, in some cases surpassing the standard antibiotic amoxicillin. Similarly, anticancer evaluations showed that NA1 and NA3 effectively inhibited the growth of MDA-MB-231 breast cancer cells, with IC_{50} values of 11.81 µg/mL and 11.08 µg/mL, respectively, comparable to standard chemotherapeutic agents. Furthermore, molecular docking studies revealed strong binding interactions between NA1–NA4 and COX-2 enzyme, indicating potential anti-inflammatory properties. These findings emphasize the value of incorporating heterocyclic moieties into the Naproxen scaffold to develop multifunctional therapeutic agents. The promising biological activities of these derivatives suggest that they hold potential for further development as antimicrobial, anticancer, and anti-inflammatory drug candidates.

Supporting Information

The Supporting Information is available free at https://ejc.buketov.edu.kz/index.php/ejc/article/view/230/191

Author Information*

—————————————————————————————————————

*The authors' names are presented in the following order: First Name, Middle Name and Last Name

Ammar Abdul-Hussein Awad (*corresponding author*) — Lecturer, Department of Chemistry, College of Education for Pure Sciences, University of Kerbala, Holly Kerbala 56001, Iraq; e-mail: ammar.abdulhussein@uokerbala.edu.iq; https://orcid.org/0000-0001-9136-5870

Mohammed Nawfal Abdul Maged — Lecturer, Department of Chemistry, College of Education for Pure Sciences, University of Kerbala, Holly Kerbala 56001, Iraq; e-mail: Mohammed.nawfal@uokerbala.edu.iq; https://orcid.org/0000-0003-4512-726X

Dhulfiqar Ali Abed — Lecturer, Department of Pharmaceutical Chemistry, College of Pharmacy, Al Mustaqbal University, Babylon 51001, Iraq; e-mail: thulfiqar.ali@uomus.edu.iq; https://orcid.org/0000-0002-6004-9602

Osamah Ne'meh Wennas — Lecturer, Department of Pharmaceutical Chemistry, College of Pharmacy, Al-Zahraa University for Women, 56001, Karbala, Iraq; e-mail: osama.wenas@alzahraa.edu.iq; https://orcid.org/0000-0001-7229-7243

Noor Zuhair Kbah — Lecturer, Department of Pharmaceutics, College of Pharmacy, Al-Zahraa University for Women, 56001, Karbala, Iraq; e-mail: noor.kbah@alzahraa.edu.iq; https://orcid.org/0000-0002-4750-595X

Ayad Ali Disher — Lecturer, Department of Chemistry, College of Science, University of Babylon, Babylon 51001, Iraq; e-mail: sci.ayad.ali@uobabylon.edu.iq; https://orcid.org/0000-0002-5941-9127

Author Contributions

The manuscript was written through contributions of all authors. All authors have given approval to the final version of the manuscript. CRediT: **Ammar Abdul Hussein Awad** conceptualization, data curation, formal analysis, funding acquisition, resources, supervision, validation, writing-original draft, writing-review & editing; **Mohammed Nawfal Abdul Maged** conceptualization, data curation, investigation, methodology, validation, visualization, writing-review & editing; **Dhulfiqar Ali Abed** data conceptualization, data curation, investigation, methodology, validation, visualization, writing-review & editing; **Osamah Ne'meh Wennas** data curation, formal analysis, visualization; **Noor Zuhair Kbah** data curation, formal analysis; **Ayad Ali Disher** conceptualization, data curation, investigation.

Acknowledgments

Conflicts of Interest

The authors declare no conflict of interest.

References

1   Alam, M. M., Malebari, A. M., Syed, N., Neamatallah, T., Almalki, A. S., Elhenawy, A. A., Obaid, R. J., & Alsharif, M. A. (2021). Design, synthesis and molecular docking studies of thymol based 1, 2, 3-triazole hybrids as thymidylate synthase inhibitors and apoptosis inducers against breast cancer cells. *Bioorganic & medicinal chemistry*, *38*, 116136. https://doi.org/10.1016/j.bmc.2021.116136

2   Lorenzoni, V., Chaturvedi, A. K., Vignat, J., Laversanne, M., Bray, F., & Vaccarella, S. (2022). The current burden of oropharyngeal cancer: a global assessment based on GLOBOCAN 2020. *Cancer Epidemiology, Biomarkers & Prevention*, *31*(11), 2054–2062. https://doi.org/10.1158/1055-9965.EPI-22-0642

3   El-Sayed, A. A., El-Hashash, M. A., & El-Sayed, W. M. (2022). Synthesis, Antiproliferative Activity, and Apoptotic Profile of New Derivatives from the Meta Stable Benzoxazinone Scaffold. *Anti-Cancer Agents in Medicinal Chemistry (Formerly Current Medicinal Chemistry-Anti-Cancer Agents)*, *22*(6), 1226–1237. https://doi.org/10.2174/1871520621666210706152632

4   Ranatunge, R. R., Augustyniak, M. E., Dhawan, V., Ellis, J. L., Garvey, D. S., Janero, D. R., Letts, L. G., Richardson, S. K., Shumway, M. J., & Trocha, A. M. (2006). Synthesis and anti-inflammatory activity of a series of N-substituted naproxen glycola-

mides: Nitric oxide-donor naproxen prodrugs. *Bioorganic & medicinal chemistry*, *14*(8), 2589–2599. https://doi.org/10.1016/j.bmc.2005.11.040

5   Elhenawy, A. A., Al-Harbi, L., Moustafa, G. O., El-Gazzar, M., Abdel-Rahman, R. F., & Salim, A. E. (2019). Synthesis, comparative docking, and pharmacological activity of naproxen amino acid derivatives as possible anti-inflammatory and analgesic agents. *Drug design, development and therapy*, 1773–1790. https://doi.org/10.2147/dddt.s196276

6   Ullah, N., Huang, Z., Sanaee, F., Rodriguez-Dimitrescu, A., Aldawsari, F., Jamali, F., Bhardwaj, A., Islam, N. U., & Velázquez-Martínez, C. A. (2016). NSAIDs do not require the presence of a carboxylic acid to exert their anti-inflammatory effect–why do we keep using it? *Journal of enzyme inhibition and medicinal chemistry*, *31*(6), 1018–1028. https://doi.org/10.3109/14756366.2015.1088840

7   Shah, K., Gupta, J. K., Chauhan, N. S., Upmanyu, N., Shrivastava, S. K., & Mishra, P. (2017). Prodrugs of NSAIDs: A review. *The open medicinal chemistry journal*, *11*, 146. https://doi.org/10.2174/1874104501711010146

8   Nedeljković, N., Dobričić, V., Bošković, J., Vesović, M., Bradić, J., Anđić, M., Kočović, A., Jeremić, N., Novaković, J., & Jakovljević, V. (2023). Synthesis and investigation of anti-inflammatory activity of new thiourea derivatives of naproxen. *Pharmaceuticals*, *16*(5), 666. https://doi.org/10.3390/ph16050666

9   Sohail, R., Mathew, M., Patel, K. K., Reddy, S. A., Haider, Z., Naria, M., Habib, A., Abdin, Z. U., Chaudhry, W. R., & Akbar, A. (2023). Effects of non-steroidal anti-inflammatory drugs (NSAIDs) and gastroprotective NSAIDs on the gastrointestinal tract: a narrative review. *Cureus*, *15*(4). https://doi.org/10.7759/cureus.37080

10   Gouda, A. M., Beshr, E. A., Almalki, F. A., Halawah, H. H., Taj, B. F., Alnafaei, A. F., Alharazi, R. S., Kazi, W. M., & Al-Matrafi, M. M. (2019). Arylpropionic acid-derived NSAIDs: New insights on derivatization, anticancer activity and potential mechanism of action. *Bioorganic Chemistry*, *92*, 103224. https://doi.org/10.1016/j.bioorg.2019.103224

11   Han, M. İ., & Küçükgüzel, Ş. G. (2020). Anticancer and antimicrobial activities of naproxen and naproxen derivatives. *Mini reviews in medicinal chemistry*, *20*(13), 1300–1310. https://doi.org/10.2174/1389557520666200505124922

12   Kumar, G., Madka, V., Singh, A., Farooqui, M., Stratton, N., Lightfoot, S., Mohammed, A., & Rao, C. V. (2021). Naproxen inhibits spontaneous lung adenocarcinoma formation in KrasG12V mice. *Neoplasia*, *23*(6), 574–583. https://doi.org/10.1016/j.neo.2021.05.010

13   Nirogi, R. V., Bandyala, T. R., Konda, J. B., Reballi, V., Gudla, P., Kambhampati, R., & Khagga, M. (2012). Design, synthesis and biological activity of novel substituted 2-Aryl sulfonyl methyl tryptamines as potential 5-HT6 Receptor ligands. *Der Pharma Chem*, *4*(4), 1552–1566. https://www.derpharmachemica.com/pharma-chemica/design-synthesis-and-biological-activity-of-novel-substituted-2aryl-sulfonyl-methyl-tryptamines-as-potential-5ht6-recept.pdf.

14   Alam, M. M., Nazreen, S., Almalki, A. S., Elhenawy, A. A., Alsenani, N. I., Elbehairi, S. E. I., Malebari, A. M., Alfaifi, M. Y., Alsharif, M. A., & Alfaifi, S. Y. (2021). Naproxen based 1,3,4-oxadiazole derivatives as EGFR inhibitors: Design, synthesis, anticancer, and computational studies. *Pharmaceuticals*, *14*(9), 870. https://doi.org/10.3390/ph14090870

15   Han, M. I., Atalay, P., Tunç, C. Ü., Ünal, G., Dayan, S., Aydın, Ö., & Küçükgüzel, Ş. G. (2021). Design and synthesis of novel (S)-Naproxen hydrazide-hydrazones as potent VEGFR-2 inhibitors and their evaluation in vitro/in vivo breast cancer models. *Bioorganic & medicinal chemistry*, *37*, 116097. https://doi.org/10.1016/j.bmc.2021.116097

16   Chen, P. C., Patil, V., Guerrant, W., Green, P., & Oyelere, A. K. (2008). Synthesis and structure–activity relationship of histone deacetylase (HDAC) inhibitors with triazole-linked cap group. *Bioorganic & medicinal chemistry*, *16*(9), 4839–4853. https://doi.org/10.1016/j.bmc.2008.03.050

17   Mohamed, S. K., El Bakri, Y., Abdul, D. A., Ahmad, S., Albayati, M. R., Lai, C. -H., Mague, J. T., & Tolba, M. S. (2022). Synthesis, crystal structure, and a molecular modeling approach to identify effective antiviral hydrazide derivative against the main protease of SARS-CoV-2. *Journal of Molecular Structure*, *1265*, 133391. https://doi.org/10.1016/j.molstruc.2022.133391 Get rights and content

18   Paes Leme, R. C., & da Silva, R. B. (2021). Antimicrobial activity of non-steroidal anti-inflammatory drugs on biofilm: Current evidence and potential for drug repurposing. *Frontiers in microbiology*, *12*, 707629. https://doi.org/10.3389/fmicb.2021.707629

19   Terrier, O., Dilly, S., Pizzorno, A., Chalupska, D., Humpolickova, J., Bouřa, E., Berenbaum, F., Quideau, S., Lina, B., & Fève, B. (2021). Antiviral properties of the NSAID drug naproxen targeting the nucleoprotein of SARS-CoV-2 coronavirus. *Molecules*, *26*(9), 2593. https://doi.org/10.3390/molecules26092593

20   Deb, J., Majumder, J., Bhattacharyya, S., & Jana, S. S. (2014). A novel naproxen derivative capable of displaying anti-cancer and anti-migratory properties against human breast cancer cells. *BMC cancer*, *14*, 1–8. https://doi.org/10.1186/1471-2407-14-567

21   Lubet, R. A., Steele, V. E., Juliana, M. M., & Grubbs, C. J. (2010). Screening agents for preventive efficacy in a bladder cancer model: study design, end points, and gefitinib and naproxen efficacy. *The Journal of urology*, *183*(4), 1598–1603. https://doi.org/10.1016/j.juro.2009.12.001

22   Keri, R. S., Chand, K., Budagumpi, S., Somappa, S. B., Patil, S. A., & Nagaraja, B. M. (2017). An overview of benzo[b]thiophene-based medicinal chemistry. *European journal of medicinal chemistry*, *138*, 1002–1033. https://doi.org/10.1016/j.ejmech.2017.07.038

23   Mo, X., Rao, D. P., Kaur, K., Hassan, R., Abdel-Samea, A. S., Farhan, S. M., Bräse, S., & Hashem, H. (2024). Indole Derivatives: A Versatile Scaffold in Modern Drug Discovery—An Updated Review on Their Multifaceted Therapeutic Applications (2020–2024). *Molecules*, *29*(19), 4770. https://doi.org/10.3390/molecules29194770

24   Paoletti, N., & Supuran, C. T. (2024). Benzothiazole derivatives in the design of antitumor agents. *Archiv der Pharmazie*, e2400259. https://doi.org/10.1002/ardp.202400259

25 Saha, M., Mandal, S., Sarkar, S., Biswas, A., Ghati, A., Cordes, D. B., Slawin, A. M., & Saha, N. C. (2024). Anticancer, antimicrobial and photocatalytic activities of a new pyrazole containing thiosemicarbazone ligand and its Co (III) and Ni (II) complexes: Synthesis, spectroscopic characterization and X-ray crystallography. *Journal of Inorganic Biochemistry*, *257*, 112577. https://doi.org/10.1016/j.jinorgbio.2024.112577

26 Kashyap, P., Verma, S., Gupta, P., Narang, R., Lal, S., & Devgun, M. (2023). Recent insights into antibacterial potential of benzothiazole derivatives. *Medicinal Chemistry Research*, *32*(8), 1543–1573. https://doi.org/10.1007/s00044-023-03077-z

27 Bresciani, A., Missineo, A., Gallo, M., Cerretani, M., Fezzardi, P., Tomei, L., Cicero, D. O., Altamura, S., Santoprete, A., Ingenito, R., Bianchi, E., Pacifici, R., Dominguez, C., Munoz-Sanjuan, I., Harper, S., Toledo-Sherman, L., & Park, L. C. (2017). Nuclear factor (erythroid-derived 2)-like 2 (NRF2) drug discovery: Biochemical toolbox to develop NRF2 activators by reversible binding of Kelch-like ECH-associated protein 1 (KEAP1). *Arch. Biochem. Biophys.*, *631*, 31–41. https://doi.org/https://doi.org/10.1016/j.abb.2017.08.003

28 Mahdi, Z. H., Alsalim, T. A., Abdulhussein, H. A., Majed, A. A., & Abbas, S. (2024). Synthesis, molecular docking, and anti-breast cancer study of 1-H-indol-3-Carbohydrazide and their derivatives. *Results in Chemistry*, *11*, 101762. https://doi.org/10.1016/j.rechem.2024.101762

29 Wang, R., Wang, J., Dong, T., Shen, J., Gao, X., & Zhou, J. (2019). Naringenin has a chemoprotective effect in MDA‑MB‑231 breast cancer cells via inhibition of caspase‑3 and‑9 activities. *Oncology letters*, *17*(1), 1217–1222. https://doi.org/10.3892/ol.2018.9704

30 Ayaz, M., Alam, A., Zainab, Assad, M., Javed, A., Islam, M. S., & Ahmad, M. (2023). Biooriented synthesis of ibuprofen-clubbed novel bis-schiff base derivatives as potential hits for malignant glioma: In vitro anticancer activity and in silico approach. *ACS omega*, *8*(51), 49228–49243. https://doi.org/10.1021/acsomega.3c07216

31 Duggan, K. C., Walters, M. J., Musee, J., Harp, J. M., Kiefer, J. R., Oates, J. A., & Marnett, L. J. (2010). Molecular basis for cyclooxygenase inhibition by the non-steroidal anti-inflammatory drug naproxen. *Journal of biological chemistry*, *285*(45), 34950–34959. https://doi.org/10.1074/jbc.m110.162982

32 Mohammad-Aghaie, D., & Jafari, Z. (2013). Docking and Molecular Dynamics Simulation Studies of Interactions between Cyclooxygenases Enzymes and Celecoxib drug. *1st Tabriz International Life Science Conference and 12th Iran Biophysical Chemistry Conference*. https://doi.org/10.1080/07391102.2020.1823884

33 Nekkaz, K., Daoud, I., Younes, K., Merghache, S., Khebichat, N., & Ghalem, S. (2014). Docking Studies on Cyclooxygenases-2 Inhibitors based on Potential Ligand Binding Sites. *International Journal of Computer Applications*, *87*(1). https://doi.org/10.5120/15173-3086

34 Awad, A., Kareem, M., Rasheed, O., & Eesa, M. (2024). Synthesis, Biological Screening, and Molecular Dockingof Drug Carrier Maleimide Derivatives. *Russian Journal of Bioorganic Chemistry*, *50*(3), 991–1000. https://doi.org/10.1134/s1068162024030245

35 Pathania, S., Narang, R. K., & Rawal, R. K. (2019). Role of sulphur-heterocycles in medicinal chemistry: An update. *European journal of medicinal chemistry*, *180*, 486–508. https://doi.org/10.1016/j.ejmech.2019.07.043

Review

UDC 547.7; 577.1

https://doi.org/10.31489/2959-0663/1-25-1

Amita Joshi Rana[1] [iD], Sanjana Bisht[2]* [iD], Kumud Upadhyaya[2] [iD],
Pawan Singh[3] [iD], Mahendra Rana[2] [iD], Shweta Singh[2] [iD]

[1]Graphic Era Hill University, Bhimtal, Uttarakhand, India;
[2]Kumaun University, Nainital, Uttarakhand, India;
[3]Faculty of Pharmaceutical Sciences, Amrapali University, Haldwani, India
(*Corresponding author′s e-mail: Sanjanab997@gmail.com)

Benzodioxole Scaffold Incorporating Compound with Promising Anti-Fungal Potential: An Overview

This review focuses on the compounds with 1,3-benzodioxole scaffold and their antifungal potential. Different online sources including Google Scholar, Pubchem and Science Direct were used to collect information on benzodioxole containing compounds as antifungal agents from articles published between 2003 and 2022. The health threat posed by fungal infections to humans makes an ongoing search for more different antifungal agents necessary. Diverse heterocyclic moiety proves beneficial in fungal infection, among all of them benzodioxole incorporation into the compound was also found to be effective. The 1,3-benzodioxole or methylenedioxy benzene scaffold is highly adaptable, enabling a range of chemical modifications. The biophoric nature of this scaffold imparts distinctive pharmacological properties, contributing to its broad-spectrum activity. It was shown that the addition of heterocyclic moiety (e.g. primidinone, imidazole, thiazole, etc.), aliphatic linker, amide linker at position 5 and furthermore electron withdrawing group at position 6 enhances the antifungal potential against various phytopathogenic and human pathogenic fungi species. This review highlights the anti-fungal status of benzodioxole scaffold-containing compounds focusing on their efficacy against both phytopathogenic and human pathogenic fungal species. Additionally, the review discusses the structural modification and the future prospects of these compounds in antifungal therapy.

Keywords: Heterocyclic**,** 1,3-benzodioxole, fungal infection, biophoric nature, phytopathogenic, human pathogenic, Pharmacological properties, antifungal therapy.

Content

List of Abbreviations

ATCC — American Type culture collection
BDO   — 1,3-benzodioxole
CYP   — Cytochrome
DIZ   — Diameter of the zone of inhibition
IC50   — Half-maximal inhibitory concentration
MIC   — Minimum Inhibitory Concentration
NPBD — Nitropropenyl benzodioxole
NRRL — Northern Regional Research Laboratory

Review Plan

The present review focuses on threats of phytopathogenic and human pathogenic fungal infection and also highlights the benzodioxole incorporating compounds as an antifungal agent and their future prospects. The data presented in the past and recent research publications have been overviewed to provide a clearer understanding of the benzodioxole-containing compound as antifungal surrogates against phytopathogenic and human pathogenic fungal infection.

Various online sources, including Google Scholar, Pubchem, and Science Direct were used to gather information from studies that summarize both phytopathogenic and human pathogenic fungal infection and incorporated benzodioxole against them. This review focuses on the articles published between 2003 to 2022, with studies done before 2003 excluded from our review.

1 Introduction

Fungal infections have increased rapidly over the last several decades, posing a danger to human health and life. The increasing number of immunocompromised patients who are highly vulnerable to invasive fungal infections due to clinical treatment in intensive care units or the use of immunosuppressive therapy, as well as the increasing prevalence of drug-resistant fungi species, is an alarming trend [1]. In addition to invasive fungal infections in humans, the agricultural challenge of providing an adequate and safe food supply for all populations is currently threatened due to the infestation of food crops by virulent pathogens, particularly fungi, and evidence that resistant pathogenic species multiply rapidly once resistance sets in, posing a new challenge to drive the design and synthesis of bioactive chemical agents with high efficiency, more excellent selectivity, biocompatibility, and benign to human health as better alternatives to traditional synthetic fungicides [2, 3]. For decades, imidazole, pyrimidine, and some benzodioxole moieties, etc., have been crucial in and pesticides [4].
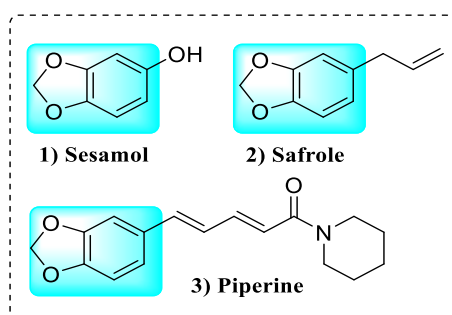
Figure 1. Benzodioxole scaffold containing compounds
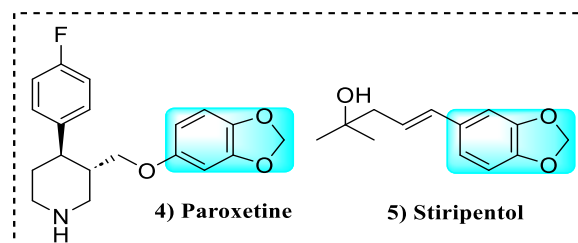
Figure 2 Benzodioxole-containing medicines

The 1,3-benzodioxole nucleus having methylenedioxy unit [5] is an isostere of benzothiazole nucleus [6], also known as BDO [7], and the existence of this pharmacophore confers potential biological activity and demonstrates its diverse character, which can be recognized by different receptors via hydrogen bonding and/or hydrophobic interaction [5, 8]. The key structure of this pharmacophore is present in many natural products (Fig. 1) [9–12] and medicines (Fig. 2) [13, 14]. This nucleus is found in a number of natural plant alkaloids, including Sanguinarine, Liriodenine, and Berberine, which have broad-spectrum action in both medicine and pesticides (Fig. 3) [15].
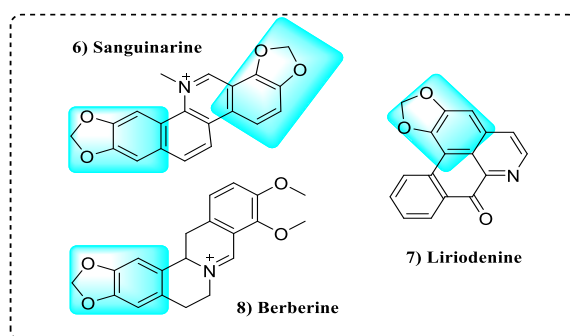
Figure 3. Plant alkaloids containing benzodioxole

1,3-Benzodioxole (BDO) are well-known heterocyclic units in the province of natural and synthetic organic chemistry due to their multiple existences as inhibitors of mono-oxygenase B enzymes [16, 17], antidepressant [14], anticonvulsant [18], pesticides [19], herbicides [20], antioxidant [21], antimicrobials [22–25], in addition, it also *possesses* antitumor [26], antihelminthic [27], antifungals [28–35], and antibacterial [6], anti-inflammatory and analgesic activity [36], anticancer [37], antiepileptic [38], antihypertensive [39], hepatoprotective and hypolipaedemic [40], immunomodulatory [41], antidiabetic [42] as shown in Figure 4. No cytotoxic effects of 1,3-benzodioxole derivatives were observed at a concentration of 10^{-4} M. The relatively low mammalian toxicity, in particular, is of significant interest [26].
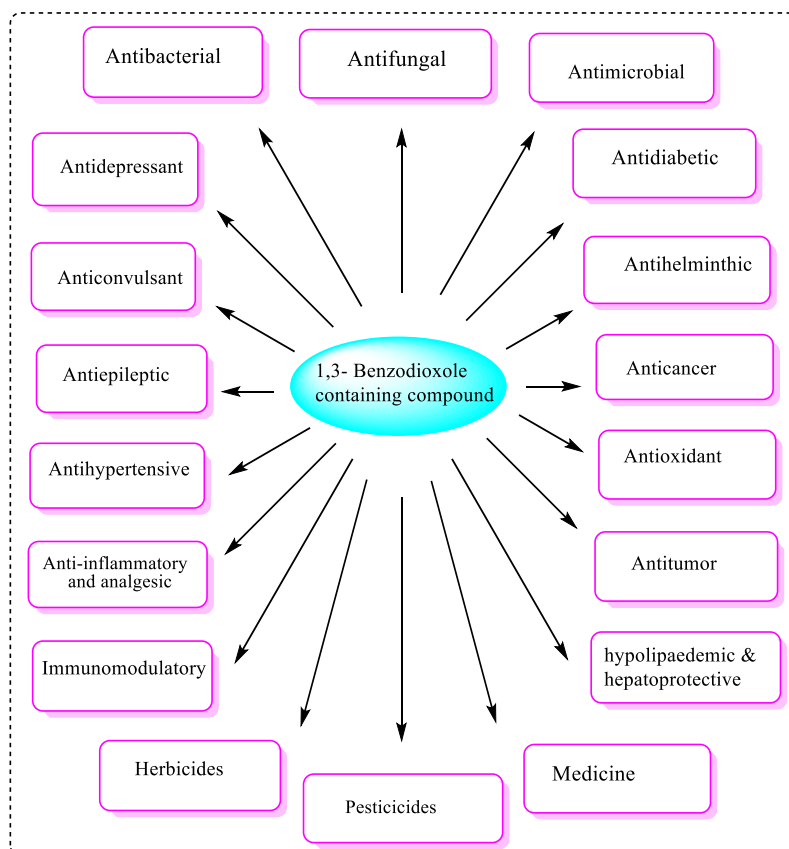
Figure 4. Benzodioxole scaffold containing compound with multiple pharmacological activities

2 The Anti-Fungal Activity Status of Benzodioxole Containing Compounds

2.1 Implication against Human Pathogenic Isolates

A brand-new pyrimidinone derivative incorporating 1,3-Benzodioxole moiety namely, 6-(1,3-benzodioxole-5-ylmethyl)-5-ethyl-2-{[2-(morpholin-4yl)ethyl]sulfanyl}pyrimidin-4(3H)-one was created by Attia et al. (Fig. 5) [22]. The diameter of the inhibition zone (DIZ) assay and the minimum inhibitory concentration (MIC) assay were carried out on agar to assess the target compound's antimicrobial potential against gram-positive bacteria (*Staphylococcus aureus* ATCC 29213, *Bacillus subtilis* NRRL 4219, and *Bacillus cereus*), as well as pathogenic fungi (*Candida albicans* ATCC 10231 and *Aspergillus niger* NRRL). The outcomes were contrasted with Ampicillin trihydra, an antibacterial reference standard, and Clotrimazole, an anti-fungal reference standard. They confirmed the target compound's structure using single X-ray crystallography, particularly its S-alkylation., and they also emphasized its molecular packing, which is maintained by a weak intermolecular interaction. Additionally, they claimed that the targeted chemical was effective only against gram-positive bacteria (MIC value = 0.0619 towards *Staphylococcus aureus*) and some fungus species (MIC value = 0.1859 towards both *Candida albicans* and *Aspergillus niger*) [22].

Figure 5. Novel primidinone derivative incorporating 1,3-benzodioxole moiety, namely,6-(1,3-5-ylmethyl)-5-ethyl-2-{[2-(morpholin-4-yl) ethyl]sulfanyl}pyrimidine-4(3H)-one

Figure 6. ({[(1E)-1-(1,3-Benzodioxole-5-yl)-3-(1H-imidazole-1-yl) propylidene]amino}oxy)-(furan-2-yl)methanone

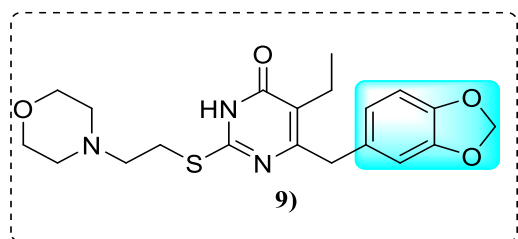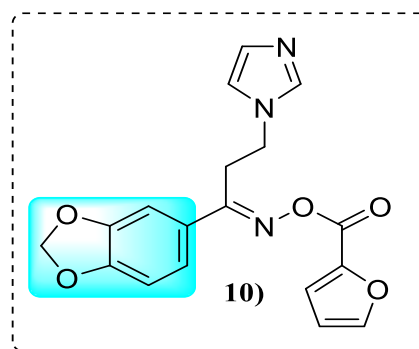New bioactive anti-fungal candidate ({[(1E)-1-(1,3-Benzodioxol-5-yl)-3-(1H-imidazol-1-yl)propylidene]-amino}oxy)(furan-2-yl) methanone was synthesized by Wabli and co-workers (Fig. 6) [28]. Their E-configuration identification of the imine fragment of the title compound was determined via single X-ray crystallography. The reported Natural bond analysis interpreted the chemical hyper-conjugative interactions and electron density transfer and also demonstrated the formation of intramolecular hydrogen bond interaction between n1(N9) and *(C23-H39) anti-bonding orbital with a stabilization energy of 0.65 kcal/mol, respectively, along with Natural population analysis to depict electron distribution and collectively provided the System with stability. The targeted chemical's Hirschfeld surface examination, frontier molecular orbital analysis, and molecular docking investigations were also completed. The optimization of the title compound's molecular structure was approximated using DFT theory at the B3LYP/6-311+G basis level set with the Gaussian 09 software program. The investigated conformation of the target molecule revealed its non-planarity due to steric hindrance. The computed wavenumbers were compared to the FT-Raman and FT-IR wavenumbers obtained experimentally. In the broth microdilution experiment, the title compound has shown equipotent action against *Candida albicans* and *Candida parapsilosis* with a MIC value of 0.724 mol/ mL and compared results with reference anti-fungal [28].

To combat various bacteria and fungi, Shahavar Sultana et al. [25] synthesized a novel series of 20 compounds of thiophene and benzodioxole-linked thiazolyl-pyrazolines (Fig. 7). The findings showed that the majority of the synthesized compounds exhibited antimicrobial activities against 8 bacteria*; Salmonella typhimurium, Klebsiella pneumonia, Proteus vulgaris, Shigela flexneri, Micrococcus luteus, Enterobacter aerogens, Staphylococcus aureus and staphylococcus aureus (MRSA-methicillin resistant)*; 2 fungi: *Candida albicans* and *Malassesia pachydermatis*. To compare results, streptomycin, Gentamicin (antibacterial), Ketoconazole, and fluconazole (anti-fungal) were taken as reference drugs. Gram-positive and Gram-negative bacteria and fungi were found to have significant MIC values. Comparing compounds 11e, 11o, 11r, and 11t to other studied compounds, they showed highly excellent antibacterial activity. When tested against the identified micro-organisms, compound 11o outperformed all other compounds with a MIC value of 31.25 μg/mL [25].
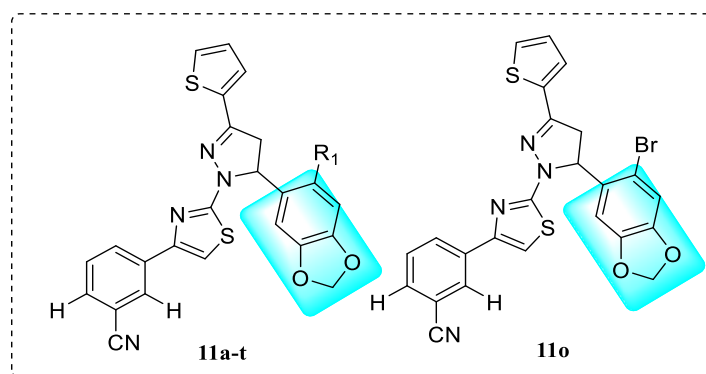

Figure 7. Some thiophene and benzodioxole-linked thiazolyl-pyrazolines derivatives

The cellular target of the studied compound was identified as Sec14p by Pries et al. [32], who also reported the existence of picolinamide and benzamide chemotypes with anti-fungal activities (Fig. 8). Sec14p is a key player in the pathogenicity and virulence of pathogenic fungi. According to the guidelines of the Clinical Laboratory Standards Institute, the inhibitory effect of compounds 2 and 3 were assessed in vitro against four different and clinically significant pathogens: two dimorphic fungi from the Candida genus (*C. albicans* and *C. glabrata*), one filamentous fungus (*Aspergillus brasiliensis*), and the yeast *Cryptococcus neoformans* as a representative of the Basidiomycota. A triazole chemical called posconazole was utilized as a positive control [32].
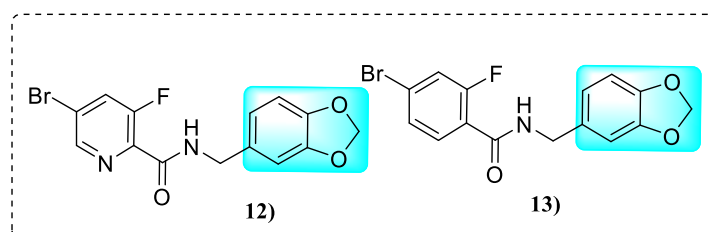

Figure 8. A few picolinamide and benzamide chemotypes with anti-fungal potential

The phenotypic effects of NPBD (Nitropropenyl benzodioxole) on saprophytic, commensal, and parasitic fungal species were studied by Nicoletti and White (Fig. 9) [31]. They examined the variety of distribution and function of cysteine-based enzymes and redox-active thiol compounds, as well as how to select pathogens of interest with desirable properties for an anti-fungal medication candidate. Nitropropenyl benzodioxole was shown to have more potent antibacterial and anti-fungal action than nitroethenyl compounds. Except for parasitic dermatophytes, NPBD demonstrated wide, robust, and rather homogeneous anti-fungal efficacy against 27 saprophytic, commensal, and parasitic species from three orders and twelve families. Hyphae may have a higher MIC and Minimum Fungicidal Concentration (MFC) titre than micro-conidial inocula. In vitro efficacy of NPBD against hyphal forms of thermally dimorphic *fonsecaea, Hortaea, Phialophora, S. apiospermum*, and *C. neoformans, Blastomyces dermatitis, Histoplasma capsulatem, Coccidiodes* species (MIC_{90}: 0.25–2 mg/L), *Cryptococcus gatti* (2mg/L), *Candida glabrata* (0.5–2 mg/L). In the literature, they advocated that NPBD be developed as a therapy for mucocutaneous opportunistic fungal infections [31].
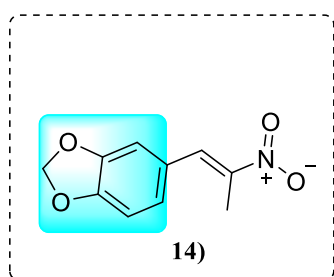
Figure 9. Nitropropenyl Benzodioxole
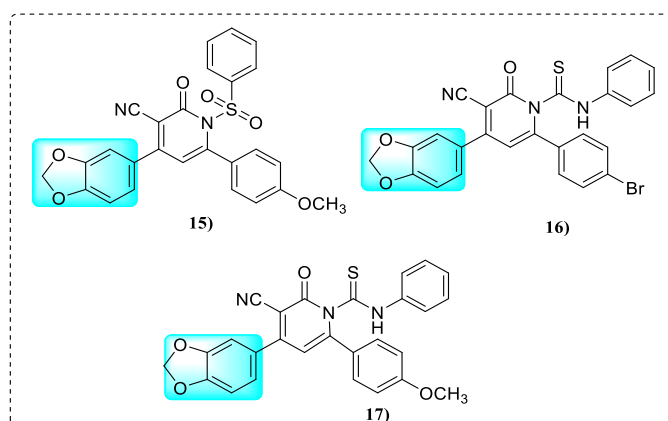
Figure 10. 1,4,6-trisubstituted-2-oxo-1,2-dihydropyridine-3-carbonitriles containing benzodioxole functionalities

A series of 35 unique 1,4,6-trisubstituted-2-oxo-1,2-dihydropyridine-3-carbonitriles were synthesized by Faidallah et al. [23] with some functionalities claimed to have substantial chemotherapeutic potential (Fig. 10). The antimicrobial activity was assessed using an agar cup diffusion technique and a two-fold serial dilution method against Gram-positive bacteria *Staphylococcus aureus* (ATCC 6538), *Bacillus subtilis* (ATCC 6633), & *Micrococcus luteus* (ATCC 21881), Gram-negative bacteria *Escherichia coli* (ATCC 25922), *Pseudomonas aeruginosa* (ATCC 27853). The cytotoxic activity against three cell lines was also reported, and ampicillin, Clotrimazole, and doxorubicin were used as standard reference drugs for comparing the activity with the synthesized compound. According to the literature, 17 analogs showed antimicrobial

activity, whereas 13 analogs had cytotoxic potential against three human tumor cell lines. In a series of 35 compounds, compound 15 was shown to be the most potent cytotoxic agent and antimicrobial agent, making compounds 15, 16, and 17 attractive dual antimicrobial-anticancer possibilities [23].
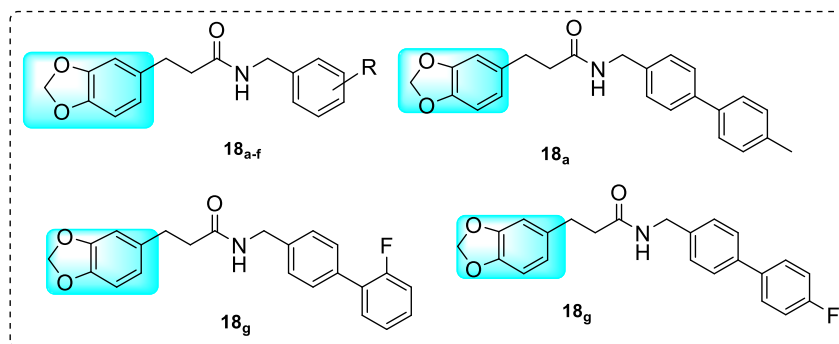
Figure 11. Some 3-(benzo [1,3] dioxol-5yl)-N-(substitutedbenzyl0-propanamides derivatives are arranged

In vitro testing and synthesis of fluconazole-synergistic 3-(benzo[d][1,3]-dioxol-5yl)-N-(substituted benzyl)-propanamide was performed by Cai et al. (Fig. 11) [29]. The lead compound 7d's amide moiety was swapped out for a retro-amide moiety to create the series 18a-f, and compounds 18a, 18e, and 18g showed more potent compounds to boost fluconazole's anti-fungal activity against the most prevalent fungal pathogen, *Candida albicans*, and reported that while they did not individually have anti-fungal activity when combined, they increased fluconazole's susceptibility to fluconazole-resistant *Candida albicans* [29].

2.2 Implication against Phytopathogenic Fungi

In 2020, based on a piperine scaffold, a series of 21 novel compounds (19–21a-g) were designed and synthesized by Wang et al. [35], which were derived from naturally occurring phenolic compounds found in essential oils (Fig. 12). They then tested the compound's potential anti-fungal activity using mycelial growth rate against six phytopathogenic species, including *Gloeosporium thea-sinensis*, *Fusarium graminearum,* and *Phomopsis adianti*. Among 21 essential oil derivatives, some target compounds showed good inhibitory action, some had more decisive inhibitory action, and some had more vigorous inhibitory activity than the original piperine and carbendazim against the tested fungus. They carried out the preliminary assay value and IC_{50} value determination steps in the primary screening and secondary screening. They claimed that compound 20b had broad-spectrum fungicidal and broad-spectrum bacteriostatic activity [35].
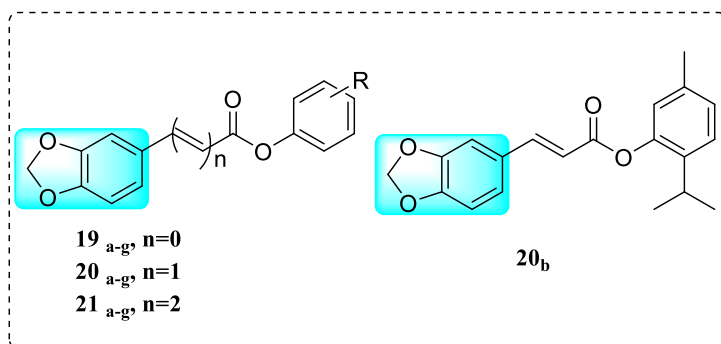
Figure 12. Piperine based essential oil derivatives;
18b: -(2-Isopropyl-5-methylphenyl 3-(benzo[d] [1,3] dioxol-5-yl)acrylate

The series of lactam analogs containing 1,3-benzodioxole, 21(a-o), and the 2(5H)- furanone derivatives, 21(p-s) were designed and synthesized by Song et al. (Figure 13) [34]. Their anti-fungal activities were assessed against four serious crop-threatening agricultural fungi, including *Rhizoctonia solani, Alternaria tenuis Nees, Gloesporium theae-sinensis*, and *Fusarium graminearum* and carbendazim and piperine were used as a standard reference drug. Against particular phytopathogenic fungi, some of the compounds demonstrated strong anti-fungal efficacy. Compound 7b demonstrated the best anti-fungal activity in vitro against *Gloeosporium theae-sinensis* and *Fusarium graminearum*, with +IC_{50} values of 64.47 and 113.47 mg/L, respec-

tively. Compounds 21a, 21b, and 21i, which emerged as a novel lead compound, showed stronger inhibitory effects against Alternaria tenuis Nees than the widely used fungicide carbendazim. In addition, 1,3-benzodioxole was found to enhance the activity [34].
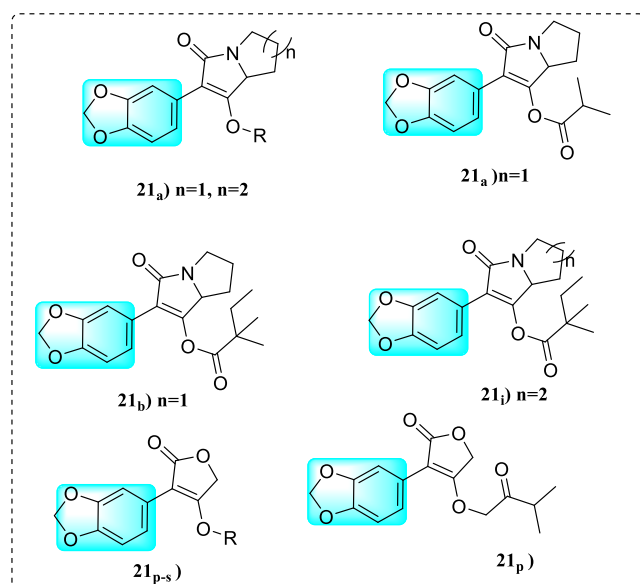
Figure 13. Lactam analog (21a-o) and furanone analog (21p-s) derivatives containing benzodioxole
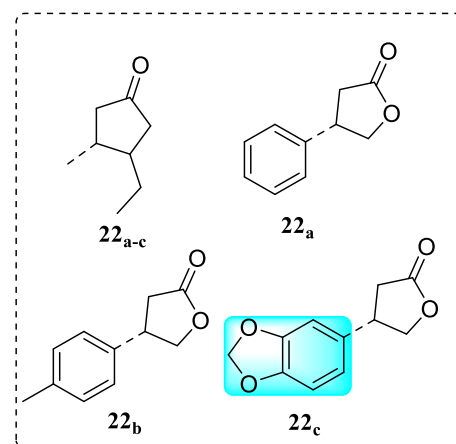
Figure 14. Some β-aryl-γ-lactone derivative/benzodioxole containing lactone derivative

Eighteen derivatives of racemic β-aryl-γ-lactones through chemical synthesis were prepared, characterized, and tested for their antifeedant and fungistatic activity by Skrobiszewski et al. (Fig. 14) [33]. The aromatic substituent structure was the most important element in anti-fungal action. The lactones with benzo[d][1,3]dioxole ring (22c etc.) were the most active whereas those with an unsubstituted benzene ring had a little action. Didecyldimethylammonium chloride (DDAC) was utilized as a reference compound. Eight lactones were shown to be effective against *Tribolium confusum, Trogoderma granarium, SitophilusGranaries,* and four species of *fusarium* species. The highest inhibition was observed for lactone 22c, which inhibited the growth of *F.oxysporum* AM13 in 70 %, F. avenaceum AM 11 and *F. solani* AM 203 in 66 %, and F. culmorum AM 9 in 55 %.The highest activities were found in the group of trans-γ-ethyl-γ-lactones (22a-c): lactone 22a and 22b were strong antifeedants, whereas lactone 22c exhibited the highest anti-fungal activity [33].
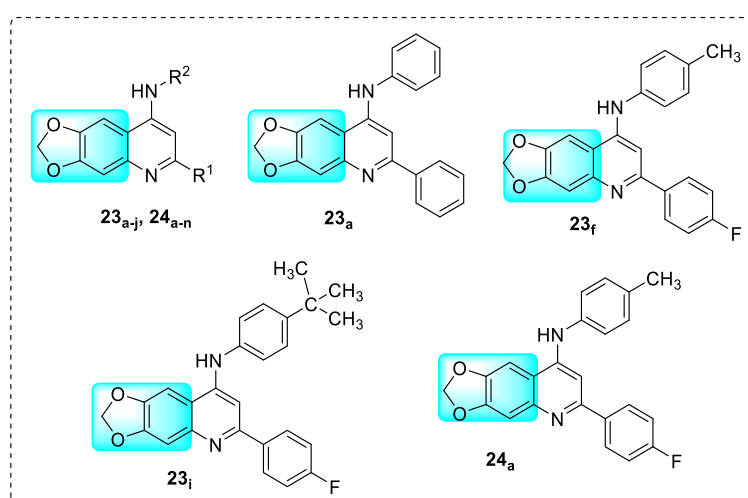
Figure 15. Some of the 4-aminoquinoline derivative containing 1,3-benzodioxole moiety

In 2021, a series of aminoquinolines bearing a 1,3-benzodioxole moiety were prepared and characterized by Yang et al. [4]. All of the target compounds (23a-23j and 24a-24n) and the positive control azoxystrobin (a commercial agricultural fungicide) were tested in vitro for anti-fungal activity against five phytopathogenic fungi (*P. piricola, A. brassicae, C. lunata, P. grisea*, and *A. alternate*) at 50g/mL using the mycelium growth rate method (Fig. 15). It was discovered that quinolone compounds with a phenyl substitution at position 2 and an aniline moiety at position 4 were effective anti-fungal possibilities, with the aniline moiety at position 4 playing a significant role in anti-fungal activity. Among compounds 23a-23j, compounds 23f and 23i possessed potent anti-fungal activities against the five tested fungi with an inhibition rate of more than 51.1 %. In most cases, their anti-fungal potencies were superior to the positive control azoxystrobin against the matching fungal strains. Moreover, compound 23a demonstrated anti-fungal solid activity against *C. lunata* and *A. alternative*, with 71.5 % and 63.1 % inhibition rates, respectively. After that, compound 24a–24n was produced by derivatization from compound 23f further to investigate the impact of C-2 substituents on anti-fungal efficacy. Most of the compounds 24a–24n demonstrated good to exceptional anti-fungal activity against the bulk of the fungal strains examined [4].

Anti-fungal activity against *C. lunatus* strain MUCL 38696 (m118), *A. niger* N402 cspA1, and *P. ostreatus* Plo5, Korosec et al. [30] tested 42 selected compounds of cinnamic acid derivatives (Fig. 16). Compound 25 was the most effective *C. lunatus* inhibitor. Additionally, the methyl piperidine in compound 28 anticipated that it would be able to generate Vander Waals and hydrophobic contacts with Ile274. Compound 28 demonstrated broad and robust anti-fungal activity, suppressing fungal growth by 75 % in all three tested species. Compound 25 literature predictions of the interaction between benzodioxole oxygen and heme iron may help to explain why both compounds 25 and 28 have more inhibitory activity than cinnamic acid. They show that the fungus benzoate 4-hydroxylase, CYP53A15, is competitively inhibited by cinnamic acid and four (25, 26, 27, and 28) of the 42 investigated derivatives [30].
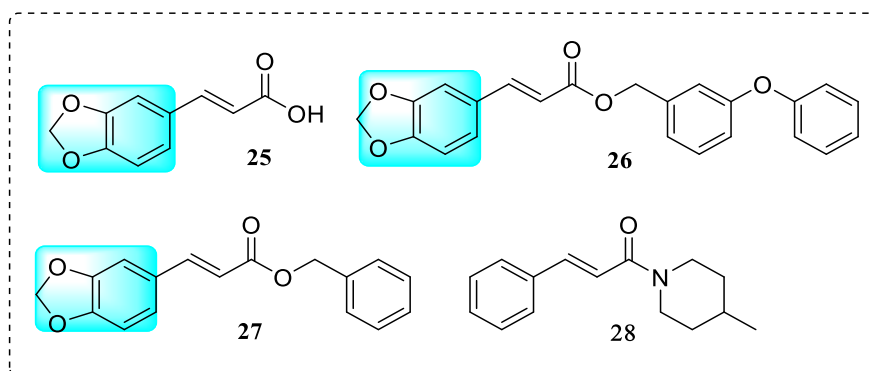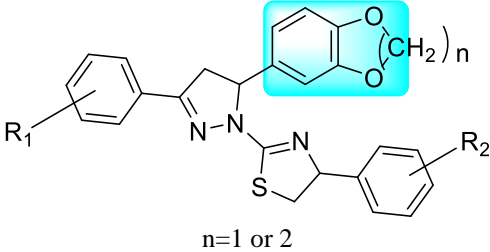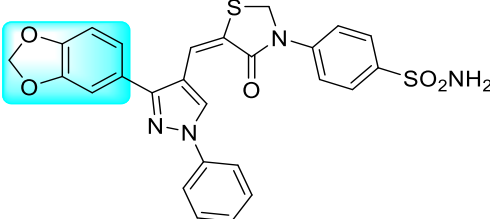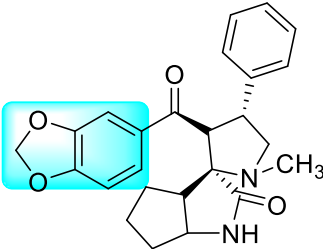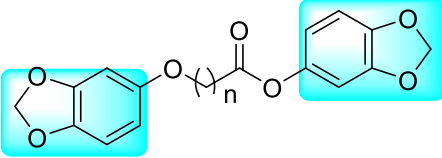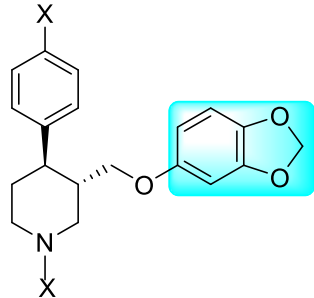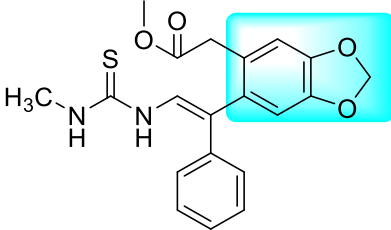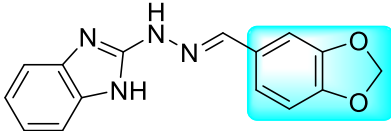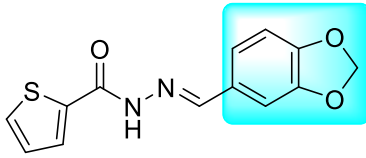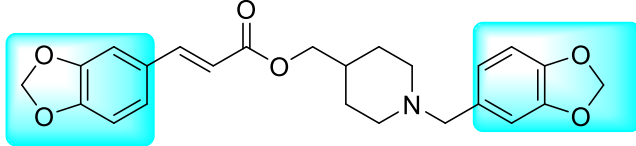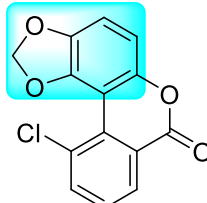
Figure 16. Some of the Cinnamic acid derivatives are 25. (E)-3-(benzo [d][1,3] dioxol-5-yl) acrylic acid, 26. (E)-3-phenoxybenzyl-3-(benzo[d][1,3] dioxol-5-yl)acrylate, 27. (E)-benzyl 3-(benzo[d][1,3]dioxol-5-yl)acrylate, 28. (E)-1-(4-methylpiperidin-1-yl)-3-phenyl prop-2-en-1-one

2.3 Miscellaneous Activity of Benzodioxole Incorporating Compounds

The benzodioxole moiety is a structural feature commonly found in numerous bioactive compounds, particularly in the field of medicinal chemistry. Its versatility allows it to exhibit a wide range of pharmacological activities. Table presents some of the miscellaneous potential associated with benzodioxole nucleus-containing compounds.

T a b l e

Miscellaneous activity of benzodioxole nucleus-containing compounds

S.No.	Biological activity	Chemical compound	Reference
1.	Anticancer activity	n=1 or 2	(H.H. Wang et al., 2013) [37]thirtythree
2.	Anti-inflammatory and analgesic		(Abd El Razik et al., 2017) [36]
3.	Antidiabetic		(Nivetha et al., 2022) [42]
4.	Hypolipaedemic & hepatoprotective		(Xie et al., 2021) [40]
5.	Antidepressant		(Slack et al., 2019) [14]
6.	Anticonvulsant		(Aboutabl et al., 2020a) [13]
7.	Antihelminthic		(Anichina et al., 2021) [27]

S.No.	Biological activity	Chemical compound	Reference
8.	Antihypertensive		(Leal et al., 2012) [39]
9.	Leishmanicidal		(Fernandes et al., 2015) [43]
10.	Antioxidant		(Zhou et al., 2021a) [21]

3 Future Perspectives of 1,3-Benzodioxole as an Antifungal Agent

The substances discussed in this review show promising antifungal activity. It is essential to understand the molecular mechanisms that drive the antifungal effect of these drugs. In order to find ways to increase the efficacy of these compounds, reduce their toxicity and increase their bioavailability, future research could focus on further optimising their structures. It is possible to increase efficacy and lower the likelihood of resistance development by combining antifungal drugs with various modes of action. The compounds containing 1,3-benzodioxole may have synergistic effects with currently available antifungal agents or with one another. It's critical to evaluate the environmental impact of these compounds in light of agricultural applications that were highlighted in the assessment. If these substances demonstrate efficacy in clinical trials and agricultural settings, factors such as large-scale manufacturing, affordability, and regional accessibility will be critical to their practicality.

4 Conclusions

The emergence of resistance to the existing anti-fungal drugs is a threatening condition for agroecosystems apart from a severe threat to human health. Therefore, researchers are motivated to find novel, secure, low-toxicity, low-resistance, high-efficacy anti-fungal compounds because of the progressive rise in the resistance profile and host toxicity of the currently available anti-fungal medications. The 1,3-benzodioxole scaffold in the arena of anti-fungal treatment against several pathogenic fungus species is well explained in this article. The material gathered from multiple reliable papers briefly explains that attachment of heterocycle moiety (e.g., primidinone, imidazole, thiazole, etc), aliphatic linker, amide linker at position 5, and in addition electron-withdrawing group (e.g., Br$_2$, etc.) at position 6 enhances the antifungal potential against various phytopathogenic and human pathogenic fungus species. The review may facilitate the creation of novel anti-fungal lead candidates and be very helpful to researchers and readers in medicinal chemistry.

Author Information*

*The authors' names are presented in the following order: First Name, Middle Name and Last Name

Amita Joshi Rana — PhD in Pharmaceutical Chemistry, Associate Professor, College of pharmacy, Graphic Era Hill University, SatTal Road, Bhimtal, Nagri Gaon, 263136, Uttarakhand, India; e-mail: amitapharmacy10@gmail.com; https://orcid.org/0000-0003-1907-4459

Sanjana Bisht (*corresponding author*) — Candidate of Pharmaceutical Chemistry, M.Pharm, Department of Pharmaceutical Sciences, Sir J.C. Bose Technical Campus, Kumaun University, Bhimtal-Nainital (Bhimtal Campus), block road, 263136, Uttarakhand, India; e-mail: sanjanab997@gmail.com; https://orcid.org/0009-0006-8799-1354

Kumud Upadhyaya — Professor, Dean of the Faculty of Technology, Sir J.C. Bose Technical Campus, Department of Pharmaceutical Sciences, Kumaun University, Bhimtal-Nainital, Bhimtal-Nainital (Bhimtal Campus), block road, 263136, Uttarakhand, India; e-mail: upkuupku@gmail.com; https://orcid.org/0000-0002-5871-1708

Pawan Singh — Assistant Professor, Faculty of Pharmaceutical Sciences, Amrapali University, Kaladhungi Road, Shiksha Nagar, 263139, Haldwani, Uttarakhand, India; e-mail: pawansinghhld02@gmail.com; https://orcid.org/0009-0005-5486-153X

Mahendra Rana — Associate Professor, Dean, Biomedical Sciences, Sir J.C. Bose Technical Campus, Department of Pharmaceutical Kumaun University, Bhimtal-Nainital, Bhimtal-Nainital (Bhimtal Campus), block road, 263136, Uttarakhand, India; e-mail: ranamahendra214@gmail.com; https://orcid.org/0000-0001-7967-7505

Shweta Singh — Candidate of Pharmaceutical Chemistry, M.Pharm, Department of Pharmaceutical Sciences, Kumaun University, Bhimtal-Nainital, Bhimtal-Nainital (Bhimtal Campus), block road, 263136, Uttarakhand, India; e-mail: shweta.s@rbmi.in; https://orcid.org/0009-0008-8410-921X

Author Contributions

The manuscript was written through contributions of all authors. All authors have given approval to the final version of the manuscript. CRediT: **Amita Joshi Rana, Sanjana Bisht, Kumud Upadhyaya** — conceptualization, data curation, investigation, methodology, validation, visualization, writing-review and editing; **Pawan Singh, Mahendra Rana, Shweta Singh** — data curation, formal analysis; **Sanjana Bisht, Pawan Singh** — conceptualization, data curation, resources, supervision, writing — original draft, writing — review and editing.

Acknowledgment

Conflict of interest

The authors declare no conflict of interest.

References

1 Shafiei, M., Toreyhi, H., Firoozpour, L., Akbarzadeh, T., Amini, M., Hosseinzadeh, E., Hashemzadeh, M., Peyton, L., Lotfali, E., & Foroumadi, A. (2021). Design, Synthesis, andIn VitroandIn VivoEvaluation of Novel Fluconazole-Based Compounds with Promising Antifungal Activities. *ACS Omega*, 6(38), 24981–25001. https://doi.org/10.1021/acsomega.1c04016

2 Ngo, H. X., Garneau-Tsodikova, S., & Green, K. D. (2016). A complex game of hide and seek: The search for new antifungals. *MedChemComm*, 7(7), 1285–1306. https://doi.org/10.1039/c6md00222f

3 Wang, R. X., Du, S. S., Wang, J. R., Chu, Q. R., Tang, C., Zhang, Z. J., Yang, C. J., He, Y. H., Li, H. X., Wu, T. L., & Liu, Y. Q. (2021). Design, Synthesis, and Antifungal Evaluation of Luotonin A Derivatives against Phytopathogenic Fungi. *Journal of Agricultural and Food Chemistry*, 69(48), 14467–14477. https://doi.org/10.1021/acs.jafc.1c04242

4 Yang, R., Li, Z., Xie, J., Liu, J., Qin, T., Liu, J., & Du, H. (2021). *4-Aminoquinolines Bearing a 1, 3-Benzodioxole Moiety : Synthesis and Biological Evaluation as Potential Antifungal Agents,* 2–9. https://doi.org/10.1002/cbdv.202100106

5 Al-harbi, R. A. K., El-sharief, M. A. M. S., & Abbas, S. Y. (2019). Bioorganic Chemistry derivatives with molecular docking study. *Bioorganic Chemistry*, 90(June), 103088. https://doi.org/10.1016/j.bioorg.2019.103088

6 Dutta Gupta, S., Rao, G. B., Bommaka, M. K., Raghavendra, N. M., & Aleti, S. (2016). Eco-sustainable synthesis and biological evaluation of 2-phenyl 1,3-benzodioxole derivatives as anticancer, DNA binding and antibacterial agents. *Arabian Journal of Chemistry*, 9, S1875–S1883. https://doi.org/10.1016/j.arabjc.2014.08.004

7 Shi, S., Xiao, P., Wang, K., Gong, Y., & Nie, J. (2010). Influence of chemical structures of benzodioxole-based coinitiators on the properties of the unfilled dental resin. *Acta Biomaterialia*, 6(8), 3067–3071. https://doi.org/10.1016/j.actbio.2010.02.022

8 Leite, A. C. L., Peixoto Da Silva, K., De Souza, I. A., Magali De Araújo, J., & Brondani, D. J. (2004). Synthesis, antitumour and antimicrobial activities of new peptidyl derivatives containing the 1,3-benzodioxole system. *European Journal of Medicinal Chemistry*, 39(12), 1059–1065. https://doi.org/10.1016/j.ejmech.2004.09.007

9   Carrasco, H., Raimondi, M., Svetaz, L., Di Liberto, M., Rodriguez, M. V., Espinoza, L., Madrid, A., & Zacchino, S. (2012). Antifungal activity of eugenol analogues. Influence of different substituents and studies on mechanism of action. *Molecules*, *17*(1), 1002–1024. https://doi.org/10.3390/molecules17011002

10   Lima, L. M. (2015). Safrole and the versatility of a natural biophore. *Revista Virtual de Quimica*, *7*(2), 495–538. https://doi.org/10.5935/1984-6835.20150023

11   Wang, J., Wang, W., Xiong, H., Song, D., & Cao, X. (2020a). Natural phenolic derivatives based on piperine scaffold as potential antifungal agents. *BMC Chemistry*, *14*(1), 1–12. https://doi.org/10.1186/s13065-020-00676-4

12   Zhou, S., Zou, H., Huang, G., & Chen, G. (2021b). Preparations and antioxidant activities of sesamol and it's derivatives. *Bioorganic and Medicinal Chemistry Letters*, *31* (November 2020), 127716. https://doi.org/10.1016/j.bmcl.2020.127716

13   Aboutabl, M. E., Hassan, R. M., El-Azzouny, A. A. S., Aboul-Enein, M. N., & Abd-Allah, W. H. (2020a). Design and synthesis of novel parabanic acid derivatives as anticonvulsants. *Bioorganic Chemistry*, *94* (October). https://doi.org/10.1016/j.bioorg.2019.103473

14   Slack, R. D., Abramyan, A. M., Tang, H., Meena, S., Davis, B. A., Bonifazi, A., Giancola, J. B., Deschamps, J. R., Naing, S., Yano, H., Singh, S. K., Newman, A. H., & Shi, L. (2019). A Novel Bromine-Containing Paroxetine Analogue Provides Mechanistic Clues for Binding Ambiguity at the Central Primary Binding Site of the Serotonin Transporter. *ACS Chemical Neuroscience*, *10*(9), 3946–3952. https://doi.org/10.1021/acschemneuro.9b00375

15   Wu, Z., Ding, N., Lin, D., Hu, A., Ye, J., & Li, G. (2016). Synthesis and fungicidal activity of some novel thiazole Schiff bases derived from benzo[d][1,3]dioxole. *Chemical Research in Chinese Universities*, *32*(1), 49–54. https://doi.org/10.1007/s40242-016-5284-6

16   Chavarria, D., Fernandes, C., Silva, V., Silva, C., Gil-Martins, E., Soares, P., Silva, T., Silva, R., Remião, F., Oliveira, P. J., & Borges, F. (2020). Design of novel monoamine oxidase-B inhibitors based on piperine scaffold: Structure-activity-toxicity, drug-likeness and efflux transport studies. *European Journal of Medicinal Chemistry*, *185*, 111770. https://doi.org/10.1016/j.ejmech.2019.111770

17   Sivakumar, K., Ramesh, S., & Lalitha, A. (2011). Cu(II)-impregnated sulfated MCM-41: An efficient and convenient protocol for the synthesis of 1,3-benzodioxoles. *Synthesis and Reactivity in Inorganic, Metal-Organic and Nano-Metal Chemistry*, *41*(1), 91–93. https://doi.org/10.1080/15533174.2010.538018

18   Aboutabl, M. E., Hassan, R. M., El-Azzouny, A. A. S., Aboul-Enein, M. N., & Abd-Allah, W. H. (2020b). Design and synthesis of novel parabanic acid derivatives as anticonvulsants. *Bioorganic Chemistry*, *94* (August). https://doi.org/10.1016/j.bioorg.2019.103473

19   Walia, S., Saha, S., & Parmar, B. S. (2004). Liquid chromatographic method for the analysis of two plant based insecticide synergists dillapiole and dihydrodillapiole. *Journal of Chromatography A*, *1047*(2), 229–233. https://doi.org/10.1016/j.chroma.2004.07.009

20   Cimmino, A., Fernández-Aparicio, M., Avolio, F., Yoneyama, K., Rubiales, D., & Evidente, A. (2015). Ryecyanatines A and B and ryecarbonitrilines A and B, substituted cyanatophenol, cyanatobenzo[1,3]dioxole, and benzo[1,3]dioxolecarbonitriles from rye (*Secale cereale* L.) root exudates: Novel metabolites with allelopathic activity on Orobanche seed germin. *Phytochemistry*, *109*, 57–65. https://doi.org/10.1016/j.phytochem.2014.10.034

21   Zhou, S., Zou, H., Huang, G., & Chen, G. (2021). Preparations and antioxidant activities of sesamol and it's derivatives. *Bioorganic & Medicinal Chemistry Letters*, 31, 127716. https://doi.org/10.1016/j.bmcl.2020.127716

22   Attia, M. I., El-Brollosy, N. R., Kansoh, A. L., Ghabbour, H. A., Al-Wabli, R. I., & Fun, H. -K. (2014). Synthesis, Single Crystal X-Ray Structure, and Antimicrobial Activity of 6-(1,3-Benzodioxol-5-ylmethyl)-5-ethyl-2-{[2-(morpholin-4-yl)ethyl]sulfanyl}pyrimidin-4(3H)-one. *Journal of Chemistry,* 2014, 1–8. https://doi.org/10.1155/2014/457430

23   Faidallah, H. M., Rostom, S. A. F., Badr, M. H., Ismail, A. E., & Almohammadi, A. M. (2015). Synthesis of Some 1,4,6-Trisubstituted-2-oxo-1,2-dihydropyridine-3-carbonitriles and Their Biological Evaluation as Cytotoxic and Antimicrobial Agents. *Archiv Der Pharmazie*, *348*(11), 824–834. https://doi.org/10.1002/ardp.201500175

24   Mohammad Arshad (2020). Design, Drug-Likeness, Synthesis, Characterization, Antimicrobial Activity, Molecular Docking, and MTT Assessment of 1,3-Thiazolidin-4-one Bearing Piperonal and Pyrimidine Moieties. *Russian Journal of Bioorganic Chemistry*, *46*(4), 599–611. https://doi.org/10.1134/S1068162020040056

25   Shahavar Sulthana, S., Arul Antony, S., Balachandran, C., & Syed Shafi, S. (2015). Thiophene and benzodioxole appended thiazolyl-pyrazoline compounds: Microwave assisted synthesis, antimicrobial and molecular docking studies. *Bioorganic and Medicinal Chemistry Letters*, *25*(14), 2753–2757. https://doi.org/10.1016/j.bmcl.2015.05.033

26   Shi, X. M., She, W. Y., Liu, T. T., Gao, L. X., Liu, Y. J., & Liu, Y. (2022). 1,3-Benzodioxole Derivatives Improve the Anti-Tumor Efficiency of Arsenicals. *International Journal of Molecular Sciences*, *23*(13), 1–21. https://doi.org/10.3390/ijms23136930

27   Anichina, K., Argirova, M., Tzoneva, R., Uzunova, V., Mavrova, A., Vuchev, D., Popova-Daskalova, G., Fratev, F., Guncheva, M., & Yancheva, D. (2021). 1H-benzimidazole-2-yl hydrazones as tubulin-targeting agents: Synthesis, structural characterization, anthelmintic activity and antiproliferative activity against MCF-7 breast carcinoma cells and molecular docking studies. *Chemico-Biological Interactions*, *345* (June). https://doi.org/10.1016/j.cbi.2021.109540

28   Al-Wabli, R. I., Al-Ghamdi, A. R., Aswathy, S. V., Ghabbour, H. A., Al-Agamy, M. H., Joe, I. H., & Attia, M. I. (2019). Synthesis, single crystal X-ray structure, DFT computations, hirshfeld surface analysis and molecular docking simulations on ({[(1E)-1-(1,3-benzodioxol-5-yl)-3-(1H-imidazol-1-yl) propylidene]amino}oxy)(furan-2-yl)methanone: A new antifungal agent. *Crystals*, *9*(1), 1–15. https://doi.org/10.3390/cryst9010025

29 Cai, Z., Ding, Z., Hao, Y., Ni, T., Xie, F., Zhao, J., Li, R., Yu, S., Wang, T., Chai, X., Jin, Y., Gao, Y., Zhang, D., & Jiang, Y. (2017). Bioorganic & Medicinal Chemistry Letters Design, synthesis, and SAR study of 3- (benzo [d][1, 3] dioxol-5-yl)-N-benzylpropanamide as novel potent synergists against fluconazole — resistant Candida albicans. *Bioorganic & Medicinal Chemistry Letters*, *27*(19), 4571–4575. https://doi.org/10.1016/j.bmcl.2017.08.053

30 Korošec, B., Sova, M., Turk, S., Kraševec, N., Novak, M., Lah, L., Stojan, J., Podobnik, B., Berne, S., Zupanec, N., Bunc, M., Gobec, S., & Komel, R. (2014). Antifungal activity of cinnamic acid derivatives involves inhibition of benzoate 4-hydroxylase (CYP53). *Journal of Applied Microbiology*, *116*(4), 955–966. https://doi.org/10.1111/jam.12417

31 Nicoletti, G., & White, K. (2022). The Anti-Fungal Activity of Nitropropenyl Benzodioxole (NPBD), a Redox-Thiol Oxidant and Tyrosine Phosphatase Inhibitor. *Antibiotics*, *11*(9). https://doi.org/10.3390/antibiotics11091188

32 Pries, V., Nöcker, C., Khan, D., Johnen, P., Hong, Z., Tripathi, A., Keller, A. L., Fitz, M., Perruccio, F., Filipuzzi, I., Thavam, S., Aust, T., Riedl, R., Ziegler, S., Bono, F., Schaaf, G., Bankaitis, V. A., Waldmann, H., & Hoepfner, D. (2018). Target Identification and Mechanism of Action of Picolinamide and Benzamide Chemotypes with Antifungal Properties. *Cell Chemical Biology*, *25*(3), 279–290.e7. https://doi.org/10.1016/j.chembiol.2017.12.007

33 Skrobiszewski, A., Gładkowski, W., Walczak, P., Gliszczyńska, A., Maciejewska, G., Klejdysz, T., Nawrot, J., & WawrzeNćzyk, C. (2015). Synthesis of β-aryl-γ-lactones and relationship: Structure — Antifeedant and antifungal activity. *Journal of Chemical Sciences*, *127*(4), 687–699. https://doi.org/10.1007/s12039-015-0823-0

34 Song, D., Cao, X., Wang, J., & Ke, S. (2020). Discovery of γ-lactam derivatives containing 1,3-benzodioxole unit as potential anti-phytopathogenic fungus agents. *Bioorganic and Medicinal Chemistry Letters*, *30*(2). https://doi.org/10.1016/j.bmcl.2019.126826

35 Wang, J., Wang, W., Xiong, H., Song, D., & Cao, X. (2020b). Natural phenolic derivatives based on piperine scaffold as potential antifungal agents. *BMC Chemistry*, 1–12. https://doi.org/10.1186/s13065-020-00676-4

36 Abd El Razik, H. A., Badr, M. H., Atta, A. H., Mouneir, S. M., & Abu-Serie, M. M. (2017). Benzodioxole–Pyrazole Hybrids as Anti-Inflammatory and Analgesic Agents with COX-1,2/5-LOX Inhibition and Antioxidant Potential. *Archiv Der Pharmazie*, *350*(5), 1–19. https://doi.org/10.1002/ardp.201700026

37 Wang, H. H., Qiu, K. M., Cui, H. E., Yang, Y. S., Yin-Luo, Xing, M., Qiu, X. Y., Bai, L. F., & Zhu, H. L. (2013). Synthesis, molecular docking and evaluation of thiazolyl-pyrazoline derivatives containing benzodioxole as potential anticancer agents. *Bioorganic and Medicinal Chemistry*, *21*(2), 448–455. https://doi.org/10.1016/j.bmc.2012.11.020

38 Easwar, S., & Argade, N. P. (2003). Amano PS-catalysed enantioselective acylation of (±)-α-methyl-1,3-benzodioxole-5-ethanol: An efficient resolution of chiral intermediates of the remarkable antiepileptic drug candidate, (-)-talampanel. *Tetrahedron Asymmetry*, *14*(3), 333–337. https://doi.org/10.1016/S0957-4166(02)00836-4

39 Leal, C. M., Pereira, S. L., Kümmerle, A. E., Leal, D. M., Tesch, R., De Sant'Anna, C. M. R., Fraga, C. A. M., Barreiro, E. J., Sudo, R. T., & Zapata-Sudo, G. (2012). Antihypertensive profile of 2-thienyl-3,4-methylenedioxybenzoylhydrazone is mediated by activation of the A2A adenosine receptor. *European Journal of Medicinal Chemistry*, *55*, 49–57. https://doi.org/10.1016/j.ejmech.2012.06.056

40 Xie, Y. D., Xu, Y. H., Liu, J. P., Wang, B., Shi, Y. H., Wang, W., Wang, X. P., Sun, M., Xu, X. Y., & Bian, X. L. (2021). 1,3-Benzodioxole-based fibrate derivatives as potential hypolipidemic and hepatoprotective agents. *Bioorganic and Medicinal Chemistry Letters*, *43* (December 2020), 127898. https://doi.org/10.1016/j.bmcl.2021.127898

41 Ferreira, R. C., Batista, T. M., Duarte, S. S., Silva, D. K. F., Lisboa, T. M. H., Cavalcanti, R. F. P., Leite, F. C., Mangueira, V. M., Sousa, T. K. G. de, Abrantes, R. A. de, Trindade, E. O. da, Athayde-Filho, P. F. de, Brandão, M. C. R., Medeiros, K. C. de P., Farias, D. F., & Sobral, M. V. (2020). A novel piperine analogue exerts in vivo antitumor effect by inducing oxidative, antiangiogenic and immunomodulatory actions. *Biomedicine and Pharmacotherapy*, *128* (May), 110247. https://doi.org/10.1016/j.biopha.2020.110247

42 Nivetha, N., Martiz, R. M., Patil, S. M., Ramu, R., Sreenivasa, S., & Velmathi, S. (2022). Benzodioxole grafted spirooxindole pyrrolidinyl derivatives: synthesis, characterization, molecular docking and anti-diabetic activity. *RSC Advances*, *12*(37), 24192–24207. https://doi.org/10.1039/d2ra04452h

43 Fernandes, Í. A., Almeida, L. De, Espuri, P., Marques, M. J., Rocha, R. P., Coelho, L. F. L., Carvalho, D. T., & Viegas, C. (2015). Synthesis and biological evaluation of novel piperidine-benzodioxole derivatives designed as potential leishmanicidal drug candidates. *Bioorganic & Medicinal Chemistry Letters,* 10–13. https://doi.org/10.1016/j.bmcl.2015.05.068

PHYSICAL AND ANALITICAL CHEMISTRY

Mudar A. Abdulsattar[1] [iD]*, Sawsan M. Almaroof[2]

[1]Ministry of Science and Technology, Baghdad, Iraq;
[2]Engineering Construction Office, Ministry of Construction, Housing, Municipalities and Public Works, Baghdad, Iraq
(*Corresponding author′s e-mail: mudarahmed3@yahoo.com)

H2S Properties and Temperature Effects
on the Response of Pristine and Al-Doped ZnO Gas Sensor

H2S is a poisonous gas that needs to be censored to protect humans from its exposure. H2S gas sensitivity and interaction with pristine and Al-doped ZnO clusters were studied using the transition state theory method. The reaction of ZnO with H2S gas is usually weak and can be enhanced by doping. Elements or their oxides, such as platinum group elements, are traditionally used as doping substances. However, the use of other cheaper elements or oxides such as Al or Mn also increases the reaction rate. The mechanism of increasing the reaction rate and sensitivity by Al doping is the subject of present work. The calculation results show that Al-doped ZnO increases the sensitivity towards H2S by growing the resistance of Al-doped ZnO due to lattice distortion. The Gibbs activation energy remains almost the same as calculated by the present model. In conclusion, it should be noted that good agreement between theory and experiment was achieved in terms of temperature-dependent reaction rate, gas response, recovery and response time for different doping ratios. For the first time, the autoignition reaction and temperature of H2S were considered in sensors. Further improvement in transition state theory is needed to include further gas sensor features.

Keywords: Al doping, ZnO cluster, pristine, H2S gas sensor, DFT, transition state, autoignition temperature, activation energy

Introduction

Zinc oxide is one of the most studied materials in the scientific literature due to its unique properties and wide application [1], such as paints, cosmetics, rubber, composites, etc. One of its applications is as a gas sensor [2]. ZnO is used to monitor gases such as ethanol [3], CO_2 [4], NO_2 [5], H_2S [6] etc. The response of pure ZnO or other pure compounds can be enhanced by doping. Platinum group elements such as ruthenium, rhodium, and palladium are usually most effective in addition to other transition elements [7, 8]. The response enhancement is generally explained by the reduction of activation energy needed for the reaction between the gas and sensitive material to proceed [9, 10]. However, cheaper doping with non-transition elements enhances the sensor's response to the targeted gas [6, 11]. Optimized ZnO small molecules, which resemble the wurtzite lattice structure, can be used to study the behavior of ZnO properties and reactions [12, 13]. The most appropriate molecule in terms of size and computation time is $Zn_{13}O_{13}$, called ZnO wurtzoid2c [14].

Hydrogen sulfide is a poisonous gas that reacts with the human body or materials, so it must be monitored [15]. H_2S can be explosive when its concentration exceeds certain limits in air [16]. The electronic structure and shape of the H_2S molecule are similar to the structure and shape of the water molecule, in which oxygen is replaced by sulfur. H_2S can be ignited by an external ignition source if its temperature exceeds its flash point temperature at –82 °C [17]. However, H_2S can explode at temperatures above its au-

toignition temperature of 232 °C without an external ignition source [17]. H_2S can be removed from fuel using ZnO [18, 19], so it is natural to expect that ZnO will be used as a H_2S gas detector [20, 21].

Despite the substantial experimental literature on gas sensors, including thousands of scientific papers [22, 23], theoretical studies related to gas sensors are limited to a few gases and gas-sensitive materials. A common theoretical approach involves density functional theory (DFT) for gas sensing analysis [22, 23]. Theoretical modeling of the reaction is carried out using either the Arrhenius equation or the more modern transition state theory [10].

This study uses transition state theory and DFT to investigate pure or Al-doped ZnO as an H_2S gas sensor. The H_2S reaction rate and response temperature dependence are compared with existing experiment. Response and recovery time trends are also compared to available experiment.

Computational Details and Theoretical Background

Gaussian 09 software was used to perform present calculations [24]. The calculation used B3LYD theory level of DFT and 6-311G** basis set. Gas reaction with solids usually contains long-range forces that enforce dispersion corrections. Dispersion corrections at the GD3BJ level are used successfully in previous and present calculations [10].

The removal of H_2S from fuel or biological materials using ZnO is a well-known process [18, 19] which can be represented by the following reaction:

$$ZnO + H_2S \rightarrow ZnS + H_2O. \tag{1}$$

In the above reaction, sulfur replaces oxygen in the ZnO lattice. Figure 1a shows the adsorption of the H_2S molecule on the $Zn_{13}O_{13}$ molecule (denoted $[Zn_{13}O_{13}\text{—}H_2S]^a$). It should be noted that the H_2S molecule loses one of its hydrogen atoms simultaneously with adsorption.

a b
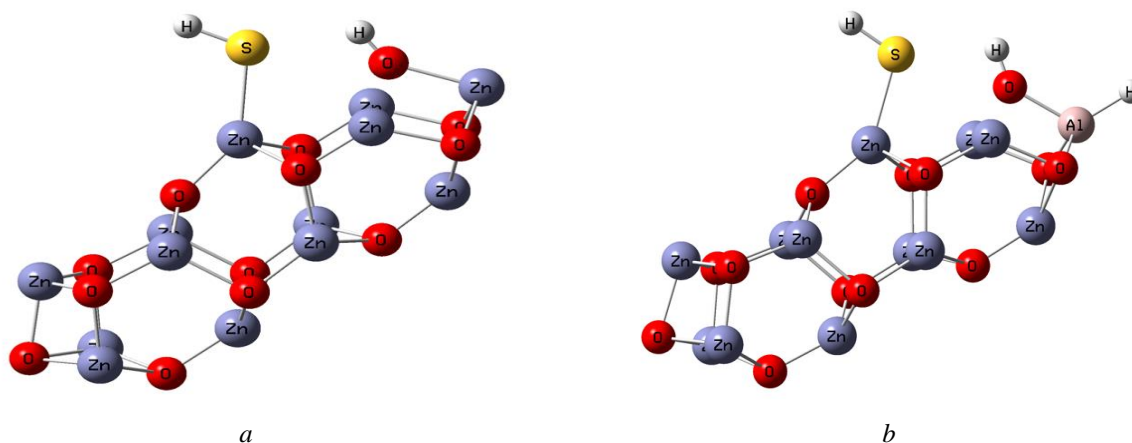
Figure 1. a — optimized geometry of $Zn_{13}O_{13}$ cluster with adsorbed H_2S molecule ($[Zn_{13}O_{13}\text{—}H_2S]^a$);
b — optimized geometry $HAlZn_{12}O_{13}$ cluster with adsorbed H_2S gas ($[HAlZn_{12}O_{13}\text{—}H_2S]^a$)

Figure 1b shows the effect of H_2S adsorption when one Zn atom is replaced by aluminum in $Zn_{13}O_{13}$ (denoted $HAlZn_{12}O_{13}\text{—}H_2S]^a$). A hydrogen atom was added to the Al-doped molecule to compensate the difference in oxidation state of Al(+3) and Zn(+2).

The transition state is the state of the highest potential energy along the reaction coordinates. A double dagger is added to this state to differentiate it from other states (denoted $[Zn_{13}O_{13}\text{—}H_2S]^{\ddagger}$). The slight movement of atoms in the transition state decreases its molecular Gibbs free energy ($\Delta G^{\ddagger}$) by 0.0617 eV for the pure and 0.0581 eV for the Al-doped ZnO molecule in normal temperature and pressure, as shown in Figure 2.

In transition state theory, the reaction rate of H_2S gas with ZnO can be determined by the formula [25–27]:

$$\frac{d[ZnO]}{dt} = -[ZnO]\,[H_2S]_e\,k(T), \tag{2}$$

$$k(T) = AT^m \exp^{\left(\frac{-\Delta G^{\ddagger}}{k_B T}\right)}. \tag{3}$$

In the above equations, [ZnO] and $[H_2S]_e$ are the ZnO and H_2S gas concentrations, respectively. The subscript (e) in $[H_2S]_e$ concentration indicates the effective available concentration due to H_2S burning in high temperatures as it approaches the autoignition temperature. $k(T)$ is the temperature-dependent term in the rate equation. k_B is the Boltzmann constant. A in Eq. (3) is a scaling constant corresponding to the sensitive material's area in the experiment. The value of the temperature exponent (m) in (T^m) can be fit to experimental results and depends on the type of interacting materials and diffusion of reaction gases. The Gibbs free energy of transition ($\Delta G^{\ddagger}$) is related to the enthalpy of transition ($\Delta H^{\ddagger}$) and entropy of transition ($\Delta S^{\ddagger}$) by the equation:

$$\Delta G^{\ddagger} = \Delta H^{\ddagger} - T\Delta S^{\ddagger}. \tag{4}$$

The Gibbs free energy of the transition is usually impossible to obtain with the required ratio of ingredients due to computational size problems. This problem can be solved using the modified Evans–Polanyi principle [10]:

$$\Delta G^{\ddagger} = \Delta G_0^{\ddagger} + \beta \Delta G_1^{\ddagger}. \tag{5}$$

In Eq. (5), $\Delta G_0^{\ddagger}$ and $\Delta G_1^{\ddagger}$ there are two known values of the Gibbs free energy of activation for specific concentrations of the dopants. These points can be used to obtain $\Delta G^{\ddagger}$ through the interpolation parameter β. The above equation is a modification of the Evans–Polanyi principle with the inclusion of entropy in the formalism [10, 28].

A logistic function can be used to account for the decrease in H_2S gas content as it approaches the autoignition temperature of 232 °C:

$$f(T) = \frac{1}{1 + e^{k_s(T-T_0)}}. \tag{6}$$

In Eq. (6), k_s is the steepness of the decrease in H_2S concentration, while T_0 is the temperature at which H_2S reaches half of its concentration.

The experimental sensitivity of a gas sensor is obtained by dividing the resistance of the sensor in the air (R_a) by the resistance when the detected gas (H_2S) is added (R_g). This ratio (R_a/R_g) is proportional to the calculated reaction rate:

$$\text{Response}(\text{theoretical}) = 1 + C\left|\frac{d[\text{ZnO}]}{dt}\right|. \tag{7}$$

C in the above equation is the proportionality constant, and a value of one (1) is added to account for the response value in the absence of the detected gas.

The most important parts of any theory are the results that can be compared to experiments. In gas sensors, 90 % of the response and recovery time corresponds to the moment when the resistivity changes to 90 % of its original resistance.

By integrating Eq. (2), the 90 % of response time can be determined by the formula:

$$t_{res(90\%)} = \frac{\ln(10)}{[\text{H}_2\text{S}]_e \, AT^m \, \exp^{\left(\frac{-G^{\ddagger}}{k_B T}\right)}}. \tag{8}$$

On the other hand, the 90 % of recovery time is the time that corresponds to the return of the resistivity to 90 % of its original value. This time corresponds to the oxygen retrieval of the oxygen-reduced ZnO, as in the reaction:

$$\text{Zn}_{13}\text{O}_{12} + \tfrac{1}{2}\text{O}_2 \rightarrow \text{Zn}_{13}\text{O}_{13}. \tag{9}$$

In this case, the recovery time corresponding to the above reaction can be estimated using the equation:

$$t_{rec(90\%)} = \frac{\ln(10)}{[\text{O}_2]_e \, AT^m \, \exp^{\left(\frac{-G^{\ddagger}}{k_B T}\right)}}. \tag{10}$$
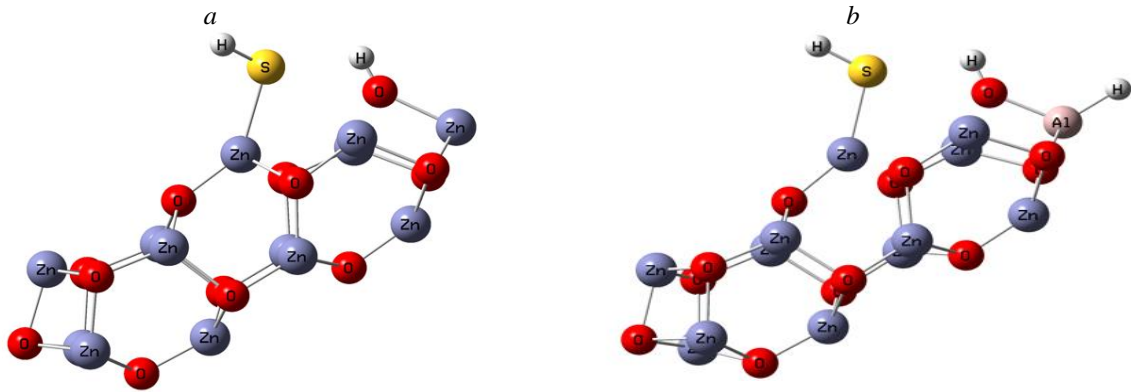
Figure 2. *a* — optimized geometry of transition state of adsorbed H$_2$S on Zn$_{13}$O$_{13}$ ([Zn$_{13}$O$_{13}$—H$_2$S]‡);
b — optimized geometry of transition state of HAlZn$_{12}$O$_{13}$ with H$_2$S gas ([HAlZn$_{12}$O$_{13}$—H$_2$S]‡)

Results and Discussion

Figure 3 shows the variation of Gibbs energy of transition as a function of temperature for pure ZnO doped with 2 % and 4 % Al (molar) upon absorption of H$_2$S gas.
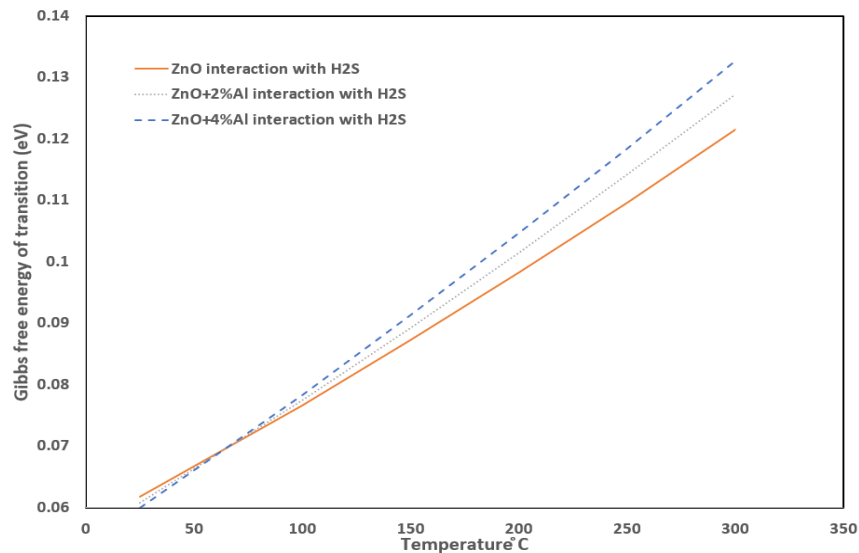
Figure 3. Gibbs free energy of transition for pure, 2 %, and 4 % Al doped ZnO
as a function of temperatures upon interaction with H$_2$S gas

As can be seen in Figure 3, the Gibbs energies are very close and intersect at low temperatures from 50 to 100 °C. The reason for the intersection is the increase in activation entropy of the doped ZnO [29]. This shows that the reaction rate is nearly equal in the pure and Al-doped ZnO. The increase in response in the Al-doped ZnO is mainly due to an increase in resistance due to doping. The imperfections in the lattice structure interact with electrons and increase resistivity. This increase has been proven for other binary systems as well [30].

Figure 4 shows the response of pure ZnO to H$_2$S.
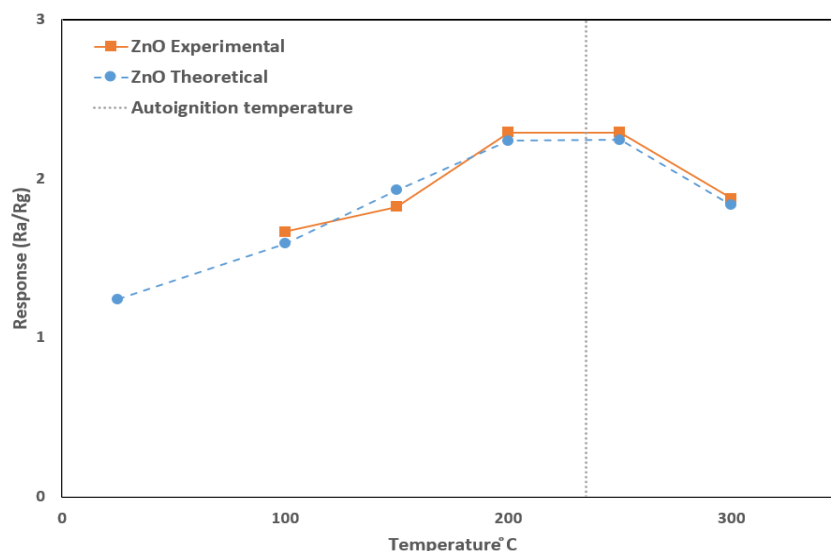
Figure 4. The experimental [6] and theoretically calculated responses of the pure ZnO sensor to 600 ppm H$_2$S gas at different temperatures. The autoignition temperature of H$_2$S gas [17] is indicated by the dotted line

As can be seen in Figure 4, pure ZnO responds poorly to H$_2$S gas due to difficulty in oxygen pick-up from its tight structure by H$_2$S gas. The theoretical temperature-dependent exponent part (T^m) in Eq. (3) is T^4. The temperature dependence is higher than the usual exponent (0 to 1) in different reaction theories. This temperature dependence is the hydrogen (in H$_2$S) fast diffusion into the ZnO structure. The autoignition temperature of H$_2$S gas is indicated in Figure 4, which shows the usual trend of optimum response temperature just before the autoignition temperature [11].

Figure 5 shows the response of 2 % Al (molar) doped ZnO.
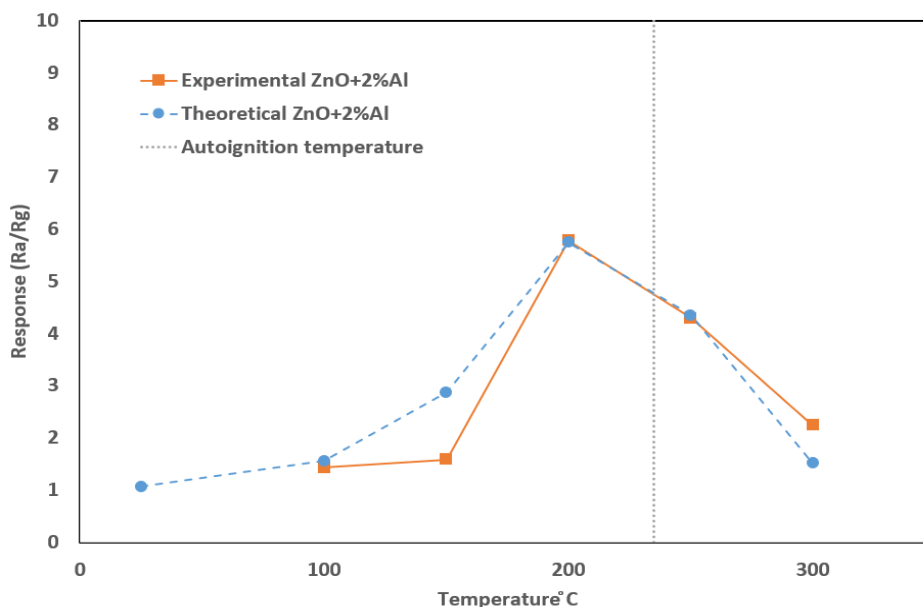
Figure 5. The experimental [6] and calculated theoretical responses of the 2 % Al (molar) doped ZnO sensor to 600 ppm H$_2$S gas at a range of temperatures. The autoignition temperature of H$_2$S gas [17] is indicated by the dotted line

As can be seen in Figure 5, the response of the 2 % Al doped ZnO is more than twice that of pure ZnO. The increase in response is because doping with 2 % Al destroys the periodic lattice structure of pure ZnO. The imperfections in the lattice structure interact with electrons and increase resistivity. The theoretical temperature exponent dependence (T^m) is also high with $m = 10$.

Figure 6 shows the response of 4 % Al (molar) doped ZnO.
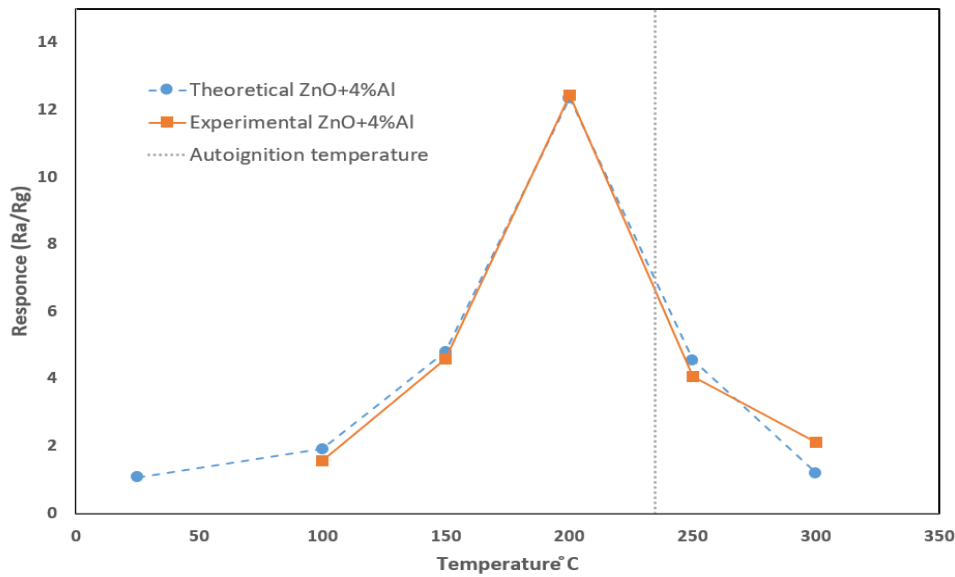
Figure 6. The experimental [6] and calculated theoretical responses of the 4 % Al (molar) doped ZnO sensor to 600 ppm H$_2$S gas at a range of temperatures. The autoignition temperature of H$_2$S gas [17] is indicated by the dotted line

As can be seen in Figure 6, the response of the 4 % Al doped ZnO is higher than pure and 2 % Al-doped ZnO. The 4 % Al-doped ZnO is near the highest possible response in Al-doped ZnO. As in the case of 2 % Al, the imperfections in the lattice structure interact with electrons and increase resistivity. The theoretical temperature exponent dependence (T^m) is also high with $m = 12$.

The three theoretical parts of Figures (4–6) show good agreement with experiments except for one point in Figure 5, that violets even the trend of the original experimental results [6].

The experimental response time data for the present system is scarce [6]. However, Figure 7 compares theoretical results and the experimental data available in reference [6] for the 4 % Al-doped ZnO. As shown in Figure 7, the 90 % response time is high except for a small range of temperatures. Theoretical results were obtained using Eq. (8).
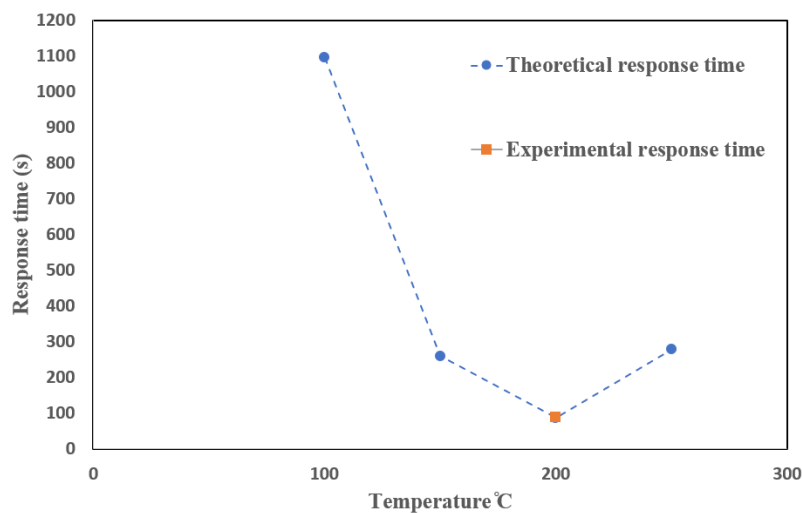
Figure 7. Response time of 4 % Al-doped ZnO at a range of temperatures for 600 ppm H$_2$S. Experimental data are taken from the reference [6]

At the recovery stage in the gas sensor in which atmospheric air (with no detected gas) passes over the sensitive material, the sulfurized surface of pure or Al-doped ZnO is desulfurized and re-oxidized as in the equations:

$$ZnS + O_2 \rightarrow Zn + SO_2 \tag{11}$$

$$Zn + \tfrac{1}{2}O_2 \rightarrow ZnO. \tag{12}$$

The desulfurization occurs in the response and recovery phase as well; however, at the end of the response phase, an oxygen-deficient ZnO surface occurs that will be oxidized in the recovery phase. Figure 8 shows the Gibbs free energy of the transition of oxygen-deficient pure and 4 % Al-doped ZnO as they interact with oxygen in the recovery phase.
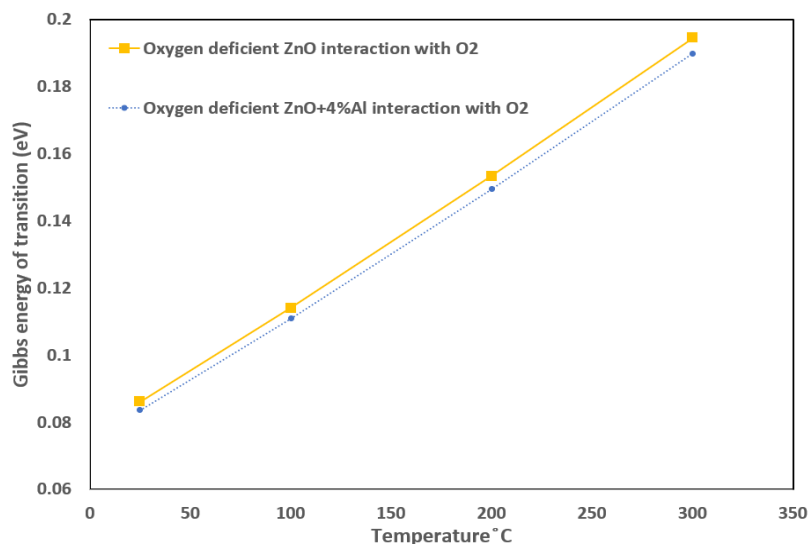
Figure 8. Gibbs free energy of the transition for pure oxygen-deficient and 4 % Al doped ZnO
as a function of temperatures as they interact with O_2

Figure 9 shows the recovery time of 4 % Al-doped ZnO to 600 ppm H_2S gas. The theoretical 90 % recovery time increases with temperature due to the increase in Gibbs free energy of transition as in Figure 8. The temperature exponent (T^m) in Eq. (10) is ($m = 0$). The negligible temperature exponent is due to the lack of oxygen diffusion into the ZnO structure.
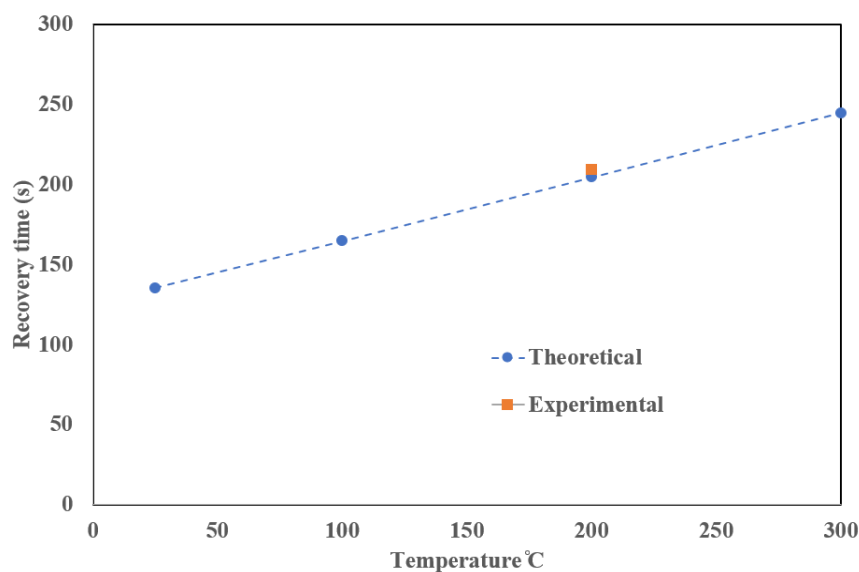
Figure 9. Recovery time of 4 % Al-doped ZnO as a function of temperature for 600 ppm H_2S.
Experimental data are taken from reference [6]

Table summarizes the Gibbs energy of transition and the five parameters used in each reaction corresponding to the several doping percentages and O_2 retrieval. The Gibbs free energy of transition is taken at $25\,°C$ temperature and normal pressure. Gibbs energy of transitions for other temperatures is given in Figures 3 and 8.

T a b l e

Parameters used to simulate H_2S gas sensing and O_2 recovery reaction model of pure and Al-doped ZnO

| No.	Reaction	$\Delta G^{\ddagger}$ (eV)*	A	m	k_s (K^{-1})	T_0 (°C)	C (s)
1	[ZnO—H$_2$S]^a ↓ [ZnO—H$_2$S]‡	0.0617	1.4 10^{-8} s^{-1}·K^{-4}	4	0.025	260	40
2	[2 % Al/ZnO—H$_2$S]^a ↓ [2 % Al/ZnO—H$_2$S]‡	0.0608	4.2 10^{-23} s^{-1}·K^{-10}	10	0.06	230	47
3	[4 % Al/ZnO—H$_2$S]^a ↓ [4 % Al/ZnO—H$_2$S]‡	0.0599	4.4 10^{-29} s^{-1}·K^{-12}	12	0.08	220	53
4	[4 % Al/Zn<u>O</u>—O$_2$]^a ↓ [4 % Al/Zn<u>O</u>—-O$_2$]‡	0.0836	2.1 s^{-1}	0	–	–	–
*Note: $\Delta G^{\ddagger}$ values are at 25 °C temperature and normal pressure. An underscore is added to the oxygen in the fourth reaction to indicate an oxygen-deficient cluster of ZnO.							

It can be seen in Table that as the doping percentage increases, the Gibbs free energy of transition decreases. However, this is reversed as the temperature increases (as shown in Fig. 8) because of entropy, as explained previously. The parameter (A) has different units due to different temperature dependence and concentrations of each doping percentage. This is reflected by the exponent (m) that increases as the doping percentage increases. The parameter (A) for the fourth reaction differs from the first three reactions due to the difference in oxygen concentration (20 % of air) compared to ppm values of H_2S. The reason for the temperature exponent (m) increase in the reaction of H_2S gas with Al-doped ZnO is the distortion of the ZnO lattice due to doping. The distortion of the ZnO periodic lattice allows the H_2S gas to enter deeper (diffuse) and react with deep Al/ZnO layers, which makes the reaction more vigorous with the increase in temperature. In addition, since the Al oxidation state (3) is higher than Zn (2), several vacancies are created. Some vacancies are filled with atmospheric oxygen, and others remain unfilled. In both cases, the reaction increases. The filled vacancies (with oxygen atoms) will add additional oxygen sites so that H_2S will collide with more oxygen atoms and react as in Eq. (1). The remaining unfilled vacancies with Al dangling bonds trap H_2S molecules, making an increase in the reaction rate that finally increases the sensor response. All these reactions are governed by the rise in diffusion that depends itself (diffusion) on temperature. The steepness of the decrease in H_2S concentration (k_s) increases as the doping percentage increases. This is the reverse behavior of (T_0), which is the temperature at which the density of H_2S reaches half of its original density due to autoignition. Finally, the parameter (C) that correlates the resistance with the reaction rate increases as the doping percentage rises due to imperfections in the ZnO lattice caused by doping. The last reaction does not include autoignition parameters because the O_2 gas does not have autoignition temperature, and the percentage of O_2 in the air is nearly constant.

Conclusions

Theoretical simulation of gas sensors rarely deals with calculating response or recovery reaction kinetics of gas sensing. The present model uses transition state, including its DFT tool, to calculate reaction rate, response, response time, and recovery time. The results as a function of temperature are in good agreement with the experiment. The present model describes the sensing mechanism as interplay between the reaction of the detected gas (H_2S) with the sensitive material (pure or Al-doped ZnO) or the reaction of the oxygen-deficient detection material with O_2 in air. As the temperature approaches the autoignition temperature, the detected gas prefers the reaction with O_2 in the air before reaching the sensitive material. The maximum response value is at a temperature just below the autoignition temperature. The temperature dependence of the reaction of H_2S is more robust as the Al doping increases to reach the optimum doping percentage at 4 %.

The temperature dependence of the reaction of H_2S with O_2 in the air becomes more robust as the optimum doping percentage at 4 % Al is reached. This indicates that Al doping increases H_2S reaction with the sensitive material and also increases the reaction of H_2S with O_2 in the air due to lattice distortion.

Author Information*

The authors' names are presented in the following order: First Name, Middle Name and Last Name

Mudar Ahmed Abdulsattar — Chief Scientific Researcher, Head of Solid-State Department, Ministry of Science and Technology, Rusafa Street, 52, 10045, Baghdad, Iraq, e-mail: mudarahmed3@yahoo.com; https://orcid.org/0000-0001-8234-6686

Sawsan Mudar Almaroof — Senior Engineer, Information Technology Department, Engineering Construction Office, Ministry of Construction, Housing, Municipalities and Public Works, Baghdad Governorate, 10011, Baghdad, Iraq; e-mail: sawsanalmaroof@outlook.com

Author Contributions

The manuscript was written through contributions of all authors. All authors have given approval to the final version of the manuscript. CRediT: **Mudar Ahmed Abdulsattar** — supervision, data curation, methodology, review & editing, **Sawsan Mudar Almaroof —** investigation, formal analysis, writing-original draft.

Conflicts of Interest

The authors declare no conflict of interest.

References

1 Noman, M.T., Amor, N., & Petru, M. (2022). Synthesis and Applications of ZnO Nanostructures (ZONSs): A Review. *Critical Reviews in Solid State and Materials Sciences*, *47*, 99–141. https://doi.org/10.1080/10408436.2021.1886041.

2 Vanga, S.R., & Sarada, V. (2022). Improving sensitivity of ZnO nanorods for the application of gas sensors at low temperatures: a review. *Proceedings — 2nd International Conference on Next Generation Intelligent Systems*, ICNGIS 2022. https://doi.org/10.1109/ICNGIS54955.2022.10079894.

3 Zhang, L., Kang, Y., Tang, Y., & Yu, F. (2024). UV-Activated ZnO–NiO Heterojunction Sensor for Ethanol Gas Detection at Low Working Temperature. *Materials Science in Semiconductor Processing*, *169*. https://doi.org/10.1016/j.mssp.2023.107925.

4 Abdelkarem, K., Saad, R., El Sayed, A.M., Fathy, M.I., Shaban, M., & Hamdy, H. (2023). Design of High-Sensitivity La-Doped ZnO Sensors for CO_2 Gas Detection at Room Temperature. *Scientific Reports*, *13*. https://doi.org/10.1038/s41598-023-45196-y.

5 Feng, Z., Wang, H., Zhang, Y., Han, D., Cheng, Y., Jian, A., & Sang, S. (2023). ZnO/GaN n-n Heterojunction Porous Nanosheets for Ppb-Level NO_2 Gas Sensors. *Sensors and Actuators B: Chemical*, *396*. https://doi.org/10.1016/j.snb.2023.134629.

6 Kolhe, P.S., Shinde, A.B., Kulkarni, S.G., Maiti, N., Koinkar, P.M., & Sonawane, K.M. (2018). Gas Sensing Performance of Al Doped ZnO Thin Film for H_2S Detection. *Journal of Alloys and Compounds*, *748*, 6–11. https://doi.org/10.1016/j.jallcom.2018.03.123.

7 Kumar, S., Lawaniya, S.D., Agarwal, S., Yu, Y.-T., Nelamarri, S.R., Kumar, M., Mishra, Y.K., & Awasthi, K. (2023). Optimization of Pt Nanoparticles Loading in ZnO for Highly Selective and Stable Hydrogen Gas Sensor at Reduced Working Temperature. *Sensors and Actuators B: Chemical*, *375*. https://doi.org/10.1016/j.snb.2022.132943.

8 Xuan, J., Wang, L., Zou, Y., Li, Y., Zhang, H., Lu, Q., Sun, M., Yin, G., & Zhou, A. (2022). Room-Temperature Gas Sensor Based on in Situ Grown, Etched and W-Doped ZnO Nanotubes Functionalized with Pt Nanoparticles for the Detection of Low-Concentration H2S. *Journal of Alloys and Compounds*, *922*. https://doi.org/10.1016/j.jallcom.2022.166158.

9 Abdulsattar, M.A. (2020). Transition State Theory Application to H_2 Gas Sensitivity of Pristine and Pd Doped SnO_2 Clusters. *Karbala International Journal of Modern Science*, 6, 13. https://doi.org/10.33640/2405-609X.1615.

10 Abdulsattar, M.A. (2023). The Reaction of Pristine and Rh-Doped SnO_2 Clusters with Acetone: Application of Evans–Polanyi Principle to Transition State Theory. *Journal of Molecular Modeling*, *29*. https://doi.org/10.1007/s00894-023-05710-5.

11 Abdulsattar, M.A. (2023). $Ga_xIn_2–XO_3$ Surface Pyramids Interaction with Formaldehyde: Thermodynamic and Sensing Analysis. *Karbala International Journal of Modern Science*, *9*, 8. https://doi.org/10.33640/2405-609X.3324.

12 Abdulsattar, M.A. (2015). Capped ZnO (3, 0) Nanotubes as Building Blocks of Bare and H Passivated Wurtzite ZnO Nanocrystals. *Superlattices and Microstructures*, *85*, 813–819. https://doi.org/10.1016/j.spmi.2015.07.015.

13 Abdulsattar, M.A., Abduljalil, H.M., & Abed, H.H. (2022). Effect of Au Doping on ZnO Nanoparticles Sensitivity to Ethanol: A Thermodynamic and Density Functional Theory Study. *New Materials, Compounds and Applications*, *6*, 230–242.

14 Hasan, F.A., & Hussein, M.T. (2021). Study of Some Electronic and Spectroscopic Properties of ZnO Nanostructers by Density Functional Theory. *Materials Today*: *Proceedings*, 2638–2644. https://doi.org/10.1016/j.matpr.2020.12.593.

15 Mousavi, S.P., Nakhaei-Kohani, R., Atashrouz, S., Hadavimoghaddam, F., Abedi, A., Hemmati-Sarapardeh, A., & Mohaddespour, A. (2023). Modeling of H2S Solubility in Ionic Liquids: Comparison of White-Box Machine Learning, Deep Learning and Ensemble Learning Approaches. *Scientific Reports*, *13*. https://doi.org/10.1038/s41598-023-34193-w.

16 Kanth, S., Chikara, A.K., Choudhury, S., & Betty, C.A. (2023). Portable and Room Temperature Operating H2S Gas Detection and Alert System Using Nanocrystalline SnO2 Thin Films. *IEEE Sensors Letters*, *7*. https://doi.org/10.1109/LSENS.2023.3267510.

17 Hydrogen Sulfide (2023). Wikipedia. https://en.wikipedia.org/wiki/Hydrogen_sulfide.

18 Li, L., & King, D.L. (2006). H2S Removal with ZnO during Fuel Processing for PEM Fuel Cell Applications. *Catalysis Today*, *116*, 537–541. https://doi.org/10.1016/j.cattod.2006.06.024.

19 Novochinskii, I.I., Song, C., Ma, X., Liu, X., Shore, L., Lampert, J., & Farrauto, R.J. (2004). Low-Temperature H2S Removal from Steam-Containing Gas Mixtures with ZnO for Fuel Cell Application. 1. ZnO Particles and Extrudates. *Energy and Fuels*, *18*, 576–583. https://doi.org/10.1021/ef030137l.

20 Yang, X.Y., Zhang, W.J., Yue, L.J., Xie, K.F., Jin, G.X., Fang, S.M., & Zhang, Y.H. (2023). Co Sites Induced Synergistic Effect in Hollow Co3O4/ZnO Nanocage for Enhanced H2S Sensing Performance. *Applied Surface Science*, *640*. https://doi.org/10.1016/j.apsusc.2023.158417.

21 To, D.T.H., Park, J.Y., Yang, B., Myung, N.V., & Choa, Y.H. (2023). Nanocrystalline ZnO Quantum Dot-Based Chemiresistive Gas Sensors: Improving Sensing Performance towards NO2 and H2S by Optimizing Operating Temperature. *Sensors and Actuators Reports*, *6*. https://doi.org/10.1016/j.snr.2023.100166.

22 Li, X., Jia, F., Luo, N., Cai, H., Chen, J., Ren, W., Cheng, J., & Xu, J. (2024). Self-Assembly Tourmaline@BiFeO3 Composites with Enhanced Polarization for Dual-Selective C3H6O and H2S Detection. *Sensors and Actuators B: Chemical*, *399*. https://doi.org/10.1016/j.snb.2023.134806.

23 Kumar, N., Jasani, J., Sonvane, Y., Korvink, J.G., Sharma, A., & Sharma, B. (2024) Unfolding the Hydrogen Gas Sensing Mechanism across 2D Pnictogen/Graphene Heterostructure Sensors. *Sensors and Actuators B: Chemical*, *399*. https://doi.org/10.1016/j.snb.2023.134807.

24 Frisch, M.J., Trucks, G.W., Schlegel, H.B., Scuseria, G.E., Robb, M.A., Cheeseman, J.R., Scalmani, G., Barone, V., Mennucci, B., Petersson, G.A., Nakatsuji, H., Caricato, M., Li, X., Hratchian, H.P., Izmaylov, A.F., Bloino, J., Zheng, G., Sonnenberg, J.L., Hada, M., Ehara, M., Toyota, K., Fukuda, R., Hasegawa, J., Ishida, M., Nakajima, T., Honda, Y., Kitao, O., Nakai, H., Vreven, T., Montgomery, J.A.J., Peralta, J.E., Ogliaro, F., Bearpark, M., Heyd, J.J., Brothers, E., Kudin, K.N., Staroverov, V.N., Kobayashi, R., Normand, J., Raghavachari, K., Rendell, A., Burant, J.C., Iyengar, S.S., Tomasi, J., Cossi, M., Rega, N., Millam, J.M., Klene, M., Knox, J.E., Cross, J.B., Bakken, V., Adamo, C., Jaramillo, J., Gomperts, R., Stratmann, R.E., Yazyev, O., Austin, A.J., Cammi, R., Pomelli, C., Ochterski, J.W., Martin, R.L., Morokuma, K., Zakrzewski, V.G., Voth, G.A., Salvador, P., Dannenberg, J.J., Dapprich, S., Daniels, A.D., Farkas, Ö., Foresman, J.B., Ortiz, J. V., Cioslowski, J., & Fox, D.J. (2013). Gaussian 09, Revision D.01. Gaussian, Inc., Wallingford CT.

25 Abdulsattar, M.A., Almaroof, H.M., & Almaroof, N.M. (2020). Transition State Theory Application to ZnO Nanocluster Sensitivity to H2 Gas. *Optik*, *219*. https://doi.org/10.1016/j.ijleo.2020.165278.

26 Abdulsattar, M.A., Jabbar, R.H., Abed, H.H., & Abduljalil, H.M. (2021). The Sensitivity of Pristine and Pt Doped ZnO Nanoclusters to NH3 Gas: A Transition State Theory Study. *Optik*, *242*. https://doi.org/10.1016/j.ijleo.2021.167158.

27 Abdulsattar, M.A. (2024). Effect of Acetylene Properties on Its Gas Sensing by NiO Doped ZnO Clusters: A Transition State Theory Model. *Eurasian Journal of Chemistry*, *29*, 35–43. https://doi.org/10.31489/2959-0663/4-24-8.

28 Abdulsattar, M.A., & Mahmood, T.H. (2023). Enhancement of SnO2 Sensitivity to Acetone by Au Loading: An Application of Evans–Polanyi Principle in Gas Sensing. *Optik*, *275*, 170604. https://doi.org/10.1016/j.ijleo.2023.170604.

29 Hosseinpour, P. (2020). Effect of Gaussian Impurity Parameters on the Valence and Conduction Subbands and Thermodynamic Quantities in a Doped Quantum Wire. *Solid State Communications*, *322*. https://doi.org/10.1016/j.ssc.2020.114061.

30 Misják, F., Nagy, K.H., Lobotka, P., & Radnóczi, G. (2014). Electron Scattering Mechanisms in Cu-Mn Films for Interconnect Applications. *Journal of Applied Physics*, *116*. https://doi.org/10.1063/1.4893718.

Marina G. Shcherban'* , Ekaterina A. Ivanchina , Ilya V. Sedusov ,
Valeriya V. Sosunova , Konstantin P. Novosyolov

Perm State National Research University, Perm, Russia
(*Corresponding author's e-mail: ma-sher74@mail.ru)

Study of the Effect of Potassium Chloride
on the Coagulation of PTFE Dispersion by Optical Methods

Electrolyte stability of fluoroplastic-4D dispersion was investigated by optical methods. Potassium chloride (KCl) solutions of various concentrations were used as electrolytes causing coagulation. The kinetic dependences of the influence of KCl concentration on the optical density of polytetrafluoroethylene (PTFE) dispersion were obtained. The maximum in the time dependences of optical density is associated with the particle aggregation processes and the subsequent loss of sedimentation stability of the system. With increasing KCl concentration, this dependence changes: induction period decreases and the peak of the curve narrows. The change in the shape of the kinetic curves with an increase in the electrolyte concentration is associated with the processes of particle dehydration of dispersed phase, desorption of the stabilizer into the solution and the transition of the system from an adsorption-saturated to an adsorption-unsaturated state. The results of measuring the coagulate size of the PTFE dispersion with 2.5 M KCl in different sections of the kinetic curve by the dynamic light scattering (DLS) method correlate with the results of optical density measurements. The data obtained confirm the multi-stage coagulation process, in which the stages of latent coagulation, aggregation, inhibition of coagulation, and loss of sedimentation stability of the system can be distinguished.

Keywords: PTFE, dispersion, surfactant stabilization, coagulation, aggregate stability, optical density, spectrophotometry, dynamic light scattering

Introduction

Highly concentrated dispersed polymer systems have attracted significant interest from both industry and academia owing to their physical and chemical properties. Due to the high electronegativity, low polarizability, and small van der Waals radius of fluorine atom, fluorinated polymers exhibit outstanding properties for a wide range of applications in modern life [1, 2]. Among these, polytetrafluoroethylene (PTFE), widely known as Teflon, is the most useful of the fluorinated polymers.

Owing to the high-energy C–C (346 kJ·mol^{-1}) and C–F (485 kJ·mol^{-1}) bonds, PTFE has a number of unique properties such as wear resistance and corrosion resistance, resistance to high temperatures, low surface energy and low dielectric constant [3, 4]. Because of its properties, PTFE is used in composite coatings [5], membrane technologies [6], fuel industry [7]. It is known that metal particles (for instance, Al) can be coated with a PTFE layer instead of an oxide film on the surface to increase their reactivity and stability [8].

Emulsion polymerization is the primary method used to yield an aqueous colloidal PTFE dispersion in industry, where the tetrafluoroethylene monomer is added into an aqueous medium containing water-soluble initiator, anionic fluorinated dispersant, and other additives (under pressure) [3, 9]. To ensure the stable polymerization and desirable particle size, typically ranging from 100 to 500 nm, the PTFE solid content in dispersion are monitored at approximately 30 % by weight or lower [10]. However, such dilute and unstable as-polymerized dispersion has no practical utility in preparing PTFE articles, and the low solid content also increases the storage and transportation cost. To address this shortcoming, the resulting dilute dispersion should be further concentrated following the polymerization, to typically achieve a content of 60 % by weight [11]. An increase in the solid content leads to an irreversible coagulation of PTFE particles, which renders it useless for various applications. The DLVO theory (abbreviated as Deryagin, Landau, Vervey, Overbeck) explains the aggregate stability of lyophobic dispersed systems, and coagulation is one of the consequences of the aggregation of colloidal particles, in which this stability is lost [12]. Therefore, it is impera-

tive to develop a methodology to concentrate dilute PTFE dispersion with long-term stability and elucidate the stabilization mechanism.

The tendency of hydrophobic PTFE particles to aggregate has prompted many of the studies. The surface properties of PTFE depend on the pH and the ionic strength of the electrolyte solution had studied [13]. The motion of Newtonian and well-characterized elastic liquids with constant viscosity under the impulse inclination of hydrophobic PTFE surfaces has been investigated [14]. New methods of modifying the surface of PTFE, that lead to a change from hydrophobic to hydrophilic, and a perfect recovery from hydrophilic to hydrophobic behavior have been developed [15]. Moreover, dynamic contact angles of pure surfactants and surfactants with electrolyte solutions on PTFE surface have been studied [16].

Surfactants play an important role in the stabilization of hydrophobic nanoparticles [17]. It was found that the surfactants could adsorb on the surface of the PTFE particles and remarkably improve their surface wettability, thus significantly improving the interaction with the bulk phase [18]. In addition, polymers are used as stabilizers for PTFE dispersion, for example polymethylmethacrylate [19]. Long Bai and others analyzed four types of surfactants including cationic dodecyltrimethylammonium bromide (DTAB), anionic sodium dodecyl sulfate, zwitterionic lauryl betaine (LB), and nonionic lauryl alcohol polyoxyethylene Brij 30, are used to stabilize 60 % PTFE dispersions from the as-polymerized dilute mixture [20]. As shown in Figure 1, the surfactants show different capabilities for stabilizing PTFE particles in aqueous solutions. While the cationic surfactant causes particle flocculation, the anion, zwitterionic and nonionic surfactants can be used to prepare concentrated dispersions [20, 21].
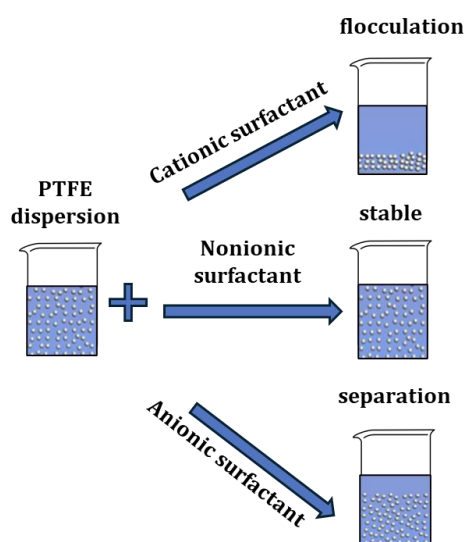
Figure 1. Scheme of the stabilization mechanism of PTFE dispersion with different surfactants.
Adapted and redrawn from Ref. [20] with permission from Elsevier

In addition, the applicability of surfactants to PTFE has been investigated not only in aqueous solutions, but also in oil solutions [22].

Despite the high popularity of PTFE dispersion, their coagulation has not been thoroughly studied. Therefore, it is necessary to investigate the effect of electrolytes on PTFE dispersions in order to develop methods for stabilizing this system. Electrolytic coagulation is a process of particle aggregation, the study of which will lead to the development of effective methods to ensure the long-term stability of the studied dispersions. The aim of this work is to study the coagulation of PTFE dispersion under the action of potassium chloride.

Experimental

The subject of the study was a dispersion of fluoroplastic F-4D with a dispersed phase concentration of 55 % by weight., stabilized with the non-ionic surfactant OP-7, obtained by emulsion polymerization. The main dispersion parameters are shown in Table 1.

The main measures of dispersion

pH	Kinematic viscosity, cSt	Dry residue, mg·ml^{-1}	Density, $kg·m^{-3}$
9.82±0.11	7.179±0.001	871.24±8.19	1510.59±9.09

The particle size of the PTFE dispersed phase was studied using a scanning electron microscope (SEM) (Hitachi, S-4800 SEM, Tokyo, Japan). The micrograph of the dry residue of the investigated dispersion is shown in Figure 2.
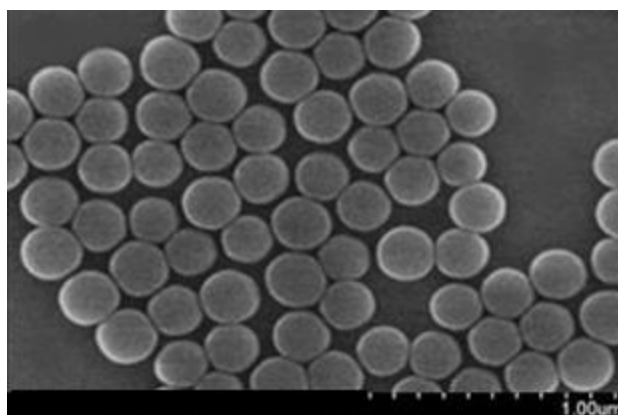
Figure 2. Micrograph of the dry residue of the dispersion

The degree of polydispersity is an important characteristic of such systems. In addition to the predominant number of particles of a certain specific size, there are usually also particles of other, noticeably different sizes due to difficult polymerization conditions. Secondary particles of adhered primary globules can form in stable systems in a number of cases. In order to ensure their absence, as well as to determine the degree of polydispersity of the system, we used the method of dynamic light scattering (DLS), based on the analysis of the spectrum of scattered laser radiation on the sample under investigation. The coagulum particle size was determined using a particle size analyzer (Delsa Nano C, Beckman Coulter, Inc., Fullerton, CA, USA) at 160° scattering angle.

For dispersions obtained by the method of emulsion polymerization, the issues of aggregation stability and coagulation are extremely important, which can lead to the destruction of the dispersion system and the release of PTFE in the macroscopic state. The presence of an insignificant amount of aggregates and coagulum can have an extremely negative effect on the functional properties of coatings based on fluoroplastic dispersions. To prevent aggregation of PTFE particles during polymerization, a stabilizer is introduced into the system. These are usually non-ionogenic surfactants such as OP-7 or Neonol.

Disruption of stability and coagulation of dispersions can be caused by various methods: the introduction of an electrolyte, mechanical interaction, freezing, a change in pH, etc.

We investigated the case of electrolyte stability of the fluoroplastic F-4D dispersion by a spectrophotometric method based on measuring the degree of reflection or absorption of monochromatic light rays [23]. Optical density of nanoparticle dispersions was measured with KFK-3KM spectrophotometer (Russia) in a cuvette with an optical path length of 10 mm (λ=400 nm). Potassium chloride solutions of various concentrations were used as electrolytes causing coagulation. The KCl solutions were prepared using bidistilled water from a reagent produced by Sigma–Aldrich (St. Louis, Missouri, USA). Unfortunately, photometry imposes limitations on the optical density of the studied solutions and this allows observations to be carried out only in low-concentration dispersion systems. However, according to the literature data, the kinetic curves of coagulation obtained for dilute and concentrated dispersions do not have fundamental differences. This does not mean that the processes occurring in concentrated and dilute systems are completely identical, since dilution not only reduces the number of possible collisions per unit volume, but also changes the state of the protective adsorption surfactant layer on the surface of the particles, its saturation and structuring, changes the surface charge, the degree of hydration, and so on. This indicates the commonality of the main regularities of coagulation. All experiments were carried out at 20 °C.

Results and Discussion

The distribution of particles in dispersion obtained using the DLS method is shown in Figure 3.
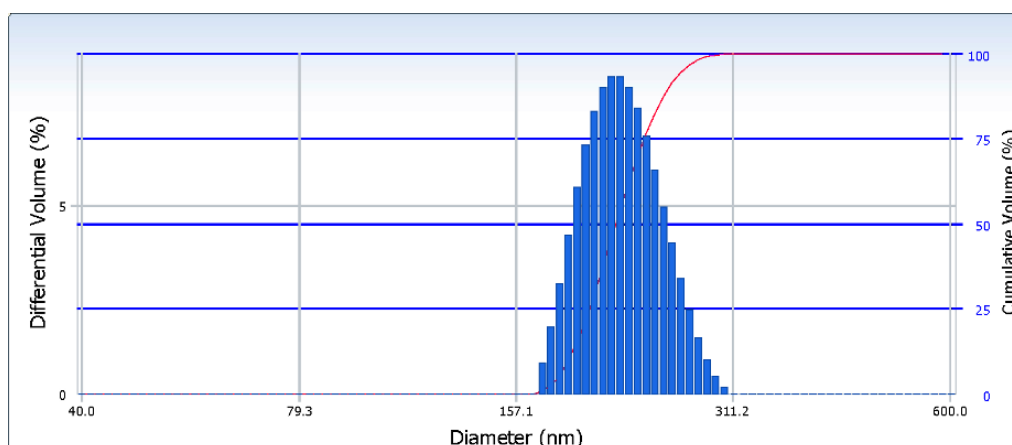
Figure 3. Particle distribution in dispersion

According to the results obtained, the average particle size in the system was 220±26 nm with a polydispersity index of 0.002, which gives reason to consider the studied system as monodisperse. No agglomerates of particles were detected either by microscopy or by the DLS method. Therefore, this dispersion can be used as a model to study aggregation processes.

Experimental normalized dependences of the relative optical density on time (Fig. 4) were obtained using the spectrophotometric method.
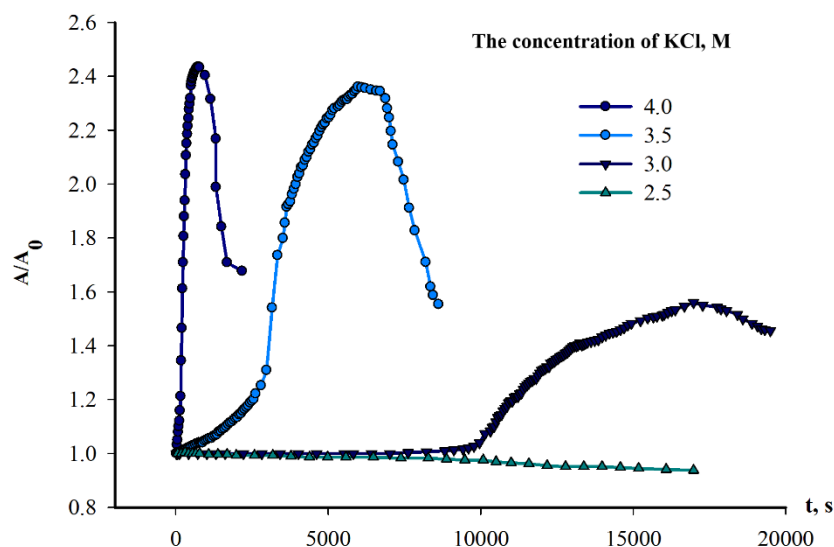
Figure 4. Normalized curves of coagulation of PTFE aqueous dispersion under the action of KCl

The obtained dependences allow us to conclude that the concentration of the electrolyte causing coagulation has a significant effect on aggregation processes occurring in dispersion. The coagulation curve under the action of a 2.5 M solution can be identified as the coagulation curve of an adsorption saturated system — a long (10.000 sec) induction period is observed on it, during which no visible changes occur in the system. The increase of the electrolyte concentration leads to its reduction and almost complete disappearance in a 4 M solution. A similar extreme type of turbidity dependence on time, as in the case of 3.5 and 4 M KCl solutions, was observed by the authors of [24] for copolymers of N,N-dimethylaminoethyl methacrylate with N-vinyl caprolactam. However, a decrease in turbidity did not lead to the formation of a coagulum, as in our case, when this behavior is the result of aggregation of dispersed particles and their sedimentation.

At 2.5 M, the constancy of optical density during the induction period suggests the absence of particle aggregation or their flocculation through the medium interlayer. In more concentrated solutions, the steepness of the initial sections increases, as a result of which a significant increase in interparticle interaction can be assumed due to an increase in the dehydration of the stabilizing layers with an increase in the electrolyte concentration.

A narrowing and an increase in the height of the peak with an increase in the concentration of the electrolyte is observed (the kinetic characteristics of the curves are shown in Table 2).

T a b l e 2

Kinetic parameters of electrolyte coagulation curves for aqueous dispersion of PTFE-KCl

The concentration of KCl, M	Coagulation rate, sec^{-1}		Peak width at half height, sec
	I section	II section	
4.0	$1.2 \cdot 10^{-3}$	$5.5 \cdot 10^{-3}$	600
3.5	$5.5 \cdot 10^{-5}$	$8.7 \cdot 10^{-4}$	3300
3.0	$2.7 \cdot 10^{-7}$	$1.3 \cdot 10^{-4}$	7600
2.5	$2.0 \cdot 10^{-8}$	$1.2 \cdot 10^{-7}$	–

Figure 5 shows the initial sections of the coagulation curves, the determination of the angular coefficients of which makes it possible to obtain the dependence of the coagulation rate on the concentration of electrolyte (Fig. 6).
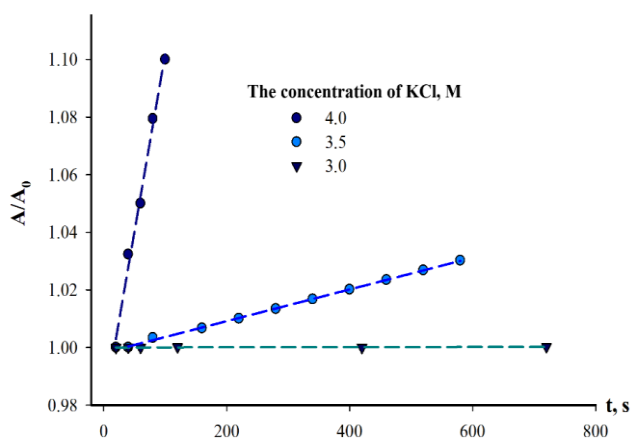
Figure 5. Initial sections of coagulation curves

Figure 6. Effect of the KCl concentration on the aggregative stability of PTFE aqueous dispersion based on results of processing of initial sections of kinetic coagulation curves

Based on the obtained dependence, we can define the concentration range up to 3.5 M KCl as a zone of latent coagulation, 3.5–4.0 — as a zone of slow coagulation, when the coagulation rate depends on the electrolyte concentration, and the concentration of 4.0 M, presumably as the threshold of rapid coagulation.

The patterns mentioned above are preserved for the following sections of the kinetic curves, on which the growth of aggregates occurs (Fig. 7, 8).

Concentration dependences characterized by the presence of plateaus (Figs. 6 and 8) were observed in [25] for aqueous dispersions of crosslinked poly-N-vinyl caprolactam stabilized with hydrophobically modified polyacrylamide. The values of the critical concentration of coagulation for sodium chloride of this system varied in the range of 1,500–2,500 mmol/l and were explained by the peculiarities of the stabilizing effect and the charge of the stabilizer.

Apparently, in our case, the concentration of 2.5 M is inadequate in reducing the energy barrier. However, it has been observed to disrupt the stability of the adsorbed solvation layers of particles, which aggregate and form coagulation contacts in the affected areas of the layer. Thus, the processes of thinning of the

hydration shells and the weakening of the forces of structural repulsion persist, albeit at an undetectable rate. The rate of coagulation slows down significantly and the curve reaches a plateau after 3.5 hours from the moment of initiation. Presumably, the primary aggregation of particles at the sites of disruption of the hydration shells leads to the outflow of the surfactant from the contact zone and the compaction of the surfactant adsorption layers on the growing aggregates. Consequently, hydration increases temporarily, the structural component of the wedging pressure increases, which inhibits coagulation. The presence of electrolyte leads to a decrease in the thickness of the interlayers in the inter-aggregate space, again weakening the structural component, and the aggregates increase in size. As a result, at some point in time, the system loses its sedimentation stability, which is accompanied by a drop in optical density.
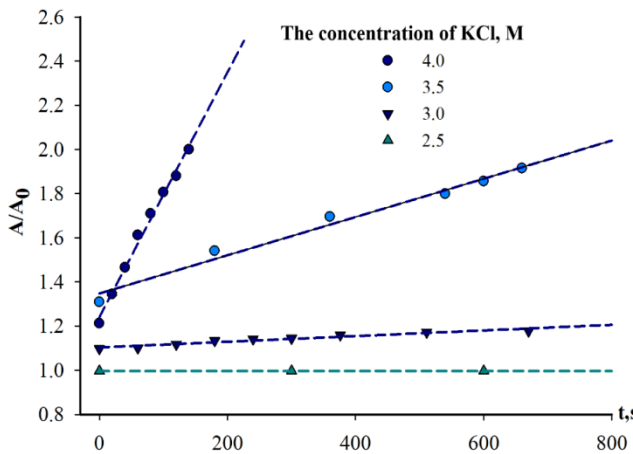
Figure 7. Effect of the concentration of KCl on the rate of aggregation of PTFE dispersion
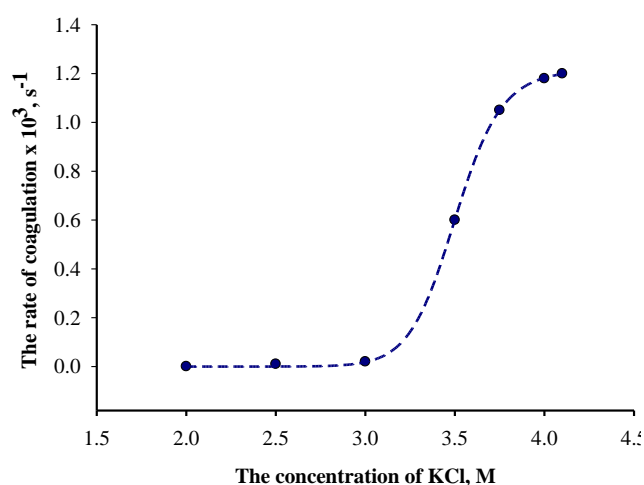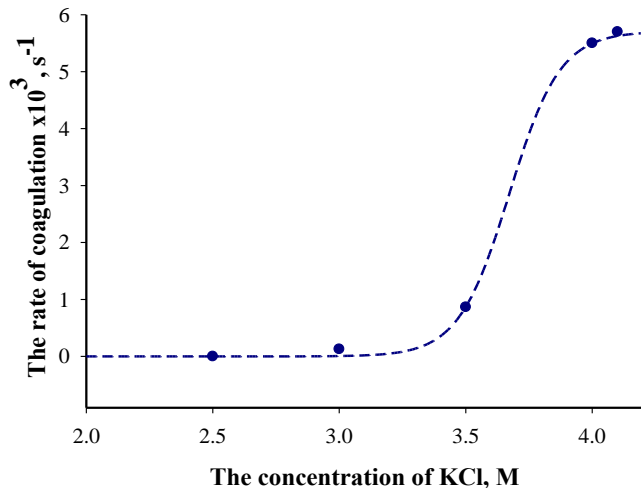
Figure 8. Effect of the KCl concentration on the aggregative stability of PTFE aqueous dispersion based on results of processing of second sections of kinetic coagulation curves

As the electrolyte concentration increases, the dehydration processes occur at a higher rate, and the inhibition of coagulation proceeds with a greater degree of particle aggregation, while the duration of the inhibition stage decreases, as evidenced by the narrowing of the peaks of the kinetic curves.

To confirm the above assumptions, the DLS method was used to determine the sizes of coagulum particles in different parts of the kinetic curve of coagulation of the dispersion with 2.5 M KCl.

At the first stage, the particle size of the initial dispersion was determined at a similar dilution to ensure its stability (Fig. 9).
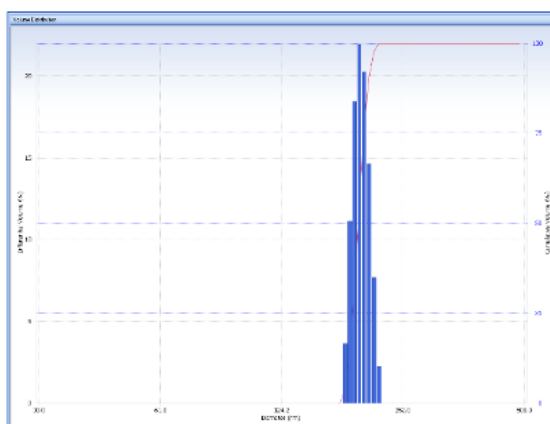
$d = 197.6 \pm 9.3$

(*a*)
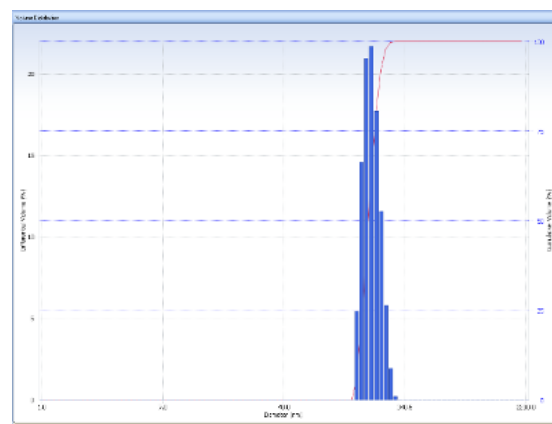
$d = 199.4 \pm 26.5$

(*b*)

Figure 9. Study of the aggregate stability of the initial diluted dispersion.
The lifetime of system: (*a*) — 10 minutes, (*b*) — 360 minutes

The obtained distributions confirm the aggregate stability and monodispersity of the system. The increase in polydispersity over time can be associated with the desorption of a part of the stabilizer into the bulk of the solution, loosening of the stabilizing layers, a slight decrease in the structural component of the wedging pressure, but it is not critical, and the diluted dispersion can be considered aggregatively stable during the observation period.

In the presence of KCl, visible changes in the distribution are observed after 30 minutes. They are expressed in a slight enlargement of particles and an increase in the width of the maximum (Fig. 10, *a, b*).

d=216.5±10.4 nm

a

d=221.6±34.9 nm

b

$d = 210.9 \pm 86.8$ nm

c

$d = 340.5 \pm 141.4$ nm

d

$d = 217.3 \pm 155.3$ nm
$d = 1233.5 \pm 307.2$ nm

e

$d = 10.5 \pm 0.5$ nm
$d = 227.7 \pm 38.4$ nm
$d = 1112.0 \pm 347.2$ nm

f

Figure 10. Study of the aggregate stability of PTFE dispersion under the action of 2.5 M KCl.
The lifetime of system: *a* — 10 minutes; *b* — 30 minutes; *c* — 180 minutes; *d* — 240 minutes;
e —300 minutes; *f* — 330 minutes

The symmetry of the system is lost three hours after the introduction of the electrolyte, of the system is lost the end of the induction period. A more than one and a half-fold increase in the particle size against the background of an even more significant increase in the polydispersity of the system occurs after four hours (Fig. 10, *c, d*) and an increase in the kinetic curve is observed.

Another maximum appears in the inhibition zone (300 min) on the distribution. It is rather weakly expressed, but, nevertheless, it indicates the presence of sufficiently large aggregates in the system with a size of 1.0–1.5 microns (Fig. 10 *e*).

After 30 minutes, the maximum corresponding to the primary particles almost completely degenerates, and a new narrow peak appears, characterizing particles with a size of about 10 nm. These may correspond to micelles formed by the stabilizer desorbed from the surface of the dispersed phase particles during the coagulation process (Fig. 10, *f*). This time interval corresponds to a gradual decrease in optical density and visually recorded separation of the system into a dispersion medium and a dispersed phase.

Thus, the results obtained by the DLS method correlate with the results of measuring the optical density and confirm the multistage process of coagulation, in which the stages of latent coagulation, aggregation, inhibition of coagulation and loss of sedimentation stability of the system can be distinguished.

Conclusions

The studied aqueous dispersion of PTFE is an adsorption saturated aggregatively stable system. An insignificant increase in the polydispersity of the system during its dilution is caused by the desorption of the stabilizer and a decrease in the density of the adsorption layer of the stabilizer layer on the particles of the dispersed phase. The change in the shape of the kinetic curves with the increase in the concentration of the electrol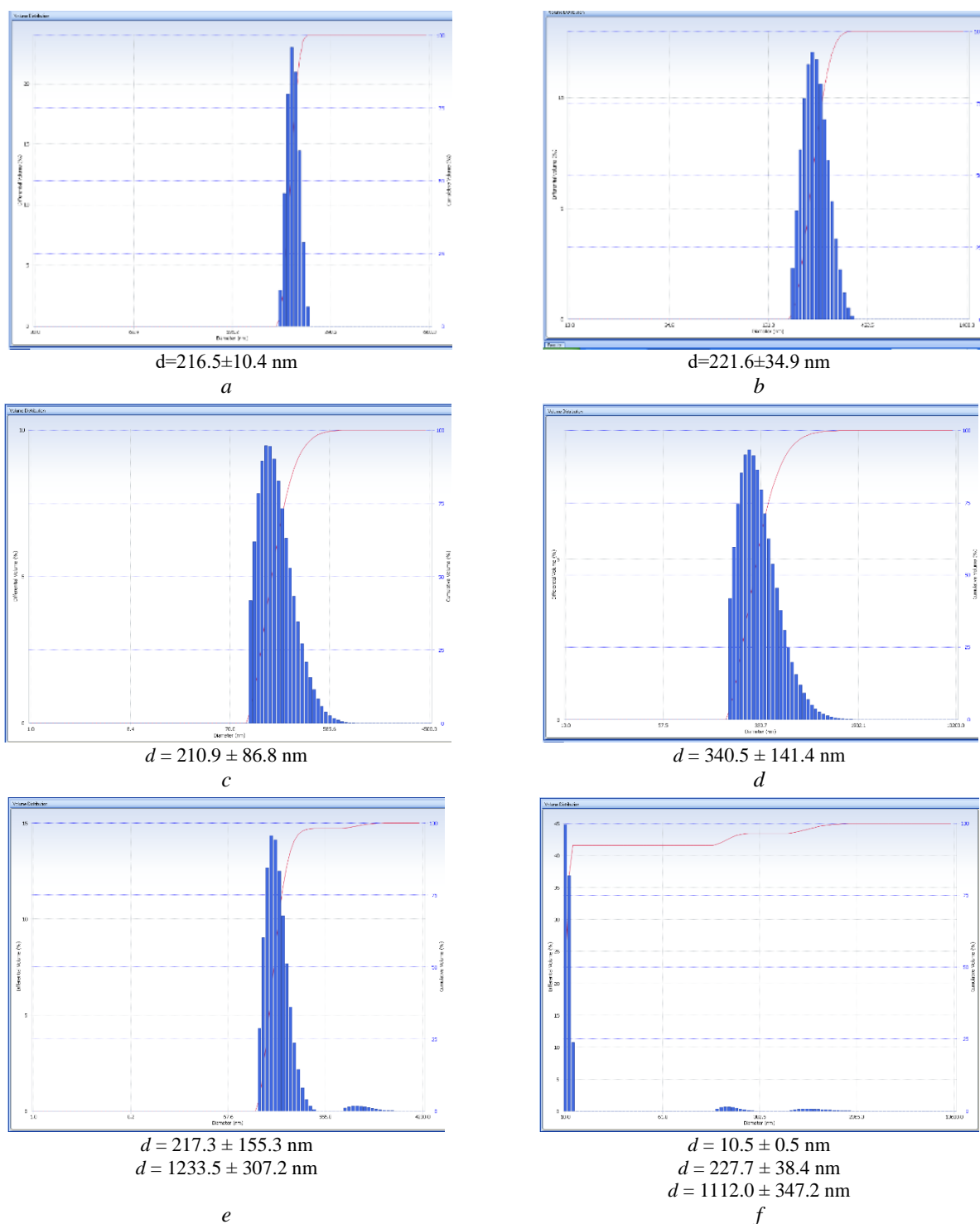yte is associated with the processes of dehydration of particles of the dispersed phase and the transition from the adsorption-saturated to the adsorption-unsaturated state of the system.

The results obtained by the DLS method correlate with the results of measuring the optical density and confirm the multistage process of coagulation, in which the stages of latent coagulation, aggregation, inhibition of coagulation and loss of sedimentation stability of the system can be distinguished. The process of inhibition of coagulation is associated with the rearrangement of the adsorbed solvation layer on the surface of the aggregates.

Author Information*

*The authors' names are presented in the following order: First Name, Middle Name and Last Name

Marina Grigoryevna Shcherban' (*corresponding author*) — Candidate of Chemical Sciences, Assistant professor of Physical Chemistry Department, Perm State National Research University, Bukireva street, 614990, Perm, Russia; e-mail: ma-sher74@mail.ru; https://orcid.org/0000-0002-6905-6622

Ekaterina Alekseevna Ivanchina — 5th year student (specialist), Perm State National Research University, Bukireva street, 614990, Perm, Russia; e-mail: ivanchinaekaterina@yandex.ru; https://orcid.org/0000-0002-2742-6074

Ilya Vladislavovich Sedusov — 5th year student (specialist), Perm State National Research University, Bukireva street, 614990, Perm, Russia; e-mail: isedusov@gmail.com; https://orcid.org/0009-0000-5114-9081

Valeriya Vasil'evna Sosunova — Master student in Physical Chemistry, Perm State National Research University, Bukireva street, 614990, Perm, Russia; e-mail: sosunovavaleria@yandex.ru; https://orcid.org/0009-0003-8421-7919

Konstantin Pavlovich Novosyolov — Undergraduate student, Perm State National Research University, Bukireva street, 614990, Perm, Russia; e-mail: 9519406173@mail.ru; https://orcid.org/0000-0003-0147-0015

Author Contributions

The manuscript was written through contributions of all authors. All authors have given approval to the final version of the manuscript. CRediT: **Marina Grigoryevna Shcherban'** conceptualization, supervision, data curation, investigation, methodology, validation, visualization, writing-review & editing; **Ekaterina Alekseevna Ivanchina** data curation, formal analysis, visualization; **Ilya Vladislavovich Sedusov** data cura-

tion, formal analysis; **Valeriya Vasil'evna Sosunova** data curation, **Konstantin Pavlovich Novosyolov** literature review, design.

Conflicts of Interest

The authors declare no conflict of interest.

References

1   Giannetti, E. (2001). Semi-crystalline fluorinated polymers. *Polymer International, 50(1),* 10–26. https://doi.org/10.1002/1097-0126(200101)50:1<10::aid-pi614>3.0.co;2-w

2   Pagliaro, M., & Ciriminna, R. (2005). New fluorinated functional materials. *Journal of Materials Chemistry*, *15*(47), 4981. https://doi.org/10.1039/b507583c

3   Puts, G. J., Crouse, P., & Ameduri, B. M. (2019). Polytetrafluoroethylene: Synthesis and Characterization of the Original Extreme Polymer. *Chemical Reviews*, *119*(3), 1763–1805. https://doi.org/10.1021/acs.chemrev.8b00458

4   Dhanumalayan, E., & Joshi, G. M. (2018). Performance properties and applications of polytetrafluoroethylene (PTFE) — A review. *Advanced Composites and Hybrid Materials*, *1*(2), 247–268. https://doi.org/10.1007/s42114-018-0023-8

5   Kucharska, B., & Sobiecki, J. R. (2020). The corrosion properties of Ni/Al$_2$O$_3$/PTFE composite coatings in NaCl and CMA solutions. *Corrosion Engineering, Science and Technology*, 1–7. https://doi.org/10.1080/1478422X.2019.1710662

6   Zhang, Y., Shen, F., Cao, W., & Wan, Y. (2020). Hydrophilic/hydrophobic Janus membranes with a dual-function surface coating for rapid and robust membrane distillation desalination. *Desalination*, *491*, 114561. https://doi.org/10.1016/j.desal.2020.114561

7   Lee, W. J., Lee, J. S., Park, H.-Y., Park, H. S., Lee, S. Y., Song, K. H., & Kim, H.-J. (2020). Improvement of fuel cell performances through the enhanced dispersion of the PTFE binder in electrodes for use in high temperature polymer electrolyte membrane fuel cells. *International Journal of Hydrogen Energy*, *45*(57), 32825–32833. https://doi.org/10.1016/j.ijhydene.2020.03.095

8   Kim, D. W., Kim, K. T., Lee, D. U., Jung, S.-H., & Yu, J. (2020). Synergetic enhancement in the reactivity and stability of surface-oxide-free fine Al particles covered with a polytetrafluoroethylene nanolayer. *Scientific Reports*, *10*(1), 14560. https://doi.org/10.1038/s41598-020-71162-z

9   Kim, C. U., Lee, J. M., & Ihm, S. K. (1999). Emulsion polymerization of tetrafluoroethylene: Effects of reaction conditions on the polymerization rate and polymer molecular weight. *Journal of Applied Polymer Science, 73, 777*–793. https://doi.org/10.1002/(sici)1097-4628(19990801)73:5<777::aid-app18>3.0.co;2-c

10   Hoshikawa, J., Kobayashi, S. (2006). European Patent No. EP 1059333B1. Munich, Germany: European Patent Office.

11   Su, J., Wu, G., Liu, Y., & Zeng, H. (2006). Study on polytetrafluoroethylene aqueous dispersion irradiated by gamma ray. *Journal of Fluorine Chemistry*, *127*(1), 91–96. https://doi.org/10.1016/j.jfluchem.2005.10.005

12   Shah, V., Bharatiya, B., Shah, D. O., & Mukherjee, T. (2015). Correlation of dynamic surface tension with sedimentation of PTFE particles and water penetration in powders. *Langmuir*, 31(51), 13725–13733. https://doi.org/10.1021/acs.langmuir.5b03725

13   Barišić, A., Lützenkirchen, J., Lefévre, G., & Begović, T. (2019). The influence of temperature on the charging of polytetrafluoroethylene surfaces in electrolyte solutions. *Colloids and Surfaces A: Physicochemical and Engineering Aspects*, *579*, 123616. https://doi.org/10.1016/j.colsurfa.2019.123616

14   Xu, H., Clarke, A., Rothstein, J. P., & Poole, R. J. (2018). Viscoelastic drops moving on hydrophilic and superhydrophobic surfaces. *Journal of Colloid and Interface Science*, *513*, 53–61. https://doi.org/10.1016/j.jcis.2017.10.105

15   López, C. D., Cedeño-Mata, M., Dominguez-Pumar, M., & Bermejo, S. (2020). Surface modification of polytetrafluoroethylene thin films by non-coherent UV light and water treatment for electrowetting applications. *Progress in Organic Coatings*, *149*, 105593. https://doi.org/10.1016/j.porgcoat.2020.105593

16   Chaudhuri, R. G., & Paria, S. (2009). Dynamic contact angles on PTFE surface by aqueous surfactant solution in the absence and presence of electrolytes. *Journal of Colloid and Interface Science*, *337*(2), 555–562. https://doi.org/10.1016/j.jcis.2009.05.033

17   Kratohvil, S., & Matijević, E. (1976). Stability of colloidal teflon dispersions in the presence of surfactants, electrolytes, and macromolecules. *Journal of Colloid and Interface Science*, 57(1), 104–114. https://doi.org/10.1016/0021-9797(76)90180-6

18   Sharma, M., Bharatiya, B., Mehta, K., Shukla, A., & Shah, D. O. (2014). Novel strategy involving surfactant–polymer combinations for enhanced stability of aqueous Teflon dispersions. *Langmuir*, 30(24), 7077–7084. https://doi.org/10.1021/la5012605

19   Peng, S., Zhang, L., Xie, G., Guo, Y., Si, L., & Luo, J. (2019). Friction and wear behavior of PTFE coatings modified with poly (methyl methacrylate). *Composites Part B: Engineering*, *172*, 316–322. https://doi.org/10.1016/j.compositesb.2019.04.047

20   Bai, L., Chen, Y., Yin, H., Sui, X., Wu, D., & Feng, Y. (2020). Insights into the stability of polytetrafluoroethylene aqueous dispersion: Role of surfactant. *Journal of Molecular Liquids*, *314*, 113662. https://doi.org/10.1016/j.molliq.2020.113662

21   Zhang, G., Chen, Y., Sui, X., Kang, M., Feng, Y., & Yin, H. (2022). Nonionic surfactant stabilized polytetrafluoroethylene dispersion: Effect of molecular structure and topology. *Journal of Molecular Liquids*, 345, 116988. https://doi.org/10.1016/j.molliq.2021.116988

22 Shah, V., Panchal, T., Bharatiya, B., Patel, N. S., Shukla, A. D., & Shah, D. O. (2020). Colloidal PTFE dispersion in commercial engine oil: Lubrication by Pluronic adsorption at the interface. *Colloids and Surfaces A: Physicochemical and Engineering Aspects*, *597*, 124775. https://doi.org/10.1016/j.colsurfa.2020.124775

23 Mengual, O., Meunier, G., Cayre, I., Puech, K., & Snabre, P. (1999). Characterisation of instability of concentrated dispersions by a new optical analyser: the TURBISCAN MA 1000. *Colloids and Surfaces A: Physicochemical and Engineering Aspects*, 152(1–2), 111–123. https://doi.org/10.1016/S0927-7757(98)00680-3

24 Shatalov, G., Verezhnikov, V., Plaksitskaya T., Kuznetsov, V., Poyarkova, T. & Yanshina A. (2006). Synthesis of N,N-dimethylaminoethylmethacrylate copolymers with N-vinylcaprolactam and their behavior during complexation and flocculation. *Polymorphism, Series A,* 48, 563–568. https://doi.org/10.1134/S0965545X06060022

25 Kuznetsov, V., Kushchev, P., Blagodatskikh, I., Ostankova, I., Vyshivannaya, O. & Sleptsova, O. (2016). Aqueous dispersions of cross-linked poly-N-vinylcaprolactam stabilized with hydrophobically modified polyacrylamide: synthesis, colloidal stability, and thermosensitive properties. *Colloid and Polymer Science,* 294(5), 889–899. https://doi.org/10.1007/s00396-016-3843-5

Article

https://doi.org/10.31489/2959-0663/1-25-5

Manimegalai Ramasamy[1] , Gurunathan Velayutham[2] , Ramar Pitchaipillai[1*]

[1]PG and Research Department of Chemistry, Government Arts College, Bharathidasan University, Ariyalur, Tamilnadu, India;
[2]Research Department of Chemistry, Bishop Heber College, Bharathidasan University, Tiruchirappalli District, Tamilnadu, India
(*Corresponding author's e-mail: drsairam202110@gmail.com)

A Novel Mannich Based Metal II Complexes: Synthesis and Characterization of Magnetic, Conductivity and Antimicrobial Properties

A novel Mannich base (2R,9R)-2-((S)-((2-aminoethyl)amino)(2-hydroxyphenyl)methyl)-6-hydroxy-9-phenyl-2,3,4,9-tetrahydro-1H-xanthen-1-one (LI), composed from xanthene, salicylaldehyde, and ethylenediamine, was employed to synthesize unique complexes of Ni(II), Mn(II), Cr(II), Co(II), and Cu(II). The structural characteristics of the complexes were determined by studying microanalytical findings and using analytical methods such as EPR, FT-IR, ^{1}H & ^{13}C NMR, and UV-visible spectroscopy. The electronic spectra of the complexes suggested that the metal ion is fenced with octahedral structure. The molar conductivity of the metal chelates in DMSO was shown in the range of 18–28 $\Omega^{-1}mol^{-1}cm^2$. The EPR studies of the copper complex dissolved in dimethyl sulfoxide (DMSO) was obtained at temperature of 300 K, and its unique characteristics were analysed. The antimicrobial potential of the ligand and its complexes has been thoroughly examined towards *K. pneumaniae, S. aureus, P. aeruginosa, E. coli, C. albicans, C. neoformans, M. audouinii, A. niger* microorganisms. Experimental results have demonstrated that all of the complexes exhibit substantial antimicrobial action when related to both the unbound ligand and the standard. Furthermore, the validity of the biological research was verified through molecular docking antifungal and antibacterial tests. Overall, the obtained results confirm the multidirectional antimicrobial efficacy of the new Mannich base complexes and demonstrate their high pharmaceutical potential for further studies.

Keywords: Antimicrobial activity, Docking, Grindstone, Ligands, Mannich base, Metal complexes, Xanthene.

Introduction

The emergence of antimicrobial resistance has evolved into a major worldwide health crisis, threatening to revert mortality rates to those observed in the pre-antibiotic era. Recent research by Murray et al. indicated that bacterial antimicrobial resistance was responsible for approximately 1.27 million fatalities in 2019 [1–3]. The alarming statistics are partly attributable to the incorrect and indiscriminate use of antibiotics, inadequate infection and disease prevention measures, and unequal access to quality, inexpensive medication [4]. As a result, bacteria have evolved several resistance mechanisms against nearly all medicines available today, jeopardizing the continuation of the 80-year "era of antibiotics". Examples of both innate and derived mechanisms of drug resistance in bacteria encompass target protection, alteration of target sites, enzymatic inactivation of antibiotics, active efflux, reduced inflow, and biofilm formation [5]. Microbial infestation refers to the process in which microbes, which include bacteria, viruses, and fungi, invade a living thing, replicate within it, and communicate with the host tissue [6]. These pathogens provide a significant public hazard to infections related to healthcare and are accountable for the mainstream of diseases in hospitals, leading to increased death and load on world health systems [7]. Specifically, metal complexes with heterocyclic ligands have a dominant role in medicinal chemistry due to its broad spectrum of characteristics [8–12]. Transition metal complexes are regarded as highly effective metallo-drugs for remedying the hazards posed by microorganisms [13, 14].

The production of heterocycles containing oxygen and nitrogen has long been a of great interest in organic chemistry. These compounds are often found in the fields of drug design, medical and pharmaceutical, and materials science [15–17]. Chromene and its analogues, specifically 2-amino-4H-chromene and 2H-chromene-2-one [6, 18], are a significant group of oxygen-containing heterocycles. These compounds incorporate a cyano moiety at the C-3 location which provides the possibility of being utilized in the dealing of several illnesses comprising psoriatic arthritis, rheumatoid arthritis, cancer therapy, Alzheimer's disease, Huntington's disease, Parkinson's disease, and amyotrophic lateral sclerosis [19–22]. They commonly occur

in the fundamental structure of numerous herbal remedies and manufactured potential medicines. They are of great importance in medicinal chemistry due to its significant pharmacological functions, which include anti-fungal, antioxidant, antiproliferative, antimicrobial, antitumor, anticoagulant, and anti-allergic properties (Fig. 1) [23–27]. In recent decades, various material science applications like laser dyes, optical brighteners, and fluorescence markers have been developed [28–30]. In addition, they find use in beauty products, recyclable agrochemicals, colourants, and other areas [31–33].
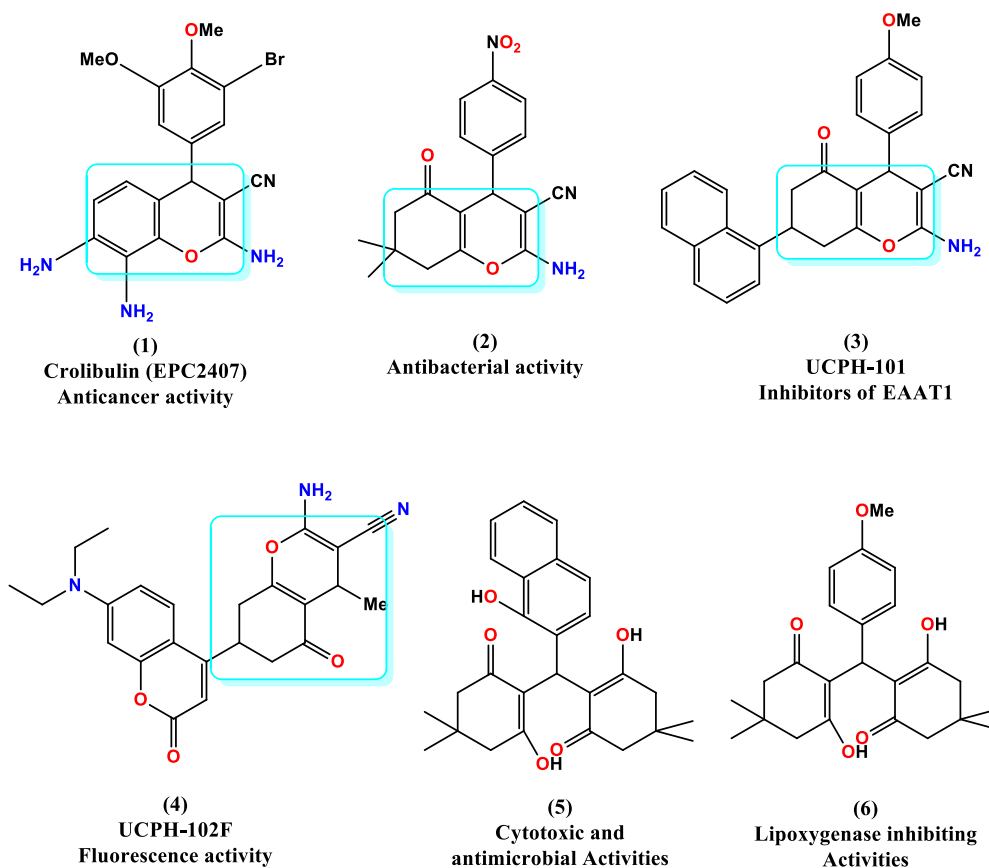
Figure 1. 2-amino-4*H*-chromene (1–4) and tetraketones (5–6) with probable optoelectronic and medicinal uses

Mannich transformations provide an unswerving and effectual method for synthesising β-amino carbonyl substances, which are important in the manufacturing of various medicines, synthetic materials, and natural substances [34–36]. These methods are used to produce distinctive carbon-carbon bonds in the creation of nitrogen-bearing substances in organic synthesis [37, 38]. Mannich bases play a crucial role in medicinal chemistry due to their ability to form substantial 3d-metal complexes with unique therapeutic value [39, 40]. The progress of innovative catalytic approaches for the fabrication of Mannich bases is crucial in the field of synthetic chemistry. Several scholars have documented Mannich derivatives having catalysis action [41–43]. The complexation behaviour of Mannich analogues was crucial in advancing the field of inorganic chemistry [44].

Metal complexes with heterocyclic ligands demonstrate a wide range of actions, including antimicrobial, antibacterial, anti-inflammatory, antioxidant, antitumor, antiviral, antidiabetic, antifungal, antimalarial, anticonvulsant, anticancer, antiamoebic, antiproliferative, and anti-HIV properties [45–49]. However, the production of metal complexes mediated by Xanthene is not well documented. Consequently, this study was conducted on the Mannich base ligand (L1), emphasizing its biological relevance. The current investigation was undertaken on the Mannich base ligand (L1), taking into consideration its biological significance. The compound was produced through the condensation reaction of xanthene, salicylaldehyde, and ethylenediamine. The Mannich base that was synthesised was subsequently coordinated with chlorides of Mn(II), Co(II), Ni(II), Cr(II), and Cu(II). The synthesised compounds were characterised using several spectroscopic and chemical approaches, and their antimicrobial capabilities were assessed.

Experimental

Chemistry

All the substances and solvents used were of extremely pure grade (Analar grade, A.R.) and obtained from Sigma-Aldrich. The identification of complexes was achieved by acquiring FT-IR spectra of the ligand and complexes within the frequency array of 400–4000 cm^{-1}. This was done by KBr pellets and an Agilent Resolutions spectroscopy. The absorbance spectra of the ligand (**L1**) and associated complexes (**1-5**) were acquired using a Shimadzu UV mini-1240 UV spectroscopy in the wavelength range of 300–1100 nm to determine the potential electronic transitions.

Synthesis of Ligand (L1)

A blend of salicylaldehyde (2.4 mL, 0.02 mol), xanthene (5.85 g, 0.02 mol), and ethylenediamine (1.2 mL, 0.02 mol) were pulverised together in a mortar for a duration of 10 minutes through grindstone chemistry technique. The progression of the reaction was monitored by thin-layer chromatography (TLC). Once the chemical process designated by TLC was finished, the resulting mixture was placed in crushed ice. The raw product was filtered and dehydrated. To purify the ligand, it was recrystallized using hot ethanol. The production of ligand (**L1**) is shown in Figure 2.
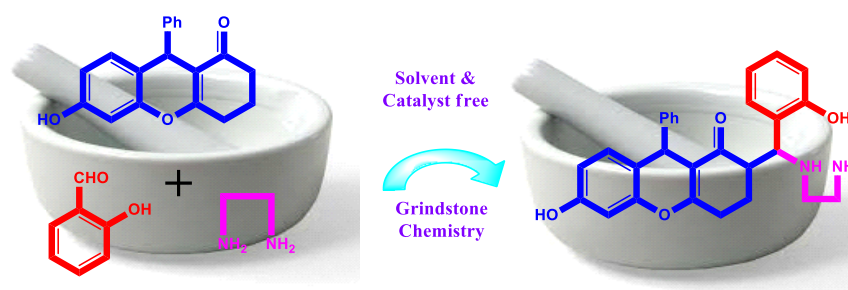
Figure 2. Preparation of ligand (**L1**)

Synthesis of Metal Complexes (1-5)

Under reflux, a hot ethanolic solution containing (0.02 mol) of ligand **L1** was gradually combined with (0.01 mol) of metal chlorides in a hot ethanolic solution with continuous stirring. After the final reaction stage, the reaction mixture was left at ambient temperature to evaporate. The impure metal complex was refined by column chromatography employing a combination of elutant DCM:CH$_3$CN:CH$_3$OH (2:3:5 v/v) over silica gel. Metal complexes (**1–5**) were synthesised as shown in Figure 3.
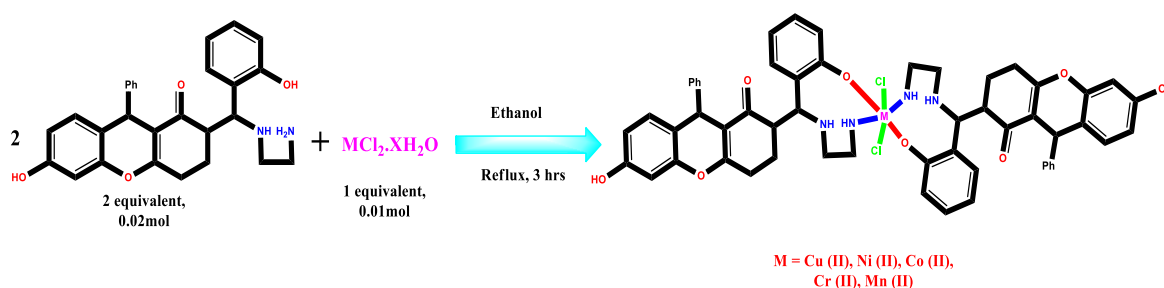
Figure 3. Preparation of metal complexes (**1–5**)

Solubility Measurements

The solubility of the ligand and complex in protic and aprotic solvents was determined. Water, alcohol, acetone, chloroform and dimethylsulfoxide were used as solvents. Based on the findings of the solubility evaluations more investigations were constructed.

Magnetic Susceptibility Measurement

The combination of magnetic susceptibility investigations and absorbance spectra can be employed to determine the structure of the complex. Magnetic characteristics can be utilised to ascertain the stereochemistry of a metal ion complex with d^5, d^6, d^7, d^8, or d^9 electron configuration, specifically whether it adopts a tetrahedral, square planar, or octahedral arrangement. Additionally, these parameters can indicate if the complex is spin-free or spin-paired. The magnetic properties of the metal atoms in the current complexes were inspected utilizing a Gouy magnetic balance to identify the most favourable magnetic moment for each atom at ambient temperature. The Gouy tube was standardized with mercury(II) tetrathiocyanatocobaltate(II), also known as $Hg[Co(SCN)_4]$. The diamagnetic modifications for several atomic and structural components were determined using Pascal's coefficients. The effective magnetic moments ($\mu_{eff.}$) were determined based on the molar magnetic susceptibilities (M_{corr}) of the complexes employing Curie's formula, $\mu_{eff} = 2.84 [M_{corr} T]^{1/2}$ B.M., where T represents the absolute temperature at which the measurements were made. The number of metal ions with unpaired electrons, 'n', can be calculated by analysing its effective magnetic moment, eff. The equation $\mu S = [n (n+2)]^{1/2}$ demonstrates the contribution of the electronic spin effect (S) to the moment.

Antibacterial Effect

The ligand (**L1**) and its complexes (**1–5**) were subjected to *in vitro* antibacterial evaluations towards *P. aeruginosa* (PA14), *K. pneumoniae* (342), *E. coli* (k12), and *S. aureus* (PS80) bacteria using the Kirby Bauer Disc diffusion technique [50]. Ciprofloxacin's antibacterial effect was used as a standard. The bacterial specimens were grown on petri plates containing nutrient agar medium. The test samples were made up of DMSO and placed inside a filter paper disc with a width of 5 mm and a width of 1 mm. Following a 24-hour period, the breadth of the inhibitory zone [51, 52] around each disc was assessed to determine its antibacterial effectiveness. The discs were then positioned on the pre-existing plates and incubated at a temperature of 37 °C. The minimum inhibitory concentrations (MIC) were employed to indicate the antibacterial effectiveness of ligand (**L1**) and its associated complexes (**1–5**).

Antifungal Action

The antifungal effect of ligand (**L1**) and its complexes (**1–5**) was evaluated using the regular disc-agar diffusion approach [53, 54]. The antifungal activity was tested using *A. niger* (ATCC20611), *C. neoformans* (H99), *C. albicans* (WO-1), and *M. audouinii* (ATCC-10216) species. The materials underwent sterilisation by filtration through 0.22 m Millipore filters upon their dissolution in 10 % DMSO to achieve a target dosage of 30 mg/mL. Subsequently, antifungal tests were conducted using the disc diffusion method. A solution comprising 100 litres and 10^4 spores/mL of fungi was disseminated across PDA medium. The 6 mm diameter discs were subjected to a treatment of 10 mL of the samples, with each disc weighing 300 g. Subsequently, the discs were placed on the agar that was contaminated. The conventional medication prescribed was clotrimazole. Negative controls were prepared using a 10 % solution of dimethyl sulfoxide (DMSO). The fungal specimens were cultured at 37 °C for 72 hours on inoculation plates. Plant-associated fungi were cultivated at a temperature of 27 °C. The antifungal effectiveness was assessed by gauging the ZOI towards the investigated microorganisms. Every experiment in the present investigation was performed three times.

Determination of MIC

The microbial cultures often used to make 0.5 McFarland were cultured overnight at 37 °C. Each culture was inoculated in aseptic conditions with 1 mL of the specific bacterial culture (around 10^8 CFU/mL) from a minimum of a 10 mL tube nutritional broth medium. In sterile deionized water, five dilutions of ligand (L1), metal complexes (**1–5**) (100, 75, 50, and 25 mg/mL) were made, as well as a blank sample (without ligand (**L1**), metal complexes (**1–5**)). All isolate evaluations were carried out in triplicate. The implanted tubes were maintained at 37 °C overnight. During the cultivation period, the perceived turbidity in every tube was evaluated. The MIC is demonstrated as the lowermost concentration of the observed strain without turbulence.

Molecular Docking

The relationship and binding mechanism amongst the ligand (**L1**), complexes (**1–5**), and the Mevalonate 5-diphosphate decarboxylase (PDB ID: 1FI4) and Topimerase II DNA gyrase B (PDB ID: 1KZN) proteins were examined through docking analyses using Autodock vina 1.1.2 software [55]. The crystal structures of Mevalonate 5-diphosphate decarboxylase (PDB ID: 1FI4) and Topimerase II DNA gyrase B (PDB

ID: 1KZN) were gotten from the Protein Data Bank for the purpose of assessing their antimicrobial and capabilities. The 3D conformation of ligand **L1** and its complexes (**1–5**) were obtained using ChemBio Office suite software. The required inputs for docking process were generated through the AutoDock Tools 1.5.6 software. The grid dimensions for the 1KZN receptor was determined to have a centre position at x-coordinate 18.839, y-coordinate 26.702, and z-coordinate 37.939. The parameters of the grid are as follows: size_x = 22, size_y = 20, and size_z = 20. The distance between each point on the grid is 1.0 Å. The grid dimensions for the 1FI4 receptor were determined to have a centre position of x: 21.935, y: 57.745, and z: 20.018, with size of x: 24, y: 22, and z: 24, with a spacing of 1.0 Å. The exhaustiveness score was assigned a numerical value of 8. The remaining settings were fixed to their actual parameters for Vina docking and were not specified. The substance with the lowest binding score is considered the potential compound. The docking results were evaluated with the Discovery Studio 2019 application.

Statistical Analysis

Data are presented as mean ± standard error (SEM). All variables were analyzed for statistics by one-way ANOVA subsequently by Tukey's post-hoc comparison test. $P < 0.05$ was considered statistically significant.

Results and Discussion

Physical Data and Solubility

Table 1 displays the physio-chemical properties and solubility of the ligand (**L1**) and its complexes (**1–5**). Solubility experiments indicate that each of the ligand (**L1**) and the metal complexes (**1–5**) exhibit higher solubility in aprotic solvents as opposed to protic solvents.

T a b l e 1

Physical data and solubility of the metal complexes (1–5) and ligand (L1)

Compound	Colour	Melting point (ºC)	Solubility			
			Chloroform	Water	DMSO	Ethanol
Ligand (L1)	Yellow	164	Sparingly soluble	Insoluble	Soluble	Soluble
Copper complex (1)	Blue	186	Insoluble	Insoluble	Soluble	Insoluble
Nickel complex (2)	Green	194	Insoluble	Insoluble	Soluble	Sparingly soluble
Cobalt complex (3)	Pale brown	206	Insoluble	Insoluble	Soluble	Insoluble
Chromium complex (4)	Dark brown	182	Partially soluble	Insoluble	Soluble	Insoluble
Manganese complex (5)	Black	234	Insoluble	Insoluble	Soluble	Insoluble

Spectral Data of Ligand (L1)

(2R,9R)-2-((S)-((2-aminoethyl)amino)(2-hydroxyphenyl)methyl)-6-hydroxy-9-phenyl-2,3,4,9-tetrahydro-1H-xanthen-1-one (L1)

Yellow solid; Mw: 456.53; mf: $C_{28}H_{28}N_2O_4$; mp: 165 °C; IR (cm^{-1}, KBr) ν_{max}: 3420 (–OH), 3230 (–NH), 1640 (–C=O), 1230 (–C–N–C); ^{1}H NMR (300 MHz, CDCl$_3$) δ 10.38 (2H, s, OH), 8.08 (1H, s, NH), 7.12–6.90 (4H, m, Ph–OH), 7.33–7.23 (5H, m, Ar–H), 6.89–6.19 (3H, m, Ph–OH), 6.25 (2H, s, NH$_2$), 4.74 (1H, s, –CH–Ph), 4.12 (1H, d, J = 1.7 Hz, CH-Ph), 2.96–1.27 (5H, m, CHD), 2.77 (2H, t, J = 2.8 Hz, –CH$_2$), 2.61 (2H, t, J = 2.8 Hz, –CH$_2$); ^{13}C NMR (300 MHz, CDCl$_3$) δ 198.6 (1C, C=O), 164.8 (1C, -C=C), 162.9, 154.5, 130.3, 112.9, 110.6, 100.1 (6C, Ar ring), 147.6, 129.2, 128.2, 126.2 (6C, Ph ring), 155.2, 127.7, 127.3, 121.1, 115.7 (6C, Ph ring), 109.7 (1C, –C=C), 57.0 (1C, –C–C–Ph), 51.1 (1C, –C–NH), 48.9 (1C, –CH$_2$–NH), 41.3 (1C, –CH$_2$–NH$_2$), 39.9 (1C, –CH–Ar), 26.3 (1C, CH$_2$), 12.6 (1C, CH$_2$); EI-MS: m/z 457.21 (M$^+$, 30 %); Elemental studies: Anal. Calcd (Found): C, 73.66 (73.62); H, 6.18 (6.20); N, 6.14 (6.16) %.

Magnetic and Conductivity Properties

The solubility of the newly synthesised metal complex was assessed in several solvents. The molar conductivity in DMSO was determined by utilising a cell constant that was standardised towards a 0.1 M KCl solution. The measurement was performed using the Equiptronics electronic conductivity meter (Model EQ-660). The complexes' neutral (non-electrolytic) character was confirmed by assessing the conductivity of

a 10^{-3} M solutions for every complex in DMSO. The mixed ligand complexes (**1–5**) exhibited a molar conductivity of 18–28 $\Omega^{-1}mol^{-1}cm^2$. The conductivity studies revealed that the chloride ions form complexes with metal ions, signifying that they act as ligands instead of independent ions. The arrangement of the synthesised complexes may be influenced by the stoichiometric ratios (1:2) and the kinds of electrolytes employed in the conductivity testing. Table 2 presents the conductivity and magnetic properties of metallic complexes (**1–5**).

<div align="right">T a b l e 2</div>

Conductivity and magnetic properties of metal complexes (1–5) with ligand (L1)

S. No	Compounds	Conductivity ($\Omega^{-1}mol^{-1}cm^2$)	Magnetic Susceptibility (μ_{eff}. B.M)
1.	Copper complex (1)	18	2.23
2.	Nickel complex (2)	26	3.54
3.	Cobalt complex (3)	23	5.23
4.	Chromium complex (4)	24	4.60
5.	Manganese complex (5)	28	5.14

NMR Spectral Studies of Ligand (L1)

In the ^{1}H NMR spectra of the Mannich base ligand (**L1**) being studied (Fig. S1, *a*). The methylene protons associated with the amine hydrogen atoms of the ethylenediamine and salicylaldehyde are observed as a peak at 4.74 ppm, while the hydroxyl protons appear at 10.38 ppm. The aromatic hydrogens exhibit a multiplet at 7.12–6.90 ppm. The lack of a signal corresponding to the proton of the secondary amine –NH$_2$, which was eliminated during the Mannich process, provides more evidence for the creation of the ligand. In the ^{13}C NMR spectra of the Mannich base ligand (**L1**) being studied, the peak at 198.6 and 164.8 ppm resemble to the –C=O and –C=C atoms of the xanthene group, respectively. The carbon atoms of the aromatic rings exhibited peaks at 162.0–100.1 ppm (Fig. S1, *b*). The appearance of a peak at 39.9 ppm indicates that the –CH$_2$ moiety is connected to the amine hydrogens of the ethylenediamine and salicylaldehyde.

Mass Spectral Studies of Ligand (L1)

The mass spectra of the studied Mannich base ligand (**L1**) is shown in Figure 4. The mass of ligand (**L1**) was determined to be 456.53 through observation, and this was further validated by mass spectral tests, which showed a mass-to-charge ratio (m/z) of 457.23. The molecular ion peak was detected at a m/z of 380.44. The other fragmentation peaks seen had m/z of 412.03, 291.32, 225.26 and 209.26, accordingly. The fragmentation pattern of ligand (L1) was depicted in Figure 5.
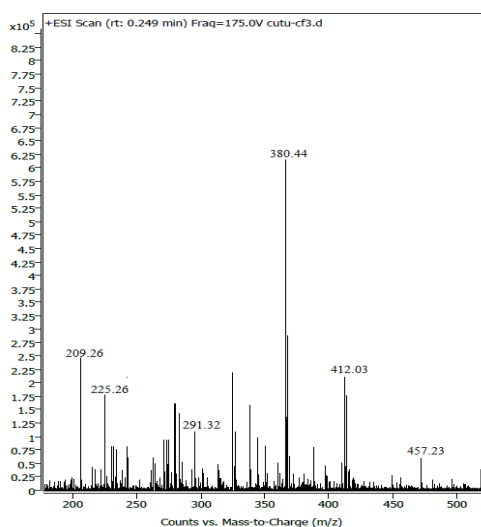
Figure 4. Mass spectra of ligand (L1)
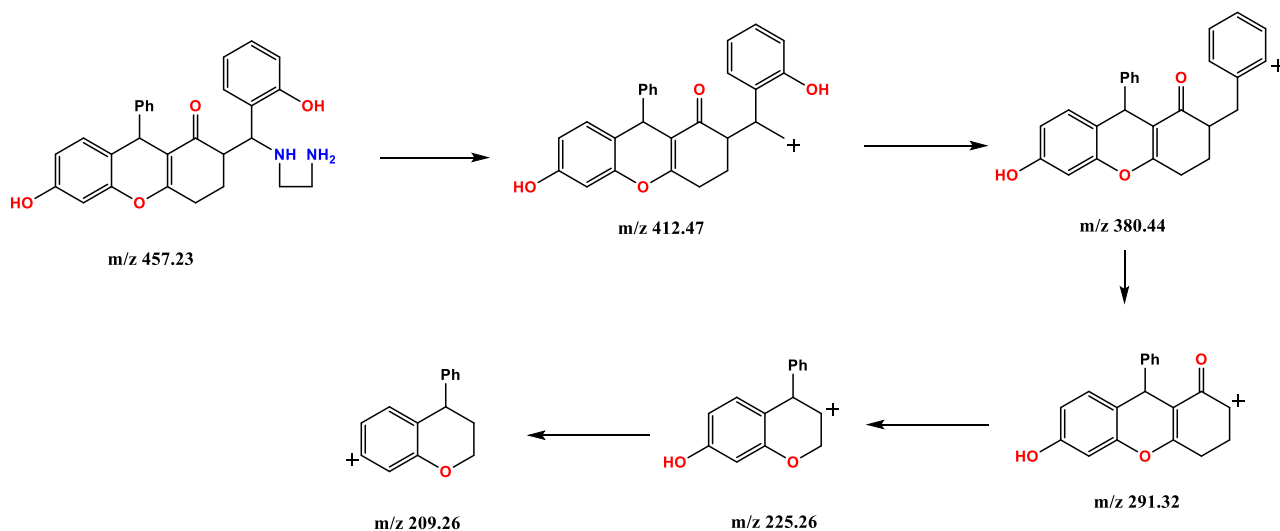
Figure 5. Mass spectral fragmentation types of Ligand (L1)

IR Spectra

A notable discovery in the ligand FT-IR spectra (Fig. 6a) displayed a prominent band at 3446 and 3145 cm^{-1}, which can be ascribed to the νOH and the NH amine molecule [56, 57]. The N–H and O–H bands exhibited a shift towards lower frequency in all of the complexes (Figs 6b–f), demonstrating that the hydroxyl oxygen and amine nitrogen were tangled in coordination with the metal ions. The formation of metal complexes (**1–5**) is indicated by the emergence of a distinct peak at a wavelength of 760–752 cm^{-1}, which resembles to the M–O bond [58]. The M–Cl bond is shown by the emergence of a distinct peak in the spectral array of 546–514 cm^{-1}. Table 3 presents the IR spectral information for ligand **L1** and complexes **1–5**.

T a b l e 3

FT-IR studies of complexes (1-5) and the ligand (L1)

Compound	IR stretching frequency (cm^{-1})			
	–OH	–NH	M–O	M–Cl
Ligand (L1)	3446	3145	–	–
Copper complex (1)	3423	2938	760	514
Nickel complex (2)	3478	3062	756	546
Cobalt complex (3)	3437	3058	752	542
Chromium complex (4)	3427	2939	756	523
Manganese complex (5)	3441	2940	752	528
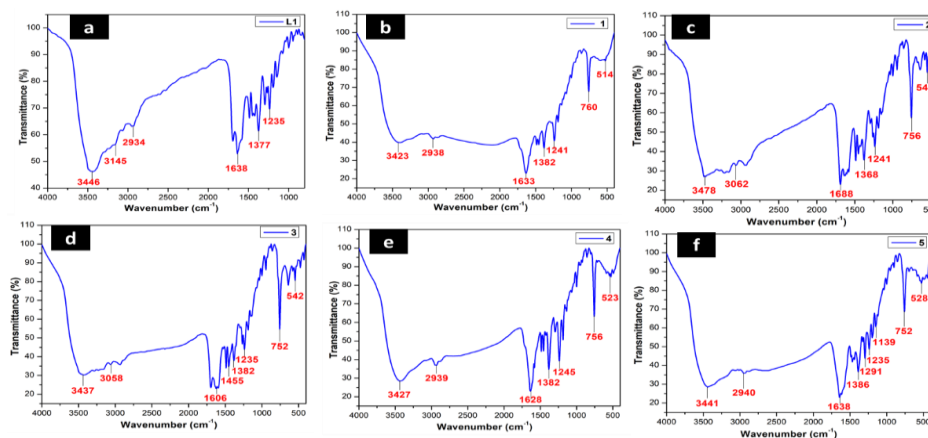
Figure 6. FT-IR spectra of (*a*) Ligand **L1** (*b*) Copper complex **1** (*c*) Nickel complex **2** (*d*) Cobalt complex **3** (*e*) Chromium complex **4** (*f*) Manganese complex **5**

UV-Visible studies

The UV-Vis spectra of ligand (**L1**) displayed two absorption maxima in the area of 219 and 266 nm, which can be attributed to $\pi-\pi^*$ and $n-\pi^*$ shifts separately (Fig. 7a). The spectra of the complexes in DMSO solution revealed three distinct peaks. The intra-ligand shifts were identified by two distinct bands observed at 272–278 nm and 245–258 nm. The presence of the complex was described by the peak observed in the 343–332 nm area, which is recognized to the ligand-to-metal charge transfer (LMCT) shifts (Figs 7b-f).
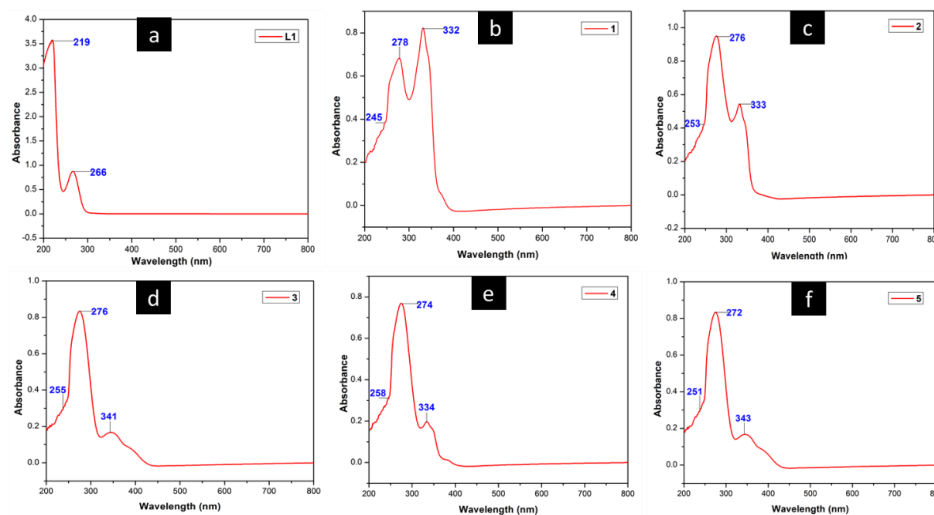
Figure 7. UV-Vis spectra of (*a*) Ligand L1 (*b*) Copper complex 1 (*c*) Nickel complex 2 (*d*) Cobalt complex 3 (*e*) Chromium complex 4 (*f*) Manganese complex 5

EPR Spectra

EPR spectrum study can provide insights on the formation of ligand-metal bonds and the distribution of unpaired and paired electrons. Copper (II) complexes exhibit distinct characteristics in coordination chemistry, displaying several geometries including square pyramidal, octahedral, square planar, and tetrahedral, which can be differentiated by EPR spectra. The EPR parameters $g\perp$, g_{avg}, $g\parallel$, and G are used to determine whether a chemical has an octahedral or tetrahedral structure. The occurrence of an unpaired electron in the $d_{x^2-y^2}$ orbital is confirmed by the following criterion: the parallel g-value ($g\parallel$) is larger than the perpendicular g-value ($g\perp$), which is more than 2.0023. The $g\parallel$ and $g\perp$ values for the copper complex were measured to be 2.1465 and 2.0253, individually. The covalent character was denoted by a $g\parallel$ value less than 2.3 and anionic character is represented by a $g\parallel$ value greater than 2.3. It is evident that the $g\parallel$ value (2.1465) is less than 2.3, suggesting that the molecule is covalent. Hathaway states that G values below four suggest a substantial interaction towards metal centres, while G values above four designate a minimum transfer of charge. In this example, the G value is 11.45, indicating that the charge transfer is minimum. The Cu(II) complex has distorted octahedral geometry, as indicated by its EPR properties. The EPR spectra of copper complex (**1**) are shown in Figure 8.
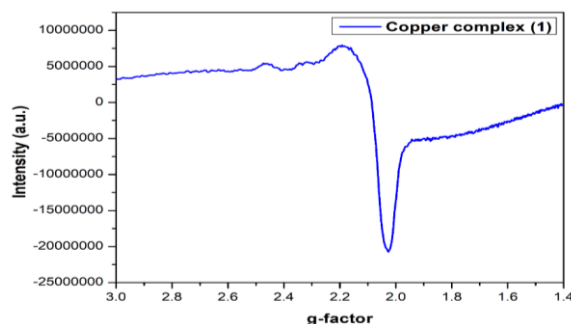
Figure 8. EPR spectra of copper complex **1**

Antibacterial Effect

The synthesised ligand (**L1**) and complexes (**1–5**) were evaluated for antibacterial properties. The ligand (**L1**) exhibited lower activity in comparison to the equivalent complexes (**1–5**). The examination was conducted within a regulated setting. Among the series of compounds (**1–5**), only complex **1** exhibited significant action (MIC = 2 mg/mL) towards *S. aureus*. The chromium complex **4** exhibited more activity towards *K. pneumoniae* compared to the control Ciprofloxacin, as seen by its lower MIC value of 4 mg/mL, in contrast to Ciprofloxacin's MIC value of 8 mg/mL. The cobalt complex 3 had higher activity towards *E.coli* related to the control Ciprofloxacin, as evidenced by its lower MIC value of 4 mg/mL, whereas Ciprofloxacin had a MIC value of 6 mg/mL. Complexes **1** (Cu(II)), **3** (Co(II)), and **4** (Cr(II)) exhibit remarkable activity when compared to complexes **1–5**. Janowska et al., reported the syn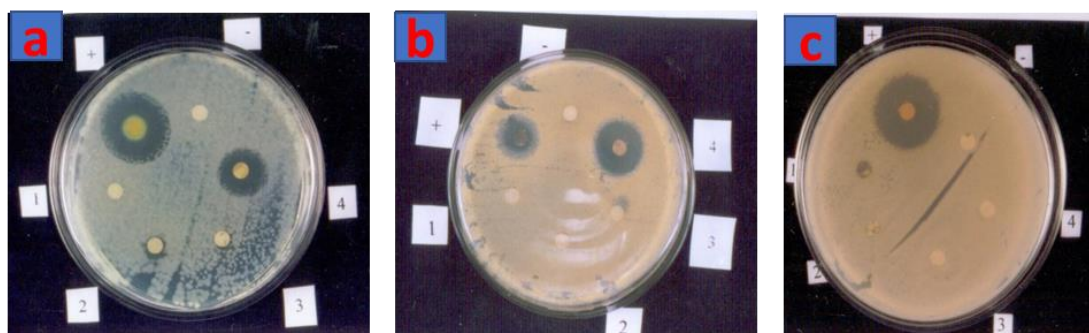thesis of metal complexes using heterocyclic Mannich base ligand and its excellent antibacterial action [59]. The outcomes are presented in Table 4 and Figure 9.

Table 4

Antibacterial effect of ligand (L1) and Complexes (1–5)

Compounds	MIC in mg/mL			
	K. pneumaniae	*S. aureus*	*P. aeruginosa*	*E. coli*
L1	16	32	32	16
1	12	2	8	10
2	28	8	8	8
3	14	10	4	4
4	4	6	4	12
5	16	12	4	8
Ciprofloxacin	8	4	2	6

Figure 9. Antibacterial action of copper complex 1 in (*a*) *K. pneumaniae,* (*b*) *S. aureus,* (*c*) *E. coli*

Antifungal Activity

The study examined the antifungal effect of the obtained ligand (**L1**) and its complexes (**1–5**). Compared to similar complexes, the ligand (**L1**) exhibited low activity (**1–5**). The complex **1** in the sequence (**1-5**) had significant activity specifically towards *C. albicans*, having MIC of 4 mg/mL. The nickel complex **2** exhibited higher activity towards *C. neoformans* compared to the normal Clotrimazole. The MIC of the nickel complex **2** was 2 mg/mL, whereas the MIC of Clotrimazole was 4 mg/mL. The cobalt complex 3 exhibited a lower MIC of 8 mg/mL against *A. niger* compared to the normal Clotrimazole, which had an MIC of 12 mg/mL. Complex **1** (Cu II), complex **2** (Ni II), and complex **3** (Co II) exhibit significant activity in comparison to complexes (**1–5**). The antibacterial efficacy of the complexes is ascribed to the existence of heterorings and heteroatoms [60]. The antibacterial efficacy of the metal complexes tends to be superior to that of the ligand alone. This results from the extensive delocalization of the ligand's electronic orbitals throughout the metal complexes, hence diminishing the metal's polarity. This, in turn, enhances the lipophilicity of the complex, which ultimately leads to the occlusion of active binding sites of microbial enzymes [61]. The findings are summarised in Table 5 and Figure 10.

Antifungal effect of ligand (L1) and complexes (1–5)

Compounds	MIC in mg/mL			
	C. albicans	*C. neoformans*	*M. audouinii*	*A. niger*
L1	14	26	16	10
1	04	08	12	16
2	12	02	10	24
3	10	16	12	08
4	12	11	10	14
5	14	11	08	15
Clotrimazole	08	04	10	12
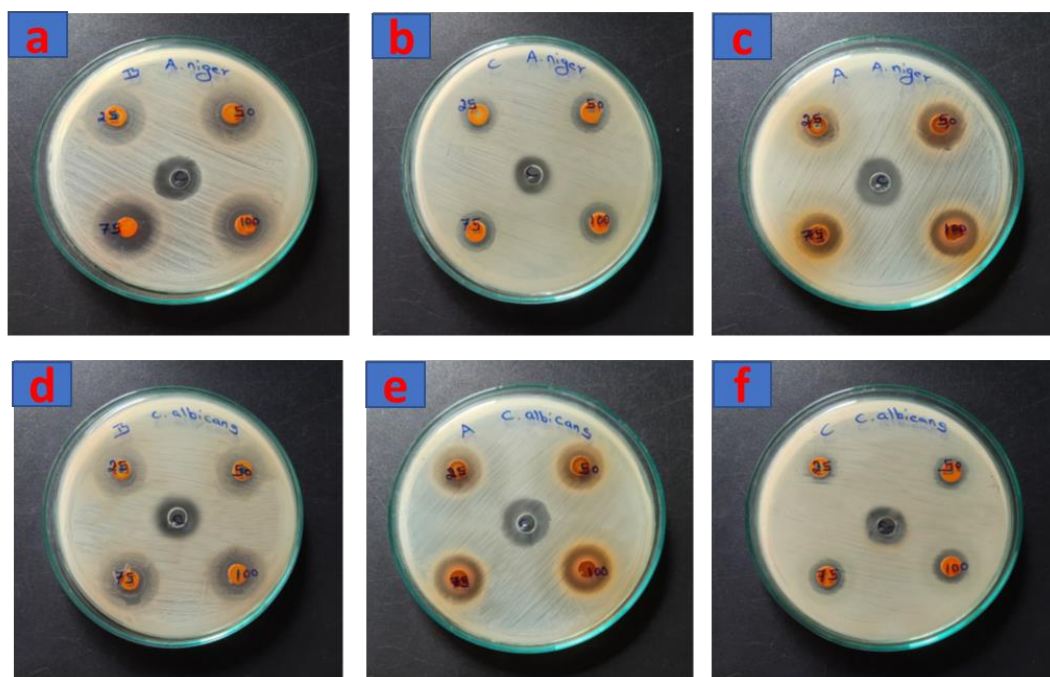
Figure 10. Antifungal action of (*a*) cobalt complex, (*b*) chromium complex, (*c*) Ligand **L1**, (*d*) copper complex, (*e*) cobalt complex, (*f*) chromium complex

Docking Studies

Docking studies were performed to have a deeper understanding of the potential mechanisms of biological processes. The anti-fungal protein mevalonate-5-diphosphatedecarboxylase (PDB ID: 1FI4) [62] which is accountable for isoprenoid/sterol production and the *E. coli* topoisomerase II DNA gyrase B (PDB ID: 1KZN) [63] were selected as protein targets for assessing antimicrobial action towards these species. The ligand **L1**, together with complexes (**1–5**) and the control substances Clotrimazole and Ciprofloxacin [64], were analysed for their docking interactions with receptors 1FI4 and 1KZN employing the Autodock Vina software. The complexes (**1–5**) exhibit higher binding affinities (–7.9, –6.2, –7.8, –7.7, –6.8 kcal/mol) compared to ligand **L1** (binding affinity: –5.3 kcal/mol) and control Ciprofloxacin (binding affinity: –6.0 kcal/mol) in complex with the 1KZN receptor. Hydrogen bonding significantly contributes to the reliability of protein-ligand interaction. The ideal bond length amongst the hydrogen-acceptor and hydrogen-donor atoms is less than 3.5 Å [65]. The hydrogen bond lengths between ligand **L1**, complexes (**1–5**), and control Ciprofloxacin were all below 3.5 Å in their respective proteins, which exhibited particularly high hydrogen bonding. The ligand **L1** establishes four hydrogen bonds with the protein 1KZN. The amino acids Glu42 (bond length: 2.90 Å), Asn46 (bond lengths: 2.43 and 2.50 Å), and Arg136 (bond length: 2.56 Å) participated in hydrogen bonding contacts. Hydrophobic contacts were mediated by the amino acids Glu50, Arg76, Gly77, Ile78, Pro79, Gly119, and Val120. Complex **3** establishes two Hydrogen bonds with the pro-

tein 1KZN. The amino acid residue Arg76 participated in a hydrogen bonding interaction, with bond lengths of 2.20 and 3.04 Å. Hydrophobic interactions were facilitated by the amino acids Asp49, Glu50, Ala53, and His95. Ciprofloxacin failed to create any hydrogen bonds with the protein 1KZN. Hydrophobic interactions occurred between each of the amino acids Asn46, Ala47, Glu50, Asp73, Ile78, and Ile90. Figures 11a–c illustrate the hydrophobic and hydrogen bonding relations between amino acids in the ligand **L1,** copper complex **(1),** Ciprofloxacin and 1KZN receptor. Figures S2–S5 illustrate the hydrophobic and hydrogen bonding relations between amino acids in the complexes (**2–5**) and 1KZN receptor. The complexes (**1–5**) exhibit higher binding affinities (–8.8, –8.0, –8.3, –7.0, –7.4 kcal/mol) compared to ligand **L1** (binding affinity: –6.2 kcal/mol) and control Clotrimazole with a binding affinity of (–6.7 kcal/mol) in the 1FI4 receptor, correspondingly. The ligand **L1** establishes six hydrogen bonds with the protein 1FI4. The amino acids Asn13, Ala119, Arg158, Asp201, Val206, and Ser208 were implicated in hydrogen bonding interactions, with bond lengths of 2.72 Å, 2.48 Å, 2.44 Å, 2.82 Å, 3.00 Å, and 2.05 Å, individually. Hydrophobic contacts were facilitated by the amino acid residues Ala15 and Asp302. Complex **2** establishes three hydrogen bonds with the target protein 1FI4. Hydrogen bonding interactions involving the amino acids Asn110 (with a bond length of 3.09 Å), Ser208 (with a bond length of 1.67 Å), and Ala303 (with a bond length of 1.82 Å). Hydrophobic relations were mediated by the amino acids Ala15, Ala119, Arg158, and Asp302. The control Clotrimazole molecule forms a single hydrogen bond with the target protein 1FI4. The amino acid Arg158, with a bond length of 5.83 Å, participated in a hydrogen bonding interaction. Hydrophobic contacts were facilitated by the amino acids Ala15, Lys18, Tyr19, Trp20, Ala119, Phe260, Asp302, and Ala303. Figures 12a–c depict the hydrophobic and hydrogen bonding contacts between amino acids in the 1FI4 protein and ligand **L1**, copper complex (**1**) and the control Clotrimazole. Figures S6–S9 depict the hydrophobic and hydrogen bonding contacts between amino acids in the 1FI4 protein and complexes (**2–5**). The results indicate that complexes (**1–5**) exhibit much higher inhibitory capacity compared to ligand **L1** and the control substances Clotrimazole and Ciprofloxacin in terms of antifungal and antibacterial properties. The findings were simplified and presented in Table 6 and Table 7.

Table 6

Docking results of ligand L1 and complexes (1–5) against protein 1KZN

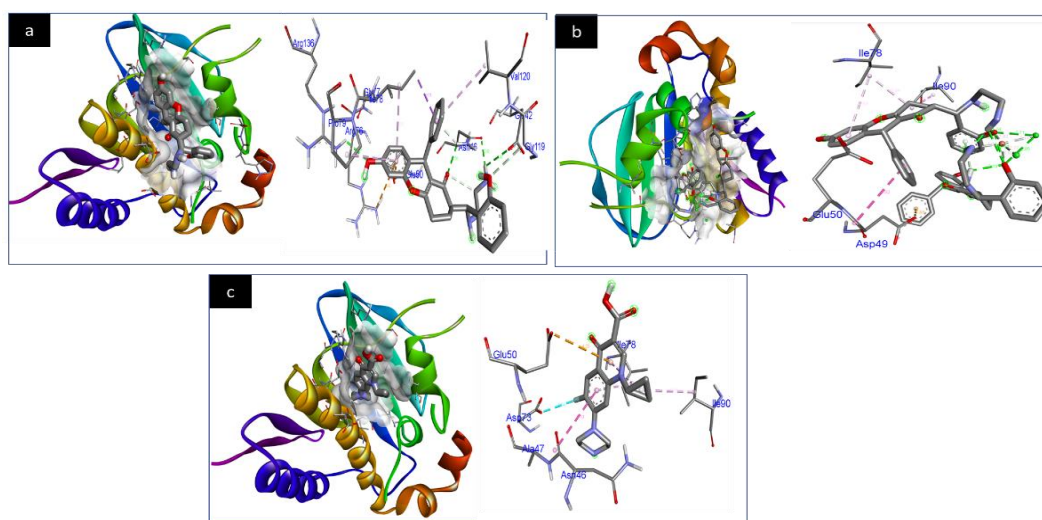| Compounds	Binding score (kcal/mol)	No. of H-bonds	H-bonding residues
L1	–5.3	4	Glu42, Asn46, Arg136
1	–7.9	0	–
2	–6.2	0	–
3	–7.8	2	Arg76
4	–7.7	0	–
5	–6.8	0	–
Ciprofloxacin	–6.0	0	–

Figure 11. Interactions of ligand L1 (*a*), copper complex 1 (*b*), Ciprofloxacin (*c*) within the binding cavity of 1KZN

Docking results of ligand L1 and complexes (1–5) against protein 1FI4

Compounds	Binding score (kcal/mol)	No. of H-bonds	H-bonding residues
L1	-6.2	6	Asn13, Ala119, Arg158, Asp201, Val206, Ser208
1	-8.8	1	Tyr19
2	-8.0	3	Asn110, Ser208, Ala303
3	-8.3	1	Leu17
4	-7.0	1	Asp302
5	-7.4	0	-
Clotrimazole	-6.7	1	Arg158
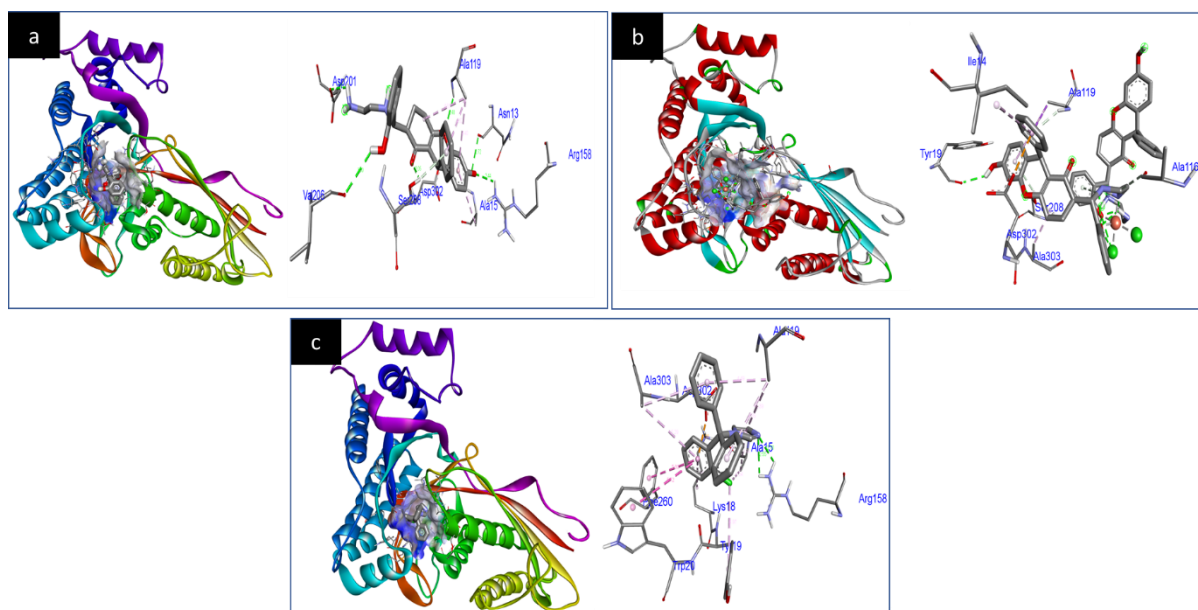
Figure 12. Interactions of ligand L1 (*a*), copper complex 1 (*b*), Clotrimazole (*c*) within the binding cavity of 1FI4

Conclusions

This study focusses on the coordination chemistry of a Mannich base ligand (2R,9R)-2-((S)-((2-aminoethyl)amino)(2-hydroxyphenyl)methyl)-6-hydroxy-9-phenyl-2,3,4,9-tetrahydro-1H-xanthen-1-one (LI), synthesised through the reaction of xanthene, salicylaldehyde, and ethylenediamine. The Mannich base ligand (**L1**) was used to form metal complexes (**1– 5**) of the [M(**L1**)$_2$Cl$_2$] type. These complexes were then analysed using analytical, magnetic, and spectroscopic methods. The Mannich base is a bidentate ligand that coordinates with the metal ion over nitrogen atom of ethylenediamine and the oxygen atom of salicylaldehyde. The conductivity behaviours indicate that the chloride atoms are bound to the metal atoms as ligands, rather than being as free ions. The synthesised complexes (**1–5**) exhibit the octahedral geometry as shown by their electrical and magnetic characteristics. Furthermore, the ligand and metal complexes underwent screening to evaluate their antibacterial efficacy towards different harmful microorganisms. The metal complexes displayed significant antimicrobial properties related to the ligand (**L1**) and control, as validated by docking experiments. The data acquired validate the multi-directional antimicrobial efficacy of the novel Mannich base complexes and demonstrate the influence of structural replacement on the activity of this kind of substances towards various microorganisms. The findings acquired are anticipated to yield significant data for additional study of this intriguing group. Pharmacological research focused on discovering novel biologically active chemicals is ongoing with a repository of acquired molecules.

Supporting Information

Author Information*

_____

*The authors' names are presented in the following order: First Name, Middle Name and Last Name

Manimegalai Ramasamy — Research Scholar, PG & Research Department of Chemistry, Government Arts College, Bharathidasan University, Ariyalur, 621713, Tamilnadu, India; e-mail: manisri627@gmail.com; https://orcid.org/0009-0002-8951-5440

Gurunathan Velayutham — Assistant Professor, PG & Research Department of Chemistry, Bishop Heber College, Bharathidasan University, Tiruchirappalli, 621002, Tamilnadu, India; e-mail: gurunathan.ch@bhc.edu.in; https://orcid.org/0009-0009-2547-5276

Ramar Pitchaipillai (*corresponding author*) — Associate Professor, PG & Research Department of Chemistry, Government Arts College, Bharathidasan University, Ariyalur, 621713, Tamilnadu, India; e-mail: drsairam202110@gmail.com; https://orcid.org/0009-0006-2022-7159

References

1 Murray C. J., Ikuta K. S., Sharara F., Swetschinski L., Robles Aguilar G., Gray A., Han C., Bisignano C., Rao P., Wool E., & Johnson S. C. (2022). Global burden of bacterial antimicrobial resistance in 2019: a systematic analysis. *Lancet*, *399,* 629–655. https://doi.org/10.1016/S0140-6736(21)02724-0

2 Cassini A., Högberg L. D., Plachouras D., Quattrocchi A., Hoxha A., Simonsen G. S., Colomb-Cotinat M., Kretzschmar M. E., Devleesschauwer B., Cecchini M., & Ouakrim D. A. (2019). Attributable deaths and disability-adjusted life-years caused by infections with antibiotic-resistant bacteria in the EU and the European Economic Area in 2015: a population-level modelling analysis. *The Lancet Infectious Diseases, 19*, 56–66. https://doi.org/10.1016/S1473-3099(18)30605-4

3 Centers for Disease Control and Prevention US, Antibiotic Resistance Threats in the United States, https://stacks.cdc.gov/view/cdc/82532, 2019. Accessed 20th February 2025.

4 WHO: Global Antimicrobial Resistance and Use Surveillance System (GLASS) Report 2022, https://www.who.int/publications/i/item/97, 2022. Accessed 20th February 2025.

5 Darby E. M., Trampari E., Siasat P., Solsona Gaya M., Alav I., Webber M. A., & Blair J. M. A. (2022). Molecular mechanisms of antibiotic resistance revisited. *Nature Reviews Microbiology, 21*, 280–295. https://doi.org/10.1038/s41579-022-00820-y

6 Prashanth, T., Ranganatha, V. L., Ramu, R., Mandal, S. P., Mallikarjunaswamy, C., & Khanum, S. A. (2021). Synthesis, characterization, docking study and antimicrobial activity of 2-(4-benzoylphenoxy)-1-[2-(1-methyl-1 H-indol-3-yl) methyl)-1H-benzo[d]imidazol-1-yl]ethanone derivatives. *Journal of the Iranian Chemical Society*, *18*, 2741–2756. https://doi.org/10.1007/s13738-021-02230-y

7 Khadri, M. N., Begum, A. B., Sunil, M. K., & Khanum, S. A. (2020). Synthesis, docking and biological evaluation of thiadiazole and oxadiazole derivatives as antimicrobial and antioxidant agents. *Results in Chemistry*, *2*, 100045. https://doi.org/10.1016/j.rechem.2020.100045

8 Abu-Dief, A. M., Alotaibi, N. H., Al-Farraj, E. S., Qasem, H. A., Alzahrani, S., Mahfouz, M. K., & Abdou, A. (2022). Fabrication, structural elucidation, theoretical, TD-DFT, vibrational calculation and molecular docking studies of some novel adenine imine chelates for biomedical applications. *Journal of Molecular Liquids*, *365*, 119961. https://doi.org/10.1016/j.molliq.2022.119961

9 Alatawi, N. M., Alsharief, H. H., Alharbi, A., Alhasani, M., Attar, R. M., Khalifa, M. E., ... & El-Metwaly, N. M. (2022). Simulation for the behavior of new Fe (III) and Cr (III)-thiophenyl complexes towards DNA polymerase: synthesis, characterization, eukaryotic DNA and Hartree–Fock computation. *Chemical Papers*, *76*(6), 3919–3935. https://doi.org/10.1007/s11696-022-02136-w

10 Abu-Dief, A. M., El-Khatib, R. M., Aljohani, F. S., Alzahrani, S. O., Mahran, A., Khalifa, M. E., & El-Metwaly, N. M. (2021). Synthesis and intensive characterization for novel Zn (II), Pd (II), Cr (III) and VO (II)-Schiff base complexes; DNA-interaction, DFT, drug-likeness and molecular docking studies. *Journal of Molecular Structure*, *1242*, 130693. https://doi.org/10.1016/j.molstruc.2021.130693

11 Abu-Dief, A. M., Abdel-Rahman, L. H., Abdelhamid, A. A., Marzouk, A. A., Shehata, M. R., Bakheet, M. A., ... & Nafady, A. (2020). Synthesis and characterization of new Cr (III), Fe (III) and Cu (II) complexes incorporating multi-substituted aryl imidazole ligand: Structural, DFT, DNA binding, and biological implications. *Spectrochimica Acta Part A: Molecular and Biomolecular Spectroscopy*, *228*, 117700. https://doi.org/10.1016/j.saa.2019.117700

12 Abdel-Rahman, L. H., Abu-Dief, A. M., El-Khatib, R. M., & Abdel-Fatah, S. M. (2016). Sonochemical synthesis, DNA binding, antimicrobial evaluation and in vitro anticancer activity of three new nano-sized Cu (II), Co (II) and Ni (II) chelates based on tridentate NOO imine ligands as precursors for metal oxides. *Journal of Photochemistry and Photobiology B: Biology*, *162*, 298–308. https://doi.org/10.1016/j.jphotobiol.2016.06.052

13 Khalaf, M. M., Abd El-Lateef, H. M., Gouda, M., Sayed, F. N., Mohamed, G. G., & Abu-Dief, A. M. (2022). Design, structural inspection and bio-medicinal applications of some novel imine metal complexes based on acetylferrocene. *Materials*, *15*(14), 4842. https://doi.org/10.3390/ma15144842

14 Abu-Dief, A. M., El-Khatib, R. M., Aljohani, F. S., Al-Abdulkarim, H. A., Alzahrani, S., El-Sarrag, G., & Ismael, M. (2022). Synthesis, structural elucidation, DFT calculation, biological studies and DNA interaction of some aryl hydrazone Cr^{3+}, Fe^{3+}, and Cu^{2+} chelates. *Computational Biology and Chemistry*, *97*, 107643. https://doi.org/10.1016/j.compbiolchem.2022.107643

15 Borah, B., Dwivedi, K. D., & Chowhan, L. R. (2021). Recent advances in metal-and organocatalyzed asymmetric functionalization of pyrroles. *Asian Journal of Organic Chemistry*, *10*(11), 2709–2762. https://doi.org/10.1002/ajoc.202100427

16 Borah, B., Dhar Dwivedi, K., & Chowhan, L. R. (2021). 4-Hydroxycoumarin: A versatile substrate for transition-metal-free multicomponent synthesis of bioactive heterocycles. *Asian Journal of Organic Chemistry*, *10*(12), 3101–3126. https://doi.org/10.1002/ajoc.202100550

17 Mermer, A., Keles, T., & Sirin, Y. (2021). Recent studies of nitrogen containing heterocyclic compounds as novel antiviral agents: A review. *Bioorganic Chemistry*, *114*, 105076. https://doi.org/10.1016/j.bioorg.2021.105076

18 Azath, I. A., Puthiaraj, P., & Pitchumani, K. (2013). One-pot multicomponent solvent-free synthesis of 2-amino-4H-benzo [b]pyrans catalyzed by per-6-amino-β-cyclodextrin. *ACS Sustainable Chemistry & Engineering*, *1*(1), 174–179. https://doi.org/10.1021/sc3000866

19 Datta, B., & Pasha, M. A. (2012). Glycine catalyzed convenient synthesis of 2-amino-4H-chromenes in aqueous medium under sonic condition. *Ultrasonics Sonochemistry*, *19*(4), 725–728. https://doi.org/10.1016/j.ultsonch.2012.01.006

20 Gourdeau, H., Leblond, L., Hamelin, B., Desputeau, C., Dong, K., Kianicka, I., ... & Tseng, B. (2004). Antivascular and anti-tumor evaluation of 2-amino-4-(3-bromo-4, 5-dimethoxy-phenyl)-3-cyano-4H-chromenes, a novel series of anticancer agents. *Molecular cancer therapeutics*, *3*(11), 1375–1384. https://doi.org/10.1158/1535-7163.1375.3.11

21 Kemnitzer, W., Drewe, J., Jiang, S., Zhang, H., Wang, Y., Zhao, J., ... & Cai, S. X. (2004). Discovery of 4-Aryl-4 H-chromenes as a new series of apoptosis inducers using a cell-and caspase-based high-throughput screening assay. 1. structure− activity relationships of the 4-Aryl group. *Journal of medicinal chemistry*, *47*(25), 6299–6310. https://doi.org/10.1021/jm049640t

22 Mohr, S. J., Chirigos, M. A., Fuhrman, F. S., & Pryor, J. W. (1975). Pyran copolymer as an effective adjuvant to chemotherapy against a murine leukemia and solid tumor. *Cancer research*, *35*(12), 3750–3754.

23 Hatakeyama, S., Ochi, N., Numata, H., & Takano, S. (1988). A new route to substituted 3-methoxycarbonyldihydropyrans; enantioselective synthesis of (–)-methyl elenolate. *Journal of the Chemical Society, Chemical Communications*, (17), 1202–1204. https://doi.org/10.1039/C39880001202

24 Bonsignore, L., Loy, G., Secci, D., & Calignano, A. (1993). Synthesis and pharmacological activity of 2-oxo-(2H)-1-benzopyran-3-carboxamide derivatives. *European Journal of Medicinal Chemistry*, *28*(6), 517–520. https://doi.org/10.1016/0223-5234(93)90020-F

25 Görlitzer, K., Dehne, A., & Engler, E. (1983). 2-(1H-Tetrazol-5-yl)-4,5-dihydro-4-oxo-indeno[1,2-b]pyran. *Archiv der Pharmazie*, *316*(3), 264–270. https://doi.org/10.1002/ardp.19833160315

26 Alvey, L., Prado, S., Huteau, V., Saint-Joanis, B., Michel, S., Koch, M., ... & Janin, Y. L. (2008). A new synthetic access to furo[3,2-f]chromene analogues of an antimycobacterial. *Bioorganic & medicinal chemistry*, *16*(17), 8264–8272. https://doi.org/10.1016/j.bmc.2008.06.057

27 Kumar, R. R., Perumal, S., Senthilkumar, P., Yogeeswari, P., & Sriram, D. (2007). An atom efficient, solvent-free, green synthesis and antimycobacterial evaluation of 2-amino-6-methyl-4-aryl-8-[(E)-arylmethylidene]-5,6,7,8-tetrahydro-4H-pyrano[3,2-c]pyridine-3-carbonitriles. *Bioorganic & Medicinal Chemistry Letters*, *17*(23), 6459–6462. https://doi.org/10.1016/j.bmcl.2007.09.095

28 Armesto, D., Horspool, W. M., Martin, N., Ramos, A., & Seoane, C. (1989). Synthesis of cyclobutenes by the novel photo-chemical ring contraction of 4-substituted 2-amino-3, 5-dicyano-6-phenyl-4H-pyrans. *The Journal of Organic Chemistry*, *54*(13), 3069–3072. https://doi.org/10.1021/jo00274a021

29 Reynolds, G. A., & Drexhage, K. H. (1975). New coumarin dyes with rigidized structure for flashlamp-pumped dye lasers. *Optics Communications*, *13*(3), 222–225. https://doi.org/10.1016/0030-4018(75)90085-1

30 Azizi, N., Mariami, M., & Edrisi, M. (2014). Greener construction of 4H-chromenes based dyes in deep eutectic solvent. *Dyes and Pigments*, *100*, 215–221. https://doi.org/10.1016/j.dyepig.2013.09.007

31 Bissell, E. R., Mitchell, A. R., & Smith, R. E. (1980). Synthesis and chemistry of 7-amino-4-(trifluoromethyl) coumarin and its amino acid and peptide derivatives. *The Journal of Organic Chemistry*, *45*(12), 2283–2287. https://doi.org/10.1021/jo01300a003

32 Ellis, G.P. Chromenes, Chromanones, and Chromones—Introduction. *Chemistry of Heterocyclic Compounds,* 1–10. Portico. https://doi.org/10.1002/9780470187012.ch1

33 Singha, R., Islam, A., & Ghosh, P. (2021). One-pot three-component tandem annulation of 4-hydroxycoumarine with aldehyde and aromatic amines using graphene oxide as an efficient catalyst. *Scientific Reports*, *11*(1), 19891. https://doi.org/10.1038/s41598-021-99360-3

34 Bui, T. H., Le, T. T., Vu, T. T., Hoang, X. T., Luu, V. C., Vu, D. H., & Tran, K. V. (2012). Design, synthesis and in vitro cytotoxic activity evaluation of new Mannich bases. *Bulletin of the Korean Chemical Society*, *33*(5), 1586–1592. http://dx.doi.org/10.5012/bkcs.2012.33.5.1586

35 Arend, M., Westermann, B., & Risch, N. (1998). Modern variants of the Mannich reaction. *Angewandte Chemie International Edition*, *37*(8), 1044–1070. https://doi.org/10.1002/(SICI)1521-3773

36 Kobayashi, S., & Ueno, M. (2004). Comprehensive asymmetric catalysis. In Comprehensive Asymmetric Catalysis (p. 143). Springer.

37 Blicke, F. F. (1942). The Mannich Reaction; Organic Reactions; John Wiley & Sons, Hoboken, New Jersey, United States, 303–341.

38 Ramón, D. J., & Yus, M. (2005). Asymmetric multicomponent reactions (AMCRs): the new frontier. *Angewandte Chemie International Edition*, *44*(11), 1602–1634. https://doi.org/10.1002/anie.200460548

39 Jayabalakrishnan, C., & Natarajan, K. (2001). Synthesis, characterization, and biological activities of ruthenium (II) carbonyl complexes containing bifunctional tridentate Schiff bases. *Synthesis and Reactivity in Inorganic and Metal-Organic Chemistry*, *31*(6), 983–995. https://doi.org/10.1081/SIM-100105255

40 Jeewoth, T., Li Kam Wah, H., Bhowon, M. G., Ghoorohoo, D., & Babooram, K. (2000). Synthesis and antibacterial/catalytic properties of Schiff bases and Schiff base metal complexes derived from 2,3-diaminopyridine. *Sythesis and Reactivity in Inorganic and Matel-Organic Chemistry*, *30*(6), 1023–1038. https://doi.org/10.1080/00945710009351817

41 List, B. (2000). The direct catalytic asymmetric three-component Mannich reaction. *Journal of the American Chemical Society*, *122*(38), 9336–9337. https://doi.org/10.1021/ja001923x

42 Eftekhari-Sis, B., Abdollahifar, A., Hashemi, M. M., & Zirak, M. (2006). Stereoselective Synthesis of β-Amino Ketones via Direct Mannich-Type Reactions, Catalyzed with ZrOCl$_2$·8H$_2$O under Solvent-Free Conditions. *European Journal of Organic Chemistry, 2006(22)*, 5152–5157. https://doi.org/10.1002/ejoc.200600493

43 Mitsumori, S., Zhang, H., Ha-Yeon Cheong, P., Houk, K. N., Tanaka, F., & Barbas, C. F. (2006). Direct Asymmetric anti-Mannich-Type Reactions Catalyzed by a Designed Amino Acid. *Journal of the American Chemical Society*, *128*(4), 1040–1041. https://doi.org/10.1021/ja056984f

44 Al-Jeboori, M. J., Al-Jebouri, F. A., & Al-Azzawi, M. A. (2011). Metal complexes of a new class of polydentate Mannich bases: Synthesis and spectroscopic characterisation. *Inorganica Chimica Acta*, *379*(1), 163–170. https://doi.org/10.1016/j.ica.2011.10.013

45 Fernández-Fariña S., Velo-Heleno I., Martínez-Calvo M., González-Noya A. M., & Pedrido R. (2022). Design, synthesis and structural characterization of a novel asymmetric hydrazone-thiosemicarbazone ligand with the aim of obtaining ınteresting metallo-supramolecular architectures. *Chemistry Proceedings*, *8*, 16. https://doi.org/10.3390/ecsoc-25-11738

46 Kirtani D. U., Ghatpande N. S., Suryavanshi K. R., Kulkarni P. P., & Kumbhar A. A. (2021). Fluorescent copper(II) complexes of asymmetric bis(thiosemicarbazone)s: Electrochemistry, cellular uptake and antiproliferative activity. *Chemistry Select*, *6*, 6063–6070. https://doi.org/10.1002/slct.202101663

47 Özdemir N., Şahin M., Bal-Demirci T., & Ülküseven B. (2011). The asymmetric ONNO complexes of dioxouranium(VI) with N1, N4-diarylidene-S-propyl-thiosemicarbazones derived from 3,5-dichlorosalicylaldehyde: Synthesis, spectroscopic and structural studies. *Polyhedron*, *30*, 515–521. https://doi.org/10.1016/j.poly.2010.11.030

48 Varadinova T., Kovala-Demertzi D., Rupelieva M., Demertzis M., & Genova P. (2001). Antiviral activity of platinum (II) and palladium (II) complexes of pyridine-2-carbaldehyde thiosemicarbazone. *Acta Virologica*, *45*, 87–94.

49 Pandeya S. N., & Dimmock J. R. (1993). Recent evaluations of thiosemicarbazones and semicarbazones and related compounds for antineoplastic and anticonvulsant activities, *Die Pharmazie*, 1993, *48*, 659–666.

50 Bauer, A. W., Kirby, W. M. M., Sherris, J. C., & Turck, M. (1966). Antibiotic susceptibility testing by a standardized single disk method. *American journal of clinical pathology*, *45*, 493–496. https://doi.org/10.1093/ajcp/45.4_ts.493

51 Ferrari, M. B., Capacchi, S., Pelosi, G., Reffo, G., Tarasconi, P., Albertini, R., ... & Lunghi, P. (1999). Synthesis, structural characterization and biological activity of helicin thiosemicarbazone monohydrate and a copper (II) complex of salicylaldehyde thiosemicarbazone. *Inorganica Chimica Acta*, *286*(2), 134–141. https://doi.org/10.1016/S0020-1693(98)00383-1

52 Abd El-Wahab, Z. H., Mashaly, M. M., Salman, A. A., El-Shetary, B. A., & Faheim, A. A. (2004). Co (II), Ce (III) and UO$_2$ (VI) bis-salicylatothiosemicarbazide complexes: binary and ternary complexes, thermal studies and antimicrobial activity. *Spectrochimica Acta Part A: Molecular and Biomolecular Spectroscopy*, *60*(12), 2861–2873. https://doi.org/10.1016/j.saa.2004.01.021

53 Wallingford, V. H., & Krueger, P. A. (1939). 5-iodoanthranilic acid. *Organic Synthesis*, *19*, 52.

54 Bauer, A. W., Kirby, W. M. M., Sherris, J. C., & Turck, M. (1966). Antibiotic susceptibility testing by a standardized single disk method. *American journal of clinical pathology*, *45*(4_ts), 493–496. https://doi.org/10.1093/ajcp/45.4_ts.493

55 Trott, O., & Olson, A. J. (2010). AutoDock Vina: improving the speed and accuracy of docking with a new scoring function, efficient optimization, and multithreading. *Journal of computational chemistry*, *31*(2), 455–461. https://doi.org/10.1002/jcc.21334

56 Al-Dobony, B. S., & Al-Assafe, A. Y. (2019). Synthesis, characterization and antimicrobial studies of some metal complexes with mixed ligands derived from Mannich bases and diamine ligands. *Journal of Physics: Conference Series, 1294*(5), 052068. https://doi.org/10.1088/1742-6596/1294/5/052068

57 Balakrishnan, A. & Sankar, A. (2016) Studies on the synthesis and characterization of the transition metal complexes of novel mannich base. *International Journal of Pharmaceutical, Chemical & Biological Sciences*, *6*, 150.

58 Raman, N., Malaramani, R.V., & Thangaraja, C. (2004). Synthesis and physico-chemical characterization of a new Mannich base, N(morpholinobenzyl)benzamide and its Cu(Il), Co(ll), Ni(II) and Zn(Il) complexes. *Indian Journal of Chemistry, 43A*, 2357–2360.

59 Janowska, S., Andrzejczuk, S., Gawryś, P. & Wujec, M. (2023). Synthesis and Antimicrobial Activity of New Mannich Bases with Piperazine Moiety. *Molecules*, *28*, 562. https://doi.org/10.3390/molecules28145562

60 Tamilvendan, D., Rajeswari, S., Ilavenil, S., Chakkaravarthy, K., & Venkatesa Prabhu, G. (2012). Syntheses, spectral, crystallographic, antimicrobial, and antioxidant studies of few Mannich bases. *Medicinal Chemistry Research*, *21*, 4129–4138. https://doi.org/10.1007/s00044-011-9944-2

61 Selvaraj, S.D., Krishnaveni, R., & Tamilvendan, D. (2020). Synthesis, characterization, anticorrosion and antimicrobial studies of novel 1-[anilino (phenyl)methyl]pyrimidine-2,4,6-trione derived from Mannich reaction and its metal complexes. *Materials Today: Proceedings*, *33*, 4271–4279. https://doi.org/10.1016/j.matpr.2020.07.400

62 Singh, V., Praveen, V., Tripathi, D., Haque, S., Somvanshi, P., Katti, S. B., & Tripathi, C. K. M. (2015). Isolation, characterization and antifungal docking studies of wortmannin isolated from Penicillium radicum. *Scientific reports*, *5*(1), 11948. https://doi.org/10.1038/srep11948

63 Gullapelli, K., Brahmeshwari, G., Ravichander, M., & Kusuma, U. (2017). Synthesis, antibacterial and molecular docking studies of new benzimidazole derivatives. *Egyptian journal of basic and applied sciences*, *4*(4), 303–309. https://doi.org/10.1016/j.ejbas.2017.09.002

64 Ali, D., Alarifi, S., Chidambaram, S. K., Radhakrishnan, S. K., & Akbar, I. (2020). Antimicrobial activity of novel 5-benzylidene-3-(3-phenylallylideneamino) imidazolidine-2,4-dione derivatives causing clinical pathogens: Synthesis and molecular docking studies. *Journal of Infection and Public Health*, *13*(12), 1951–1960. https://doi.org/10.1016/j.jiph.2020.09.017

65 Taha, M., Ismail, N. H., Khan, A., Shah, S. A. A., Anwar, A., Halim, S. A., ... & Khan, K. M. (2015). Synthesis of novel derivatives of oxindole, their urease inhibition and molecular docking studies. *Bioorganic & Medicinal Chemistry Letters*, *25*(16), 3285–3289. https://doi.org/10.1016/j.bmcl.2015.05.069

CHEMICAL TECHNOLOGY

Ayazhan M. Turarbek[1] [ID], Farida Zh. Abilkanova[2] [ID], Aitolkyn S. Uali[1*] [ID]

[1]L.N. Gumilyov Eurasian National University, Astana, Kazakhstan;
[2]Karaganda Industrial University, Temirtau, Kazakhstan
(*Corresponding author's e-mail: uali_as@enu.kz)

Development of Novel Wheat Waste-Derived Biochar and Its Potential in Pharmaceutical Wastewater Treatment

The rising concentration of pharmaceuticals in wastewater presents significant environmental and health challenges. This study aims to develop an iron (III)-activated carbon-enriched material derived from local agricultural plant waste to effectively remove pharmaceutical contaminants. The research investigates the material's composition, structure, morphology, and adsorption capacity of the material, focusing on wheat waste-derived biochar. The synthesis process includes an initial carbonization, chemical modification with FeCl3 using the wet impregnation method, and a second carbonization and washing step. The resulting carbonaceous material was characterized using the CHNS elemental analyzer, FTIR, XRD and SEM-EDX spectroscopic techniques. The results indicate the formation of a carbonaceous material with a carbon content of 77.09 %, enriched with a highly crystalline graphite phase and a porous structure containing iron (II, III) oxides. Notably, this sorbent efficiently reduced the ibuprofen concentration, with a sorption capacity of 433 mg•g^{-1}. Among the pseudo-first-order (PFO), pseudo-second-order (PSO), intraparticle diffusion and Elovich models used to describe the adsorption kinetics, the PSO model (types 1-2) fits successfully, indicating chemisorption-controlled kinetics. This study highlights the potential for converting agricultural waste into a carbonaceous material with improved structure and morphology, and demonstrates its high efficacy in purifying water from pharmaceutical contaminants.

Keywords: waste wheat, carbonization, biochar, activated carbons, iron oxides, adsorption, ibuprofen, kinetic models, pseudo-second-order kinetic model.

Introduction

Carbonaceous materials obtained from agricultural residues have great potential for development of sustainable technologies. Recent studies have demonstrated that biochar is not only applicable but also under development as an effective sorbent [1–4], electrode-active material [5–8], and catalyst [9–11]. These studies reveal the potential of waste streams to contribute to circular bioeconomy strategies that transform resource use, an issue that will highlight the evolving environment of sustainable practices [12].

Currently, there is an increasing in demand for active pharmaceutical compounds, and therefore, the pharmaceutical industry continues to increase the production of drugs. As a result, discharges of industrial effluents are regularly increasing, raising serious concerns about their harmful effects on human health and the aquatic environment. Ibuprofen (IBU), 2[4-(2-methylpropyl)phenyl]propanoic acid, is a globally recognised anti-inflammatory drug, widely used in medical practice as an antipyretic, analgesic and anti-inflammatory agent [13–15]. In the US, UK, and Poland, ibuprofen consumption is approximately 300, 162 and 58 tons per year [16]. It is metabolised in the body and the environment to form ibuprofen derivatives. It has been found that when ibuprofen is released into the environment it is initially degraded to form hydrox-

ylated ibuprofen and ibuprofen carboxylic acid; benzoquinone, quinone and catechol-like compounds are also formed during the degradation of ibuprofen [17]. Chorpa and Kumar have proposed a way for the degradation of ibuprofen, indicating various intermediate products formed during degradation (Fig. 1) [18].
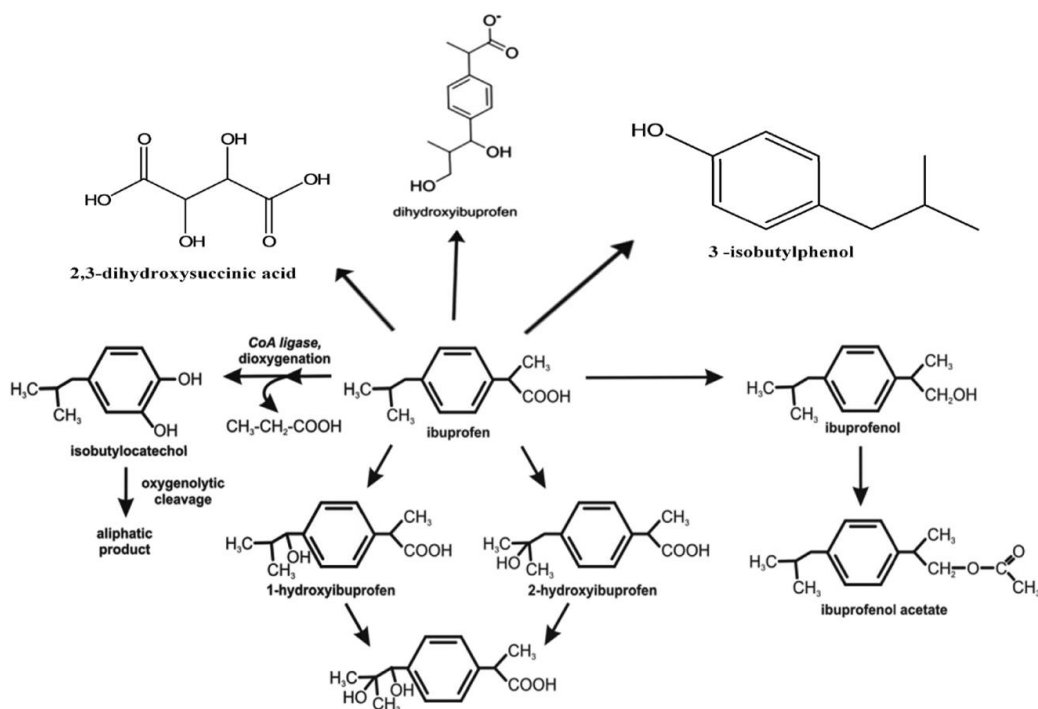
Figure 1. A way of ibuprofen degradation with various intermediate products.
Reprinted from Ref. [18] with permission under the license CC BY-NC-ND 4.0 International

Therefore, pharmaceutical contaminants need to be removed from the aquatic environment. As reported, electrocoagulation [19], oxidation [20, 21], membrane filtration [22], and adsorption [21] are recommended. Although these methods are effective in achieving high percentages of IBU removal, they also have drawbacks, including energy consumption and cost. Herein, adsorption is the most promising water treatment method in terms of effectiveness and environmental sustainability. Moreover, utilising waste biomass further reduces the price of this purification process.

According to the Food and Agriculture Organization of the United Nations [23], Kazakhstan is a leading wheat exporter, producing 16.4 million tonnes of wheat in 2022. This extensive production generates substantial biowaste (straw, husk, *etc.*). However, the literature review revealed limited studies utilising waste wheat in polluted water treatment; no data describing local biochar produced from wheat waste biomass. A critical aspect of the relevance and practical significance of this study is the proposal of a carbon sorbent from domestic agricultural waste to purify water bodies from ibuprofen. This study aims to produce biochar derived from local biowaste and test its adsorption capacity towards ibuprofen in an aqueous solution. It is expected that biochar derived from wheat waste will have an enhanced adsorption capacity for ibuprofen compared to other materials.

Experimental

2.1 Chemicals and Materials. All chemicals (1 % $FeCl_3$, 0.1 M NaOH solution) were analytical grade. DI water was used as the solvent. Ibuprofen sodium salt (Sigma Aldrich) was used to prepare its working solution.

2.2 Preparation of Biochar. Wheat wastes were used as an initial substance to prepare biochar using a three-stage treatment consisting of the first carbonisation (temperature of 600 °C, heating rate of 20 °C/min, 1 h under the Ar atmosphere), chemical modification (agent of 1 % $FeCl_3$ solution, solid-to-liquid ratio of 1/10 in wt.%) and the second carbonisation (under the same conditions as in the first stage). The chemical modification stage was conducted by immersing the intermediate into the agent's solution for 24 h at room temperature (21 °C±0.5 °C). After the second carbonization, the product was washed with hot water

(90 °C±3 °C) several times until a neutral pH value and dried at a temperature of 115 °C till its weight was constant. The final product — biochar — was then used in materials characterization and sorption tests as a sorbent.

2.3 Determination of the Ash Content. The biochar samples were oven-dried at 105 °C and then heated in a covered crucible in a muffle furnace at 750 °C for 6 h. The mass of material remaining after incineration refers to ash [24]. The ash test was conducted in three parallels to evaluate the standard deviation (SD).

2.4 Materials Characterization. The CHNS test (carbon (C), hydrogen (H), nitrogen (N) and S (sulfur)) was conducted using the Unicube organic elemental analyser. The % oxygen is obtained by recording the difference between 100 and the CHNS+ash content (in %) [24]:

$$O_{subs} = 100 - (C + H + N + S + A),$$

where C, H, N, S and A are the contents (in %) of carbon, hydrogen, nitrogen, sulfur and ash, respectively.

The BET analysis (low-temperature nitrogen adsorption) on the BSD-66OS A3 apparatus evaluated the biochar's porous structure and specific surface area. The samples were prepared at 200 °C and maintained at a residual pressure of at least 0.001 bar. Nitrogen adsorption and desorption isotherms were recorded at 77 K, utilising liquid nitrogen in the relative pressure range from 0.005 to 0.991 bar. Standard analysis of the results was performed using the Barrett-Joyner-Halenda (BJH) method, which employs a conventional cylindrical pore model. This analysis included the calculation of several parameters: the total surface area (ΣS), the micropore surface area (μS) using the Brunauer-Emmett-Teller (BET) method, the total pore volume (ΣV), the micropore volume (μV), and the average pore diameter (D_{av}). These calculations considered both micro- and mesopores and utilised the DFT approach.

The FTIR spectroscopic measurements were carried out using an Alpha II FTIR spectrometer (Bruker) operating at a frequency range between 4000 and 400 cm^{-1} at room temperature. The samples were prepared by mixing KBr and the BC sample (ratio 99.5 %:0.5 %) by weight and pressed into a disc before analysis, which consisted of 32 scans with a resolution of 1 cm^{-1}.

The SEM-EDX analysis (n=3) used the Phenom ProX Scanning Electron Microscope (Thermo Scientific) (high voltage of 15kV) with the BSD detector.

X-ray diffraction patterns were recorded using a D8 Advance Eco diffractometer (Bruker) in Bragg-Brentano geometry in the angular range of 14...100° (2θ) (step 0.05) at room temperature. An X-ray source was a copper tube with radiation (λ = 1.54060 Å).

2.5 Spectrophotometric Analysis of Ibuprofen. For the spectrophotometric determination of an aqueous solution of IBU, its powder was dissolved in a previously prepared 0.1 M NaOH solution and shaken for about 10 min. After filtration, the aqueous solution of ibuprofen was subjected to spectrophotometric analysis. Spectrophotometric measurements were done according to [25] at a wavelength of 273 nm on a spectrophotometer Specord 250. A calibration curve is given in Figure 2.
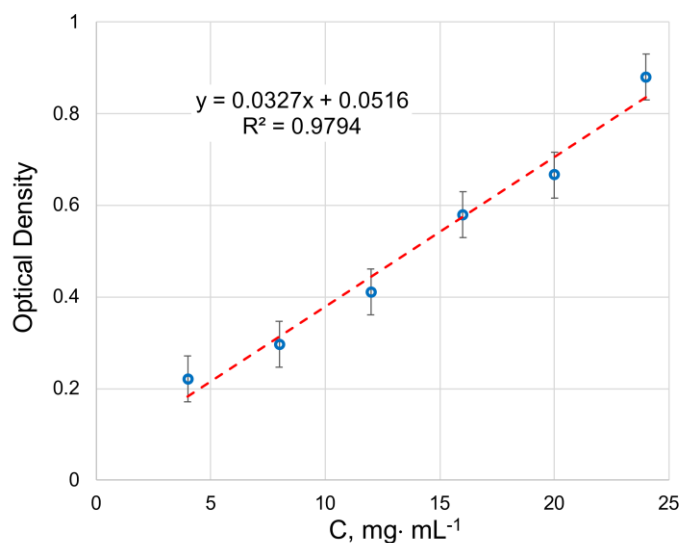

$$y = 0.0327x + 0.0516$$
$$R^2 = 0.9794$$

Figure 2. Optical density – concentration dependence for spectrophotometric analysis of IBU

2.6 Ibuprofen Adsorption Tests. Adsorption tests were carried out at static conditions according to [26]. In adsorption tests, a biochar sample (10 mg) was immersed in an IBU solution (20 ml). All adsorption tests ($n = 3$) were conducted at a controlled temperature (21 °C±0.5 °C). The total adsorption time was up to 60 min. The liquid phase was then separated by filtration. To determine the residual concentration of IBU in the liquid phase, the optical density was measured at 340 nm wavelength. The adsorption value (a) was calculated as follows:

$$\alpha = \frac{\nu}{m} = \frac{\nu\left(C_0 - C\right)}{m},$$

where ν is a solution volume on which adsorption is carried out, L; C_0 is the initial concentration of I (mol·L^{-1}); C is the residual concentration of IB (mol·L^{-1}), and m is the weight of sorbent (g).

Results and Discussion

3.1 Material Characterisation of Biochar. Table 1 demonstrates the CHNS results and waste wheat-derived biochar's ash and oxygen content.

T a b l e 1

Elemental composition of biochar, ashness and the H/C, O/C ratios

Initial material	C, %	H, %	N, %	S, %	A, %	O$_{subs}$, %	H/C	O/C	Ref.
Rapeseed wastes	72.60	4.90	6.70	0.50	–	15.30	0.07	0.21	[27]
Palm kernel shell	47.28	5.32	0	0	–	47.40	0.11	1	[28]
Rice husk	41.11	4.87	0.80	0.04	–	53.17	0.12	1.29	[29]
Coconut fibers	44.89	5.19	0.86	0.03	–	48.64	0.12	1.08	[29]
Durian peel	39.30	5.90	1.00	0.06	4.84	53.74	0.15	1.37	[30]
Waste wheat	77.09±0.22	1.91±0.02	4.15±0.04	0	12.12±0.20	4.71±0.38	0.02	0.06	Present study

As shown in Table 1, wheat-derived biochar has the highest carbon content of 77.09 % compared to rice husks, with a carbon content of 41.11 % [29]. Another noticeable difference is the O content, which is 53.74 % for durian-derived biochar, which is ≈13 times higher than wheat-derived biochar and 3-4 times higher for rapeseed residue. The lower the O/C and H/C atomic ratios, the higher the degree of aromaticity and stability of the carbonised material [31]. The relatively low value of the H/C ratio, 0.02, might be attributed to the elimination of dehydration and dehydrogenation reactions and the cleavage and cracking of weak hydrogen bonds during conversion within the biochar [32]. The O/C ratio lowers if a high degree of carbonisation occurs by removing oxygen through dehydration and decarboxylation reactions [33]. These data have revealed that biochar might demonstrate long-term chemical stability.

Regarding the porosity of biochar, the porous structure could be derived from the structure present in the raw biomass or was formed during the devolatilization process of gasification. In [34], wheat bran biochar has a lower specific surface area (SSA) of 25 m^2·g^{-1}. In comparison, Vaghela *et al.* [35] reported that wheat straw biochar produced at 600 °C has a SSA of approximately 70.12 m^2·g^{-1}. Zhu *et al.* [36] highlighted the contribution of iron oxide particles to the biochar pores. According to the BET analysis, the SSA of biochar was 227.84 m^2·g^{-1} with the pore volume distribution as follows: micropores (0.35–2 nm), mesopores (2–10 nm and 10–50 nm) and macropores (50–200 nm) are 70.48 %, 22.45 %, 3.42 % and 0.65 %, respectively. The increased SSA is most likely due to the contribution of iron oxides.

The presence of iron-containing compounds in the production of activated carbon reduces the temperature required for cellulose hydrolysis, resulting in a notable depolymerisation reaction that produces a significant amount of low-molecular-weight hydrocarbons. Iron chlorides disrupt the glycosidic bonds in cellulose at pyrolysis temperatures between 200 °C and 300 °C, simultaneously releasing water molecules from the hydrated salt and generating glucose monosaccharides. Within this temperature range, the hydrated iron chloride decomposes into amorphous FeOOH through specific chemical reactions [36]:

$$FeCl_3 + 2H_2O \leftrightarrow FeOCl \cdot H_2O + 2HCl \qquad (1)$$

$$FeOCl \cdot H_2O \leftrightarrow FeOOH + HCl \qquad (2)$$

The second stage, occurs at pyrolysis temperatures above 330 °C. As the activation temperature increases, glucose molecules successively undergo ring opening, dehydration, and cyclisation into 5-hydroxymethylfurfural, which, after decarbonylation, is converted to furfural [37]. With increasing temperature, FeOOH first decomposes into Fe_2O_3, then the carbon surface is reduced, and Fe_3O_4 is formed via the following chemical reactions [37]:

$$2FeOOH \leftrightarrow Fe_2O_3 + H_2O \tag{3}$$

$$3Fe_2O_3 + C \leftrightarrow 2Fe_3O_4 + CO \tag{4}$$
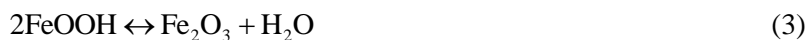
Iron oxides are crucial in catalysing microporosity formation within the carbon matrix. Overall, porous activated carbons are formed in the presence of iron species with highly stable Fe bound to their surface [38].

The EDS mapping of biochar's surface demonstrated its elemental composition and distribution (Fig. 3).

Element	Wt.% ±SD, %	Element	Wt.%+SD, %	Element	Wt.%+SD, %
C	67.68±6.81	Si	0.10±0.01	Fe	4.57±0.76
N	14.28±1.68	P	0.33±0.06	K	0.30±0.29
O	8.81±0.95	S	0.77±0.12	Σ	100
Na	0.50±0.06	Cl	2.67±0.25		
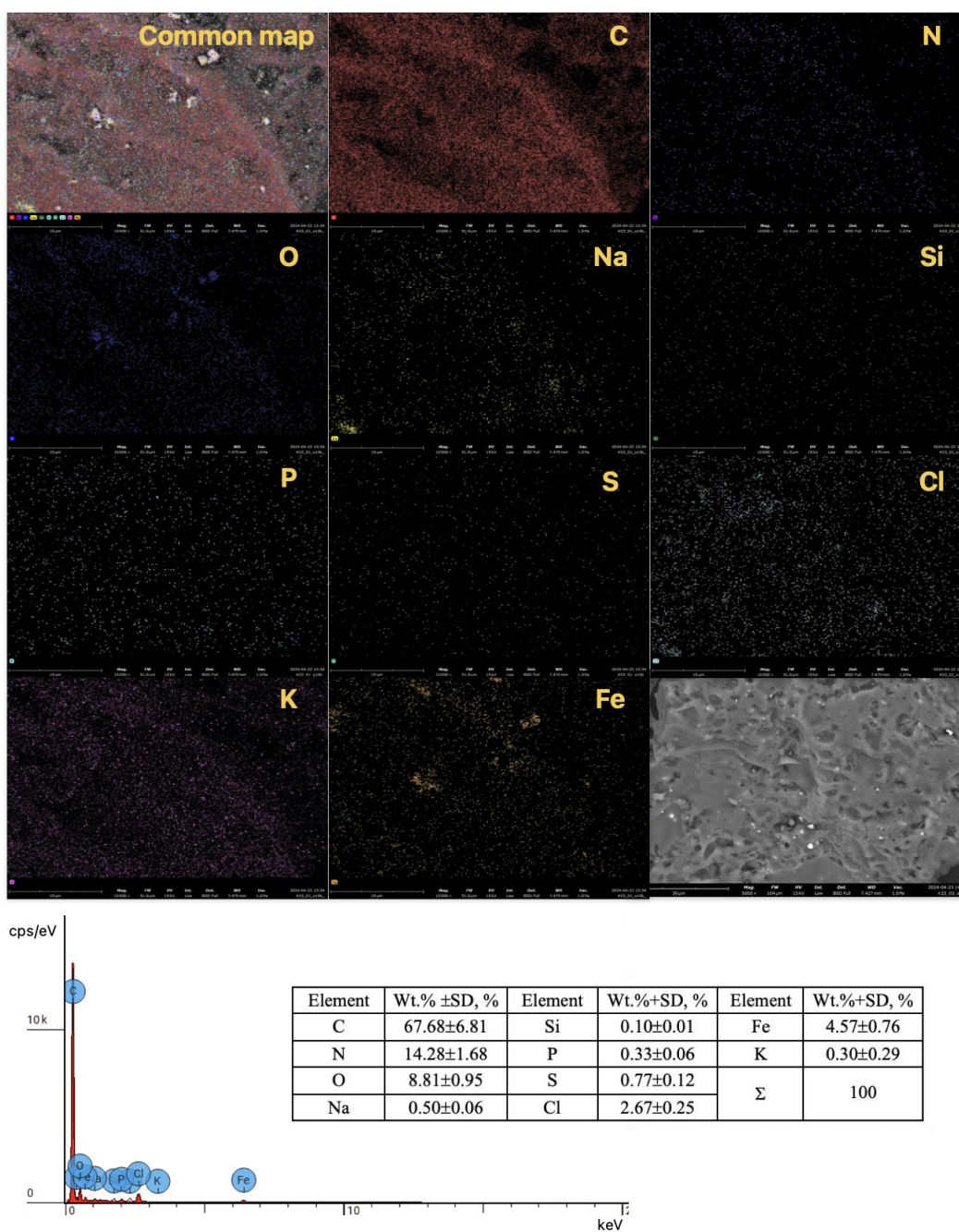
Figure 3. EDS mapping pictures and elemental content of biochar's surface

The EDS maps indicated that biochar produced from waste wheat is rich in elements such as carbon, nitrogen, and oxygen, which are relatively evenly distributed; however, some areas show higher or lower concentrations of these elements. In contrast, iron is concentrated in specific areas, particularly within pores, as suggested.

The XRD study demonstrates that biochar has a semicrystalline structure (Fig. 4). This is indicated by a broad signal between 20° and 30°, typically characteristic of the stacking structure of aromatic layers associated with highly crystalline graphite (graphite 002) [39, 40].
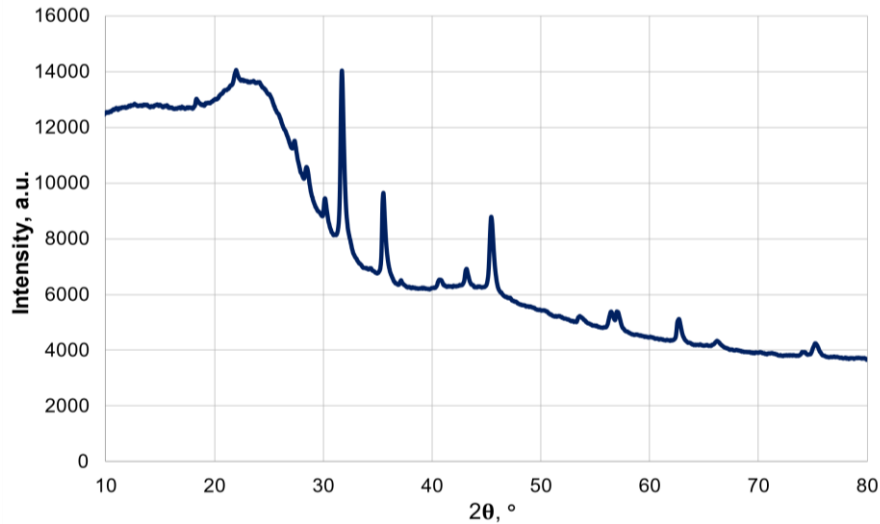
Figure 4. XRD spectrum of biochar (final product)

The sharp diffraction peaks at 32°, 35°, and 45° could be attributed to the plane interlayer reflections $Fe_2O_3 \cdot FeO$ [41]. According to the database of the Joint Committee on Powder Diffraction Standards database (JCPDS #75-0449), Fe_3O_4 appeared at 30.5°, 35.7° and 43°, which are identical to crystal plane index (220), (331) and (400) [42]. In [43], characteristic bands of hematite crystals are located at 2θ of 32.0°. Based on this, it could be suggested that iron (II, III) oxide particles were successfully injected into the carbon matrix during the modification-carbonization process.

The FTIR spectroscopy experiment was performed to identify the functional groups of waste wheat-derived biochar (Fig. 5).
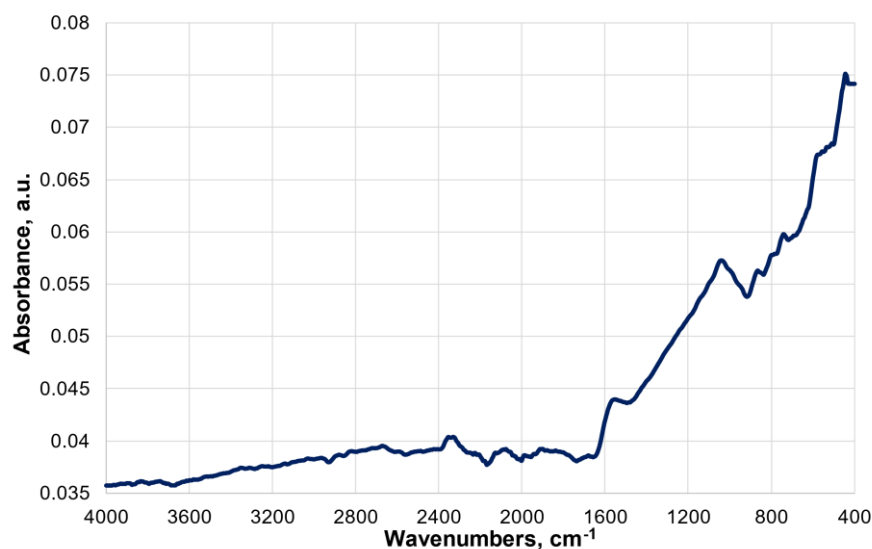
Figure 5. FTIR spectrum of biochar (final product)

Biochar's functional groups matched those of the references [44–46]. The spectral analysis shows that the three-stage treatment effectively removes or alters the functional groups present in the carbon material, resulting in a more graphitic carbon structure with fewer detectable functional groups than the FTIR spectrum of the intermediate biochar product after the first carbonisation stage, as illustrated in Figure S1 and Table S1 (see the supplemental file). For example, a peak at 1536 cm^{-1} may be attributed to the C=C stretching in the aryl double bond [47]; another peak at 1015 cm^{-1} likely corresponds to the C–OC or C–OH bonds [48]. Additionally, a peak at 580 cm^{-1} might be assigned to Fe–O vibrations [49, 50].

3.2 Ibuprofen Adsorption on Waste Wheat-Derived Biochar. The experimental data (Fig. 6) show that the adsorption process reached equilibrium after 10 min, and then the adsorption value remained stable over time. The readily accessible active sites cause the initial rapid adsorption, while the plateau indicates equilibrium with IBU molecules entering and exiting the active sites at the same rate. The same behaviour has previously been detected for ibuprofen adsorption using commercial activated carbons and polymeric resin [51], cellulosic biomass [52], and sonicated activated carbons [53].
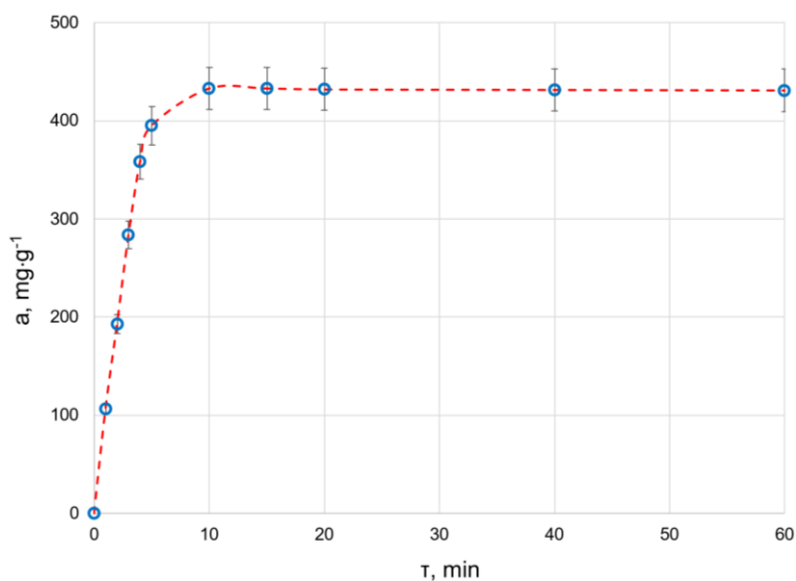
Figure 6. Adsorption kinetic curve of ibuprofen onto biochar

Comparing the adsorption capacity of the current sorbent with the references shows that, in some cases, the ibuprofen adsorption capacity is higher for the biochar of interest (Table 2).

Table 2

Comparison of waste wheat-derived biochar with others

Initial biomass	Type of activation/modification	SSA, m^2·g^{-1}	Ibuprofen uptake capacity, mg·g^{-1}	Kinetic model	Ref.
Sugarcane bagasse	Chemical	557.00 (for raw biochar)	13.51	PSO	[54]
	Steam		11.90	PSO	
Bovine bones	Chemical (ZnAl)	170.00 cm^2·g^{-1} (external)	1032.81	n.r.*	[55]
Chrysanthemum wastes	Magnetic	194.00	167.00	PSO	[56]
	Non-magnetic	220.00	140.00	PSO	
Rice husk	Chemical (H$_3$PO$_4$)	n.r.*	239.80	PSO	[57]
Babassu coconut shell	Ultrasound	732.00	134.00	PSO	[58]
Recycled textile materials	Steam	710.00	53.90	Elovich	[59]
Sunflower seed husk	Chemical (H$_3$PO$_4$)	378.80	251.10	Elovich	[60]
Cork powder	Both chemical/physical	1060.00	393.40	PSO	[61]
Wheat husk	Chemical (FeCl$_3$)	227.84	433.00	PSO	Present study
Note: * — not reported.					

It is known that higher SSA generally correlates with better adsorption capacity, but other factors such as pore size distribution and surface functional groups also play a crucial role [62]. These differences in the surface and porosity of resulting biochars may also be due to the experimental preparation conditions, including pyrolysis temperature and time, or the additional activation steps, such as using gas or steam. It is worth noting that, according to the European Biochar Certificate Standard (EBC), biochars should have an SSA larger than 150 $m^2 \cdot g^{-1}$ [56, 63].

The adsorption kinetics describes the solute uptake rate, and its knowledge is essential for a better understanding of the reaction mechanism and designing appropriate adsorption technologies. It is known that the kinetic model is fitted best if there are three conditions to be satisfied: 1) a reasonable match of experimental and calculated values of adsorption uptake, 2) the regression value (R^2) should be close to 1, 3) the values of chi-square test (χ^2) and the sum of the square of the error (SSE) should be minimum. Pseudo-first order (PFO) and pseudo-second-order (PSO) kinetic equations [64], as well as the intraparticle diffusion model and Elovich model, were tested to fit the experimental data obtained from the batch experiments (Table 3), where $k_1 \left[min^{-1} \right]$, $k_2 \left[g \cdot mg^{-1} \cdot min^{-1} \right]$ are the PFO and PSO rate constants, q_e [$mg \cdot g^{-1}$] and q_t [$mg \cdot g^{-1}$] are the adsorbate uptake at equilibrium and at time t, respectively, K_{Diff} [$mg \cdot g^{-1} \cdot min^{-1/2}$] is a measure of diffusion coefficient, C [$mg \cdot g^{-1}$] is intraparticle diffusion constant, α [$mg \cdot g^{-1} \cdot min^{-1}$] is the Elovich initial adsorption velocity, β [$g \cdot mg^{-1}$] is the Elovich constant, R^2 is the regression coefficient.

T a b l e 3

Kinetic models for the ibuprofen adsorption parameters onto biochar

PFO	k_1	q_e	R^2
$\ln\left(q_e - q_t\right) = \ln\left(q_e\right) - k_1\tau$	0.0711	67.26	0.4203
PSO, type 1	k_2	q_e	R^2
$\dfrac{\tau}{q_\tau} = \dfrac{1}{k_2 q_e^2} + \left(\dfrac{1}{q_e}\right)\tau$	0.0015	454.54	0.9975
PSO, type 2	k_2	q_e	R^2
$\dfrac{1}{q_\tau} = \left(\dfrac{1}{k_2 q_e^2}\right)\left(\dfrac{1}{\tau}\right) + \left(\dfrac{1}{q_e}\right)$	0.0073	588.23	0.9967
PSO, type 3	k_2	q_e	R^2
$\dfrac{\tau}{q_\tau} = k_2 q_e^2 - k_2 q_e q_t$	0.0005	564.06	0.6574
PSO, type 4	k_2	q_e	R^2
$q_\tau = q_e - \left(\dfrac{1}{k_2 q_e}\right)\dfrac{q_\tau}{\tau}$	0.0004	962.68	0.6574
Intraparticle diffusion	C	K_{Diff}	R^2
$q_\tau = K_{Diff}\tau^{1/2} + C$	225.38	36.76	0.4836
Elovich	α	β	R^2
$q_\tau = \dfrac{1}{\beta}\ln\left(\alpha\beta\tau + 1\right)$	286.71	0.0052	0.7344

Firstly, the PFO model calculates the kinetic parameters k_1 and q_e [65]. The k_1 value describes how quickly the adsorption equilibrium is reached in the studied system. However, since the adsorption rate is related to k_1 and α values; they must be considered together. For example, if the value of k_1 is low and the $q_e - q_t$ value is high, it indicates slow adsorption. Generally, the PFO model corresponds to a high initial adsorbate concentration, and adsorption is not controlled by adsorption at the active sites. Sometimes, the PFO model may reflect external/internal diffusion. Similar to the PFO-k_1 rate constant, the PSO-k_2 rate constant is also used to describe the rate of adsorption equilibrium [66]. This model accounts for some adsorp-

tion processes requiring more prolonged time to fill the adsorption sites [67]. The adsorption rate is assumed to be affected by the interaction of adsorption sites on the adsorbent surface with the adsorbent throughout the adsorption process. The intraparticle diffusion model describes a transport process where species move from the bulk solution to the solid phase (sorbent) [68]. It is more applicable for porous adsorbents. Although the Elovich model has been developed to describe interactions between a solid/gas interface, it has effectively defined processes that occur on a solid/liquid interface [69]. It is reported that the model considers that the actual solid surface is energetically heterogeneous and that the desorption process and interactions between adsorbed species do not significantly affect the adsorption kinetics.

In this study, the sorption kinetics may be described by a PSO model due to the values of regression coefficient (R^2) and closeness of experimental and theoretical adsorption capacity (q_e) (Table 3). According to Ghaedi *et al.* [70], the fit of the PSO model indicates that the process is controlled by chemisorption or ion exchange due to the porous surface of the carbonaceous materials. Also, the fitting of this model might be explained by the occurrence of multilayer adsorption and vertical packing of adsorbate in active sites. Another study [71] revealed that the fit of the experimental data to the PSO model indicates the adsorption of the pollutant by two active sites simultaneously. Also, the chemisorption might be the limiting stage of the kinetic processes when valence bonds between the sorbate and the adsorbent are shared or exchanged.

Various key processes are involved in the adsorption of ibuprofen onto biochar, including hydrogen bonding, chemical adsorption, pore filling, electrostatic interactions, and π-π stacking. Primarily, it's essential to consider the surface functional groups, such as carboxylic and hydroxylic, that facilitate hydrogen bonding and enhance adsorption. Additionally, the PSO kinetic model is likely indicative of chemisorption. Lastly, the pores present are adequately sized to accommodate ibuprofen. According to [64], the predicted size of the molecular structure of ibuprofen is 1.03 nm×0.52 nm×0.43 nm. Considering the pore volumes and sizes, alternative pore filling is also possible for ibuprofen held by biochar. Altogether, these interactions facilitate the effective capture of ibuprofen within the porous structure of biochar.

3.3 Spent Adsorbent Disposal. Proper disposal of used adsorbents is essential due to significant environmental concerns. The World Health Organization (WHO) has issued important guidelines titled "Guidelines for Safe Disposal of Unwanted Pharmaceuticals in and after Emergencies" [72], which emphasise that adsorbents infused with ibuprofen can be disposed of safely and responsibly by following established pharmaceutical disposal methods. This approach protects public health and helps safeguard the environment from potential contaminants. The adsorption of ibuprofen onto biochar is predominantly irreversible, emphasising its effectiveness as a long-term solution for treating water contaminants. Once ibuprofen is adsorbed, it remains securely bound to the sorbent surface, making it an ideal candidate for reliable pollution management. Incineration is a preferred disposal technique for spent adsorbents, ensuring the destruction of any residual pharmaceuticals. Since ibuprofen-loaded biochar boasts a high calorific value, it provides an eco-friendly alternative to coal and allows energy recovery through incineration or gasification for syngas production. Moreover, various other disposal methods, such as regeneration, have also been explored, further enhancing the viability of biochar in sustainable waste management.

Conclusions

The findings of this study indicate that local agricultural waste, such as wheat residue, can be effectively converted into biochar infused with a mixture of iron (II, III) oxides. This biochar has a unique composition, rich in carbon (77.09 %), with a specific surface area of 227.84 $m^2 g^{-1}$, predominantly characterised by micropores (70.48 %). Notably, the material has a high adsorption capacity for ibuprofen, reaching a sorption capacity of 433 mg·g^{-1}. Kinetic studies have shown that a pseudo-second-order model describes the adsorption process. Waste wheat presents a promising alternative for the development adsorbents to remove ibuprofen from aqueous solutions. This innovative approach tackles the challenge of agricultural waste disposal and provides a cost-effective and sustainable solution to improve water quality. The use of this method makes a significant contribution to environmental protection and effective water treatment strategies.

Supporting Information

The Supporting Information is available free at https://ejc.buketov.edu.kz/index.php/ejc/article/view/212/180

Author Information*

---

*The authors' names are presented in the following order: First Name, Middle Name and Last Name

Ayazhan Meirbekkyzy Turarbek — Student, L.N. Gumilyov Eurasian National University, K. Munaitpassov st., 13, 010000, Astana, Kazakhstan; e-mail: turarbekayazhan@gmail.com, https://orcid.org/0009-0009-6174-2837

Farida Zhumageldyevna Abilkanova — Master of Science, Karaganda Industrial University, Republic Avenue, 30, 101400, Temirtau, Kazakhstan; e-mail: f.abilkanova@tttu.edu.kz, https://orcid.org/0000-0002-6894-5276

Aitolkyn Sailaubekkyzy Uali (*corresponding author*) — Candidate of Chemical Sciences, Assoc. Professor, L.N. Gumilyov Eurasian National University, K. Munaitpassov st., 13, 010000, Astana, Kazakhstan; e-mail: uali_as@enu.kz, https://orcid.org/0000-0002-5851-6566

Author Contributions

The manuscript was written through contributions of all authors. All authors have given approval to the final version of the manuscript. CRediT: **Ayazhan Meirbekkyzy Turarbek** — investigation, formal analysis, writing-original draft, **Farida Zhumageldyevna Abilkanova** — formal analysis, visualisation, **Aitolkyn Sailaubekkyzy Uali** — supervision, data curation, methodology, review & editing.

Conflicts of Interest

The authors declare no conflict of interest.

Notes

A graphical abstract was created in BioRender. Uali, A. (2025) https://BioRender.com/k69i500

References

1   Amerkhanova, Sh.K., Shlyapov, R.M., Uali, A.S., & Tatibayeva, M.S. (2016). The concentration of cadmium (II), lead (II) and mercury (I, II) ions by adsorption on the wood-modified sorbent. *Bulletin of the Karaganda University. Chemistry series,* 4(84), 38–43. https://doi.org/10.31489/2016ch4/38-43

2   Amerkhanova, Sh.K., Uali, A.S., & Abilkanova, F.Zh. (2017). Evaluation of the thermal stability of sorbents based on modified active carbons. *Bulletin of the Karaganda University. Chemistry Series,* 2(86), 42–46. https://doi.org/10.31489/2017ch2/42-46

3   Amerkhanova, Sh., Uali, A., Shlyapov, R., & Yerkin, K. (2022). Evaluation of adsorption properties of carbon material obtained from a pinecone in relation to nitrogen. *Bulletin of the L.N. Gumilyov Eurasian National University. Chemistry. Geography. Ecology Series, 139*(2), 7–17. https://doi.org/10.32523/2616-6771-2022-139-2-7-17

4   Vinayagam, V., Murugan, S., Kumaresan, R., Narayanan, M., Sillanpää, M., Viet N Vo, D., Kushwaha, O. S., Jenis, P., Potdar, P., & Gadiya, S. (2022). Sustainable adsorbents for the removal of pharmaceuticals from wastewater: A review. *Chemosphere, 300*, 134597. https://doi.org/10.1016/j.chemosphere.2022.134597

5   Amerkhanova, Sh., Shlyapov, R., Uali, A., & Belgibaeva, D. (2022). Prospects of application of iron-containing carbon-paste electrode in electrochemical analysis. *Materials Today Proceedings, 49*, 2532–2536. https://doi.org/10.1016/j.matpr.2021.05.437

6   Kumar, Y.A., Rai, R.K., Akbar, M.A., Verma, V., Singh, S.K., & Srivastava, S.K. (2024). The landscape of energy storage: Insights into carbon electrode materials and future directions. *Journal of Energy Storage, 86*, 111119. https://doi.org/10.1016/j.est.2024.111119

7   Rahman, M.Z., Edvinsson, T., & Kwong, P. (2020). Biochar for electrochemical applications. *Current Opinion in Green and Sustainable Chemistry, 23*, 25–30. https://doi.org/10.1016/j.cogsc.2020.04.007

8   Rawat, S., Wang, C.-T., Lay, C.-H., Hotha, S., & Bhaskar, T. (2023). Sustainable biochar for advanced electrochemical/energy storage applications. *Journal of Energy Storage, 63*, 107115. https://doi.org/10.1016/j.est.2023.107115

9   Lei, X., Zhang, X., Zheng, Y., Xiang, Y., Tan, P., Luo, Z., Huang, H., Pan, B., Zhu, Y., Hu, C., & Zheng, L. (2023). High-entropy single-atom activated carbon catalysts for sustainable oxygen electrocatalysis. *Nature Sustainability, 6*(7), 816–826. https://doi.org/10.1038/s41893-023-01101-z

10   Qi, G., Wang, Q., Xiao, R., Zhang, H., & Zhou, Z. (2023). Microwave biochar produced with activated carbon catalyst: Characterization and adsorption of heavy metals. *Environmental Research, 216*, 114732. https://doi.org/10.1016/j.envres.2022.114732

11   Shan, R., Han, J., Gu, J., Yuan, H., Luo, B., & Chen, Y. (2020). A review of recent developments in catalytic applications of biochar-based materials. *Resources, Conservation and Recycling, 162*, 105036. https://doi.org/10.1016/j.resconrec.2020.105036

12 Poonia, K., Pradhan, D., Kulkarni, P.S., Saini, R., & Kothiyal, N.C. (2024). Sustainability, performance, and production perspectives of waste-derived functional carbon nanomaterials towards a sustainable environment: A review. *Chemosphere, 352*, 141419. https://doi.org/10.1016/j.chemosphere.2024.141419

13 Jan-Roblero, J., & Cruz-Maya, J.A. (2023). Ibuprofen: Toxicology and Biodegradation of an Emerging Contaminant. *Molecules, 28*(5), 2097. https://doi.org/10.3390/molecules28052097

14 Monteiro, C., Silvestre, S., Duarte, A.P., & Alves, G. (2022). Safety of Non-Steroidal Anti-Inflammatory Drugs in the Elderly: An Analysis of Published Literature and Reports Sent to the Portuguese Pharmacovigilance System. *International Journal of Environmental Research and Public Health, 19*(6), 3541. https://doi.org/10.3390/ijerph19063541

15 Parolini, M., Binelli, A., & Provini, A. (2011). Chronic effects induced by ibuprofen on the freshwater bivalve Dreissena polymorpha. *Ecotoxicology and Environmental Safety, 74*(6), 1586–1594. https://doi.org/10.1016/j.ecoenv.2011.04.025.

16 Marchlewicz, A., Guzik, U., & Wojcieszyńska, D. (2015). Over-the-Counter Monocyclic Non-Steroidal Anti-Inflammatory Drugs in Environment—Sources, Risks, Biodegradation. *Water, Air, & Soil Pollution, 226*(10), 355. https://doi.org/10.1007/s11270-015-2622-0.

17 Huang, H., & Liu, G. (2015). Ozone-Oxidation Products of Ibuprofen and Toxicity Analysis in Simulated Drinking Water. *Journal of Drug Metabolism & Toxicology, 6*(3). https://doi.org/10.4172/2157-7609.1000181.

18 Chopra, S., & Kumar, D. (2020). Ibuprofen as an emerging organic contaminant in environment, distribution and remediation. *Heliyon, 6*(6), e04087. https://doi.org/10.1016/j.heliyon.2020.e04087

19 Zaied, B.K., Rashid, M., Nasrullah, M., Zularisam, A.W., Pant, D., & Singh, L. (2020). A comprehensive review on contaminants removal from pharmaceutical wastewater by electrocoagulation process. *Science of The Total Environment, 726*, 138095. https://doi.org/10.1016/j.scitotenv.2020.138095

20 Brillas, E. (2022). A critical review on ibuprofen removal from synthetic waters, natural waters, and real wastewaters by advanced oxidation processes. *Chemosphere, 286*, 131849. https://doi.org/10.1016/j.chemosphere.2021.131849

21 Ayati, A., Tanhaei, B., Beiki, H., Krivoshapkin, P., Krivoshapkina, E., & Tracey, C. (2023). Insight into the adsorptive removal of ibuprofen using porous carbonaceous materials: A review. *Chemosphere, 323*, 138241. https://doi.org/10.1016/j.chemosphere.2023.138241

22 Costa, F.C.R., dos Santos, C.R., & Amaral, M.C.S. (2023). Trace organic contaminants removal by membrane distillation: A review on mechanisms, performance, applications, and challenges. *Chemical Engineering Journal, 464*, 142461. https://doi.org/10.1016/j.cej.2023.142461

23 The Food and Agriculture Organization of the United Nations (2024). GIEWS — Global Information and Early Warning System. *Country Briefs.* Kazakhstan. https://www.fao.org/giews/countrybrief/country.jsp? code=KAZ

24 Domingues, R.R., Trugilho, P.F., Silva, C.A., de Melo, I.C.N.A., Melo, L.C.A., Magriotis, Z.M., & Sánchez-Monedero, M.A. (2017). Properties of biochar derived from wood and high-nutrient biomasses with the aim of agronomic and environmental benefits. *PLOS ONE, 12(5)*, e0176884. https://doi.org/10.1371/journal.pone.0176884

25 ThermoFisher Scientific (2022). Spectrophotometric analysis of ibuprofen according to USP and EP monographs: Performing pharmaceutical identification tests with an Evolution UV-Visible Spectrophotometer [PDF]. ThermoFisher Scientific. https://assets.thermofisher.com/TFS-Assets/MSD/Application-Notes/AN53349-spectrophotometric-analysis-ibuprofen.pdf

26 Amerkhanova, S., Shlyapov, R., & Uali, A. (2017). The active carbons modified by industrial wastes in process of sorption concentration of toxic organic compounds and heavy metals ions. *Colloids and Surfaces A: Physicochemical and Engineering Aspects*, 532. https://doi.org/10.1016/j.colsurfa.2017.07.015

27 Rambabu, N., Rao, B.V.S.K., Surisetty, V.R., Das, U., & Dalai, A.K. (2015). Production, characterization, and evaluation of activated carbons from de-oiled canola meal for environmental applications. *Industrial Crops and Products, 65*, 572–581. https://doi.org/10.1016/j.indcrop.2014.09.046

28 Egirani, D., Latif, M.T., Wessey, N., Poyi, N.R., & Shehata, N. (2021). Preparation and characterization of powdered and granular activated carbon from Palmae biomass for mercury removal. *Applied Water Science, 11*(1), 10. https://doi.org/10.1007/s13201-020-01343-8

29 Rashidi, N.A., Yusup, S., Ahmad, M.M., Mohamed, N.M., & Hameed, B.H. (2012). Activated carbon from the renewable agricultural residues using single step physical activation: A preliminary analysis. *APCBEE Procedia, 3*, 84–92. https://doi.org/10.1016/j.apcbee.2012.06.051

30 Jun, T.Y., Arumugam, S.D., Latip, N.H.A., Abdullah, A.M., & Latif, P.A. (2010). Effect of Activation Temperature and Heating Duration on Physical Characteristics of Activated Carbon Prepared from Agriculture Waste. *Thai Society of Higher Education Institutes on Environmen. EnvironmentAsia, 3*, 143–148. https://doi.org/10.14456/ea.2010.53

31 Kookana, R.S., Sarmah, A.K., Van Zwieten, L., Krull, E., & Singh, B. (2011). Biochar Application to Soil (pp. 103–143). https://doi.org/10.1016/B978-0-12-385538-1.00003-2

32 Qian, K., Kumar, A., Patil, K., Bellmer, D., Wang, D., Yuan, W., & Huhnke, R. (2013). Effects of Biomass Feedstocks and Gasification Conditions on the Physiochemical Properties of Char. *Energies, 6*(8), 3972–3986. https://doi.org/10.3390/en6083972

33 Wei, S., Zhu, M., Fan, X., Song, J., Peng, P., Li, K., Jia, W., & Song, H. (2019). Influence of pyrolysis temperature and feedstock on carbon fractions of biochar produced from pyrolysis of rice straw, pine wood, pig manure and sewage sludge. *Chemosphere, 218*, 624–631. https://doi.org/10.1016/j.chemosphere.2018.11.177

34 Křikala, J., Diviš, P., Pořízka, J., Duborská, E., & Gajdušek, M. (2024). Application of biochar prepared from wheat bran as the binding phase in diffusive gradient in thin films technique for determination of mercury in natural waters. *Chemical Papers, 78*(6), 7815–7826. https://doi.org/10.1007/s11696-024-03635-8

35 Vaghela, D.R., & Others. (2023). Modelling and optimization of biochar-based adsorbent derived from wheat straw using response surface methodology on adsorption of Pb^{2+}. *International Journal of Environmental Research, 17*(1). Springer Science and Business Media Deutschland GmbH. https://link.springer.com/article/10.1007/s41742-022-00498-3

36 Zhu, X., Qian, F., Liu, Y., Matera, D., Wu, G., Zhang, S., & Chen, J. (2016). Controllable synthesis of magnetic carbon composites with high porosity and strong acid resistance from hydrochar for efficient removal of organic pollutants: An overlooked influence. *Carbon, 99*, 338–347. https://doi.org/10.1016/j.carbon.2015.12.044

37 Cazetta, A.L., Pezoti, O., Bedin, K.C., Silva, T.L., Paesano Junior, A., Asefa, T., & Almeida, V.C. (2016). Magnetic Activated Carbon Derived from Biomass Waste by Concurrent Synthesis: Efficient Adsorbent for Toxic Dyes. *ACS Sustainable Chemistry & Engineering, 4*(3), 1058–1068. https://doi.org/10.1021/acssuschemeng.5b01141

38 Bedia, J., Peñas-Garzón, M., Gómez-Avilés, A., Rodriguez, J.J., & Belver, C. (2020). Review on Activated Carbons by Chemical Activation with FeCl$_3$. *C. Journal of Carbon Research, 6*(2), 21. https://doi.org/10.3390/c6020021

39 Siburian, R., Sihotang, H., Lumban Raja, S., Supeno, M., & Simanjuntak, C. (2018). New Route to Synthesize of Graphene Nano Sheets. *Oriental Journal of Chemistry, 34*(1), 182–187. https://doi.org/10.13005/ojc/340120

40 Liu, Y., Zhao, X., Li, J., Ma, D., & Han, R. (2012). Characterization of bio-char from pyrolysis of wheat straw and its evaluation on methylene blue adsorption. *Desalination and Water Treatment, 46*(1–3), 115–123. https://doi.org/10.1080/19443994.2012.677408

41 Xu, Z., Zhang, T., Yuan, Z., Zhang, D., Sun, Z., Huang, Y., Chen, W., Tian, D., Deng, H., & Zhou, Y. (2018). Fabrication of cotton textile waste-based magnetic activated carbon using FeCl$_3$ activation by the Box–Behnken design: optimization and characteristics. *RSC Advances, 8*(66), 38081–38090. https://doi.org/10.1039/C8RA06253F

42 Anabalón Fuentes, P., Kopp Pailañir, M., Rocha Mella, S., González Quijón, M.E., Marzialetti Bernardi, T., & Cea Lemus, M. (2024). Development of bifunctional biochar/iron oxide composites for tetracycline removal from synthetic wastewater. *Journal of Water Process Engineering, 64*, 105509. https://doi.org/10.1016/j.jwpe.2024.105509

43 Yi, Y., Tu, G., Zhao, D., Tsang, P.E., & Fang, Z. (2020). Key role of FeO in the reduction of Cr(VI) by magnetic biochar synthesised using steel pickling waste liquor and sugarcane bagasse. *Journal of Cleaner Production, 245*, 118886. https://doi.org/10.1016/j.jclepro.2019.118886

44 Özçimen, D., & Ersoy-Meriçboyu, A. (2010). Characterization of biochar and bio-oil samples obtained from carbonization of various biomass materials. *Renewable Energy, 35*(6), 1319–1324. https://doi.org/10.1016/j.renene.2009.11.042

45 Reza, M.S., Afroze, S., Bakar, M.S.A., Saidur, R., Aslfattahi, N., Taweekun, J., & Azad, A.K. (2020). Biochar characterization of invasive Pennisetum purpureum grass: effect of pyrolysis temperature. *Biochar, 2*(2), 239–251. https://doi.org/10.1007/s42773-020-00048-0

46 Barakat, N.A.M., Mahmoud, M.S., & Moustafa, H.M. (2024). Comparing specific capacitance in rice husk-derived activated carbon through phosphoric acid and potassium hydroxide activation order variations. *Scientific Reports, 14*(1), 1460. https://doi.org/10.1038/s41598-023-49675-0

47 Chia, C.H., Gong, B., Joseph, S.D., Marjo, C.E., Munroe, P., & Rich, A.M. (2012). Imaging of mineral-enriched biochar by FTIR, Raman and SEM–EDX. *Vibrational Spectroscopy, 62*, 248–257. https://doi.org/10.1016/j.vibspec.2012.06.006

48 Adeniyi, A.G., Adeyanju, C.A., Emenike, E.C., Otoikhian, S.K., Ogunniyi, S., Iwuozor, K.O., & Raji, A.A. (2022). Thermal energy recovery and valorisation of Delonix regia stem for biochar production. *Environmental Challenges, 9*, 100630. https://doi.org/10.1016/j.envc.2022.100630

49 Anfar, Z., Zbair, M., Ait Ahsiane, H., Jada, A., & El Alem, N. (2020). Microwave assisted green synthesis of Fe$_2$O$_3$/biochar for ultrasonic removal of nonsteroidal anti-inflammatory pharmaceuticals. *RSC Advances*, 10(19), 11371–11380. https://doi.org/10.1039/d0ra00617c

50 Zhu, Q., Zhang, K., Xu, J., Wei, X., Shi, L., Sumita, Li, C., & Lichtfouse, E. (2023). Performance and Mechanism of Fe$_3$O$_4$ Loaded Biochar Activating Persulfate to Degrade Acid Orange 7. *Water*, 15(10), 1849. https://doi.org/10.3390/w15101849

51 Coimbra, R.N., Escapa, C., & Otero, M. (2018). Adsorption separation of analgesic pharmaceuticals from ultrapure and wastewater: Batch studies using a polymeric resin and an activated carbon. *Polymers, 10*(9), 958. https://doi.org/10.3390/polym10090958

52 Jean-Rameaux, B., Brice, T., Sadou, D., Jean-Baptiste, T., Berthelot, S.T., Elie, A., Georges, K.Y., & Samuel, L. (2021). Multi-functionalized cellulosic biomass by plasma-assisted bonding of α-amino carboxylic acid to enhance the removal of ibuprofen in aqueous solution. *Journal of Polymers and the Environment, 29*(4), 1176–1191. https://doi.org/10.1007/s10924-020-01958-7

53 Cao, Y., Nakhjiri, A.T., & Ghadiri, M. (2021). Numerical investigation of ibuprofen removal from pharmaceutical wastewater using adsorption process. *Scientific Reports, 11*(1), 24478. https://doi.org/10.1038/s41598-021-04062-4

54 Chakraborty, P., Show, S., Banerjee, S., & Halder, G. (2018). Mechanistic insight into sorptive elimination of ibuprofen employing bi-directional activated biochar from sugarcane bagasse: Performance evaluation and cost estimation. *Journal of Environmental Chemical Engineering, 6*(4), 5287–5300. https://doi.org/10.1016/j.jece.2018.08.017

55 Moreno-Pérez, J., Pauletto, P.S., Cunha, A.M., Bonilla-Petriciolet, A., Salau, N.P.G., & Dotto, G.L. (2021). Three-dimensional mass transport modeling of pharmaceuticals adsorption inside ZnAl/biochar composite. *Colloids and Surfaces A: Physicochemical and Engineering Aspects, 614*, 126170. https://doi.org/10.1016/j.colsurfa.2021.126170

56 Ngernyen, Y., Petsri, D., Sribanthao, K., Kongpennit, K., Pinijnam, P., Pedsakul R., & Hunt, A. (2023). Adsorption of the non-steroidal anti-inflammatory drug (ibuprofen) onto biochar and magnetic biochar prepared from chrysanthemum waste of the beverage industry. *RSC Advances, 13*(21), 14712–14728. https://doi.org/10.1039/D3RA01949G

57 Álvarez-Torrellas, S., Rodríguez, A., Ovejero, G., & García, J. (2016). Comparative adsorption performance of ibuprofen and tetracycline from aqueous solution by carbonaceous materials. *Chemical Engineering Journal, 283*, 936–947. https://doi.org/10.1016/j.cej.2015.08.023

58 Fröhlich, A.C., dos Reis, G.S., Pavan, F.A., Lima, É.C., Foletto, E.L., & Dotto, G.L. (2018). Improvement of activated carbon characteristics by sonication and its application for pharmaceutical contaminant adsorption. *Environmental Science and Pollution Research, 25*(25), 24713–24725. https://doi.org/10.1007/s11356-018-2525-x

59 Rabbat, C., Pinna, A., Andres, Y., Villot, A., & Awad, S. (2023). Adsorption of ibuprofen from aqueous solution onto a raw and steam-activated biochar derived from recycled textile insulation panels at end-of-life: Kinetic, isotherm, and fixed-bed experiments. *Journal of Water Process Engineering, 53*, 103830. https://doi.org/10.1016/j.jwpe.2023.103830

60 Nguyen, T.K.T., Nguyen, T.B., Chen, W.H., Chen, C.W., Patel, A.K., Bui, X.T., Chen, L., Singhania, R.R., & Dong, C.D. (2023). Phosphoric acid-activated biochar derived from sunflower seed husk: Selective antibiotic adsorption behavior and mechanism. *Bioresource Technology, 371*, 128593. https://doi.org/10.1016/j.biortech.2023.128593

61 Mestre, A.S., Pires, J., Nogueira, J.M.F., & Carvalho, A.P. (2007). Activated carbons for the adsorption of ibuprofen. *Carbon, 45*(10), 1979–1988. https://doi.org/10.1016/j.carbon.2007.06.005

62 Wang, G., Yong, X., Luo, L., Yan, S., Wong, J.W.C., & Zhou, J. (2022). Structure-performance correlation of high surface area and hierarchical porous biochars as chloramphenicol adsorbents. *Separation and Purification Technology, 296*, 121374. https://doi.org/10.1016/j.seppur.2022.121374

63 European Biochar Certificate (EBC) (2012–2023). European Biochar Certificate — Guidelines for a sustainable production of biochar (Version 10.3). Carbon Standards International (CSI). http://european-biochar.org

64 Mestre, A.S., Pires, J., Nogueira, J.M.F., & Carvalho, A.P. (2007). Activated carbons for the adsorption of ibuprofen. *Carbon, 45*(10), 1979–1988. https://doi.org/10.1016/j.carbon.2007.06.005

65 Wang, J., & Guo, X. (2020). Adsorption kinetic models: Physical meanings, applications, and solving methods. *Journal of Hazardous Materials, 390*, 122–156. https://doi.org/10.1016/j.jhazmat.2020.122156

66 Plazinski, W., Rudzinski, W., & Plazinska, A. (2009). Theoretical models of sorption kinetics including a surface reaction mechanism: A review. *Advances in Colloid and Interface Science, 152*(1–2), 2–13. https://doi.org/10.1016/j.cis.2009.07.009

67 Surela, A.K., Chhachhia, L.K., Surela, V.K., & Meena, P.L. (2024). Polypyrrole-Based Composites for Dyes Removal From Contaminated Water. In *Reference Module in Materials Science and Materials Engineering*. Elsevier. https://doi.org/10.1016/B978-0-323-95486-0.00019-3

68 Ramírez-Rodríguez, T., & de Landa Castillo-Alvarado, F. (2012). Application of the intra-particle diffusion model for activated carbon fibers in an aqueous medium. *MRS Proceedings, 1373*, imrc-1373-s4-24. https://doi.org/10.1557/opl.2012.311

69 Pezoti, O., Cazetta, A.L., Souza, I.P.A.F., Bedin, K.C., Martins, A.C., Silva, T.L., & Almeida, V.C. (2014). Adsorption studies of methylene blue onto ZnCl$_2$-activated carbon produced from buriti shells (*Mauritia flexuosa* L.). *Journal of Industrial and Engineering Chemistry, 20*(6), 4401–4407. https://doi.org/10.1016/j.jiec.2014.02.007

70 Ghaedi, M., Golestani Nasab, A., Khodadoust, S., Rajabi, M., & Azizian, S. (2014). Application of activated carbon as adsorbents for efficient removal of methylene blue: Kinetics and equilibrium study. *Journal of Industrial and Engineering Chemistry, 20*(4), 2317–2324. https://doi.org/10.1016/j.jiec.2013.10.007

71 Villabona-Ortíz, Á., Tejada-Tovar, C., & Ortega-Toro, R. (2021). Kinetics and adsorption isotherms of the removal of ibuprofen on a porous adsorbent made from agroindustrial waste. *Desalination and Water Treatment, 209*, 316–323. Desalination Publications. https://doi.org/10.5004/dwt.2021.27515

72 World Health Organization (1999). Guidelines for safe disposal of unwanted pharmaceuticals in and after emergencies. https://www.who.int/publications/i/item/guidelines-for-safe-disposal-of-unwanted-pharmaceuticals-in-and-after-emergencies

---

Roman M. Hasanov[1*] [ID], Rasmiyya E. Mammadova[1] [ID], Sabir Q. Amirov[1] [ID], Zumrud D. Aliyeva[2] [ID]

[1]Azerbaijan State Oil and Industry University, Baku, Azerbaijan;
[2]Institute for Scientific Research and Project-Design Construction Materials named after S.A. Dadashov, Baku, Azerbaijan
(*Corresponding author's e-mail: roman.manar6299@gmail.com)

Effect of Sunflower Oil-Based Metal Soaps on the Thermal Stability of Polyvinyl Chloride

Calcium and aluminum soaps were synthesized by metathesis method based on sunflower oil, a bio-based raw material, and were applied separately and together to polyvinyl chloride (PVC) as environmentally friendly thermal stabilizers. A number of properties of metal soaps were studied and applied to PVC, and the characterization of the mixtures was carried out using Fourier Transform Infrared Spectroscopy (FTIR). Thermogravimetric and differential thermal analysis (TG-DTA) methods were selected to evaluate the thermal stability of the polymer. A commercial NV-710123-branded thermal stabilizer based on calcium-zinc stearate was selected for the comparative evaluation of the effectiveness of metal soaps. According to the TGA results, the Ca and Al soaps were found to be more effective than the commercial thermal stabilizer. While the pure PVC sample lost 8.93 % of its mass at 269.8 °C, the samples added with Ca, Al soaps, commercial thermal stabilizer and a mixture of Ca and Al soaps at a ratio of 4:1 lost 2.7 % of their mass at 263.5 °C, 3.56 % at 265.7 °C, 4.56 % at 263 °C and 4.12 % at 261.1 °C, respectively. While pure PVC lost more than 44 % of its mass at 300 °C, the mass of the polymer sample with the Al soap added, which was the most effective component at this temperature, decreased by only 16.83 %. This is due to the fact that the Al soap component has a barrier effect and prevents the autocatalytic effect of HCl formed during the degradation of PVC. This allows these components to be used as thermal stabilizers.

Keywords: polyvinyl chloride, thermal stabilizers, sunflower oil, metal soaps, calcium soaps, aluminum soaps, metal carboxylates, thermogravimetry

Introduction

Polyvinyl chloride (PVC) is a general-purpose polymer widely used in the packaging industry, construction materials, cable insulation, and many other industries [1]. According to Our World in Data, the production of PVC was 26.20 million tons in 2000, rising to 51.39 million tons in 2019. This growth trend is forecast to continue at a rate of 3–4 % per year until 2030 [2]. The annual growth of the PVC industry and the growing environmental crisis are increasingly in conflict. The global problem of the PVC industry is its low thermal stability and the release of HCl when it decomposes under temperature. This problem also hinders the recycling of polymer waste by various methods and its use as an energy source [3–6].

Thermal stabilizers are used in the manufacture of PVC-based plastics to prevent thermal degradation. There are many brands of commercial thermal stabilizers with different compositions in the world. The most commonly used thermal stabilizer components in this field are organotin compounds, lead salts, Ca-Ba/Zn stearates, and a number of organic secondary compounds [7, 8]. Each of these compounds has its advantages and disadvantages. For instance, although organic and inorganic lead salts are effective as thermal stabilizers, the addition of heavy metal-containing additives to polymers, as lead-based additives added to gasoline, is limited or completely prohibited [9]. In addition, the PVC processing industry can only produce opaque plastics using lead-based heat stabilizers. The increasing amount of recycled plastics and the need to use them over time makes it essential to use polymer additives accordingly. For example, mixing a lead-containing plastic with a tin-mercaptide-containing plastic can lead to the formation of dark-colored lead sulfides [10]. Mixtures of calcium and barium stearates with zinc stearates are commonly used as alternatives to lead-based compounds. These mixtures exhibit comparable effectiveness as thermal stabilizers to lead-based compounds while being environmentally non-hazardous. Although Ba, Ca and Zn stearates are well studied and environmentally friendly thermal stabilizers, they also have a number of disadvantages. Soaps of these three met-

als are more effective in complex form, but Zn soaps form $ZnCl_2$ during the thermal degradation of PVC, which catalyzes the decomposition [11–15]. Several studies have been carried out to address this problem. Various secondary compounds have been investigated to prevent the formation of zinc chlorides and to mitigate the catalytic effects of the resulting chlorides [16, 17]. Another proposed solution is to replace zinc with another metal that has a similar thermal stabilizing effect. However, the synthetic nature of these compounds and their high costs in certain regions are additional disadvantages. The search for polymer additives based on renewable raw materials that are environmentally friendly is one of the current topics. Many components based on bio-based raw materials have been synthesized and investigated as thermal stabilizers for PVC, with many positive results. Metal complexes of plant-derived tannins and lignin have been prepared and investigated as PVC thermal stabilizers. Thermogravimetrically, these components have been more effective than commercial thermal stabilizers, and the aromatic and phenolic rings present in their molecular structure also give them antioxidant and photo stabilizer properties [18–20].

Vegetable oils have attracted the most attention as bio-based raw materials. Many studies have been carried out using vegetable oils and their processing industry wastes to synthesize components that can be used as primary and secondary thermal stabilizers. Epoxy vegetable oil obtained from epoxidation of soybean and sunflower oil has been applied as an auxiliary thermal stabilizer component to zinc soaps [21, 22]. In addition, Ca and Zn soaps based on free fatty acids, which are waste products of palm oil refining, have been synthesized and their effects on thermal stability have been evaluated by applying them separately and together to PVC [23]. The results obtained from all these studies are encouraging and, taking them into account, this paper evaluates the effectiveness of Ca and Al soaps synthesized on the basis of sunflower oil, a vegetable oil, as thermal stabilizer components for PVC.

Experimental

Materials

Refined sunflower oil, potassium hydroxide (KOH), ≥ 98 %; ethanol (C_2H_5OH), ≥ 95 %; hydrochloric acid (HCl), 0.1N; calcium chloride ($CaCl_2$), ≥ 99 %; aluminum sulfate ($Al_2(SO_4)_3 \cdot 18H_2O$) ≥ 98 % were used to synthesize metal soaps. To study the thermal stability, PVC synthesized in suspension of the Russian brand RUSVINYL PVC-S was selected, and for the comparative evaluation of the effectiveness of metal soaps, a NV-1710123-branded Ca/Zn-based thermal stabilizer of Chinese production, was used.

Synthesis of Metal Soaps

The synthesis of metal soaps consisted of two stages. In the first stage, water-soluble potassium soap was synthesized from sunflower oil. In the second stage, Ca and Al carboxylates were synthesized by trans-saponification and metathesis of water-soluble soap. To synthesize the initial water-soluble soap, a 20 % aqueous alkali solution, 10–20 % above the stoichiometric amount was added to vegetable oil in a reactor system equipped with a reflux condenser and heated. This stage of the process was carried out with intensive heating up to 85–90 °C and mixing. The process gradually became cloudy and eventually took on a heterogeneous form. After 40 minutes, to complete the reaction, the mixture was cooled and ethyl alcohol was added to it. As the process continued with heating and mixing, the heterogeneous mixture gradually became homogeneous and took on an orange transparent appearance. After that, the reflux condenser was turned off to ensure the release of vapors. The solution thickened due to the separation of alcohol and water vapors from the mixture and eventually became a solid mass. The soap was first diluted with water to obtain Ca and Al soaps. After neutralizing the excess alkali with a standard hydrochloric acid solution, $CaCl_2$ or $Al_2(SO_4) \cdot 18H_2O$ solution was added. Since the Ca and Al soaps obtained by trans-saponification were insoluble in water, the solution changed color and became opaque (white). The obtained soaps were dried and Ca soaps were ground and then prepared for application to the polymer.

Study of the Properties of Sunflower Oil and Metal Soaps

A number of properties of sunflower oil were investigated. These were the amount of free fatty acids present in the oil according to ISO 660-220, the iodine value according to ISO 3961-2018, the saponification value according to ISO 3657-2020, and the moisture and volatile content according to ISO 662-2016. The total alkali and acid content of the soluble potassium soap was determined according to ISO 685-2020. The moisture content of Ca and Al soaps and the ash content, including the commercial thermal stabilizer component, were determined.

Application of Thermal Stabilizer Components to PVC and Study of Its Thermal Stability

For the application of Ca (CaSUN) and Al (AlSUN) soaps synthesized from sunflower oil, as well as commercial NV-branded thermal stabilizer to the polymer, 5 phr were used and mechanically mixed with the polymer. The mixtures were melted at 180 °C and 150 bar pressure in an ECOPRESS 102 press device made in Turkey and turned into a homogeneous sample. To compare the compatibility of the thermal stabilizer components with the polymer and the degree of mixing, the samples were observed using an Olympus BX53M optical microscope, manufactured in Germany, with an aperture of 0.8. A NETZSCH STA449F3 Jupiter thermogravimeter, manufactured in Germany, was used to investigate the thermal stability of the samples. Thermogravimetric analysis was carried out in an N_2 gas atmosphere by heating to 900 °C at a heating rate of 30 °C/min. The Fourier Transform Infrared Spectroscopy (FTIR) method was selected to characterize the polymer samples. PerkinElmer Spectrum 100 made in Germany was used for FTIR.

Results and Discussion

Properties of Sunflower Oil and Thermal Stabilizer Components

The sunflower oil used for metal soaps was a food grade oil with a high content of refined linoleic and oleic esters. In order to verify the accuracy of its properties indicated by the manufacturer, the content of free fatty acids, iodine value, saponification value and moisture content were tested. From the results obtained it can be concluded that practically all the fatty acids in the vegetable oil are present in the form of glyceride esters (Table 1).

T a b l e 1

Properties of sunflower oil

Saturated fatty acids, %	Oleic acid, %	Linoleic acid, %	Linolenic acid, %	Free fatty acids, %	Iodine value, g/100g	Saponification value, mg/g	Moisture, %
10.7	20.7	67.6	≤ 1	0.062	136	191	0.05 %

By checking the total alkali and fat content of the potassium soap synthesized from sunflower oil, it was determined that the saponification of the oil by the above-mentioned method was over 90 %. CaSUN obtained by trans-saponification of potassium soap was a white hygroscopic compound insoluble in water. After drying and grinding, it formed a white-yellowish powder. When stored in the open air, the color darkened to an orange hue due to the oxidation of unsaturated fatty acids, and the powdery mass densified. When kept in an oven at 103 °C, it lost 5.84 % of its mass, which was related to the residual moisture. On the other hand, AlSUN was obtained during synthesis as a white, opaque, hydrophobic, and sticky mass. The drying process took longer, and after drying, it took on an orange-transparent, gel-like, viscous fluid form. When stored in the open air, no darkening of its color was observed, and after becoming completely transparent, the residual moisture in the oven at 103 °C was no more than 0.2 %. The residual mass (ash) of the components was determined by subjecting them to combustion in a muffle furnace at a temperature of 1000 °C. The ash percentages for CaSUN and AlSUN were determined to be 8.98 % and 4.98 %, respectively. These results were close to the theoretical values. The ash content of the NV-branded commercial thermal stabilizer component was found to be significantly higher than the theoretical ash content of Ca/Zn stearates. This discrepancy can be attributed to the incorporation of an aluminosilicate additive within the thermal stabilizer complex.

Characteristics of PVC Samples

FTIR was used to characterize PVC samples [24–26]. By comparing the spectra of pure PVC with the spectra of samples with added thermal stabilizer components, significant changes were identified and their causes were investigated. In the FTIR spectrum of PVC (Figure 1), characteristic peaks are observed in the range of 600–800 cm^{-1} due to the stretching and bending of the C–Cl bond in the base, and peaks in the range of 2850–2960 cm^{-1} due to the symmetrical and asymmetrical stretching of the bonds present in the polymer chain. All PVC samples have peaks in the corresponding ranges.

When comparing the FTIR spectrum of the PVC sample without a thermal stabilizer component to the FTIR spectrum of the sample with 5 phr commercial thermal stabilizer (Figure 2), changes were observed in the range of 1560–1580 cm^{-1}, corresponding to the asymmetric stretching of the COO$^-$ group of metal car-

boxylates, and in the range of 1400–1420 cm^{-1}, related to its symmetric stretching. In the range of 2850–2920 cm^{-1}, the stretching of the carbon chain of fatty acids overlapped with the PVC-specific peaks in this region, potentially causing changes. The peak at 1463 cm^{-1} originated from the symmetric stretching of the carboxyl groups. The characteristic change for Ca/Zn stearates occurred in the range of 1001–1033 cm^{-1}.

The main changes in the FTIR spectra of polymer samples prepared by applying 5 phr metal soaps synthesized from sunflower oil to PVC were as follows: For PVC/CaSUN (Figure 3), there are peaks at 1574 cm^{-1}, corresponding to the asymmetric stretching of the carboxylate group, and at 1469 cm^{-1}, related to its symmetric stretching. The characteristic peak of PVC at 2920 cm^{-1} was shifted towards 2905 cm^{-1}. In addition, a peak formed at 1368 cm^{-1} indicates the presence of metal soaps and the aliphatic chain of fatty acids. The addition of carboxylates overlapped with the peak at 1420 cm^{-1} resulting from the vibrations of methylene groups. The peak formed at 1716 cm^{-1} may result from –C=C– or ester-like –C=O bonds, which could be related to the unsaturation of the added plant-based components and they contained the small amounts of unreacted vegetable oil.
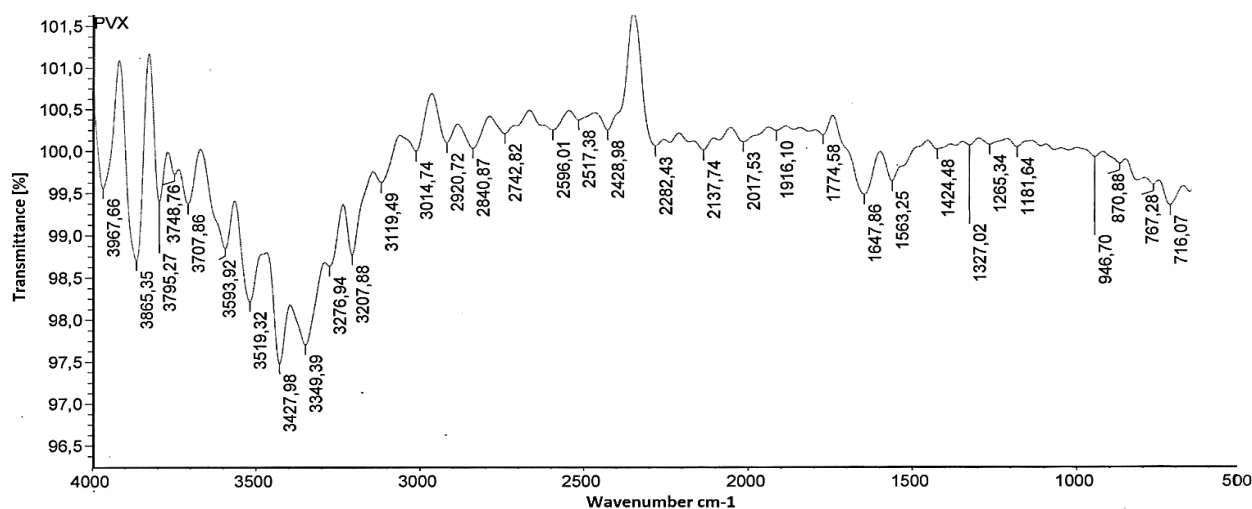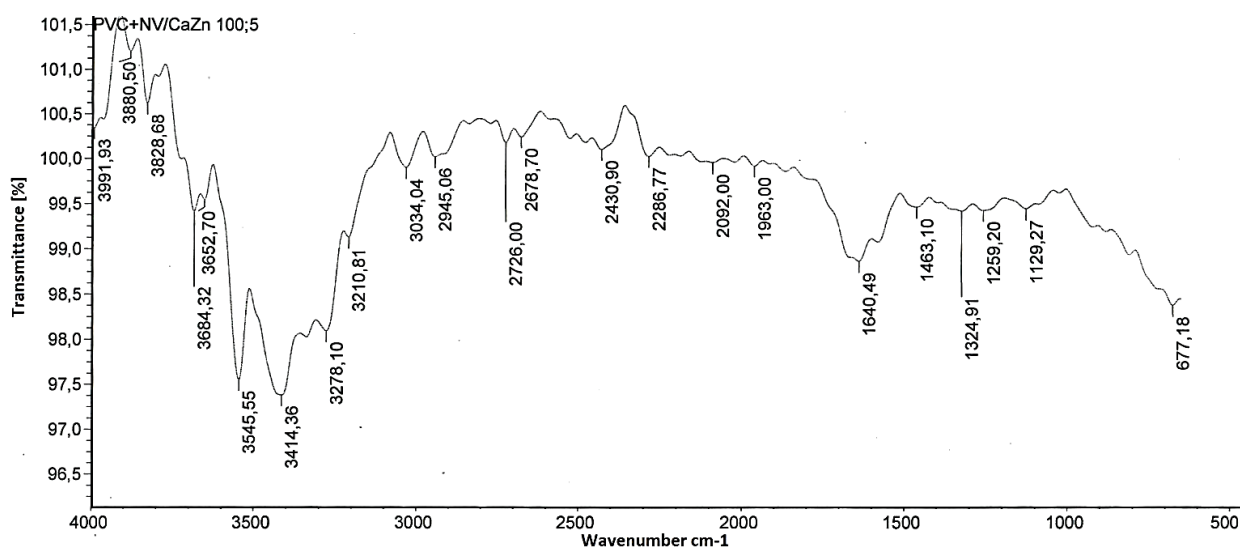

Figure 1. FTIR spectrum of PVC without additives

Figure 2. FTIR spectrum of PVC with commercial thermal stabilizer (NV-Ca/Zn) added

The FTIR spectrum of AlSUN added PVC (Figure 4) shows similarities with PVC/CaSUN. In this spectrum, there is a peak at 1452 cm^{-1} corresponding to the symmetric stretching of carboxylates. Changes occurring in the 3000–3100 cm^{-1} range indicate the formation of unsaturation in the metal soap-added sample. Changes observed in the 1640–1680 cm^{-1} interval may originate from esters or free fatty acids, suggest-

ing that unreacted plant oil or free fatty acids may be present in the composition of AlSUN. Overall, the addition of metal soaps to the polymer resulted in the appearance of new peaks associated with carboxylates in the spectra, along with various spectral changes influenced by multiple factors.
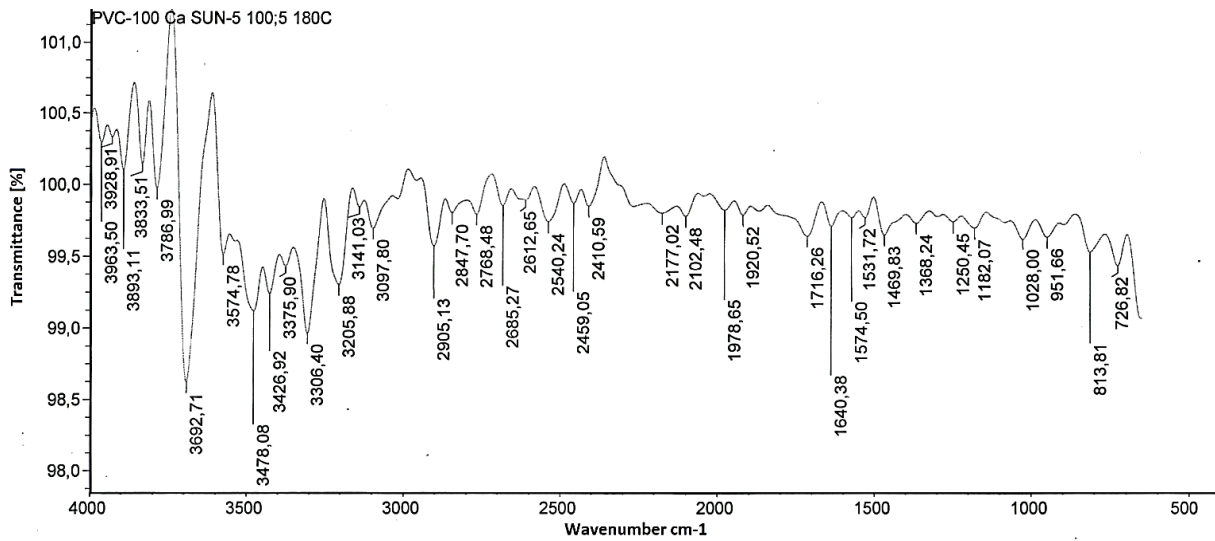

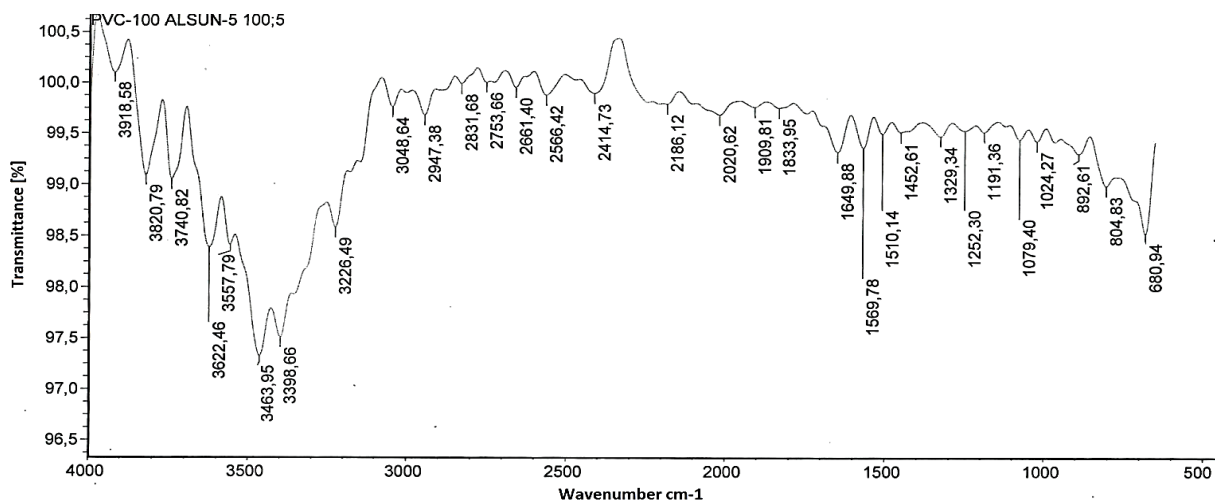Figure 3. FTIR spectrum of PVC with added CaSUN

Figure 4. FTIR spectrum of PVC with added AlSUN

Thermal Stability of PVC

Thermal analysis methods were used to evaluate the thermal properties of the polyvinyl chloride samples. According to thermogravimetric analysis results, the degradation of the polymer samples was a two-stage process. In the first stage, the polymer samples lost more than 50 % of their mass. This mass loss is related to the intense dehydrochlorination of the polymer. The polymer sample exhibited a substantial mass loss in the absence of a thermal stabilizer, commencing at 250 °C and persisting until 340 °C. Within this temperature range, a mass loss of 60 % was observed. The TG-DT-DDTA curves of the unmodified PVC sample are shown in Figure 5. PVC lost 5 % of its mass at 260.8 °C, and at 269.8 °C, it reached 8.93 %. Due to the enhanced degradation and the autocatalysis of the resulting HCl, the mass decreased by 38.23 % at 294.8 °C, 44.1 % at 300 °C, and 54.1 % at 320 °C. According to the DDTA results of the polymer samples, the endothermic reactions, i.e., the degradation, intensified starting around 200 °C, and from 245.4 °C to 286.4 °C. The most significant mass loss occurred in this region, as can be seen from the differential TG curves. Analysis of the DTA curves shows that the energy absorption during the first degradation stage was lower than that of the second stage. This observation can be attributed to the fact that the dehydrochlorination of the polymer occurred more readily than the degradation of the polymer chain.
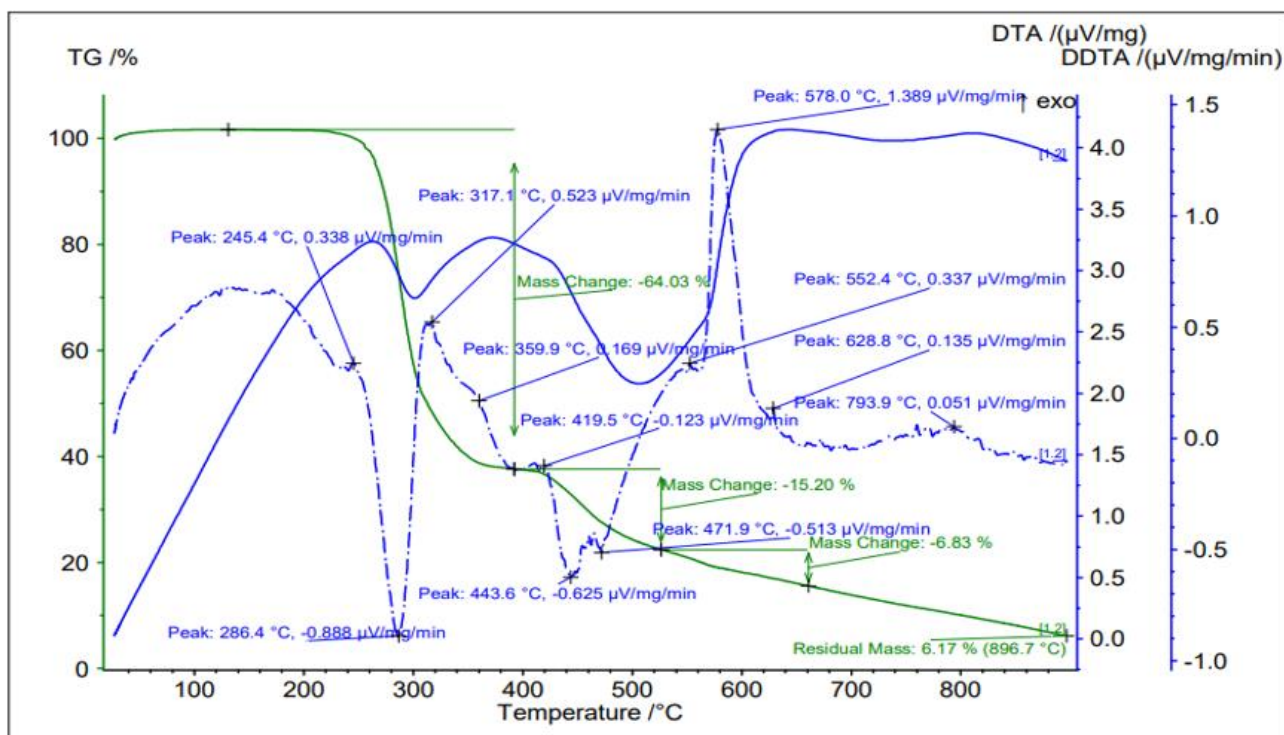
Figure 5. TG-DT-DDTA curves of a PVC sample without additives

During the degradation of the polymer sample with the added commercial thermal stabilizer, the mass loss occurred at a higher temperature and more slowly compared to the unmodified polymer. The PVC/NV sample lost 4.56 % of its mass at 263 °C, 16.14 % at 288 °C, 28.33 % at 300 °C, 46.44 % at 320 °C, and 58.21 % at 340 °C. The thermal properties of the PVC/NV sample are presented in Figure 6, and as can be seen from the curves, the polymer degradation occurred over a wider temperature range compared to the un-modified polymer according to the DDTA results. The observation that the lowest points of the DDTA curves are higher than those of pure PVC suggests that the thermal stabilizer effectively slowed down the degradation of the polymer in the initial stage. The structure of the DTA curves is similar to that of pure PVC, but the parts of the curves corresponding to energy absorption for PVC/NV correspond to higher tem-perature ranges. As can be seen from the curves, although the endothermic reactions started at 220 °C, their intensification started at 250 °C and continued up to 301.5 °C. Overall, the intense degradation reactions continued up 347.3 °C. This was significantly higher than in the sample without thermal stabilizer.

The effect of CaSUN and AlSUN components synthesized from sunflower oil on the thermal stability of PVC was positive. The polymer sample with added CaSUN lost 2.7 % of its mass up to 263.5 °C (Fig-ure 7). As heating continued, it lost 16.73 % at 288.5 °C, 27.38 % at 300 °C, 46.5 % at 320 °C, and 56.29 % at 340 °C. At these temperatures, a large proportion of the Cl atoms in the polymer mass had left the polymer chain. The effect of CaSUN on the thermal stability of PVC was similar to that of the commercial thermal stabilizer. However, as shown by the DDTA results, the intensification of endothermic reactions occurred at higher temperatures and at a faster rate compared to the commercial thermal stabilizer. The degradation reac-tions of the polymer sample with the NV thermal stabilizer component occurred over a wider temperature range and gradually increased in rate. This was due to the Zn soaps in the Ca/Zn mixture producing $ZnCl_2$, and the increase in the amount of this salt accelerated the degradation. In the samples with added CaSUN, it was assumed that the sudden increase in temperature absorption was related to the abrupt decrease in the concentration of metal soaps during the reaction. When examining the DDTA curves, the value of the lowest point of the endothermic peak in the initial degradation stage of the PVC/CaSUN sample is lower than that of the PVC/NV sample, and this is observed at a relatively lower temperature.
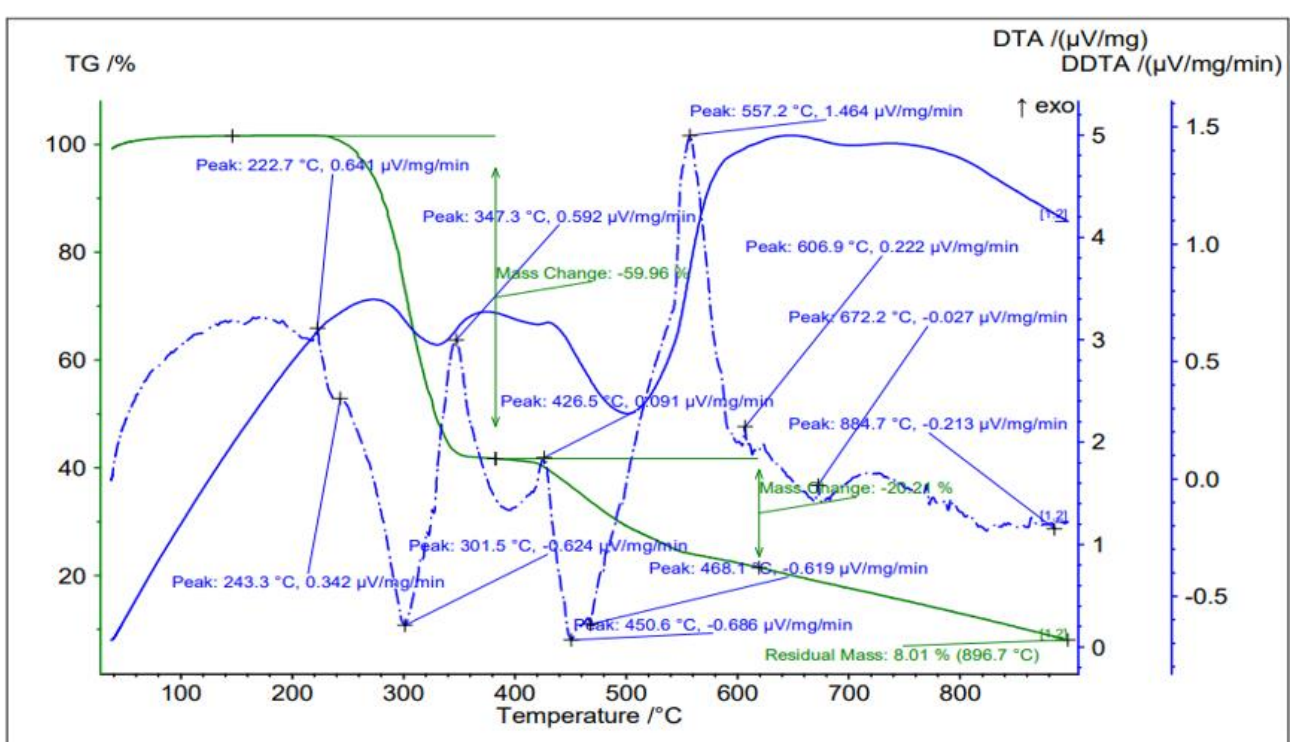
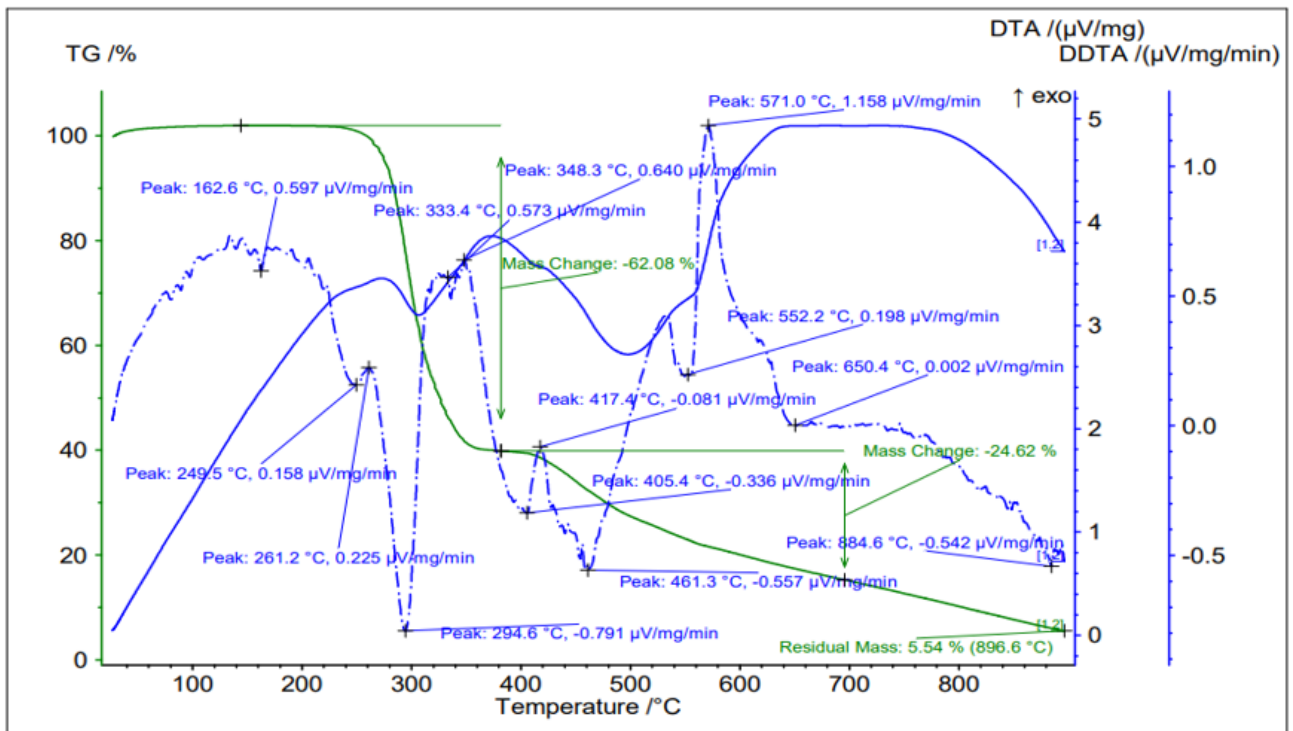Figure 6. TG-DT-DDTA curves of PVC/NV-Ca/Zn sample

Figure 7. TG-DT-DDTA curves of PVC/CaSUN sample

The effect of AlSUN on the thermal stability of PVC, contrary to expectations, was superior to that of the commercial thermal stabilizer and CaSUN. Specifically, it lost 3.56 % of its mass at 265.7 °C, 11.92 % at 290.7 °C, 16.83 % at 300 °C, 34.89 % at 320 °C and 54.22 % at 340 °C, respectively (Figure 8). Compared to other samples, the mass losses were lower at these corresponding temperatures. When comparing the DDTA curves, the intensity of the endothermic reactions continued up to 316.9 °C, which was the highest value among the samples. In addition, the value of the deepest endothermic peak in the DDTA curves is the

highest among the other samples, indicating that the initial degradation stage was relatively slow and occurred over a wide temperature range. Contrary to expectations, the formation of metal chlorides that would catalyze the degradation, as seen in Zn soaps, did not occur in the AlSUN component (or occurred later). In contrast, the mass loss of the polymer started at a higher temperature. This suggests that the hydrophobic gel-like AlSUN (aluminum soap) component synthesized from sunflower oil positively influenced the thermal stability of the polymer. Its gel form allowed it to form a layer on the surface of polymer segments, protecting them from the effects of Cl·and HCl formed during degradation. In short, it played a barrier role against autocatalysis of degradation. This can also be observed under an optical microscope with 5000 K light and a 0.8 aperture diaphragm (Figure 9). The images clearly show that AlSUN had a good compatibility with the polymer and formed a more homogeneous mixture, while the other components were distributed as local inhomogeneous aggregates. The mechanism of the effect of Ca and Al soaps on the stability of PVC is shown in Figure 10.
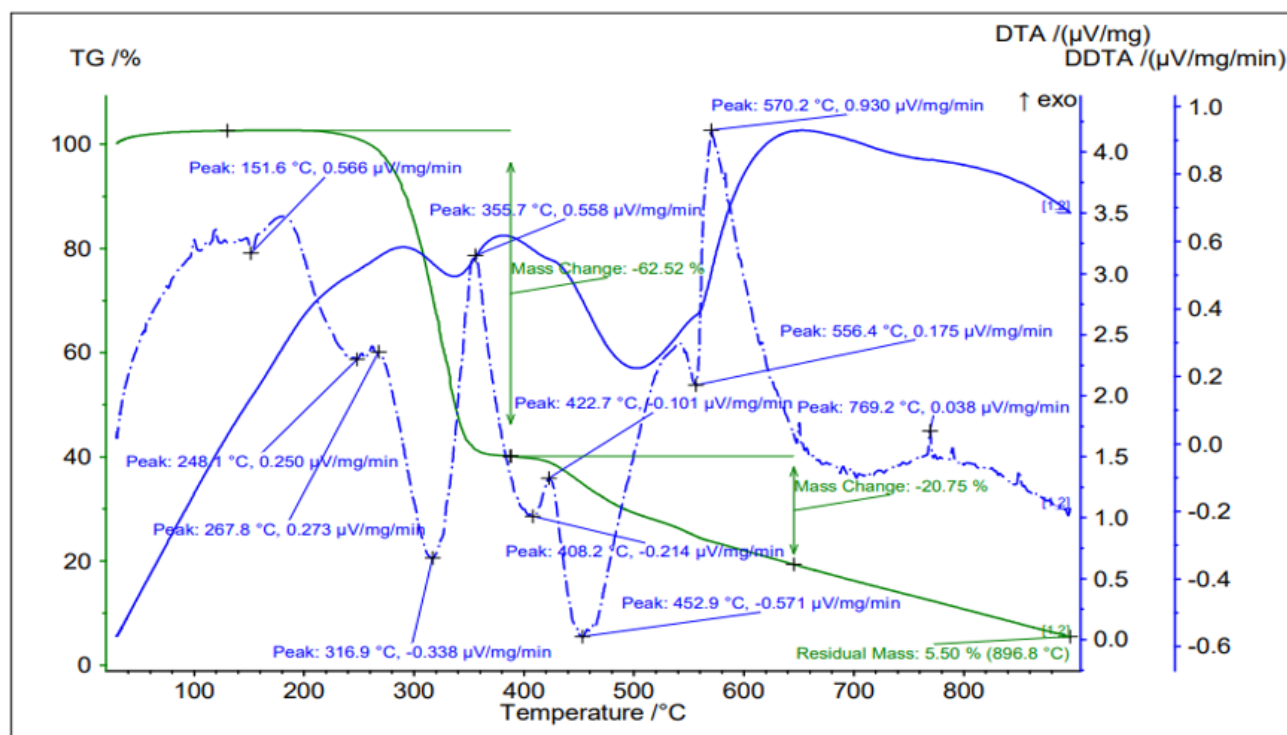

Figure 8. TG-DT-DDTA curves of PVC/AlSUN sample

As with commercial thermal stabilizer, the use of several thermal stabilizer components together in a mixture provides a synergistic effect. This phenomenon has also been observed in many studies [27–30].

Taking all this into account, to determine how the combination of CaSUN and AlSUN synthesized from sunflower oil would affect the polymer, their respective 4:1 mass ratio mixture was applied to PVC. Although the content of the thermal stabilizer mixture was more compatible with CaSUN, it was more effective in improving the thermal stability of the polymer compared to the individual components. The mass loss of the PVC/Ca-AlSUN(4:1) sample was 4.12 % at 261.1 °C, 12.8 % at 286.1 °C, 22.7 % at 300 °C, 40.16 % at 320 °C, and 55.53 % at 340 °C (Figure 11). When comparing these results to other samples, it can be observed that the combination of these two components was more effective than CaSUN and the commercial NV thermal stabilizer. The mechanism of the mixture effect, as shown in Figure 10, was related to the formation of a barrier on the polymer surface by AlSUN and the neutralization of HCl generated during degradation by CaSUN. It is also evident that the intensities of heat release and absorption in the DDTA curves vary significantly over a wide range, indicating the complexity of the process. The values of the endothermic peaks are also higher compared to the other samples, suggesting a lower intensity of degradation. The DTA curves also show that there was no sharp energy absorption during the initial degradation stage, which further supports the previous observations. In summary, the temperatures corresponding to 5 %, 10 %, 20 %, and 50 % mass loss for all the samples analyzed are presented in Table 2.

It can be determined from the optical microscope images of polymer samples with CaSUN and AlSUN components mixed in ratios of 3:1, 4:1, and 5:1, that as the proportion of AlSUN in the mixture increased, a more homogeneous mixture with the polymer was obtained (Figure 12). This suggests that the compatibility of Al soap with PVC was better than that of the Ca soap.
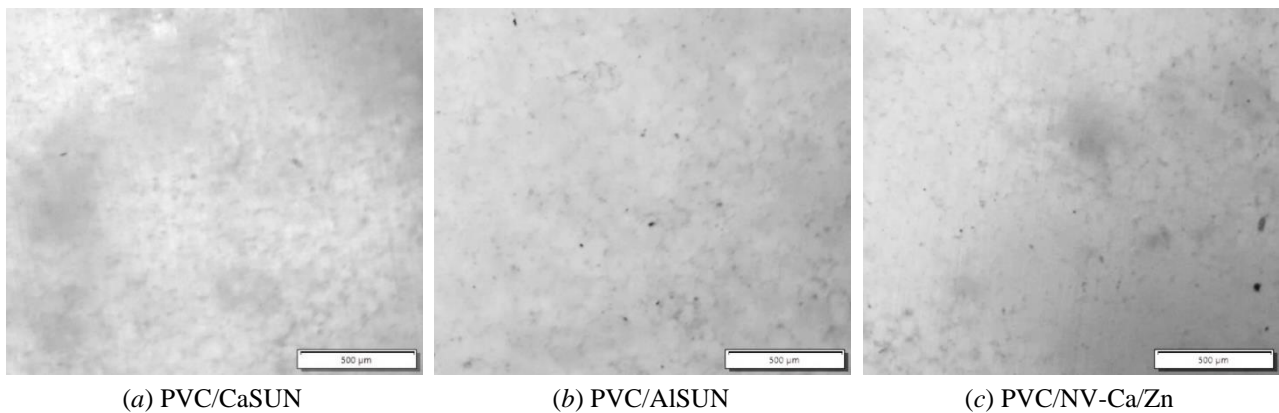

(*a*) PVC/CaSUN   (*b*) PVC/AlSUN   (*c*) PVC/NV-Ca/Zn

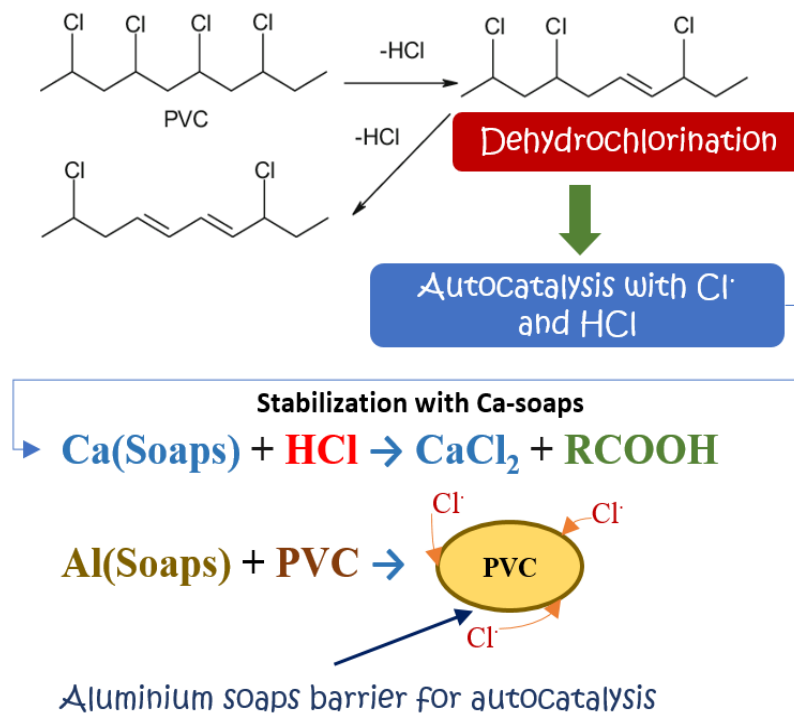Figure 9. Images of polymer samples captured under an optical microscope

Figure 10. Mechanisms of influence of CaSUN and AlSUN on the thermal stability of PVC

Comparing the DTG with a 20 °C interval and the DTA curves (Figures 13 and 14), it can be seen that degradation was most intense in the pure polymer sample. In the DTG curves, the curves for the polymer sample with CaSUN and the polymer sample with the NV commercial thermal stabilizer overlapped on the temperature axis, but degradation occurred more intensively in the sample with CaSUN. When examining the DTG curve of the sample with AlSUN, it is evident that although degradation was intense, it occurred at a higher temperature compared to the other samples. Among the polymer samples, the sample with the Ca-AlSUN mixture showed the lowest intensity of degradation.
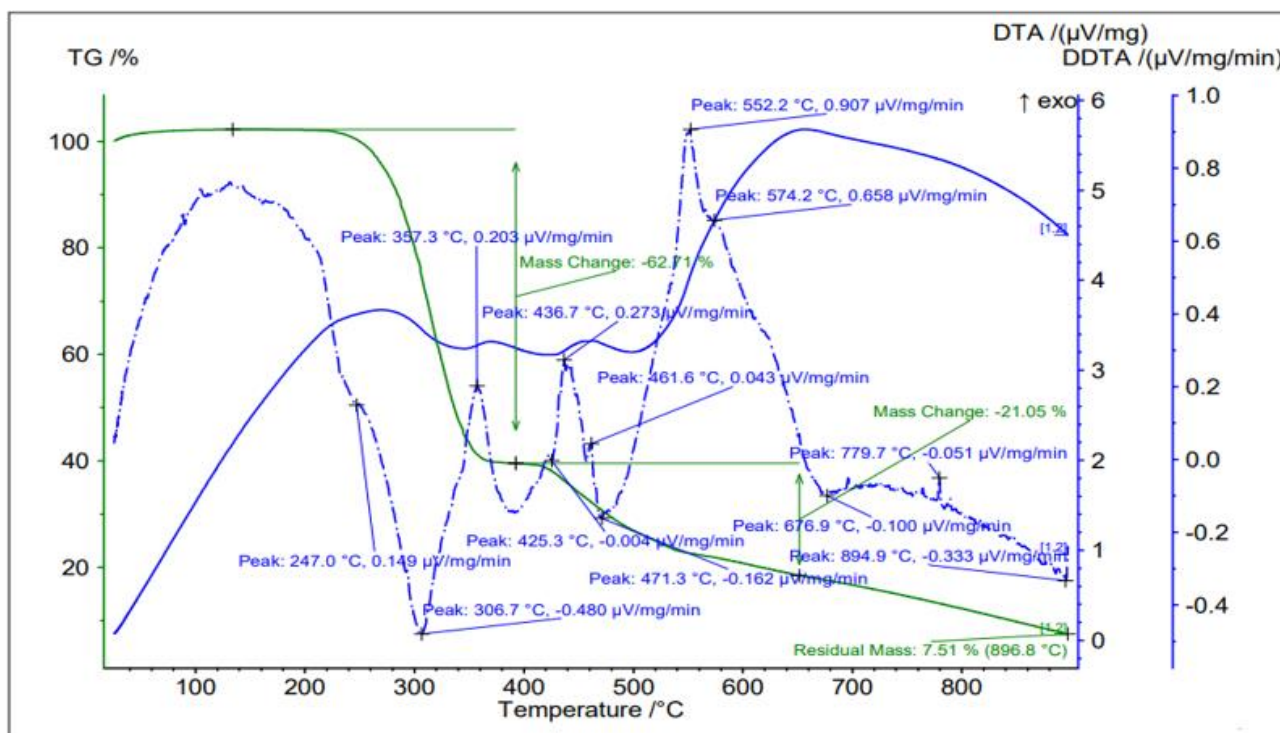
Figure 11. TG-DT-DDTA curves of PVC/Ca-AlSUN (4:1) sample

(*a*) PVC/(CaSUN:AlSUN)(3:1)   (*b*) PVC/(CaSUN:AlSUN)(4:1)   (*c*) PVC/(CaSUN:AlSUN)(5:1)
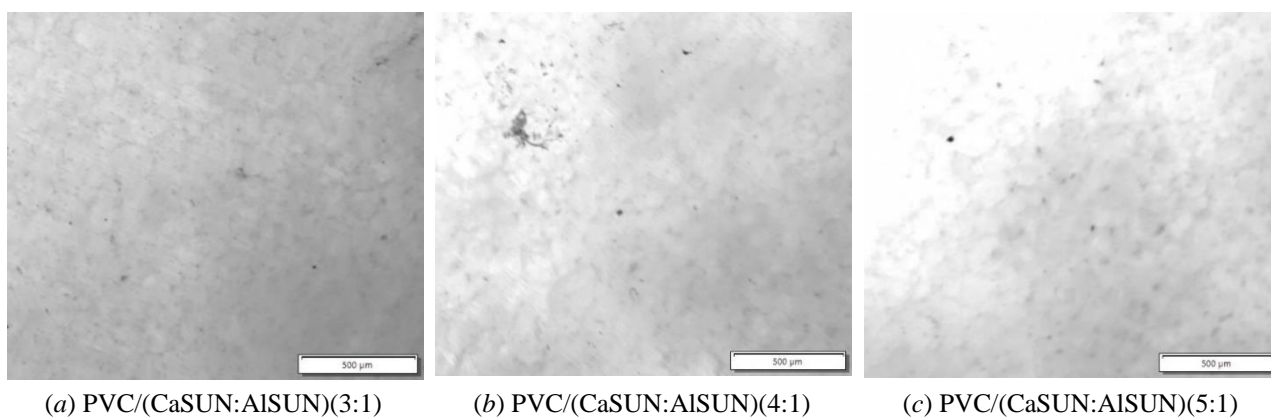
Figure 12. Optical microscope images of PVC samples containing Ca-AlSUN in different ratios

A similar result was obtained when comparing the DTA curves. Upon consideration of the energy absorption during the intensification of the degradation reactions, it can be seen that the polymer sample without additives decomposed at a lower temperature. In the sample containing CaSUN, the intensification of degradation began earlier than in the sample containing the commercial NV thermal stabilizer. Among all the samples it can also be seen from the comparison of the DTA curves that the sample containing AlSUN was which the degradation intensified the latest. In general, it can be seen that the endothermic reactions occurred more slowly in the polymer sample containing the Ca-AlSUN mixture. These findings suggest that the combined use of the two metal soaps leads to a synergistic effect. However, the results obtained and the analysis methods employed do not provide sufficient information to evaluate the color properties of the polymers.

Temperatures Corresponding to 5 %, 10 %, 20 %, and 50 % Mass Loss of Samples, °C

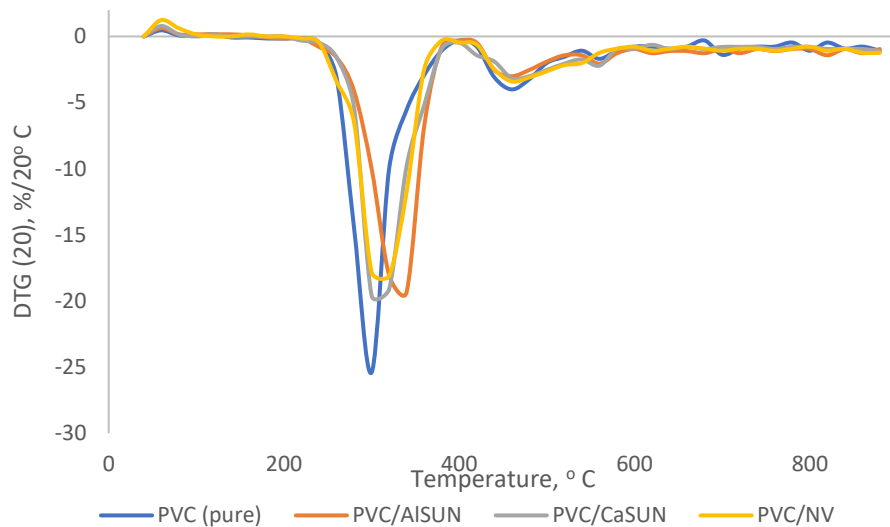| Sample	Mass loss			
	5 %	10 %	20 %	50 %
PVC-pure	256.56	270.71	279.25	313.14
PVC/NV	263.95	274.74	292.07	328.36
PVC/CaSUN	267.60	276.51	291.41	323.73
PVC/AlSUN	270.01	284.96	301.46	335.19
PVC/Ca-AlSUN(4:1)	263.63	278.04	295.66	333.57

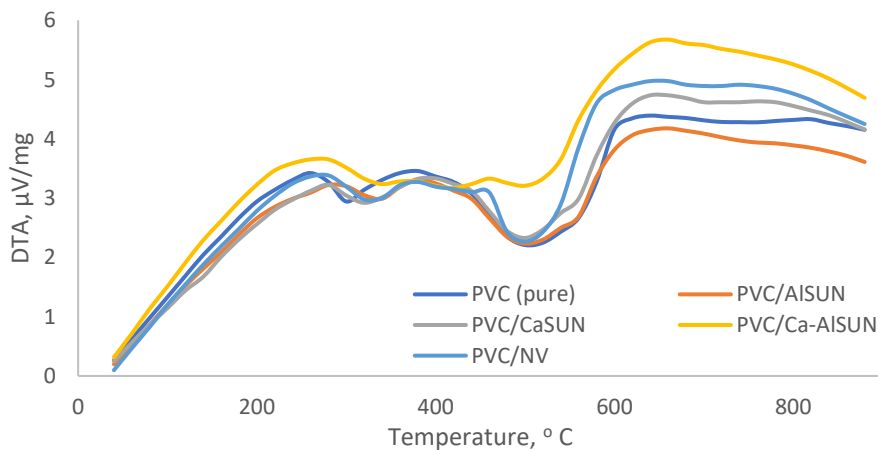Figure 13. DTG curves of polymer samples at 20 °C intervals

Figure 14. Comparison of DTA curves of polymer samples

The research found that Ca and Al soaps synthesized from sunflower oil, a plant-based raw material, improved the thermal stability of PVC as thermal stabilizer components. Compared to NV-branded $CaSt_2$ and $ZnSt_2$ based commercial thermal stabilizer, the metal soaps synthesized from vegetable oil showed several advantages. All this demonstrates the possibility of synthesizing effective polymer additives from renewable resources.

Conclusions

In order to find environmentally friendly, effective, and cost-efficient thermal stabilizer components for PVC, the effect of Ca and Al soaps synthesized from sunflower oil as renewable resource on the thermal sta-

bility of the polymer was investigated. When polymer samples were heated to 300 °C, the polymer sample without additives lost 44.1 % of its mass, while the polymer sample containing a commercial thermal stabilizer lost 28.33 %, the sample containing Ca soap synthesized from sunflower oil lost 27.38 %, the sample containing Al soap lost 16.83 %, and the sample with a mixture of Ca and Al soaps in a 4:1 weight ratio lost 22.7 %. The Ca soaps provided thermal stability by neutralizing HCl, while the Al soaps formed a layer on the surface of the polymer particles, providing a barrier effect. This reduced the autocatalytic effect of HCl generated during degradation. The using these soaps together produced a synergistic effect. This scientific research demonstrated that vegetable oils can be a potential resource for synthesizing polymer additives.

Author Information*

_____

*The authors' names are presented in the following order: First Name, Middle Name and Last Name

Roman Manar Hasanov (*corresponding author*) — 3rd year PhD Student, Department of Technology of Organic Substances and High Molecular Compounds, Azerbaijan State Oil and Industry University, Azadliq Avenue, 20, AZ1010, Baku, Azerbaijan; e-mail: roman.manar6299@gmail.com; https://orcid.org/0009-0002-3587-8393

Rasmiyya Elbrus Mammadova — PhD in Chemistry, Teacher, Azerbaijan State Oil and Industry University, Azadliq Avenue, 20, AZ1010, Baku, Azerbaijan; e-mail: rasmiyyamamedova@rambler.ru; https://orcid.org/0009-0007-8698-8302

Sabir Qarash Amirov — Candidate of Chemical Sciences, Associate professor, Azerbaijan State Oil and Industry University, Azadliq Avenue, 20, AZ1010, Baku, Azerbaijan; e-mail: sabir.54@mail.ru; https://orcid.org/0009-0000-0692-9396

Zumrud Davud Aliyeva — Researcher, Institute for Scientific Research and Project-Design Construction Materials named after S.A. Dadashov, Nasimi district Fizuli street, AZ1014, Baku, Azerbaijan; e-mail: zumrud.d.aliyeva@gmail.com; https://orcid.org/0009-0003-1020-7339

Author Contributions

The manuscript was written through contributions of all authors. All authors have given approval to the final version of the manuscript. CRediT: **Roman Manar Hasanov** conceptualization, data curation, investigation, methodology, funding acquisition, resources, visualization, writing original draft and editing; **Rasmiyya Elbrus Mammadova** data curation, formal analysis, supervision, validation; **Sabir Qarash Amirov** data curation, formal analysis, validation, supervision; **Zumrud Davud Aliyeva** conceptualization, data curation, investigation, methodology, formal analysis.

Conflicts of Interest

The authors declare no conflict of interest.

References

1   Patrick, S.G. (2005). Practical Guide to Polyvinyl Chloride. Rapra Technology Limited. https://pdfcoffee.com/practical-guide-to-polyvinyl-chloride-pdf-free.html

2   Annual production of polymer resin and fibers. (Sep. 2023). Our World in Data. https://ourworldindata.org/grapher/global-plastics-production

3   Oh, S.C. (2009). Dehydrochlorination characteristics of waste PVC wires by thermal decomposition. *Journal of Industrial and Engineering Chemistry*, 15, 438-441. https://doi.org/10.1016/j.jiec.2008.11.010

4   Zheng, XG. (2003). Dehydrochlorination of PVC Materials at High Temperature. *Energy and Fuels*, 17, – p. 896-900. https://doi.org/10.1021/ef020131g

5   Krongauz, V.V., Lee, Y., Bourassa, A. (2011). Kinetics of thermal degradation of poly(vinyl chloride). *Journal of Thermal Analysis and Calorimetry,* 106, 139-149. https://doi.org/10.1016/S0165-2370(03)00024-X

6   Fechter, R.H., Sandrock, C., Labuschagne, F.J.W.J.J. (2018). Modelling the Thermal Degradation and Stabilisation of PVC in a Torque Rheometer. *Chemical Product and Process Modeling*, 13(3), 20170039. https://doi.org/10.1515/cppm-2017-0039

7   Folarin, O.M., Sadiku, E.R. (2011). Thermal stabilizers for poly(vinyl chloride): a review. *International Journal of Physical Sciences*, 6(18), 4323-4330. https://doi.org/10.5897/IJPS11.654

8   El-Ghaffar, A.M.A., Youssef, E.A.M., Afify M.F. (2019). High performance metal stearates thermal stabilizers for poly vinyl chloride. *International journal of petrochemical science & engineering*, 4(4), 162-168. https://doi.org/10.15406/ipcse.2019.04.00116

9   Kalouskova, R., Novotna, M., Vymazal, Z. (2004). Investigation of thermal stabilization of poly(vinyl chloride) by lead stearate and its combination with synthetic hydrotalcite. *Polymer Degradation and Stability*, 85, 903-909. https://doi.org/10.1016/j.polymdegradstab.2004.04.008

10 Turner A., Filella, M. (2021). Hazardous metal additives in plastics and their environmental impacts. *Environment International,* 156, 106622. https://doi.org/10.1016/j.envint.2021.106622

11 González-Ortiz, L. J. (2005). Thermal stability of plasticized poly(vinyl chloride) compounds stabilized with pre-heated mixtures of calcium and/or zinc stearates. *Polymer Degradation and Stability,* 90(1), 154-161. https://doi.org/10.1016/j.polymdegradstab.2005.04.013

12 Li, SM., Yao, YM. (2011). Effect of thermal stabilizers composed of zinc barbiturate and calcium stearate for rigid poly(vinyl chloride). *Polymer Degradation and Stability*, 96(4), 637-638. https://doi.org/10.1016/j.polymdegradstab.2010.12.011

13 Wang, M., Xu, JY. (2006). Effect of pentaerythritol and organic tin with calcium/zinc stearates on the stabilization of poly(vinyl chloride). Polymer Degradation and Stability, 91(9), 2101-2109. https://doi.org/10.1016/j.polymdegradstab.2006.01.011

14 Liao, X., He, B., Chen, X. (2011). Chlorinated poly(vinyl chloride) stabilization by pentaerythritol/calcium-zinc stearate mixtures: the fate of pentaerythritol. *Journal of Vinyl and Additive Technology,* 17(1), 1-8. https://doi.org/10.1002/vnl.20250

15 Ye, F., Guo, X., Zhan, H. (2018). The synergistic effect of zinc urate with calcium stearate and commercial assistant stabilizers for stabilizing poly(vinyl chloride). *Polymer Degradation and Stability,* 156, 193-201. https://doi.org/10.1016/j.polymdegradstab.2018.08.012

16 Borukaev, T.A., Kitieva, L.I., Sultigova, Z.Kh. (2020). Complex Stabilizer Based on Calcium and Zinc Stearates for PVC Compound. *Key Engineering Materials*, 869, 218-223. https://doi.org/10.4028/www.scientific.net/KEM.869.218

17 Borukaev, T.A., Alakaeva, Z.T. (2019). Effect of zinc molybdate on fire-resistance and physical-mechanical of PVC-plastics. *Inorganic Materials: Applied Research*, 10, 396-401. https://doi.org/10.1134/S2075113319020084

18 Shnawa, H.A., Khalaf, Y. (2015). Efficient Thermal Stabilization of Polyvinyl Chloride with Tannin-Ca Complex as Bio-Based Thermal Stabilizer. *Materials Sciences and Applications*, 6(05), 360-372. http://dx.doi.org/10.4236/msa.2015.65042

19 Shnawa, H., Jahani, Y. (2015). The potential of tannins as thermal co-stabilizer additive for polyvinyl chloride. *Journal of Thermal Analysis and Calorimetry*, 2, 1253-1261. https://doi.org/10.1007/s10973-015-5082-2

20 Shnawa, H. (2011). Evaluation of Lignin-Calcium Complex as Thermal Stabilizer for Poly Vinyl Chloride. *Materials Sciences and Applications*, 2, 692-699. https://doi.org/10.4236/msa.2011.26095

21 Baltacioğlu, H., Balköse, D. (1999). Effect of zinc stearate and/or epoxidized soybean oil on gelation and thermal stability of PVC-DOP plastigels. *Journal of Applied Polymer Science*, 74(10), 2488-2498. https://doi.org/10.1002/(SICI)1097-4628(19991205)74:10<2488::AID-APP18>3.0.CO;2-B

22 Benaniba, M.T., Belhaneche-Bensemra, N., Gelbard, G. (2001). Stabilizing effect of epoxidized sunflower oil on the thermal degradation of poly(vinyl chloride). *Polymer Degradation and Stability*, 74(3), 501-505. https://doi.org/10.1016/S0141-3910(01)00170-7

23 Putrawan, I.D.G.A., Indarto, A., Octavia, Y. (2022). Thermal stabilization of polyvinyl chloride by calcium and zinc carboxylates derived from byproduct of palm oil refining. *Heliyon*, 8, e10079. https://doi.org/10.1016/j.heliyon.2022.e10079

24 Benes, M., Milanov, N. (2004). Thermal degradation of PVC cable insulation studied by simultaneous TG-FTIR and TG-EGA methods. *Journal of Thermal Analysis and Calorimetry*, 78, 621-630. https://doi.org/10.1023/B:JTAN.0000046123.59857.ad

25 Zhu, H.M., Jiang, X.G. (2007). TG-FTIR analysis of PVC thermal degradation and HCl removal. *Journal of Analytical and Applied Pyrolysis*, 82, 1-9. https://doi.org/10.1016/j.jaap.2007.11.011

26 Beltran, M., Marcilla, A. (1997). Fourier transform infrared spectroscopy applied to the study of PVC decomposition. *European Polymer Journal*, 33(7), 1135-1142. https://doi.org/10.1016/S0014-3057(97)00001-3

27 Atakul, S., Balköse, D., Ulku, S. (2005). Synergistic effect of metal soaps and natural zeolite on poly(vinyl chloride) thermal stability. *Journal of Vinyl and Additive Technology*, 11, 47-56. https://doi.org/10.1002/VNL.20035

28 Asawakosinchai, A., Jubsilp, C., Mora, P. (2017). Organic heat stabilizers for polyvinyl chloride (PVC): a synergistic behavior of eugenol and uracil derivative. *Journal of Materials Engineering and Performance*, 26(10). 4781-4788. https://doi.org/10.1007/s11665-017-2923-0

29 Han, W., Zhang, M., Li, D. (2019). Design and synthesis of a new mannitol stearate ester-based aluminum alkoxide as a novel tri-functional additive for poly(vinyl chloride) and its synergistic effect with zinc stearate. *Polymers*, 11(6). 1031. https://doi.org/10.3390/polym11061031

30 Balköse, D., Gökçel, HI., Göktepe, SE. (2001). Synergism of Ca/Zn soaps in poly(vinyl chloride) thermal stability. *European Polymer Journal,* 37, 1191-1197. https://doi.org/10.1016/S0014-3057(00)00233-0